

Environmental Earth Sciences

Peiyue Li
Jianhua Wu
Wanfang Zhou
James Wood LaMoreaux

Hazard Hydrogeology

 Springer

Environmental Earth Sciences

Series Editor

James W. LaMoreaux, Tuscaloosa, AL, USA

Environmental Earth Sciences encompass multidisciplinary studies of the Earth's atmosphere, biosphere, hydrosphere, lithosphere and pedosphere and humanity's interaction with them. This book series aims to provide a forum for this diverse range of studies, reporting on the very latest results and documenting our emerging understanding of the Earth's system and our place in it. The type of material published traditionally includes:

- proceedings that are peer-reviewed and published in association with a conference;
- post-proceedings consisting of thoroughly revised final papers; and
- research monographs that may be based on individual research projects


The Environmental Earth Sciences series also includes various other publications, including:


- tutorials or collections of lectures for advanced courses;
- contemporary surveys that offer an objective summary of a current topic of interest; and
- emerging areas of research directed at a broad community of practitioners.

Peiyue Li · Jianhua Wu · Wanfang Zhou ·
James Wood LaMoreaux

Hazard Hydrogeology

 Springer

Peiyue Li 
School of Water and Environment
Chang'an University
Xi'an, Shaanxi, China

Jianhua Wu 
School of Water and Environment
Chang'an University
Xi'an, Shaanxi, China

Wanfang Zhou
Zeo Environmental, LLC
Knoxville, TN, USA

James Wood LaMoreaux
PELA Geoenvironmental, Inc.
Tuscaloosa, AL, USA

ISSN 2199-9155

Environmental Earth Sciences

ISBN 978-3-031-48426-1

<https://doi.org/10.1007/978-3-031-48427-8>

ISSN 2199-9163 (electronic)

ISBN 978-3-031-48427-8 (eBook)

© The Editor(s) (if applicable) and The Author(s), under exclusive license to Springer Nature Switzerland AG 2023

This work is subject to copyright. All rights are solely and exclusively licensed by the Publisher, whether the whole or part of the material is concerned, specifically the rights of translation, reprinting, reuse of illustrations, recitation, broadcasting, reproduction on microfilms or in any other physical way, and transmission or information storage and retrieval, electronic adaptation, computer software, or by similar or dissimilar methodology now known or hereafter developed.

The use of general descriptive names, registered names, trademarks, service marks, etc. in this publication does not imply, even in the absence of a specific statement, that such names are exempt from the relevant protective laws and regulations and therefore free for general use.

The publisher, the authors, and the editors are safe to assume that the advice and information in this book are believed to be true and accurate at the date of publication. Neither the publisher nor the authors or the editors give a warranty, expressed or implied, with respect to the material contained herein or for any errors or omissions that may have been made. The publisher remains neutral with regard to jurisdictional claims in published maps and institutional affiliations.

This Springer imprint is published by the registered company Springer Nature Switzerland AG
The registered company address is: Gewerbestrasse 11, 6330 Cham, Switzerland

Paper in this product is recyclable.

Preface

Since the twentieth century, the global environment has undergone drastic changes, and humanity has faced global environmental problems such as environmental pollution, climate change, ecological degradation, species extinction, desertification, and water scarcity. In recent decades, with changing environments and intensified human activities worldwide, the water cycle and water resources on earth have undergone profound changes, leading to severe water problems and crises in many regions. Water resource issues have become crucial constraints to social and economic development in numerous countries and regions. Groundwater, as an essential component of water resources, plays a vital role in supporting agricultural development, sustaining social and economic development, and ensuring water security.

However, overexploitation and mismanagement of groundwater resources have resulted in a series of negative consequences. One major challenge is the depletion of groundwater levels, particularly in arid and semi-arid regions. Excessive pumping of groundwater for irrigation, industrial use, and domestic purposes has led to the lowering of water tables. This depletion not only affects water availability for various sectors but also causes various geohazards such as land subsidence and the formation of sinkholes. For instance, excessive groundwater pumping has resulted in more than 4000 earth fissures in the North China Plain and Xi'an, China, which pose a significant threat to urban infrastructure development. In Xi'an, the continuous decline of urban groundwater levels has triggered and worsened land subsidence and the formation of earth fissures. This has led to the emergence of seven substantial groundwater drawdown cones in the city, accompanied by eleven significant earth fissures. In the North China Plain, excessive groundwater extraction and aquifer drainage have also caused geological hazards such as land subsidence and earth fissures. As of September 2023, 482 fissures have been identified, affecting seven cities and nearly 70 counties and municipalities.

Furthermore, the long-term existence of groundwater drawdown cones can also contribute to the gradual depletion of groundwater resources, reducing the environmental capacity and self-purification ability of groundwater, thus making it more susceptible to pollution. Coastal cities, in particular, have witnessed declining groundwater levels, leading to the intrusion of seawater and the degradation of

groundwater quality. The formation of drawdown cones has extended the vertical recharge pathways and prolonged the leaching time, resulting in an increased influx of mineral ions into the groundwater. Additionally, the formation of drawdown cones alters the original groundwater flow patterns, leading to the initiation and intensification of inter-aquifer flow. This, in turn, allows poorer quality water to infiltrate freshwater aquifers, further deteriorating water quality and posing a significant threat to safe water supply. In addition, groundwater quality is also at risk due to contamination from various sources such as industrial pollutants, agricultural runoff, and improper waste disposal. This is also a hazard that must be tackled by hydrogeologists and environmentalists. Inadequate waste management practices and the improper use of fertilizers and pesticides contribute to groundwater pollution, posing a significant threat to human health as groundwater is often used for drinking water supplies.

Loess, with its widespread distribution worldwide, possesses unique characteristics such as large pores, high water sensitivity, and strong collapsibility. These characteristics make loess particularly susceptible to geological disasters like loess landslides and ground subsidence when changes occur in the water environment. Remarkably, approximately, 30% of all geological disasters in China take place within the Loess Plateau region, which covers approximately 6.5% of the country's land area. This poses a significant threat to the safety of individuals, their property, and social stability in the affected areas. The primary driving force behind these geological disasters in the Loess Plateau is water. Professor Peng Jianbing, an expert with over 30 years of experience investigating the causes of disasters in the Loess Plateau, vividly describes the infiltration of water in loess as the primary culprit behind loess landslides. Regarding ground subsidence, the urban area of Lanzhou, located in Gansu Province, China, experienced a maximum cumulative subsidence of 151.4 mm between February 2017 and October 2020. Similarly, in the Yan'an New District of Shaanxi Province, China, the maximum cumulative subsidence from 2015 to 2019 reached 250 mm. In the newly filled areas, the subsidence rate exhibited a pattern of slow-fast-very fast changes, closely linked to the specific characteristics of the loess and its hydrogeology.

Hydrogeology plays a crucial role in addressing environmental hydrogeological hazards. Understanding the relationship between hydrogeology and environmental geological hazards is of great importance for accurate disaster prediction and risk reduction. This book is based on this premise and focuses on summarizing six types of environmental hydrogeological hazards, including loess landslides, ground subsidence, earth fissures, karst collapse, mine water inrushes, and groundwater contamination.

The book is divided into seven chapters, with Chap. 1 serving as an introduction that provides the definition of hydrogeological hazards and offers a comprehensive classification of these hazards. The book categorizes hydrogeological hazards into four main types: hazards related to groundwater-induced effective pressure (such as landslides, ground subsidence, and earth fissures), hazards related to groundwater dissolution and hydrodynamics (such as karst collapse), hazards caused by groundwater sudden inflow (such as mine water inrushes), and hazards caused by groundwater contamination.

Chapter 2 Loess Landslides and Water Resources Management commences with an introduction to the characteristics and distribution of loess. It subsequently provides a comprehensive overview of the mechanisms and associated hazards of loess landslides. The chapter emphasizes the generation and progression of loess landslides triggered by agricultural irrigation and rainfall. Lastly, it concludes by outlining the fundamental principles and key measures for preventing and controlling loess landslides. Numerous causes and influencing factors contribute to the occurrence of loess landslides. However, a prevailing and pivotal process entails the interaction between water and loess during agricultural irrigation and rainfall infiltration. The frequent recurrence of loess landslides in China's Loess Plateau is intricately linked to extensive agricultural irrigation practices and concentrated rainfall patterns. Effective management and utilization of local water resources, along with the regulation of irrigation practices, are crucial measures for the prevention and control of loess landslides in loess areas.

Building upon the definition of land subsidence, Chap. 3 delves into the primary causes and consequences associated with this phenomenon. The chapter also focuses on the mechanisms of consolidation and drainage in saturated porous media. From the perspective of groundwater seepage, it introduces the principles of effective stress and theoretical models for water-saturated porous media consolidation, including one-dimensional, two-dimensional, and three-dimensional consolidation models, as well as viscoelastic consolidation models. The chapter further explores methods for predicting land subsidence and measures for its prevention and control. Finally, using the case of loess land subsidence in the Yan'an New District of China, it discusses the prediction and analysis of land subsidence in the area. Land subsidence is a slow-occurring geological hazard that can have significant consequences. Its occurrence is linked to changes in groundwater-induced effective pressure and the gravitational settlement of porous media. In some cases, these two factors can mutually influence each other. With the growth in population and ongoing development of underground spaces and natural resources, the issue of land subsidence may become more critical. Effective prediction and prevention of land subsidence will be a major focus in future hydrogeology research.

Earth fissures (also called ground fissures) are a type of macroscopic surface damage phenomenon where surface rock and soil crack, and form fissures of certain lengths and widths under the influence of internal and external forces. Chapter 4 provides a brief overview of the research history of earth fissures and introduces their different classifications and associated hazards. It explains the formation mechanisms of earthquake-induced fissures, landslide-induced fissures, subsidence-induced fissures, expansive soil-induced fissures, collapsible loess-induced fissures, and ground subsidence-induced fissures. The chapter emphasizes the relationship between groundwater development, coal resource exploitation, and earth fissures, and concludes with preventive measures for earth fissures. Earth fissure disasters directly or indirectly worsen the geological environment, posing a significant threat to human life and property safety, and causing substantial economic losses. As a typical hydrogeological hazard, further in-depth research on the mechanisms and

preventive measures of earth fissures is needed from hydrogeologists and disaster geologists.

Karst collapse often exhibits sudden and rapid development, sometimes on a large scale, with severe consequences. Chapter 5 provides a comprehensive discussion on the types, mechanisms, influencing factors, prediction, and prevention of karst collapse. Unlike ground subsidence, ground collapse tends to occur rapidly, making it difficult to predict. Therefore, effective prediction of ground collapse poses a major challenge in the field of hydrogeology and engineering geology. The contents of this chapter provide the fundamental knowledge to address this challenge.

Mine water inrush not only affects normal mining operations but can also lead to flooding of mines and mining areas, and even cause casualties, posing serious hazards. Chapter 6 focuses on mine water inrush disasters and their prediction. With the hazards of mine water inrush as a background, it analyzes and discusses the mechanisms of mine water inrush under different scenarios. It introduces various methods for calculating the amount of mine water inrush from the perspective of factors influencing it. The content covers the consequences and types of mine water inrush, as well as methods for its prediction. Finally, using the example of the Liuyuanzi Coal Mine in Gansu, China, the chapter showcases the application of numerical simulation to predicting mine water inrush.

Chapter 7 focuses on groundwater contamination and the associated risks and hazards in a karst aquifer. The flow of groundwater in a karst aquifer can be turbulent, deviating from the basic equations used to model groundwater flow. Additionally, the presence of dense non-aqueous phase liquids (DNAPLs) in such environmental settings further complicates the restoration of the aquifer. Due to the unique characteristics of karst aquifers and the behavior of specific contaminants, specialized techniques are required to understand the risks and hazards posed by contaminated groundwater. Innovative techniques are also necessary to mitigate these risks and hazards. This chapter presents a case study that demonstrates the implementation of these techniques to address these complex issues. Based on the introduction to the hydrogeological settings, this chapter analyzes the extent of groundwater contamination, investigates the fate and transport mechanisms of chlorinated hydrocarbon contaminants, and assesses the risks to human health resulting from exposure to these contaminants. Finally, it introduces a framework for mitigating the risks associated with groundwater contamination.

There are various types of hydrogeological hazards associated with groundwater, each with its unique mechanisms. To effectively and comprehensively conduct investigations, assessments, predictions, and prevention of these environmental hydrogeological hazards, it requires collaboration among numerous professionals, including hydrogeologists, geologists, engineering geologists, and environmental geologists. This book is the result of collaboration among frontline practitioners in the fields of hydrogeology, engineering geology, environmental geology, and environmental

science. It represents a small step toward promoting the development of hazard hydrogeology. It is hoped that the publication of this book will inspire more scholars to engage in future research on hazard hydrogeology.

Xi'an, China
Xi'an, China
Knoxville, USA
Tuscaloosa, USA

Peiyue Li
Jianhua Wu
Wanfang Zhou
James Wood LaMoreaux

Acknowledgements

We are immensely grateful to Springer for granting us the opportunity to publish this book. The collaboration with Jim LaMoreaux, the series editor and one of the co-authors, has been invaluable in making this book possible. Their guidance and support have greatly contributed to the success of this endeavor. He would also like to express our sincere appreciation to Annett Buettner and Vijay Kumar Selvaraj, our editorial contacts at Springer. Their prompt assistance and valuable insights have been instrumental in resolving our queries and ensuring a smooth preparation process for the book.

Writing and publishing a book is an arduous task that demands significant dedication and time. We are indebted to our families for their unwavering support throughout this endeavor. The support and understanding of the parents of Peiyue Li and Jianhua Wu have been instrumental in allowing them to focus on their research and writing. He would like to express our deep appreciation to the students who have contributed to the preparation and proofreading of the chapter drafts. Their assistance has been invaluable in ensuring the timely completion of the manuscripts. We extend our gratitude to Dan Wang, Yuanhang Wang, Fei Xu, Dawei Mu, Xiaofei Ren, Yueyue Meng, and Linjie Xie for their invaluable help. We would also like to acknowledge the researchers who engaged in discussions on the early versions of the manuscript. Their insightful comments and feedback have been crucial in enhancing the quality of the manuscripts.

In addition, we are grateful for the research grants that have supported our international research collaborations. We acknowledge the funding received from the National Natural Science Foundation of China (42072286, 42272302, 42090053, and 41761144059) as well as the Qinchuangyuan “Scientist + Engineer” Team Development Program of the Shaanxi Provincial Department of Science and Technology (2022KXJ-005). These grants have played a crucial role in enabling us to conduct our research work. We would also like to acknowledge the support from the National Ten Thousand Talents Program (W03070125), the Fundamental Research Funds for the Central Universities of CHD (300102299301), and the Fok Ying Tong Education Foundation (161098). The financial assistance provided by these organizations has been instrumental in facilitating our international research collaborations.

The year 2024 will be the remarkable milestone of Prof. Peiyue Li's 10th anniversary as a teacher and researcher at Chang'an University. He would like to take this opportunity to express his heartfelt gratitude to the numerous friends and professors who have played an integral role in his early career. Their unwavering support and guidance have been instrumental in shaping Prof. Li's reputation in the scientific community. Their mentorship, encouragement, and assistance have contributed significantly to his growth and success as a teacher and researcher. Their invaluable contributions have paved the way for Prof. Li's professional development and have had a lasting impact on his journey as a researcher.

Contents

1	Introduction to Hydrogeological Hazards	1
1.1	Classification of Hydrogeological Hazards	1
1.2	Hazards Related to Groundwater-Induced Effective Pressure	2
1.3	Hazards Related to Groundwater Dissolution and Hydrodynamics	8
1.4	Hazards Caused by Groundwater Inrushes	9
1.5	Hazards Caused by Groundwater Contamination	13
	References	16
2	Loess Landslides and Water Resources Management	19
2.1	Introduction	19
2.2	Loess Distribution and Loess Landslides	20
2.3	Hazards of Loess Landslides	23
2.4	Agricultural Irrigation and Loess Landslides	26
2.5	Rainfall and Loess Landslides	29
2.5.1	Slow Infiltration Type	30
2.5.2	Infiltration Blockage Type	31
2.5.3	Infiltration Breakthrough Type	32
2.6	Groundwater and Loess Landslides	33
2.6.1	Physical Effects on Soil	34
2.6.2	Chemical Effects on Soil	35
2.6.3	Mechanical Effects on Soil	35
2.7	Prevention and Control of Loess Landslides	38
2.7.1	Principles for Loess Landslide Prevention and Control	39
2.7.2	Main Control Measurements of Loess Landslides	40
	References	42
3	Land Subsidence and Groundwater Seepage	45
3.1	Introduction	45
3.1.1	Causes of Land Subsidence	45
3.1.2	Hazards Caused by Land Subsidence	48

- 3.2 Compressive Water Seepage Mechanisms in Saturated Porous Media 49
 - 3.2.1 Principle of Effective Stress 49
 - 3.2.2 Consolidation of Saturated Porous Media Due to Water Loss 51
- 3.3 Prediction of Land Subsidence 58
 - 3.3.1 Two-Step Calculation Model 58
 - 3.3.2 Partially Coupled Model 61
 - 3.3.3 Fully Coupled Model 62
- 3.4 Land Subsidence Prevention and Control 63
 - 3.4.1 Restricting Groundwater Extraction 63
 - 3.4.2 Managed Aquifer Recharge 64
 - 3.4.3 Adjusting Extracted Aquifers 65
- 3.5 Land Subsidence Prediction: A Case Study in Yan’an New District 66
 - 3.5.1 Prediction Method 67
 - 3.5.2 Accuracy Analysis 68
 - 3.5.3 Analysis of Prediction Results 69
- References 73
- 4 Earth Fissures and Natural Resources Mining 75**
 - 4.1 Introduction 75
 - 4.2 Classifications of Earth Fissures 76
 - 4.2.1 Classification Based on Formation Causes 77
 - 4.2.2 Classification Based on Mechanical Properties 81
 - 4.2.3 Classification Based on Morphology 82
 - 4.3 Hazards of Earth Fissures 83
 - 4.3.1 Road Surface Damage 83
 - 4.3.2 Hazards to High-Speed Railway Projects 86
 - 4.3.3 Impacts on Buildings 86
 - 4.4 Formation Mechanisms of Earth Fissures 89
 - 4.4.1 Formation Mechanisms of Earthquake-Induced Earth Fissures 89
 - 4.4.2 Mechanism of Formation for Landslide Earth Fissures 90
 - 4.4.3 Mechanism of Formation for Collapse Earth Fissures 91
 - 4.4.4 Mechanism of Formation for Expansive Soil Fissures 92
 - 4.4.5 Mechanism of Formation for Collapsible Loess Earth Fissures 93
 - 4.4.6 Mechanism of Formation for Ground Subsidence Fissures 93
 - 4.5 Groundwater Development and Earth Fissures 94
 - 4.6 Coal Development and Earth Fissures 97
 - 4.7 Prevention and Control of Earth Fissures 99
 - 4.7.1 Preventive Measures 99
 - 4.7.2 Remedial Measures 100
 - References 102

5 Karst Collapse and Its Management	105
5.1 Introduction	105
5.2 Types of Karst Collapse	108
5.2.1 Classification of Karst Collapse	108
5.2.2 Main Characteristics of Different Types of Karst Collapse	111
5.3 Mechanisms of Karst Collapse	115
5.3.1 Subsurface Erosion Theory	116
5.3.2 Vacuum Erosion Theory	117
5.3.3 Three-Mechanism Theory for Karst Collapse	118
5.4 Influencing Factors of Karst Collapse	121
5.4.1 Fundamental Conditions for the Formation of Karst Collapse	122
5.4.2 Factors Inducing Karst Collapse	125
5.5 Prediction of Karst Collapse	127
5.5.1 Comprehensive Geological Model	128
5.5.2 Mathematical and Physical Prediction Models	132
5.6 Prevention and Control of Karst Collapse	136
5.6.1 Prevention of Karst Collapse	136
5.6.2 Management of Karst Collapse	138
References	141
6 Mine Water Inrush and Its Prediction	143
6.1 Introduction	143
6.2 Hazards of Mine Water Inrush	144
6.3 Types of Mine Water Hazards	146
6.3.1 Hazards Caused by Surface Water	146
6.3.2 Hazards Caused by Abandoned Mine Pools	147
6.3.3 Hazards Caused by Pore Water	147
6.3.4 Hazards Caused by Coal Seam Roof Water	148
6.3.5 Hazards Caused by Coal Seam Bottom Water	148
6.3.6 Hazards Caused by Karst Water	149
6.3.7 Hazards Caused by the Fracture Zone	149
6.3.8 Hazards Caused by Acidic Mine Water	150
6.4 Prediction Methods of Mine Water Inrush	150
6.4.1 Overview of Mine Inrush Prediction Methods	150
6.4.2 Analytic Method	152
6.4.3 Numerical Simulation Method	157
6.5 Numerical Prediction of Mine Water Inrush: A Case Study in Liuyuanzi Coal Mine, China	162
6.5.1 Overview of the Mining Area	163
6.5.2 Model Setup	166
6.5.3 Prediction of Mine Water Inrush	171
References	176

7 Groundwater Contamination and Induced Risk and Hazard in a Karst Aquifer 179

7.1 Investigation Approaches 180

 7.1.1 On-Site Mobile Laboratory Application to Investigating Contamination Distributions 181

 7.1.2 Earth Resistivity Imaging and Induced Polarization Imaging 185

 7.1.3 Monitoring Well Installation and Aquifer Testing 190

 7.1.4 Borehole Logging and Design of Multi-port Monitoring Well 194

7.2 Hydrogeological Characterization 198

 7.2.1 Groundwater Flow 201

 7.2.2 Irregular Bedrock Surface 203

 7.2.3 Unstable Boreholes 205

 7.2.4 Large Variation in Aquifer Properties 206

7.3 Extent of Contamination 207

 7.3.1 Extent of Contamination in the Overburden 207

 7.3.2 Extent of Contamination in the Bedrock Formation 209

7.4 Fate and Transport Mechanisms of Chlorinated Hydrocarbon Contaminants 210

 7.4.1 Dense Non-aqueous Phase Liquid Transport 210

 7.4.2 Aqueous Phase Transport 214

 7.4.3 Vapor Phase Transport Processes 218

 7.4.4 CVOC Fate Processes 219

 7.4.5 Bio-reductive Dechlorination of Organic Compounds 221

 7.4.6 Abiotic Degradation 223

 7.4.7 Aerobic/Anaerobic Oxidation 225

 7.4.8 Secondary Sourcing 226

 7.4.9 Evidence of Natural Attenuation 230

7.5 Pathway-Focused Risk Assessment 235

 7.5.1 Exposure Pathway Model 236

 7.5.2 Exposure Point Concentrations 237

 7.5.3 Exposure Parameters and Exposure Intake Equations 238

 7.5.4 Toxicity Assessment for Non-carcinogens 238

 7.5.5 Toxicity Assessment for Carcinogenicity 245

 7.5.6 Toxicity Assessment for TCE 246

 7.5.7 Risk Characterization 247

 7.5.8 Risk Assessment Uncertainty 249

7.6 Cost-Effective Approach for Groundwater Contamination Induced Risk Mitigation 251

7.7 Summary 252

References 255

Index 257

About the Authors



Prof. Peiyue Li is currently working as a full professor in the field of hydrogeology and environmental sciences at Chang'an University, China. Professor Peiyue Li holds a Ph.D. in Groundwater Science and Engineering from Chang'an University (2014) and has wide experience in groundwater quality assessment, hydrogeochemistry, and groundwater modeling. He has edited and co-edited nine textbooks and academic monographs and published over 180 articles in refereed journals on topics that range from groundwater quality assessment and groundwater hydrochemistry to groundwater pumping tests and in situ tracer tests. He at present serves as Associate Editors for *Exposure and Health*, *Mine Water and the Environment*, *Archive of Environmental Contamination and Toxicology*, *Environmental Monitoring and Assessment*, *Discover Water*, *Human and Ecological Risk Assessment*, and *Frontiers in Environmental Science*, published by Springer Nature, Taylor and Francis, and Frontiers, and is an editorial board member for *Water*, *Hydrology*, and some national key journals. He was selected into the national "Ten Thousand Talents Program" and awarded the Ministry of Education's Young Changjiang Scholars in 2018. He has led or is leading more than 30 research projects funded by the National Natural Science Foundation of China (NSFC) and other national and provincial agencies and has been awarded one of the most highly cited researchers by Clarivate, Elsevier, and other organizations.



Dr. Jianhua Wu is currently working as a full professor in the Department of Hydrology at the School of Water and Environment, Chang'an University. Her research mainly focuses on hydrology and water resources in arid areas, loess seepage and its disaster mechanisms, and groundwater environmental protection. She has led and participated in more than ten research projects funded by the National Natural Science Foundation of China (NSFC). She has published more than 80 academic papers in international journals, including over 50 as the first/corresponding author in SCI-indexed journals. The topics of her publications cover groundwater quality assessment, groundwater hydrochemistry, human health risk assessment related to exposure to groundwater pollution and groundwater circulation in loess aquifers. She has 16 papers selected as highly cited papers and hot papers by Essential Science Indicators (ESI). Her paper co-authored with colleagues was published in *Nature* and was recognized as one of the top ten highlights of *Nature Journal* in 2014. She currently serves as an associate editor for the international journal *Exposure and Health* and is a reviewer for various international journals. She has been awarded one of the most highly cited researchers by Clarivate, Elsevier, and other organizations.



Dr. Wanfang Zhou has more than 30 years' experience in hydrogeology and environmental engineering. His research interests include environmental and engineering impacts of karst, prevention and mitigation of mining-induced hazards, development of eco-friendly coal mining methods, and characterization and remediation of contaminated land. He provided technical support to more than 300 research and consulting projects. He is the author or co-author of eight professional books, six topical journal issues, and more than 80 peer-reviewed articles. He serves as an associate editor of *Mine Water and the Environment* and on editorial board in *Environmental Earth Sciences* and *Carbonates and Evaporites*.



Dr. James Wood LaMoreaux is Chairman of P. E. LaMoreaux and Associates, Inc. (www.pela.com), an international consulting firm providing services in hydrogeology, geology, environmental sciences, and engineering. He received his M.S. and Ph.D. and degrees from Syracuse University in 1970 and 1976, respectively. Dr. LaMoreaux serves as Editor-in-Chief of the international journals *Carbonates and Evaporites*, *Sustainable Water Resources Management* and *Discover Water* and Emeritus Editor of *Environmental Earth Sciences* published by Springer of Heidelberg Germany. He also serves on the advisory boards for Springer Briefs and Theses and is Editor of Springer's *Environmental Earth Sciences*, *Cave and Karst Systems of the World*, and *Professional Practice in Earth Sciences* Book Series. Dr. LaMoreaux serves as Chairman of the International Association of Hydrogeologists (IAH) Commission on Mineral and Thermal Water, Member of the IAH Karst Commission, and Past President of the IAH US National Committee. He is the author and/or editor of numerous technical publications. Dr. LaMoreaux has served as a member of the Ground Water, Hazardous Waste, Industrial Waste, Public Education, and Program Committees of the Water Environment Federation (WEF) and represented Alabama as State Director to WEF. He served as a member of the Science Advisory Committee for the EPA-funded Urban Waste Management and Resources Center at the University of New Orleans.

Chapter 1

Introduction to Hydrogeological Hazards



Groundwater is a vital water resource that provides beneficial uses to human beings, habitats, and the ecological environment. It also causes adverse impacts to the same beneficial users. This chapter summarizes the various adverse impacts related to groundwater.

1.1 Classification of Hydrogeological Hazards

A hydrogeological hazard refers to the potential dangers arising from the unfavorable combination of hydrogeological processes and ground conditions, which can pose risks to human health and safety, as well as the environment. Groundwater plays important roles in the generation of these geohazards. Such hazards come in various sizes and can occur naturally or be triggered by anthropogenic activities. Although not every hazard is predictable; however, many can be controlled and mitigated through land use planning, site characterization, insurance, and site-specific engineering measures. Each hazard-prone site is unique, and establishment of a site-specific conceptual site model (CSM) is essential to understand its occurrence, perform risk assessment, and identify mitigation measures. A CSM describes sources of hazards known or suspected to be present at a site and exposure pathways for current and potential receptors and identify additional information needed to develop technically sound decisions. An effective CSM may consist of the following four profiles:

- **Physical profile:** This profile encompasses the natural elements that have the potential to influence the release, fate, and transport of source materials, as well as accessibility. Example data include topographic features, meteorological data, lithological formations, geophysical and geochemical data, groundwater dynamics and aquifer characteristics.

- **Anthropogenic activity profile:** This profile describes human activities that may trigger hydrogeological hazards. Example data include construction, mining, tunneling, groundwater pumping, and waste disposal.
- **Exposure profile:** This profile entails gathering information that is utilized to identify and assess relevant exposure scenarios, receptors, and receptor locations. This includes collecting data on various factors such as the locations of resource use sites (e.g., water supply wells), infrastructure (e.g., railways), and population density.
- **Ecological environment profile:** This describes the natural habitats and ecological receptors present on and around the site. Example data include identification of any ecological receptors in relation to habitat type such as wetland, desert, endangered or threatened species.

CSM is also a great tool to classify the various hydrogeological hazards. The primary mechanisms by which groundwater can cause hydrogeological hazards can be categorized into four main categories: hazards caused by groundwater induced effective pressure, hazards caused by groundwater dissolution capability, hazards caused by groundwater itself, and hazards caused by groundwater contamination. Such a division is not independent because some hazards can be caused by more than one mechanism. For each category, the type of hazards is further classified with the three components of each CSM: the source of hazard, the receptor, and the exposure pathway. Three exposure pathways, i.e., incomplete pathway, inconclusive pathway, and complete pathway, are included for two types of receptors, human beings and the environment. The symbols used in the following classification figures are for illustrative purposes only. At each study site, these exposure pathways need to be tailored to site-specific conditions.

1.2 Hazards Related to Groundwater-Induced Effective Pressure

Figure 1.1 summarizes the hazards related to groundwater-induced effective pressure. These hazards tend to be safety-related physical damages. The source of such hazards includes rock, soil, and mud. The commonly encountered ground subsidence, landslide, mudslide, earth fissure, and earthquake belong to this group.

The groundwater level or potentiometric difference drives the groundwater flow in an aquifer but also applies pore water pressures to solid particles. Changes in either hydrostatic or hydrodynamic pressures may result in loss of force balances on the solid mass. It has been long reported that groundwater pumping is the primary cause for land subsidence. According to a report from the United States Geological Survey (USGS) (USGS 2000), it is stated that over 80% of land subsidence in the US is directly linked to the extraction of groundwater. In the arid region of Arizona, the pumping of groundwater has led to significant declines in water levels, reaching up to 500 feet, and has been associated with subsidence measurements of up to 12.5 feet

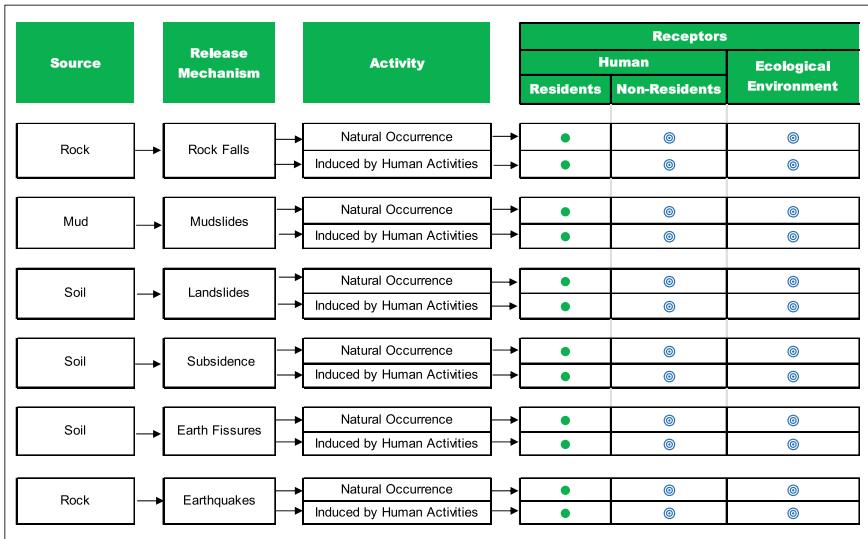


Fig. 1.1 Summary of hazards related to groundwater-induced effective pressure

(USGS 2003). The removal of groundwater from an aquifer reduces the pore water pressure, causing the soil above to lose support. As a result, the effective pressure increases, leading to compaction of the aquifer layers and an overall reduction in soil pore space, ultimately resulting in ground subsidence. The impacts of subsidence extend beyond the stability of buildings and infrastructure; they also include the formation of earth fissures, increased flooding, and the intrusion of seawater. One notable example of the devastating effects of land subsidence can be observed in the case of Hurricane Katrina in New Orleans. The city had experienced land subsidence, partly attributed to groundwater pumping, which had caused its elevation to fall below sea level (<http://www.guttertogulf.com/Why-is-New-Orleans-sinking>). It is worth noting that while certain aquifer systems can recover to some extent through artificial recharge, the vertical deformation caused by subsidence often leads to permanent changes in the aquifer system. These changes can include a loss of groundwater storage capacity and reduced water transmission abilities. This is particularly true when the compressed soil layers consist of fine-grained clays, which have low permeability and limited capacity to regain their original volume.

The effective pressure mechanism is also used to explain the 710 small earthquakes that were recorded in Denver, Colorado between 1962 and 1965. The initial seismic event occurred approximately one month after the injection of contaminated wastewater into a disposal well located near Denver. This particular well was drilled into fractured Precambrian schist and granite gneiss, reaching a depth of 3671 m. The injection process involved rates of 12–25 L/s, with injection pressures ranging from $3\text{--}7 \times 10^6 \text{ N/m}^2$. According to Evans (1966), there was a strong correlation between the frequency of earthquakes and the volume of waste injected. The elevated

fluid pressures resulting from the injection had the effect of reducing the effective pressure, which could have impeded the movement of deep-seated faults. Consequently, these changes in pressure potentially triggered minor fault movements. In addition to decreases in effective pressure, the injected water may have reduced the shear strength of some faults. The same mechanism can be used to explain small earthquakes in the vicinity of reservoirs such as those in the Three Gorge Reservoir of China (Huang et al. 2018).

Landslides are a geohazard that can occur on various scales, ranging from smaller man-made slopes in highway cuts, earth dams, and open pit mines to larger natural hills. These events often take place during or after periods of precipitation. The influence of groundwater on slope stability is a significant factor in understanding landslides in soil slopes. The concepts and failure mechanisms used in slope stability analysis apply to both large catastrophic landslides and simpler embankment failures.

Based on hillslope hydrogeology, Fig. 1.2 shows two schematic CSM of a uniform slope aquifer, one assuming horizontal submergence and the other assuming parallel submergence. The horizontal submergence scenario applies to hydrogeological conditions under which the slope is part of a regional aquifer system. The parallel submergence occurs when the slope aquifer is local. Hillslope subsurface hydrologic systems are typically characterized by their complexity and rarely maintain a steady state. When rainfall occurs, the hydrologic response of a hillslope involves intricate interactions between saturated and unsaturated conditions, resulting in a dynamic and transient process. The extent of water level rise, the duration of the rise, and the time lag between the rainfall event and the subsequent rise can exhibit significant variations, influenced by factors such as the hillslope configuration, rainfall duration and intensity, initial moisture conditions, as well as the saturated and unsaturated hydrogeologic characteristics of the materials present in the hillslope. However, the simplified conceptual models illustrate how groundwater triggers landslides.

The definitions of the various forces and symbols depicted in Fig. 1.2 under steady state are as follows:

W_A	Total weight of the slope mass.
W_P	Total weight of the passive mass.
N_A	Effective force normal to the failure plane of the slope mass.
N_P	Effective force normal to the failure plane of the passive barrier.
γ_{dry}	Dry unit weight of the cover soil.
$\gamma_{\text{sat'd}}$	Saturated unit weight of the cover soil.
γ_w	Unit weight of water.
h	Thickness of the cover soil.
L	Length of the slope measured along the failure plane.
β	Soil slope angle beneath the failure plane.
δ	Friction angle of the cover soil.
C_a	Adhesive force between the cover soil of the slope mass and the failure plane.
c_a	Adhesion between the cover soil of the slope mass and the failure plane.
C	Cohesive force along the failure plane of the passive barrier.
c	Cohesion of the cover soil.

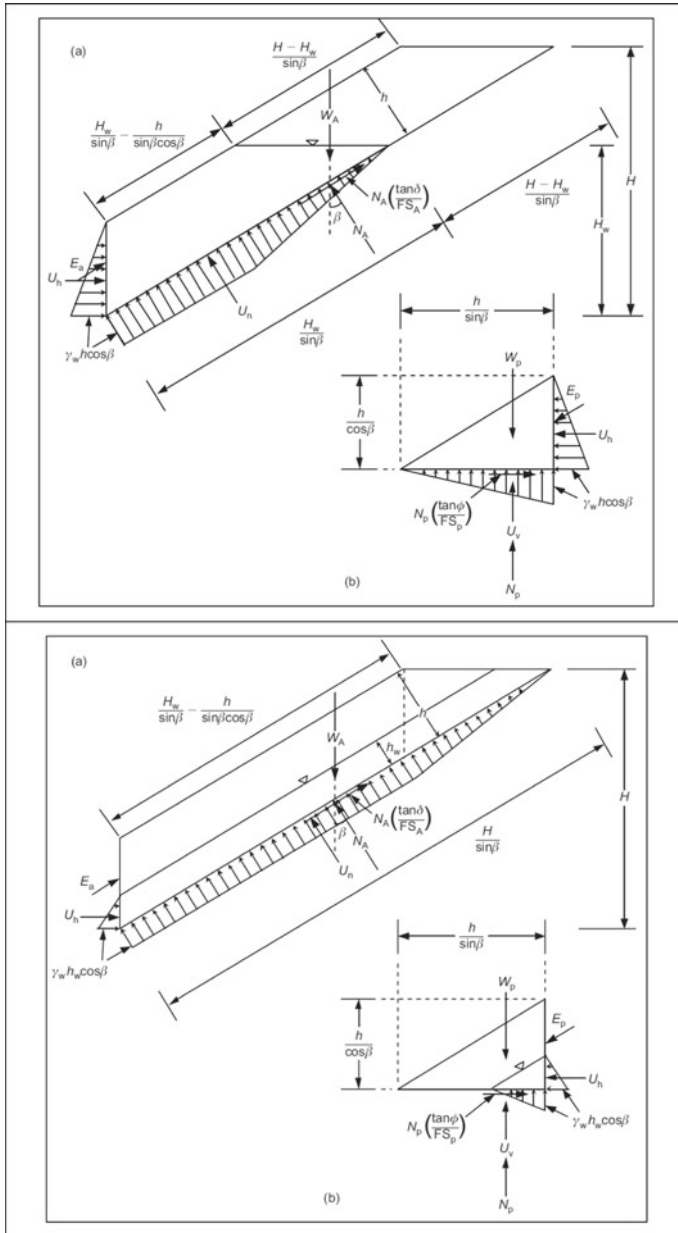


Fig. 1.2 Schematic profiles illustrating two submergence assumptions and limit equilibrium forces (top: horizontal submergence; bottom: parallel submergence)

H	Vertical height of the slope measured from the slope toe.
H_w	Vertical height of the free water surface measured from the slope toe.
h_w	Height of the free water surface measured in the direction perpendicular to the slope.
E_A	Force summary acting on the active soil mass from the passive barrier.
E_p	Force summary acting on the passive barrier from the active soil mass.
U_h	Resultant of the pore pressures acting on the interfaces.
U_n	Resultant of the pore pressures acting perpendicular to the slope.
U_v	Resultant of the vertical pore pressures acting on the passive barrier.
FS	Factor of safety against cover soil sliding on the failure plane.

Comparing the resisting forces with the driving forces, Koerner and Soong (2005) derived the following equation to calculate the factor of safety (FS):

$$FS = \frac{-b + \sqrt{b^2 - 4ac}}{2a}$$

where

$$\left. \begin{aligned} a &= W_A \sin \beta \cos \beta - U_h \cos^2 \beta + U_h \\ b &= -W_A \sin^2 \beta \tan \phi + U_h \sin \beta \cos \beta \tan \phi \\ &\quad - N_A \cos \beta \tan \delta - (W_P - U_V) \tan \phi \\ c &= N_A \sin \beta \tan \delta \tan \phi \end{aligned} \right\}$$

For the horizontal seepage, the values of parameters a , b , and c can be determined by utilizing the following equations:

$$\begin{aligned} W_A &= \frac{\gamma_{sat'd}(h)(2H_w \cos \beta - h)}{\sin 2\beta} + \frac{\gamma_{dry}(h)(H - H_w)}{\sin \beta} \\ U_n &= \frac{\gamma_w(h)(\cos \beta)(2H_w \cos \beta - h)}{\sin 2\beta} \\ U_h &= \frac{\gamma_w h^2}{2} \\ N_A &= W_A \cos \beta + U_h \sin \beta - U_n \\ W_P &= \frac{\gamma_{sat'd} h^2}{\sin 2\beta} \\ U_V &= U_h \cot \beta \end{aligned}$$

For the parallel seepage, The parameter values of W_A , U_n , U_h , and W_P can be determined via the following equations:

$$W_A = \frac{\gamma_{dry}(h - h_w)[2H \cos \beta - (h + h_w)]}{\sin 2\beta} + \frac{\gamma_{sat'd} h_w (2H \cos \beta - h_w)}{\sin 2\beta}$$

$$U_n = \frac{\gamma_w h_w \cos \beta (2H \cos \beta - h_w)}{\sin 2\beta}$$

$$U_h = \frac{\gamma_w h_w^2}{2}$$

$$W_p = \frac{\gamma_{dry}(h^2 - h_w^2) + \gamma_{sat} h_w^2}{\sin 2\beta}$$

To illustrate the behavior of these equations, an example is provided for a slope of 30 m long with an angle of 18.48° or a ratio of 1 (Vertical) to 3 (Horizontal). The slope is overlain by a layer of 0.3 m thick sandy soil. The soil is placed directly on an impermeable clay layer, and the failure plane is at contact of the soil aquifer and impermeable layer, as shown in Fig. 1.2. The soil has a unit weight of 18 kN/m³ and a friction angle of 30°. The cohesion is assumed to be zero. The overlying soil is an unconfined aquifer with part of the soil becoming saturated. The aquifer thickness is represented with the parallel submergence ratio (PSR) where PSR = h_w/h or horizontal submergence ratio (HSR) where HSR = H_w/H . The saturated unit weight increases to 21 kN/m³. The direct shear testing of the saturated soil has resulted in an interface friction angle of 22°.

Figure 1.3 shows the change of FS with soil interface friction angle for four different submergence ratios. Sliding of the cover soil on the failure plane can be expected when the calculated FS-value is less than 1.0. To ensure a minimum factor of safety, aim for a value greater than 1.0. The exact FS-value should be tailored to site-specific conditions. The following observations can be made from this example exercise:

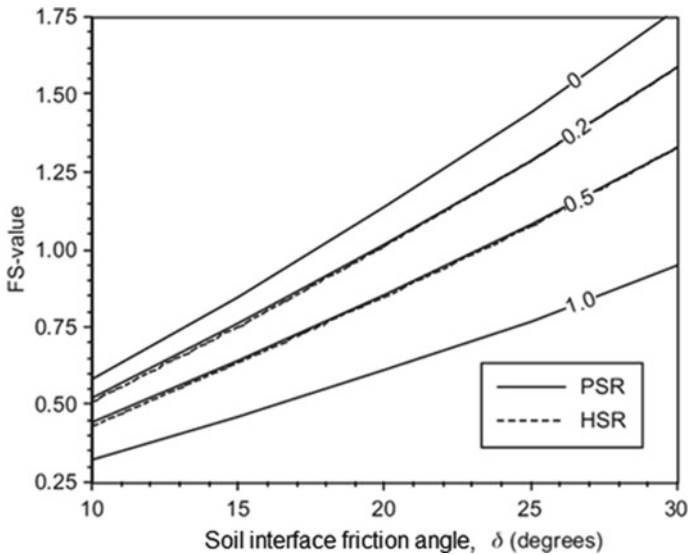


Fig. 1.3 FS change with soil interface friction angle for slopes with different pore pressures

- The variances in response curves between the parallel and horizontal submergence ratio assumptions are minimal, suggesting that the effect of groundwater on slope stability is similar regardless of the submergence scenario and thus size of the landslides.
- The adverse impact of seepage forces is immediately obvious on the slope stability. The charts illustrate a reduction in the FS-value as the submergence ratio increases, regardless of the interface friction values. When PSR or HSR is equal to 0, the slope contains no water, and the FS has the greatest values. The FS value would be the lowest if the cover soil is fully saturated.
- Saturated soil tends to have smaller friction angles or weak shear strength than dry soil. At a constant submergence ratio, decrease in soil friction angle will result in reduction of FS, increasing risk of slope failure.
- If pore pressures increase along the entire length of the slip surface due to rainfall, it is likely that the FS will decrease over time. Landslides will occur when FS becomes less than 1.0.

1.3 Hazards Related to Groundwater Dissolution and Hydrodynamics

Groundwater plays a crucial role in various geological processes, particularly in the formation of karst terranes. The term “terrane” is used to encompass both surface features and underground elements like caves and groundwater conduits. Karst collapses can occur naturally, representing a defining characteristic of karst terranes. On the contrary, human-induced karst collapses are unexpected events where the overlying earth materials move into dissolved voids within the underlying bedrock. These collapses, whether sudden and catastrophic or gradual and subsiding, can pose risks to structures and human lives. While the shapes and sizes of karst collapses may change over time, they are typically described as closed funnel-shaped or bowl-sloped depressions, ranging from centimeters to kilometers in scale. However, when it comes to engineering activities, the collapse sizes most relevant are typically tens to hundreds of meters in diameter. Since karst collapses are formed through the erosion of soil and rock material into the subsurface, human interventions in karst areas can accelerate these erosion processes. The continuous and inevitable dissolution of soluble bedrock highlights that the formation of karst collapses is an ongoing and dynamic process. Figure 1.4 shows the various karst collapse hazards.

The existence of dissolved voids in the underlying bedrock or soil is a crucial prerequisite for karst collapses (Lei et al. 2022). Consequently, carbonate rocks like limestone and dolomite are the primary geological formations susceptible to karst collapses. However, karst collapses can also occur in evaporites such as gypsum and halite, and in certain cases, even in sandstones. The rate and turbulence of water flow play a significant role in the dissolution of rock material, with higher rates leading to increased dissolution. Water acidity also influences the aggressiveness of rock dissolution, and the mixing of waters with different geochemical properties

Source	Release Mechanism	Activity	Receptors		
			Human		Ecological Environment
			Residents	Non-Residents	
Karst country rock	Cave collapse	Natural Occurrence	●	●	●
		Induced by Human Activities	●	●	●
Cover sinkhole	Cover collapse	Natural Occurrence	●	⊙	●
		Induced by Human Activities	●	●	●
	Cover subsidence	Natural Occurrence	●	⊙	⊙
		Induced by Human Activities	●	●	●
Caprock sinkhole	Caprock collapse	Natural Occurrence	●	⊙	⊙
		Induced by Human Activities	●	⊙	○
	Caprock subsidence	Natural Occurrence	●	●	●
		Induced by Human Activities	○	⊙	⊙

Fig. 1.4 Summary of safety-related hazards related to groundwater dissolution and hydrodynamics

can further enhance the dissolution process. The solubilities of calcite (CaCO_3) and dolomite [$\text{MgCa}(\text{CO}_3)_2$] in typical meteoric waters are generally less than 0.1 g/L. In comparison, the equilibrium solubilities of gypsum ($\text{CaSO}_4 \cdot 2\text{H}_2\text{O}$) and halite (NaCl) in distilled water are 2.4 g/L and 360 g/L, respectively (Lei et al. 2022). Apart from chemical reactions, sulfate-reducing bacteria can contribute to initiating and accelerating the dissolution process of carbonate rock. To a large extent, dissolution of groundwater determines geochemistry in karst or other types of aquifers.

Based on Oosthuizen and Richardson (2011), Fig. 1.5 illustrates the typical processes involved in sinkhole formation due to a decrease in groundwater levels. Groundwater withdrawal encompasses activities such as extracting groundwater for drinking, industrial purposes, irrigation, and dewatering in mines. Several factors contribute to the downward movement of unconsolidated soils, including the loss of buoyant support, an increase in groundwater velocity within the cone of depression, an amplification of water-level fluctuations, and an induced rise in surface water percolation. Physical models conducted by Lei et al. (2005) and Alrowaimi et al. (2015) have demonstrated a correlation between sinkhole occurrence and both the magnitude and rate of groundwater drawdown.

1.4 Hazards Caused by Groundwater Intrushes

As a source of hazard, groundwater can cause direct damages to human beings and the environment, including flooding and water intrushes in mining and tunneling. Mine water hazards often arise from the occurrence of mine water intrushes. Mine water intrush refers to the sudden and unanticipated rush of a significant amount of water

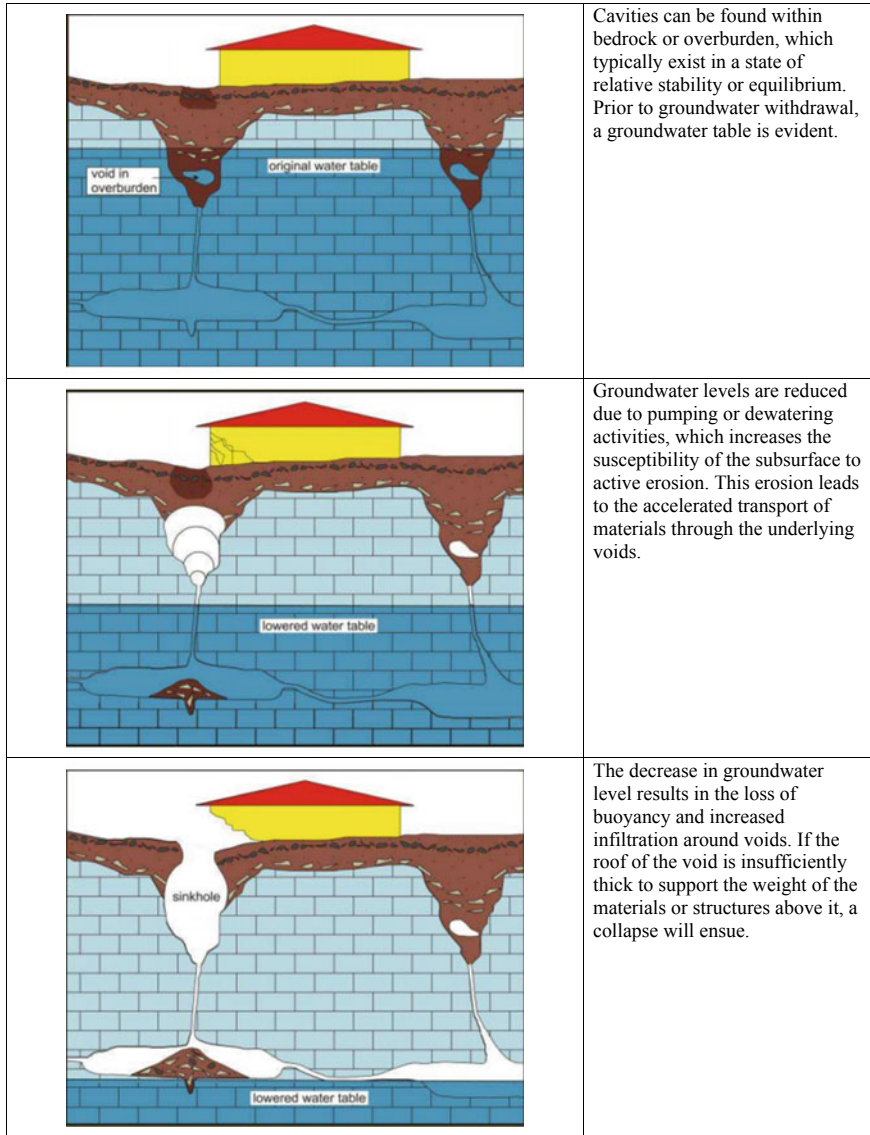


Fig. 1.5 Collapse processes caused by groundwater level drop

into underground workings or open pit mines. This phenomenon transpires when water-bearing media, such as high-pressure confined aquifers, surface water bodies, or underground mine pools, are exposed during tunneling or mining activities (Li 2018). The occurrence of mine water inrush is typically characterized by its dramatic nature, swiftly inundating underground workings and posing risks to mine production and human lives (LaMoreaux et al. 2014). According to data from China’s State

Administration of Work Safety (Sun et al. 2015), mine water inrush is the second most severe type of disaster in coal mines, following gas explosions. It is worth noting that water inrushes often bring along mud or sand in many instances. Figure 1.6 shows a water inrush process from an underlying aquifer.

Figure 1.7 summarizes hazards caused by water inrushes. The water source includes accumulated water in neighboring mine or old mining area of same mine

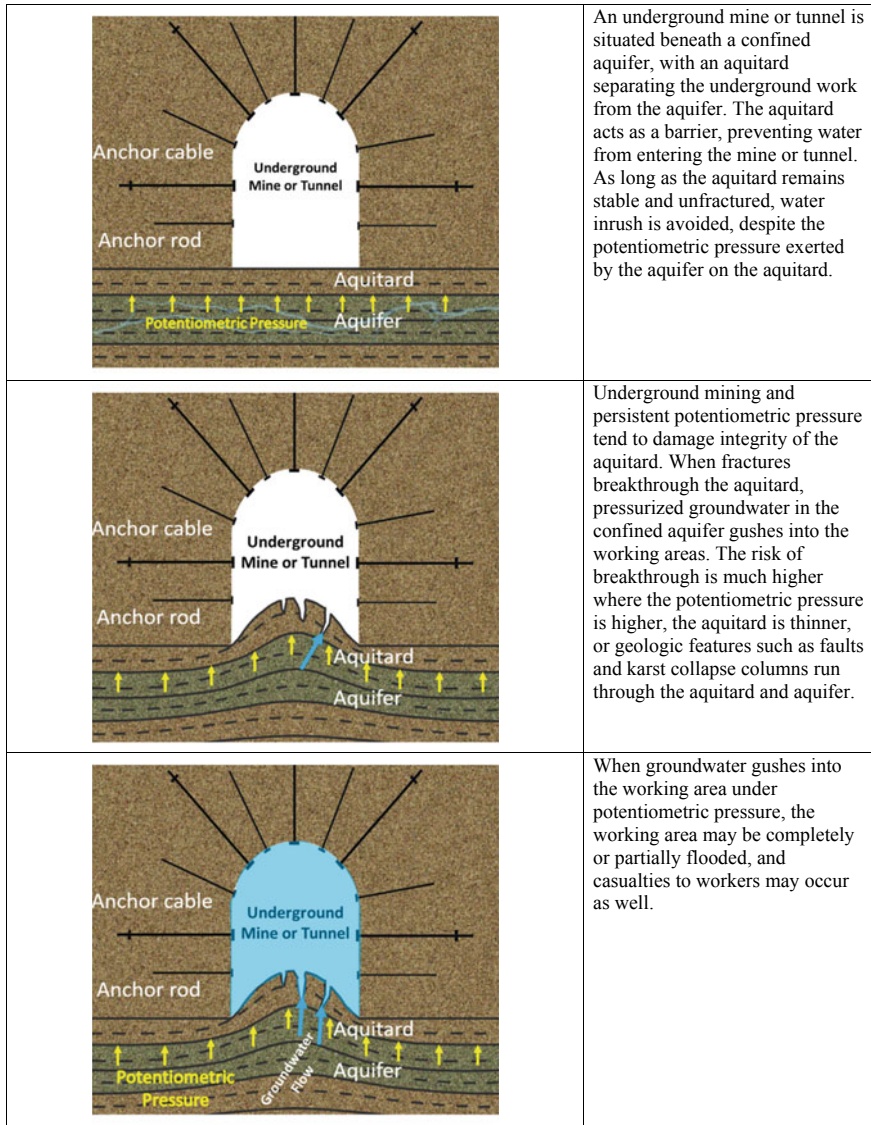


Fig. 1.6 Water inrush processes from underlying aquifer

and groundwater from aquifers underlying or overlying the mining area. Different categories are used to classify water sources based on their origins. Water intrusions pose both direct and indirect threats. Direct threats include physical harm to miners and damage to working spaces in tunnels and working panels. Indirect threats involve risks to the environment. These may include surface subsidence, reduction and contamination of water resources, and negative impacts on biodiversity. Assessments of water intrusions must consider both hazards and risks. The level of hazard and risk associated with water intrusions is typically influenced by the strength of water sources, the pumping capacity of the mine, and the ecological sensitivity to changes in water conditions. The CSM also outlines the pathways from each water source to different receptors. Potential pathways for water intrusions include direct exposure to water-bearing formations, mining-induced fractures in overlying or underlying aquitards, hydraulically conductive faults, karst collapse columns, and poorly sealed boreholes. These pathways create the conditions for water intrusions to occur (Yin et al. 2018).

Water Sources	Pathways	Direct Injury			Risk to Ecological Environment		
		Worker Safety & Health	Flooding of Tunnel	Flooding of Working Panel	Surface Subsidence	Water Resource	Habitat
Accumulated water in neighboring mine or old mining area of same mine	Direct exposure by tunneling	●	○	○	◎	●	◎
	Mining-induced fracture	●	○	○	◎	●	◎
	Hydraulically conductive fault/fracture	●	○	○	◎	●	◎
Groundwater directly intercepted by mining activities	Direct exposure by tunnel	●	○	○	◎	●	◎
	Direct exposure by mining panel	●	○	○	◎	●	◎
Groundwater overlying working area while separated by an aquitard under natural conditions	Mining-induced fracture in overlying formation	●	○	○	◎	●	◎
	Hydraulically conductive fault/fracture	●	○	○	◎	●	◎
	Hydraulically conductive karst collapse column	○	○	○	◎	●	◎
Groundwater underlying working areas while separated by an aquitard under natural conditions	Mining-induced fracture in underlying formation	●	○	○	◎	●	◎
	Hydraulically conductive fault/fracture	●	○	○	◎	●	◎
	Hydraulically conductive karst collapse column	○	○	○	◎	●	◎

Fig. 1.7 Summary of hazards caused by water intrusion

1.5 Hazards Caused by Groundwater Contamination

Anthropogenic activities have contaminated groundwater worldwide. The source includes non-point contaminant sources and point contaminant sources. Waste disposal, accidental spills or leaks of contaminants, industrial wastewater discharge fertilizer and herbicide applications in agriculture, and mine drainage contribute to groundwater contamination. Figure 1.8 presents the health-related hazards, which present risks to human health and the environment.

Human health risk assessment (HHRA) is a widely utilized method for evaluating the possible long-term exposure and health risks, including both cancer and non-cancer effects, linked to chemicals of potential concern (COPCs) found in groundwater and related media such as surface water, soil, and soil gas (Alam et al. 2023; Fida et al. 2023; Guo et al. 2022, 2023; Meng et al. 2023). HHRA follows a systematic evaluation process aimed at estimating the extent of human contact with potentially hazardous chemicals present in the environment. Additionally, it quantifies the risk of adverse health effects that may arise from such exposure. To accomplish this, an HHRA combines information on the estimated exposure of specific populations of

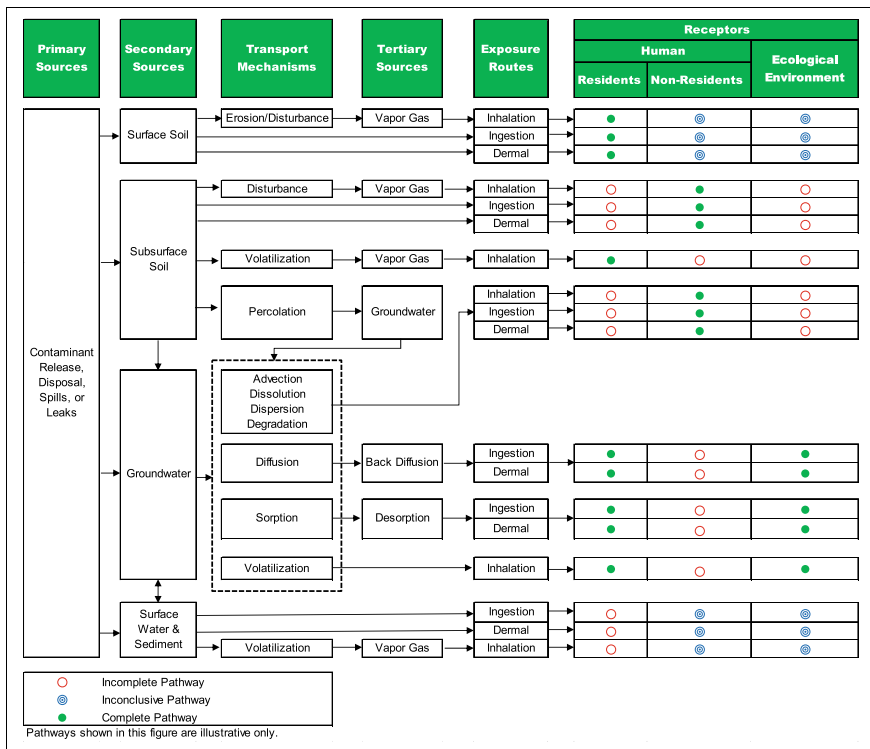


Fig. 1.8 Summary of hazard caused by groundwater contamination

people who might contact the affected environmental media (“receptors”) with information on the toxicity of the chemicals present. Regulatory authorities such as the USEPA, Agency for Toxic Substances and Disease Registry (ATSDR), and the World Health Organization (WHO) have developed a quantitative HHRA process over the past three decades, which is based on the fundamental principles of toxicology. These principles serve as the foundation for conducting a comprehensive assessment of potential health risks associated with exposure to hazardous substances.

It is vital to acknowledge that risk assessment is not a science in itself but rather a tool used to aid decision-making in remedial actions. Due to the lack of reliable scientific data for certain aspects of a risk assessment, the process relies on conservative assumptions. These assumptions are intentionally designed to overestimate potential exposures and risks rather than underestimate them. To address the limitations of conservative assumptions, a tiered approach is commonly employed in risk assessment. Initially, generic assumptions and models are utilized, and as more information becomes available, they can be replaced with more realistic assumptions and models. This tiered approach allows for the refinement of risk assessment results and ensures that they provide appropriate support for effective risk management. HHRA is based on scenarios that define the conditions under which individuals may be exposed to COPCs. Figure 1.9 shows an example of exposure pathways from potential source COPC through transport mechanisms to receptors to facilitate an HHRA.

The HHRA processes typically consist of five elements (Groundwater Sciences Corporation 2011):

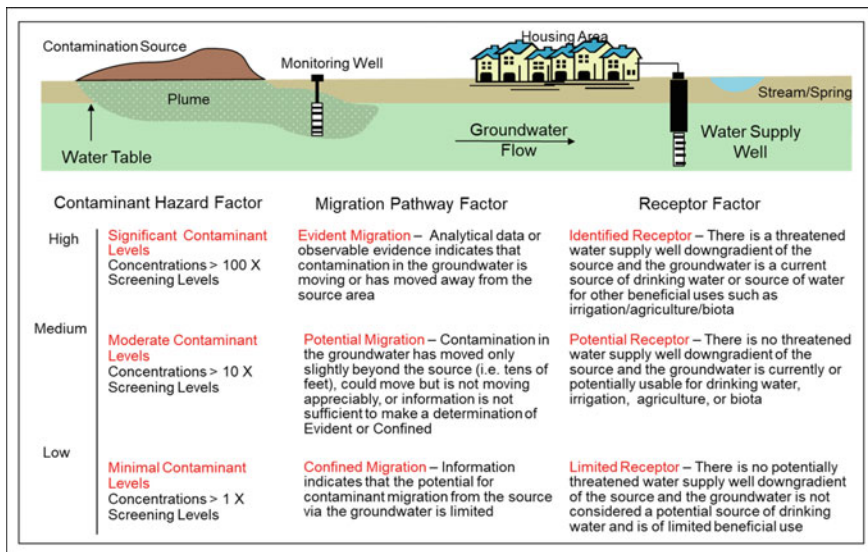


Fig. 1.9 Generalized groundwater contamination processes

Data review and evaluation: This involves reviewing available data to create datasets for the risk assessment. It includes identifying site-related COPCs (chemicals associated with the site, detected at a frequency greater than 5% and at concentrations higher than background levels or conservative screening levels). Additionally, it involves calculating representative exposure concentrations under upper-bound exposure conditions for each affected medium. The approach for developing data sets and calculating exposure concentrations will be described in a separate deliverable.

Exposure assessment: This step determines the amount, frequency, duration, and routes of receptor exposure to site-related COPCs. It considers scenarios that define the conditions of exposure to these chemicals, taking into account current and potential future site uses. The assessment focuses on potential exposure pathways to actual or probable human receptors.

Toxicity assessment: The toxicity assessment has two objectives: (1) identifying the nature and degree of toxicity for each COPC, and (2) characterizing the dose–response relationship between exposure magnitude and adverse health effects. The USEPA has established toxicity criteria for many constituents of concern in human health risk assessment. These criteria are designed to protect even sensitive subpopulations exposed daily for a lifetime. The assessment considers both non-carcinogenic and carcinogenic effects, which can be caused by the same chemical.

Risk characterization: Risk characterization combines the exposure data and toxicity data to estimate the property and magnitude of potential non-carcinogenic risks and carcinogenic risks for specific receptor populations. An acceptable target carcinogenic risk range of 10^{-4} to 10^{-6} has been determined by the USEPA (1991). This organization has also adopted a non-carcinogenic target risk level of 1.0. To account for simultaneous exposure to multiple COPCs and routes associated with the same exposure medium, risks and hazards are summed and rounded to one significant figure (USEPA 2004).

Uncertainty analysis: Risk assessment involves assumptions and estimates that carry uncertainties. Uncertainty analysis addresses variability and lack of knowledge about measured and estimated parameters. It allows decision-makers to evaluate risk estimates considering the assumptions and data used in the assessment. Major sources of uncertainty include natural variability, lack of knowledge about physical, chemical, and biological properties and processes, lack of accuracy in models used for estimation, and measurement errors. Uncertainties associated with dose–response relationships and carcinogenicity classifications tend to be greater than those of other elements. Extrapolation from rodent carcinogen bioassays or occupational exposure data to lower levels involves multiple assumptions, leading to potential overestimation of risk.

References

- Alam SMK, Li P, Fida M (2023) Groundwater nitrate pollution due to excessive use of N-fertilizers in rural areas of Bangladesh: pollution status, health risk, source contribution, and future impacts. *Expo Health*. <https://doi.org/10.1007/s12403-023-00545-0>
- Alrowaimi M, Yun HB, Chopra M (2015) Sinkhole physical models to simulate and investigate sinkhole collapses. In: Doctor DH, Land L, Stephenson JB (eds) 14th sinkhole conference NCKRI symposium vol 5, pp 559–568
- Evans DM (1966) The Denver area earthquakes and the Rocky Mountain Arsenal disposal well. *Mountain Geol* 3:23–26
- Fida M, Li P, Wang Y, Alam SMK, Nsabimana A (2023) Water contamination and human health risks in Pakistan: a review. *Expo Health* 15(3):619–639. <https://doi.org/10.1007/s12403-022-00512-1>
- Groundwater Sciences Corporation (2011) Supplemental remedial investigation groundwater report (part 1). <https://www.yorksiteremedy.com/Documents/Final%20Supl%20RI%20GW%20Rprt-Sept2011.pdf?cv=1>. Accessed 20 Nov 2023
- Guo Y, Li P, He X, Wang L (2022) Groundwater quality in and around a landfill in northwest China: characteristic pollutant identification, health risk assessment, and controlling factor analysis. *Expo Health* 14(4):885–901. <https://doi.org/10.1007/s12403-022-00464-6>
- Guo W, Li P, Du Q, Zhou Y, Xu D, Zhang Z (2023) Hydrogeochemical processes regulating the groundwater geochemistry and human health risk of groundwater in the rural areas of the Wei River Basin, China. *Expo Health*. <https://doi.org/10.1007/s12403-023-00555-y>
- Huang R, Zhu LP, Encarnacion J, Xu YX, Tang CC, Luo S, Jiang XH (2018) Seismic and geologic evidence of water-induced earthquakes in the three gorges reservoir region of China. *Geophys Res Lett* 45(12):5929–5936
- Koerner RM, Soong TY (2005) Analysis and design of veneer cover soils. *Geosynth Int* 12(1):28–49
- LaMoreaux JW, Wu Q, Zhou WF (2014) New development in theory and practice in mine water control in China. *Carbonates Evaporites* 29:141–145. <https://doi.org/10.1007/s13146-014-0204-7>
- Lei M, Gao Y, Jiang X, Hu Y (2005) Experimental study of physical models for sinkhole collapses in Wuhan, China. In: Proceedings of the tenth multidisciplinary conference on sinkholes and the engineering and environmental impacts of karsts, ASCE Geotechnical Special Publication, pp 91–102
- Lei M, Zhou W, Jiang X, Dai J, Yan M (2022) Atlas of karst collapses. Springer, Cham. <https://doi.org/10.1007/978-3-030-92912-1>
- Li P (2018) Mine water problems and solutions in China. *Mine Water Environ* 37(2):217–221. <https://doi.org/10.1007/s10230-018-0543-z>
- Meng Y, Wu J, Li P, Wang Y (2023) Distribution characteristics, source identification and health risk assessment of trace metals in the coastal groundwater of Taizhou City, China. *Environ Res* 238:117085. <https://doi.org/10.1016/j.envres.2023.117085>
- Oosthuizen AC, Richardson S (2011) Sinkholes and subsidence in South Africa. *Counc Geosci* 31
- Sun WJ, Zhou WF, Jiao J (2015) Hydrogeological classification and water inrush accidents in China's coal mines. *Mine Water Environ* 35:214–220. <https://doi.org/10.1007/s10230-015-0363-3>
- USEPA (1991) Role of the baseline risk assessment in superfund remedy selection decisions. OSWER Directive 9355.0-30

- USEPA (2004) Risk assessment principles and practices. Office of the Science Advisor Staff Paper. EPA/100/B-04/001. <http://www.epa.gov/osa/ratf-final.pdf>
- USGS (2000) Land subsidence in the United States, USGS fact sheet-165-00. U.S. Department of the Interior, USGS, Reston, VA. Government Printing Office
- USGS (2003) Groundwater depletion across the nation, USGS fact sheet-103-03. U.S. Department of the Interior, USGS, Reston, VA. Government Printing Office
- Yin HY, Zhou W, LaMoreaux JW (2018) Water inrush conceptual site models for coal mines of China. *Environ Earth Sci* 77:746. <https://doi.org/10.1007/s12665-018-7920-6>

Chapter 2

Loess Landslides and Water Resources Management



2.1 Introduction

Loess is composed of unique porous and weakly cemented sediments formed since the Quaternary period. It is widely distributed in Asia, Europe, North America, South America, and other regions. In China, loess is extensively distributed in the northwest, north, and northeast regions, particularly concentrated in the provinces and regions known as the Loess Plateau, including Shaanxi, Gansu, Shanxi, and Ningxia. The area covered by loess accounts for 6.67% of China's land area or 4.9% of the global loess coverage. The Loess Plateau is one of the four major plateaus in China and is considered one of the birthplaces of ancient Chinese civilization. It is also the most concentrated and largest loess region on Earth.

Located in a semiarid to arid region, the Loess Plateau has a fragile geological and ecological environment. It suffers from severe soil erosion, frequent landslides, and collapses, posing significant threats to local agricultural and industrial production, as well as the safety of people's lives and properties. According to statistics, nearly one-third of landslides in China occur in loess areas (Zhu et al. 2002). These landslides, varying in scale and numbering in the tens of thousands, often result in transportation disruptions, blockage of rivers and canals, destruction of farmland, damage to factories and mines, burial of villages, and casualties among humans and livestock. They have become major geological issues threatening human lives, property, urban areas, and major engineering projects in loess regions.

Loess landslides refer to geological disasters that occur in loess-covered slopes, where unstable loess structures exist. Under the influence of gravity, these structures experience overall sliding along shear surfaces. Loess landslides are one of the most frequent and destructive sudden geological disasters in China, primarily due to the characteristics of loess itself, such as its large pores, sensitivity to water, poor mechanical properties, and developed joints and fractures. They often exhibit characteristics such as occurrence in clusters, concealed nature, catastrophic consequences,

and complexity. In the continuous loess-covered area of 440,000 km² in China, tens of thousands of landslides of various sizes have occurred (Peng et al. 2019a).

Water is generally considered the most active triggering factor for geological disasters such as landslides. The sources of water include precipitation and irrigation (Leng et al. 2018; Xu et al. 2014). The increase in moisture content in slope soils reduces the unsaturated soil's shear strength, while rising water levels decrease the strength of saturated soil, thereby leading to decreased slope stability. Loess is a special type of soil that is highly sensitive to water, with a significant decrease in strength when exposed to water, making it more susceptible to landslides under the influence of water. However, field infiltration monitoring indicates that the infiltration depth of rainwater in normal loess is relatively shallow, which may suggest a limited impact on the stability of loess slopes. In reality, numerous and diverse types of loess landslides with significant hazards occur under the influence of water, and the mechanisms involved are complex. Research has shown that factors such as the dominant seepage characteristics of loess slopes, irrigation patterns, and rainfall characteristics play important roles in the formation of loess landslides.

2.2 Loess Distribution and Loess Landslides

Loess is a Quaternary aeolian deposit formed in arid and semiarid climatic environments. It has a loose texture, well-developed vertical joints, and a relatively uniform porous structure. It consists mainly of quartz and feldspar particles and is predominantly yellow or yellow-brown in color. Loess is a fine-grained aeolian sediment that is slightly cohesive and typically lacks stratification. It is often calcareous (Sun 2005). Loess is distributed in the mid-latitude climate zones of both the Northern and Southern Hemispheres, including countries such as China, the United States, Russia, Central Asia, and Western Europe (Fig. 2.1), as well as Argentina and New Zealand in the Southern Hemisphere (Li and Qian 2018a). In the Southern Hemisphere, apart from South America and New Zealand, loess is rarely found in other regions. The climate in this region is characterized by aridity, semi-aridity, and warm, low-rainfall seasons with pronounced seasonal variations. Loess is rarely found in high-latitude and low-latitude regions (Li and Qian 2018b). This is because high-latitude regions are cold and in high-pressure wind source areas where loess material is lifted and transported. In the mid-latitude zone, the climate is warm, grasslands are developed, rainfall is low, and erosion is weak, which facilitates the deposition and preservation of loess. In low-latitude regions, loess is less abundant due to being far from the source of windborne loess material. Additionally, abundant rainfall and strong erosion lead to prevalent lateritic weathering, which is unfavorable for the preservation of loess. As shown in Fig. 2.1, the total area of loess and loess-like deposits worldwide is approximately 13,000,000 km², accounting for 9.3% of the land area. Among these countries, China has the largest and thickest loess deposits in the world, with a loess-covered area exceeding 640,000 km² (Li and Qian 2018a; Zhu et al. 2018).

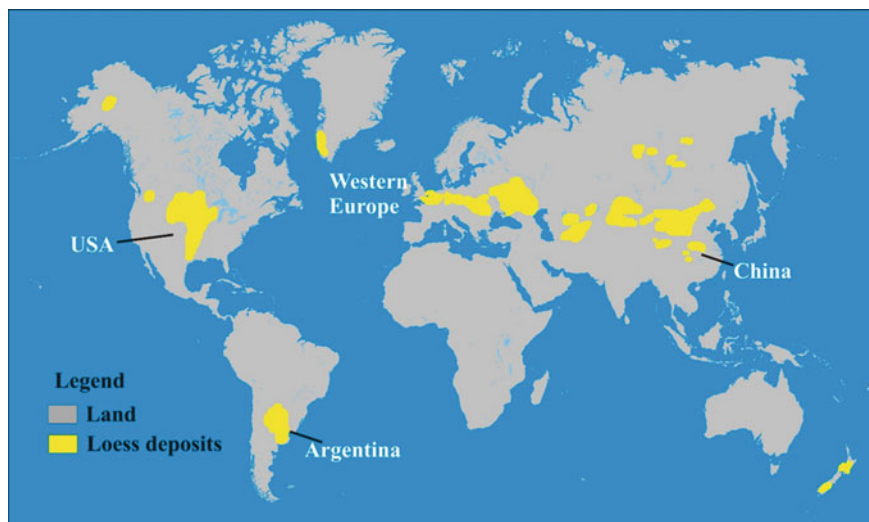


Fig. 2.1 Schematic map showing the world distribution of loess (Li and Qian 2018b)

The distribution of loess in China extends from the western edge of the Tarim Basin and Junggar Basin in Xinjiang to the eastern part of the Songliao Plain, southward to the northern side of the Qinling Mountains, and northward to the Great Wall (Liu 1985; Xu et al. 2021a) (Fig. 2.2). The Loess Plateau in China is the main region of loess distribution in the country. It is also the most typical area for loess distribution (Wei et al. 2017). It includes Shaanxi, Gansu, southeastern Ningxia, and western Shanxi. The terrain gradually decreases from northwest to southeast in this region. The loess stratigraphy in this area is the most complete, with the thickest deposits and the most continuous distribution.

Loess is predominantly distributed in arid and semiarid regions, and its unique depositional and geological conditions give rise to typical unsaturated soil engineering characteristics. It exhibits extreme sensitivity to water, making the Loess Plateau one of the most severely affected areas by soil erosion, landslides, and collapses in the world. The interplay of tectonic forces, surface water geomorphological processes, and groundwater geological processes has shaped fragmented loess landforms such as loess tablelands, ridges, and mounds, as well as a network of gullies and ravines, making it one of the most geologically hazardous regions in China (Peng et al. 2020). According to statistics, nearly one-third of landslides in China occur in loess areas. These landslides, ranging in scale from small to large, often result in disastrous accidents such as road blockages, damming of rivers and channels, farmland destruction, destruction of industrial and mining facilities, burial of villages, and casualties to humans and livestock. With the advancement of the national “Belt and Road” initiative, the economy of the loess region will experience further development, and human engineering activities will become increasingly intense. Consequently, the number of geological hazards encountered will rapidly increase. Loess

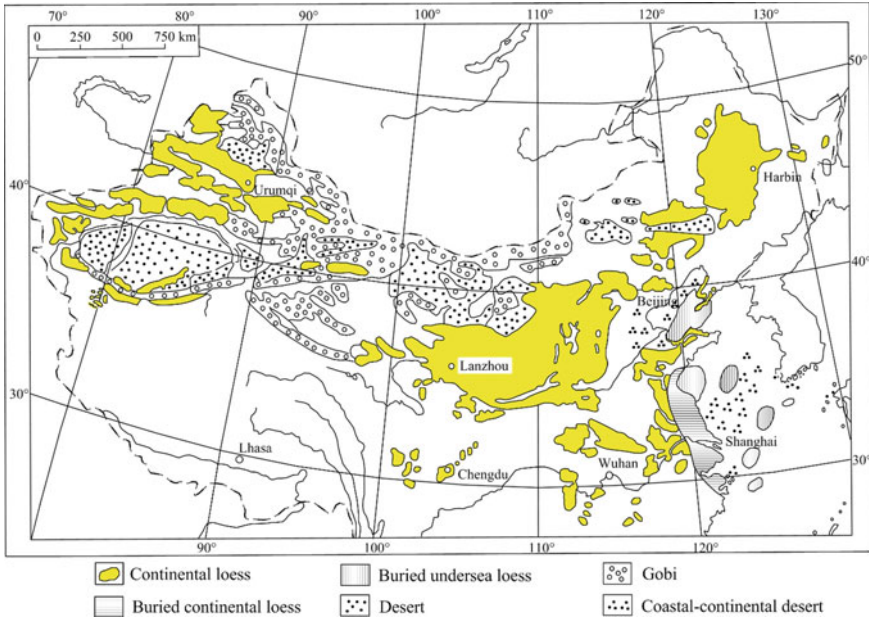


Fig. 2.2 Loess distribution in China and the major part of the Chinese Loess Plateau (Li and Qian 2018b)

landslide disasters pose a significant geological problem that threatens the lives and property of people on the Loess Plateau, as well as the construction and operation of urban areas and major engineering projects.

Landslides are the most common form of slope failure driven by gravity. The equilibrium stability of a slope essentially depends on the balance between stress and shear strength. External factors can alter the stress, strength, or both, leading to the disruption of this balance and resulting in failure. Factors that change the stress on a slope include earthquakes, river erosion, and additional loads from engineering unloading and loading. Factors that alter the strength include rainfall, freeze–thaw cycles, irrigation, and reservoir water storage, which can cause the groundwater level to rise. The rise in groundwater level reduces the effective normal stress on the sliding surface, thereby decreasing the shear strength (Peng et al. 2019a). In reality, landslides often result from the combination of multiple factors, such as the interaction between engineering excavation and rainfall or irrigation and freeze–thaw cycles. Due to the strong water sensitivity of loess, water becomes the most active triggering factor for loess landslides. Numerous engineering examples of landslide prevention and control, both domestically and internationally, have shown that groundwater activity has a significant impact on the stability of landslide masses. It is often said that nine out of ten landslides are caused by water. The common understanding among landslide control experts and geological technicians is that water management comes first in landslide control. Geological hazards on the Loess Plateau are concentrated

during the rainy season from June to October, and water is one of the most active triggering factors for loess landslides (Zhuang and Peng 2014; Wang et al. 2015).

Water has four main impacts on loess slopes. First, surface runoff generated by precipitation or irrigation can erode the surface of loess slopes. Prolonged erosion can cause displacement of surface soil particles, thereby altering the surface morphology. Second, water infiltrates into the slope and becomes groundwater. Under the long-term soaking and runoff effects of groundwater, the mechanical strength of the rock–soil mass decreases, especially in the case of mudstone layers and some rock–soil masses with expansive and disintegrating properties, where the decrease in mechanical strength is significant. Third, as water enters the soil, it initially increases the bulk density of the slope, thereby increasing the weight of the sliding mass. At the same time, the increase in moisture content in the saturated zone of the loess leads to a decrease in effective stress, and in some soils that become saturated, the effective unit weight of the soil below the water table changes from total unit weight to buoyant unit weight, reducing the weight of the sliding mass. In addition, water entering the slope forms underground water runoff, generating seepage forces during the runoff process. When the seepage forces are significant, they severely affect the stability of the slope. The rise in groundwater level also weakens the shear strength of the loess in the saturated zone. All of these factors can cause deformation and failure of loess slopes (Wang et al. 2018; Garakani et al. 2015).

2.3 Hazards of Loess Landslides

The Loess Plateau region in China possesses the most extensive distribution, complete stratigraphy, and thickest deposits of loess in the world. It has also formed unique landforms, geomorphology, and geological structures, including loess tablelands, ridges, mounds, loess terraces, and loess basins. Located in a tectonically active zone, the Loess Plateau is influenced by seismic activity and seasonally concentrated rainfall. Urbanization, rapid population growth, and frequent human activities have accelerated the transformation of the geomorphological structure of the Loess Plateau, making loess landslides and debris flow disasters the most frequent and destructive geological hazards in the region. Landslides are the most common geological hazard observed in the Shaanxi, Gansu, and Ningxia regions of the Loess Plateau and are characterized by their dense distribution, extensive range, poor stability, and significant property damage. According to statistics, as of 2017, there were as many as 6802 landslides in the Shaanxi, Gansu, and Ningxia regions of the Loess Plateau, with 783 landslide hazards (Table 2.1), accounting for 62.6% of the total number of geological hazards, which amounted to 12,122 (Zheng 2017).

Landslides, one of the common geological hazards in loess regions, occur in specific environments and have their own dynamic processes, development, evolution, and eventual disappearance. They mainly occur along the banks of mature rivers and their tributaries, which are also areas where human engineering activities are relatively active. Loess landslides are characterized by fast sliding speed, rapid

Table 2.1 Summary of landslides in the Shaanxi-Gansu-Ningxia region of the Loess Plateau

Items	Shaanxi	Gansu	Ningxia	Subtotal
Total geological hazards	5330	4258	2534	12,122
Number of landslides in Loess Plateau	3665	1700	1437	6802
Number of hidden dangers of landslides in the Loess Plateau	83	267	433	783
Percentage of landslides in total geological hazards (%)	70.3	46.2	73.8	62.6

deformation, and strong destructive power. These characteristics severely restrict the regional economic development in loess areas and pose a threat to the life and property safety of the general population. In view of the deadly consequences caused by landslides, Xu et al. (2017) conducted a systematic statistical analysis of landslides in the Loess Plateau. From 1980 to 2015, a total of 53 fatal landslides occurred, resulting in 717 deaths. The specific manifestations of landslide hazards are as follows:

- **Threaten the safety of people’s lives and property.** When landslides occur, they can destroy buildings, roads, farmland, and human and livestock populations on the surface, resulting in severe casualties and property damage. For example, on March 7, 1983, the high-speed loess landslide in Sule Mountain, Dongxiang County, Gansu Province, destroyed three villages in less than 30 s, with a sliding mass of 31 million m³, resulting in 237 deaths. It became the most severe catastrophic loess landslide in China in the 1980s. In 2006, the “10.6” landslide in Huaxian County, Shaanxi Province, caused 12 deaths. In 2009, the Gaolan Mountain landslide in Lanzhou city triggered multiple small-scale landslides in the central and front parts during urban construction, resulting in economic losses of millions of yuan. In 2010, the “3.10” landslide in Zizhou, Shaanxi Province, caused 27 deaths. In 2011, the “9.17” landslide in Xi’an City caused 32 deaths and had a significant negative impact. Lanzhou, a loess mountain city, has experienced 24 large-scale catastrophic landslides since 1949, resulting in a total of 670 deaths and direct economic losses of 776 million yuan. Currently, Lanzhou City is threatened by loess hazards, with a population of 667,000 and property at risk worth 260 billion yuan. In addition, human irrigation activities have triggered a large number of catastrophic landslides in areas such as Heifangtai, Gansu, and Jingyangnanyuan, Shaanxi (Peng et al. 2019b).
- **Destroy the ecological environment.** Landslides undermine the stability of the land, leading to vegetation destruction and soil erosion, which in turn affects the restoration of ecosystems and the sustainable use of land. Loess landslides often sweep away large areas of vegetation, including trees, herbaceous plants, and plant roots in the soil. This results in the destruction and loss of vegetation, thereby undermining the stability and ecological functions of the ecosystem. At the same time, the loose soil material brought by landslides is difficult to stabilize and is easily washed away by wind and rain, leading to soil erosion. Soil erosion causes soil and water loss, resulting in a decrease in soil fertility and

adverse effects on farmland and biodiversity. After a landslide, the soil and plant residues in the sliding mass may be carried into water bodies, polluting rivers, lakes, and reservoirs. This affects the quality and supply of water, posing a threat to aquatic organisms and human health. The ecological environment in loess regions is fragile, and landslides often disrupt the existing ecological balance and species diversity, causing damage and loss of wildlife habitats. Fragmentation and fragmentation of the landscape make it difficult for organisms to migrate and reproduce, making ecosystem restoration challenging. Moreover, large-scale landslides can potentially alter the flow direction of rivers, leading to changes in river channels and even the formation of new channels. This directly impacts the water cycle, flood management, and the utilization of natural water resources in the watershed.

- **Impact on regional economic development.** The losses caused by landslides require a substantial amount of funding for restoration and reconstruction, which adversely affects local economic development. According to statistics, the Chinese government's investment in landslide disaster prevention and control mainly focuses on direct engineering measures and indirect monitoring and early warning systems. These engineering measures primarily target potential landslides that pose a direct threat to human production and livelihood, especially in residential areas and transportation hubs. Landslide disaster reduction measures mainly involve various engineering measures for the sliding mass, including various types of retaining walls, anti-sliding piles, and diverse monitoring measures. According to incomplete statistics, a total of 244,559 projects have been conducted for prevention and control, with a cumulative economic investment of 109.6 billion yuan. These direct prevention measures and preventive measures have achieved significant results. The statistical results show that 13,603 landslides were successfully predicted, avoiding casualties of 588,349 people and preventing economic losses of up to 10.08 billion yuan (Huang 2019).
- **Induce a chain reaction of geological disasters.** Landslides can trigger the occurrence of other geological hazards, such as debris flows and collapses, further exacerbating the severity and extent of disasters. The occurrence of geological hazards is not isolated; many disasters are accompanied by the formation of other disasters, forming a chain of disasters. For example, the Salashan landslide in 1983 occurred in an area with a relative height difference of over 300 m. The sliding mass crossed the Nale Temple River, blocking the river and pushing toward the front edge of the opposite floodplain, forming a chain of landslide-debris flow-dammed lake disasters. Due to continuous heavy rainfall, on the evening of July 21, 2013, a landslide occurred in the southern channel of Dagou Village in Tianshui City. The sliding mass swept away the collapsed bodies on both sides of the valley during its movement, continuously increasing in scale. Combined with the action of rainwater, it transformed into a debris flow, forming a landslide-debris flow disaster chain, burying roads and destroying more than 10 houses in the village. The occurrence of most loess disasters affects the surrounding environment, thereby providing certain conditions for the occurrence of other disasters,

leading to delayed or subsequent disasters and forming a complex chain of loess geological hazards (Ma 2020).

2.4 Agricultural Irrigation and Loess Landslides

The Loess Plateau in China is located in arid and semiarid regions with extremely scarce precipitation. To address the livelihood issues of the people, the government has had to extract water from rivers for large-scale agricultural irrigation (extensive irrigation, flood irrigation). Although agricultural production has improved to some extent, it has led to widespread and intense soil subsidence on the loess tableland and widespread damage to water conservancy facilities. Large-scale landslides along the tableland edges occur continuously, forming dense landslide clusters. In the Loess Plateau region, loess landslides induced by irrigation infiltration are widely distributed, mainly in six provinces (Shaanxi, Gansu, Ningxia, Qinghai, Henan, and Shanxi). Among them, the most concentrated development of landslides is found in the Heifangtai irrigation area in Yongjing County, Gansu Province, the southern edge of the Baoji-Changxing loess terrace in the Guanzhong irrigation area of Shaanxi Province, and the northern edge of the loess terrace on the southern bank of the Jing River downstream, often occurring in the form of belt-like clusters and even forming landslide clusters tens of kilometers long.

The main cause of loess landslides induced by irrigation is the rise in the groundwater level. When the groundwater level rises, the total stress of the soil in the slope remains relatively unchanged, while the pore water pressure increases continuously, resulting in a decrease in effective stress and soil failure. If the groundwater level rises by 20–30 m, the pore water pressure in the slope soil increases by 20–30 kPa. The Mohr circle on the Mohr strength envelope shifts to the left as a whole, approaching the failure line. The Heifangtai irrigation area is located on the left bank of the Yellow River in Yongjing County, Gansu Province. Since the artificial extraction of Yellow River water for irrigation in 1968, a large number of loess landslides have occurred. The irrigated area covers 753 ha, with an annual water extraction volume of 6–8 million m³. Long-term flood irrigation has resulted in groundwater accumulation of over 20 m at the bottom of the loess, which discharges to the surrounding areas and forms more than 60 springs. According to surveys, there are 72 well-preserved landslide features along the 10 km edge of the loess terrace in that area (Peng et al. 2017). In the Baixia Canal section of the main canal on the Baoji Xia Terrace, from Linjiacun Canal Head to Changxing, a distance of 98 km, the groundwater level has also risen by 20–30 m over the past 40 years, resulting in more than 110 collapses. According to observation data from the loess terraces on the southern bank of the Jing River in 1992, the groundwater level in Miaodian Village, Taiping Township, has risen by 13 m compared to 1976, 17.5 m in Zhaitou Village, 20 m in Yujia Village, Jiangliu Township, 37 m in Jiangliu Village, and 28 m in Dabaozi Village. Along the slopes of the terraces from Li Quan to Mijia Cliff, a distance of 40.7 km downstream

of the Jing River, there are a total of 41 new and old landslides (Leng et al. 2018; Ma et al. 2019).

Through observations of multiple landslides, it was found that the back wall of such landslides is composed of dry and hard loess, while the soil at the toe of the back wall is moist. Springs emerge from the landslide, forming wetlands. There are numerous open cracks and sinkholes at the top of the back wall, indicating that, similar to loess landslides triggered by heavy rainfall, irrigation water enters the subsurface through concentrated channels. The mechanism of loess landslides induced by irrigation infiltration along the edges of loess terraces is related to fractures. The infiltration of surface water, fractures, and landslides are mutually influential and causative factors. The infiltration of surface water can lead to the generation of fractures, and the fractures, in turn, promote the infiltration of surface water, resulting in landslides. However, the formation of landslides also leads to the development of new fractures and improved drainage conditions for groundwater, causing changes in water levels and promoting the occurrence of a new round of landslides. Therefore, irrigation-induced landslides exhibit a certain cyclic nature. The formation of irrigation-induced loess landslides can be divided into three stages (Peng et al. 2019b) (Fig. 2.3).

- **Stage of landslide incubation.** In the early stages of agricultural irrigation, although extensive irrigation has little impact on the moisture content of the soil, surface water can slowly migrate through the thick unsaturated zone into the deep layers of the loess slope. Although the infiltration process is extremely slow, it has a significant influence on the rising groundwater level. Due to the high water sensitivity of loess, long-term water erosion causes surface collapses and the formation of sinkholes of various sizes. The development of fractures accelerates, and a well-extended fracture network penetrates the slope, providing preferential pathways for surface water infiltration (Lian et al. 2020).
- **Stage of preferential pathway infiltration.** With the development of the above process, the groundwater level gradually rises, and the pore water pressure increases. Long-term water erosion causes surface collapses and the formation of sinkholes of various sizes. The development of fractures accelerates, and a well-extended fracture network penetrates the slope, providing preferential pathways for surface water infiltration. This allows surface water to directly enter the interior of the loess slope. In addition, drilling profiles reveal distinct hydraulic gradients near the edge of the terrace. Along this zone, the hydraulic gradient is higher, resulting in increased hydraulic pressure and the development of slope fractures. Under continuous chemical dissolution and mechanical erosion from irrigation and rainfall, numerous sinkholes and fractures of various sizes appear. Irrigation water or surface runoff from rainfall is discharged from the surface through sinkholes and fractures to the slope or foot of the slope.
- **Stage of landslide movement.** Rainfall and surface irrigation water continuously infiltrate the interior of the loess slope through preferential pathways. This accelerates the formation of a fully connected sliding surface. The ancient soil layer at the foot of the slope rapidly softens upon water contact, eventually generating

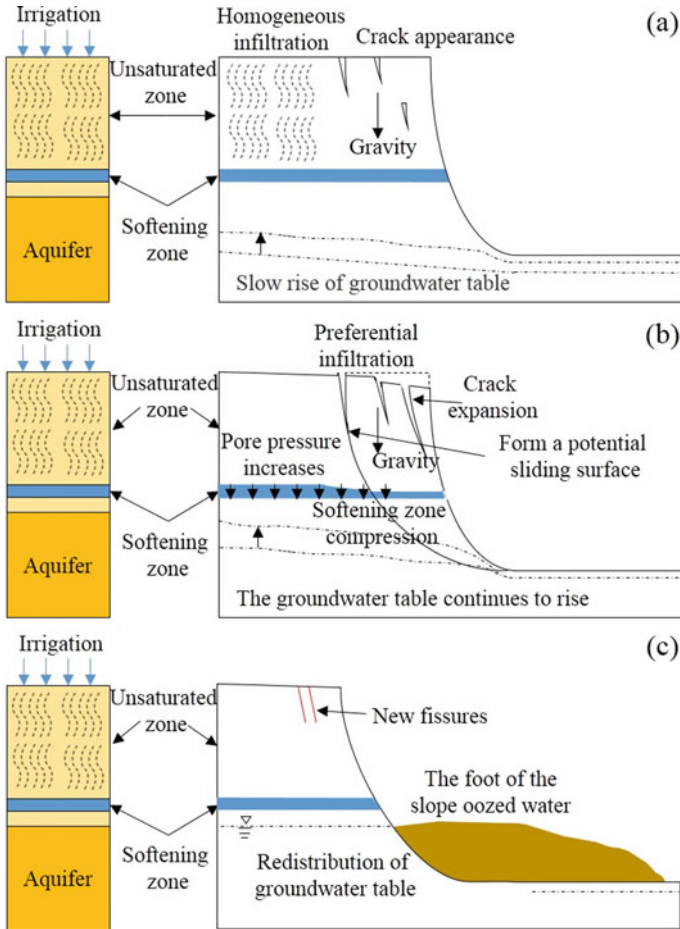


Fig. 2.3 Genetic mechanism of irrigation-induced loess landslides (modified after Peng et al. 2019b)

a potential sliding surface. The softened zone undergoes compression, leading to settlement at the edge of the loess terrace and ultimately triggering a loess landslide. The formation of the landslide deposit redistributes the water table, and seepage occurs at the foot of the slope. As the loess landslide progresses, new terrace fractures begin to appear at the top of the slope and within the slope.

Loess landslides induced by irrigation often exhibit the following characteristics (Wang and Xi 2002):

- Landslides are mostly distributed in groups. Within a small watershed, a series of landslides often occur due to the presence of similar landslide structures and the application of the same external forces. These landslides have high sliding speeds

and long sliding distances. The unstable high and steep back wall formed by the previous landslide is prone to subsequent sliding in the short term. As a result, the landslides are interlocked, making it challenging to distinguish individual landslides and forming a “landslide cluster.”

- Most landslides are characterized by extensive collapse pits with deep and wide wetting-induced cracks at the edges of terraces. These cracks exhibit depths ranging from 15 to 20 m and widths ranging from 0.4 to 1.6 m, often with displacement. The sliding surface of the landslide often develops from these deep and large wetting-induced cracks.
- The position of the shear outlet of the landslide is relatively high, which is the fundamental reason for the formation of high-speed and long-distance landslides.
- The rear part of the sliding surface develops from wetting-induced cracks, while the middle and front parts often correspond to the contact surface between loess and the red clay layer. The inclination of the clay layer aligns with the slope direction, with an inclination angle ranging from 5° to 15°.
- The entire development process of the landslide is closely related to loess collapse and loess liquefaction. These characteristics highlight the complex nature of loess landslides induced by irrigation.

2.5 Rainfall and Loess Landslides

Intense precipitation (rainfall or snowmelt) is a common trigger for landslides. Landslides induced by intense precipitation occur worldwide under various climatic, geological, and topographic conditions. Heavy rainfall or prolonged rainstorms can trigger landslides over large geographical areas, many of which result in significant casualties and extensive property damage (Acosta et al. 2016). In loess regions of China, although the rainfall amount is relatively small, it is concentrated in the months of June to October, often in the form of heavy rainstorms. Therefore, loess landslides tend to occur spatially in areas with high rainfall and temporally during the rainy season. Both rainfall and irrigation primarily alter the groundwater conditions in reservoir areas and adjacent slopes (Meng et al. 2021). The rise in water level reduces the effective stress of the soil, thereby decreasing its resistance to sliding. Additionally, during water level recession, there is an additional downslope permeating force. Loess has low permeability but exhibits a high hydraulic gradient. Bank erosion also alters the stress state of the slope, leading to destabilization (Wu et al. 2017; Tang 2014). These factors highlight the hydrological processes and their impact on the stability of loess slopes during rainfall events. Understanding the interactions between precipitation, irrigation, and slope stability is crucial for landslide hazard assessment and mitigation strategies.

The triggering mechanism of loess landslides by rainfall is highly complex. This complexity arises from the uncertainties in rainfall intensity, duration, and intermission duration, as well as the uncertainties in the lithology, microstructure, and

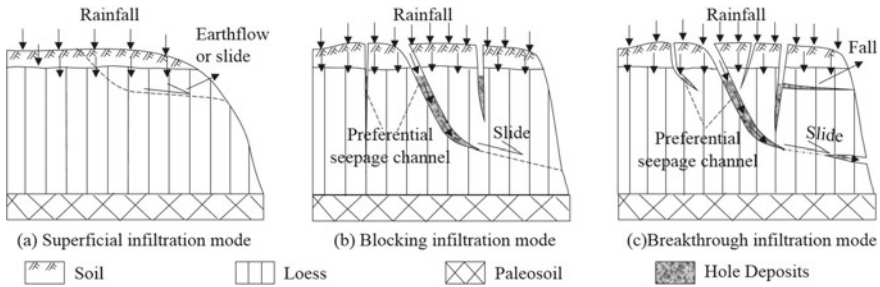


Fig. 2.4 Classification of rain-induced loess landslides (Tang et al. 2015)

macrostructure of loess slopes. The combination of these factors results in more intricate characteristics, such as rainfall infiltration intensity, infiltration depth, depth of evaporative influence, soil moisture content, self-weight, pore water pressure, shear strength, and failure modes. The scale of loess landslides varies from a few m^3 to tens of thousands of m^3 , exhibiting both shallow surface failure patterns and medium-depth failure patterns. This indicates that the dominant sliding surface occurs at different depths when the slope reaches its limit equilibrium state. This suggests that the infiltration depth of rainfall has a considerable range of variation, and the infiltration patterns are diverse. The influence of rainfall on the internal soil of the slope is also diverse, leading to different mechanisms of slope failure. Based on a comprehensive analysis, loess landslides induced by precipitation can be classified into three types: slow infiltration type, infiltration blockage type, and infiltration breakthrough type (Fig. 2.4) (Zhou et al. 2014; Tang et al. 2015).

2.5.1 Slow Infiltration Type

In slope areas with relatively undeveloped joints, fractures, and cavities, as well as intact loess layers, surface runoff generated by rainfall primarily infiltrates through the pores of the loess under the influence of gravity. The infiltration rate is mainly related to the throat radius of the pores, connectivity, and initial saturation of the soil. The infiltration rate is slow, and the infiltration depth is limited (only 1–3 m), thus this type of landslide is also called superficial infiltration mode. Excess rainfall is either discharged as surface runoff or consumed through evaporation (Dolojan et al. 2023). This type of infiltration saturates the shallow soil layer, increases the self-weight of the soil, reduces its shear strength, and leads to shear failure and sliding of the slope (Fig. 2.4a). These types of loess landslides typically occur on steep slopes where tensile fractures are usually absent or poorly developed, and the development of loess caves, sinkholes, subterranean voids, and swallow holes is limited. The slope is relatively intact. Under these circumstances, rainfall cannot infiltrate through fast preferential pathways but rather infiltrates as sheet-like homogeneous infiltration,

resulting in slower infiltration rates (Wu et al. 2017). In this case, the permeability of the rock and soil mass that constitutes the slope is the key factor determining the depth of infiltration and slope stability. Such landslides mostly occur on loess slopes with gradients of $30\text{--}50^\circ$, thicknesses ranging from 3 to 5 m, and small scales, typically ranging from tens to hundreds of cubic meters. Field investigations have found that steep or near-vertical loess slopes are rarely subjected to rainwater, resulting in dry slope surfaces. If the slope toe is wetted, it is prone to collapse. Conversely, slopes that are not subjected to rainwater or erosion tend to be more stable than gentle slopes. Even if the shallow layer is completely wetted, slopes with gradients less than 30° can remain stable. However, slopes with gradients of $30\text{--}50^\circ$ are more susceptible to rainwater infiltration, which affects their stability. Nevertheless, loess has low permeability, and both field observations after rainfall and artificial rainfall infiltration experiments indicate that the depth of direct rainfall infiltration is limited. Under long-term rainfall, continuous infiltration softens the surface loess, increasing the self-weight of the soil and eventually leading to sliding under the influence of gravity. This type of landslide is common, distributed in patches on both sides of loess gullies and linearly along the interface between bedrock and loess. Although the damage caused by these landslides is not significant, they are the main sediment sources for soil erosion. The rainfall conditions required for this type of landslide are as follows: only long-term continuous rainfall can effectively infiltrate the strata, regardless of heavy rain, moderate rain, or light rain, but it can be intermittently continuous (Tang et al. 2015).

2.5.2 Infiltration Blockage Type

During the formation process of loess, various types of fractures are developed, including vertical joints, structural joints, unloading fractures, collapsible fractures, weathering fractures, leaching fractures, erosion cavities, sinkholes, subterranean voids, artificial caves, animal burrows, and plant cavities. Among them, sinkholes and subterranean voids, commonly known as swallow holes, have the greatest impact on slope stability (Sun et al. 2021). The fillings within these fractures or cavities can be in a loose or partially filled state. If these fracture or cavity units can be connected in three-dimensional space, they form preferential flow channels for surface water infiltration. At this stage, these fracture channels are locally interconnected within the slope mass, but there is no outlet at the lower part of the slope surface (Fig. 2.4b). Surface water can rapidly infiltrate along these preferential channels, but it encounters resistance at the front end of the fractures, resulting in increased hydrostatic pressure and enhanced lateral flow velocity. Gradually, an infiltrated surface is formed, with its saturation level continuously increasing, leading to a reduction in shear strength and ultimately resulting in sliding.

These types of loess landslides typically occur on slopes with a certain gradient, where the slope mass is relatively fragmented and various fractures and cavities are well developed. Rainfall on such slopes usually drains through three pathways:

(1) surface runoff, (2) sheet-like infiltration into the slope mass, and (3) infiltration into the slope interior through fast pathways such as fractures and cavities depicted in Fig. 2.4b. The third pathway has the greatest impact on slope stability. Under a certain amount of rainfall and sufficient infiltration time, water gradually saturates the fractures, cavities, and other fast pathways, leading to landslide occurrence. In this infiltration mode, there are no specific requirements for the type of rainfall, which can be heavy rain, moderate rain, light rain, or continuous rainfall. However, a certain cumulative rainfall amount is needed, along with sufficient antecedent rainfall and an adequate infiltration period without rainfall.

2.5.3 Infiltration Breakthrough Type

This type of landslide represents the continued development of the infiltration-blocking model. Due to the infiltration of rainfall, the slope soil undergoes internal erosion, causing further deepening and enlargement of fractures and cavities within the soil mass. Over the long term, one or several preferential flow channels that penetrate the entire slope mass are eventually formed. During rainfall events, water rapidly infiltrates or flows along these preferential flow channels, softening the soil mass and reducing its shear strength, leading to landslide occurrence. It is worth noting that although this landslide was triggered by continuous rainfall, the loess on the back of the landslide remained dry and unaffected by moisture. The landslide mass is also unsaturated, and the intact pathways, vegetation, and microtopography on the sliding mass remain unchanged, indicating that rainfall infiltrates through the preferential channels (Fig. 2.4c).

This type of landslide often occurs on slopes with well-developed fractures and cavities. During rainfall events, water primarily infiltrates through various fast pathways, while sheet-like infiltration plays a minor role. Additionally, due to the interception of rainfall by swallow holes, the amount of surface runoff is limited. The most significant impact on slope stability comes from the development of swallow holes of various sizes on the slope. These swallow holes extend longitudinally in the three-dimensional space of the slope, have a wide lateral expansion, and extend deeply vertically. When rainwater enters these swallow holes, it forms a horizontal infiltration surface of a certain area, expanding the infiltration range and quickly forming a saturated zone or surface water, softening the soil mass, and triggering landslides or collapses. In this infiltration mode, rainfall intensity is crucial, as at a certain rainfall intensity, it can trigger this type of landslide. Sufficient daily or hourly rainfall intensity is required (Zhang and Li 2011).

In general, the impact of rainfall on slopes can be divided into three types of effects: (1) Physical effects, which alter the porosity, fracture density, and moisture content of the slope mass, modifying the shape of the slope. This is mainly manifested by the infiltration of rainwater, causing an increase in pore water pressure, leading to slope deformation and further expansion of existing fractures. As a result, more rainfall infiltrates into the slope mass, increasing the moisture content. Rainfall

also causes erosion and scouring of the slope toe and slope surface, resulting in an increase in the exposed slope area. (2) Chemical effects, which alter the properties of the slope material. For example, it can lead to the liquefaction or expansion of the sliding surface material, and chemical reactions such as hydrolysis, dissolution, and carbonation can change the mineral composition of the soil and rock mass. (3) Mechanical effects, which increase the weight of the slope mass, intensify the driving force for downslope movement, reduce the matric suction of the slope mass, and generate dynamic and static water pressures, weaken the strength parameters of the slope mass.

2.6 Groundwater and Loess Landslides

The occurrence and movement of groundwater are among the primary natural factors that influence the stability of landslides. In most cases, rainfall-induced changes in groundwater conditions serve as the direct triggering factor for landslide disasters in China. The presence of groundwater in landslides is controlled and influenced by the hydrogeological structure of the landslide mass. This structure refers to the combination of water-bearing layers within the landslide mass, including the sliding body, sliding zone, sliding bed, and relative impervious bed. It governs groundwater recharge, runoff, drainage conditions, and their dynamic variations (Pan et al. 2019). Groundwater infiltrates along fracture surfaces and often overflows at the bottom of valleys, altering the hydrogeological conditions of slopes. On the one hand, it increases the weight of the slope mass, exerting static or dynamic water pressure and upward buoyant forces on the unstable soil mass. On the other hand, it reduces the shear strength of weak structural surfaces within the slope mass and plays a role in dissolution and erosion, decreasing the lateral frictional forces between unstable and stable soil masses and reducing the stability of loess slopes.

As an important geological force, groundwater acts as a lubricating medium between frictional surfaces, providing lubrication. The friction coefficient between loess particles and between fracture surfaces decreases significantly within a certain range as the groundwater humidity increases, reducing the cohesive forces between loess particles and fracture surfaces. In the formation conditions of loess landslides, the activity of groundwater provides crucial dynamic conditions for slope deformation and failure. The interaction between groundwater and soil not only changes the physical, chemical, and mechanical properties of the soil and rock mass but also affects the physical and mechanical properties and chemical composition of the groundwater itself. Moving groundwater exerts three types of effects on soil and rock masses: physical effects (including lubrication, softening and infiltration effects, and enhanced binding by pore water), chemical effects (including ion exchange, dissolution, hydration, hydrolysis, dissolution, oxidation–reduction, precipitation, and slaking), and mechanical effects (including static water pressure and dynamic water pressure). The results of the interaction between groundwater and soil and

rock masses influence the deformability and strength of the soil and rock mass and simultaneously reduce the stability coefficient of landslides.

2.6.1 Physical Effects on Soil

The physical effects of groundwater on soils include lubrication, softening and infiltration and the strengthening effect of bound water. The lubrication effect reduces the frictional resistance on discontinuous structural surfaces (such as the particle surfaces of unconsolidated sediments and soils or the fracture surfaces, joint surfaces, and fault surfaces in hard rocks) and enhances the shear stress effect acting on these surfaces, resulting in the initiation of shear movement in the rock–soil mass along the discontinuous structural surfaces. This process is particularly significant when the groundwater level rises above the sliding surface due to rainfall infiltration on slopes. The lubrication effect of groundwater on the rock–soil mass is reflected in mechanics by reducing the friction angle and frictional resistance of the rock–soil mass (Li et al. 2022a).

In general, in mountainous areas with groundwater recharge and a vadose zone (unsaturated groundwater), groundwater strengthens the mechanical properties of the rock–soil mass. In the groundwater saturated zone (gravity water), especially in the discharge zone of groundwater, groundwater reduces the mechanical properties of soils. The increase in capillary pressure and the thinning of the bound water film can create negative pressure, but at the same time, it also causes the soil to crack, creating favorable conditions for future surface water infiltration. The role of water then becomes the weakening effect of lubricating soil particles and softening the soil.

The softening effect of groundwater on soils is manifested in the physical changes of hydrophilic fillers in rock–soil mass and rock structures. With the variation in water content, the fillers in the soil and rock structures undergo a softening effect from the solid-state to the plastic state and even the liquid state. Generally, mudization occurs easily in fault zones, and the sliding materials of most landslides are hydrophilic clays or mud-like substances, which are prone to softening when encountering water, thus directly causing landslides. The softening effect greatly reduces the mechanical properties of the rock–soil mass, including a decrease in cohesion and friction angle (Pan et al. 2019).

For soils in the vadose zone, since the soil is in an unsaturated state and the groundwater is under negative pressure, the groundwater in the soil is not gravity water but bound water. According to the principle of effective stress, the effective stress in unsaturated soils is greater than the total stress of the soil. Therefore, the effect of groundwater strengthens the mechanical properties of the soil, i.e., it increases the strength of the soil. When the soil is devoid of water, the pores of the unsaturated soil are filled with air, and the air pressure is positive. At this time, the effective stress of the sandy soil is less than its total stress, causing it to behave like loose sand. However, when an appropriate amount of water is added, the strength of the sandy soil can increase rapidly. When gravity water appears in the vadose zone soil, the role

of water becomes the weakening effect of lubricating soil particles and softening the soil (Li et al. 2022b).

2.6.2 Chemical Effects on Soil

The chemical effects of groundwater on soils are mainly achieved through processes such as ion exchange, dissolution (in the case of loess collapse and karst), hydration (expansion of expansive rocks), hydrolysis, dissolution, oxidation–reduction, precipitation, and mudization. Ion exchange can soften natural groundwater and increase its permeability. The ion exchange between groundwater and soil alters the structure of the soil mass, thereby affecting its mechanical properties. Clay minerals in loess, such as kaolinite, montmorillonite, illite, chlorite, silica, and zeolite, are the main substances involved in ion exchange. Dissolution and erosion result in the formation of dissolution cracks, voids, and cavities in rock masses, increasing the porosity and permeability of the rocks. Hydration causes microscopic, mesoscopic, and macroscopic changes in the structure of rocks, reducing the cohesion of soils. Hydrolysis not only changes the pH value of groundwater but also alters the composition of rock–soil materials, thereby affecting the mechanical properties of the soil mass. The oxidation–reduction reactions occurring between groundwater and rock–soil materials not only change the mineral composition of loess but also alter the chemical composition and corrosiveness of groundwater, thus influencing the mechanical characteristics of loess slopes (Xu et al. 2021a, b; Ling et al. 2022).

2.6.3 Mechanical Effects on Soil

The mechanical effects of groundwater on rock–soil masses in landslides are primarily exerted through the influence of pore water pressure and dynamic water pressure on the mechanical properties of the rock–soil mass. The former reduces the effective stress of the rock–soil mass, thereby lowering its strength. In fractured rock masses, the pore water pressure can cause expansion deformation of the fractures. The latter generates tangential thrust on the rock–soil mass, increasing the downslope force. When groundwater flows through loose soils, loose fragmented rock masses, and weak interlayers, it exerts volumetric forces on the soil particles. Under the action of dynamic water pressure, fine particle materials in the soil can be mobilized and even transported out of the rock–soil mass, resulting in seepage erosion and damage to the rock–soil mass. This phenomenon is known as piping. Cracks are widely distributed in loess, and water infiltrating and eroding along structural planes can loosen the planes and exert static and dynamic water pressure on the slopes, resulting in significant lateral pressure and increased downslope movement force (Wang et al. 2018; Peng et al. 2020).

Based on the dynamic characteristics of groundwater and the mode of action of the seepage field in landslides, the types of hydraulic effects of groundwater in landslides can be divided into the hydrostatic water pressure effect, buoyancy effect, seepage pressure (or hydrodynamic pressure) effect, increase in weight due to water filling in the sliding mass, and softening effect of fully saturated sliding zone soil (Fig. 2.5). These effects generally coexist in landslides and act together on the landslide mass. However, the emphasis on the calculation of their impact on landslide stability may vary, depending on the specific mechanical effects in a particular landslide. Ultimately, these mechanical effects fundamentally reduce the shear strength and stability coefficient of the landslide mass. Under the influence of rapid changes in hydraulic conditions, the safety factor of loess slopes is significantly reduced. The abrupt changes in hydraulic conditions in the soil of loess slopes mainly include two aspects: the sudden increase in groundwater supply caused by sudden heavy rainfall or long-term continuous rainfall infiltration, leading to drastic changes in water level; and the sudden rise or fall of reservoir water level, causing abnormal changes in groundwater supply or discharge. As a result, the seepage field within the slope undergoes changes, generating large hydraulic gradients within a short period, increasing static and dynamic water pressure within the slope, and ultimately leading to slope instability and landslides.

- Hydrostatic pressure effect.** Based on saturated soil mechanics and seepage theory, the earliest studies focused on saturated seepage and its impact on slope stability within rock–soil masses. In the 1920s, Terzaghi first proposed that the increase in hydrostatic pressure is the main factor leading to the reduction in shear strength along potential sliding surfaces and the initiation of slope movement.

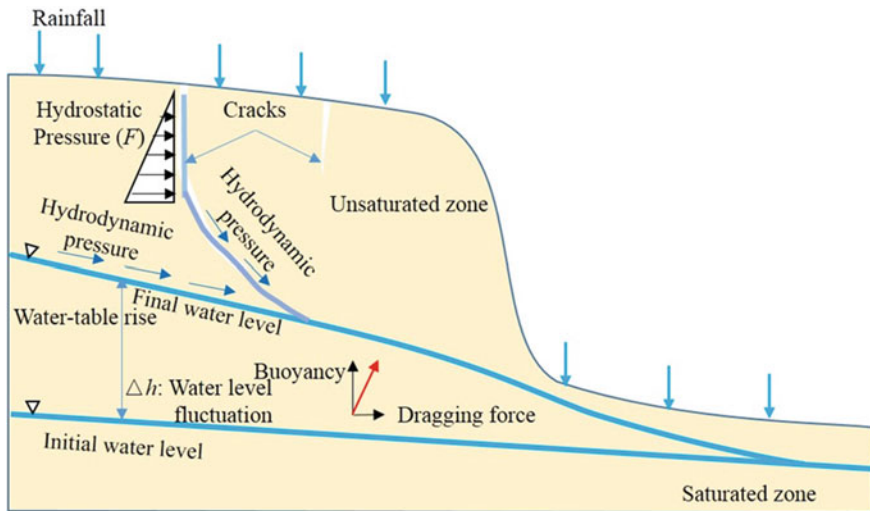


Fig. 2.5 Static and dynamic water pressure of the slope (modified after Peng et al. 2020)

This directly revealed the contribution of elevated pore water pressure during the seepage process to slope movement. Intense rainfall infiltration can cause abnormal accumulation and strong flow of groundwater within the slope, resulting in an increase in pore water pressure and a rapid decrease in effective stress along potential sliding surfaces, thus triggering large-scale landslides.

- **Hydrodynamic pressure effect.** When groundwater infiltrates through the pores in loess, it exerts dynamic water pressure on the surrounding framework. If the vector direction points toward the slope exterior, it will reduce the stability of the rock–soil mass on the slope and may trigger landslides. Dynamic water pressure acts on all soil particles in the seepage field and is derived from the pore water pressure, converting the external force of seepage flow into a uniformly distributed internal force or volumetric force. The greater the hydraulic gradient is, the greater the dynamic water pressure. Dynamic water pressure primarily causes two types of slope failure: erosion and piping. Currently, research both domestically and internationally primarily focuses on the influence of dynamic water pressure resulting from changes in reservoir water levels on slope stability, while there is relatively less research on the effects of dynamic water pressure caused by rainfall. This may be due to the more significant impact of dynamic water pressure resulting from changes in reservoir water levels on slope stability. However, in landslide prevention and mitigation work, the impact of dynamic water pressure caused by rainfall on slope stability should not be ignored. This is because high-intensity or prolonged rainfall can mobilize fine particles in the slope soil through the pores formed by larger particles, leading to a decrease in particle cohesion and shear strength of the slope soil, ultimately resulting in slope movement. Cracks on the slope surface are important conditions for rainfall-induced loess landslides. During rainfall, water accumulates in the cracks, causing pressurized infiltration and increasing the inflow, leading to the continuous expansion of the saturated zone in the slope soil and a decrease in its shear strength. At the same time, the saturated seepage in the slope soil generates dynamic water pressure, increasing the downslope force.
- **The load increases due to filled water.** Under this effect, landslides exhibit characteristics of loose structure and good permeability. Atmospheric rainfall infiltrates the landslide, saturating it and increasing its self-weight, thereby enhancing the downslope force and triggering sliding on slopes with suitable inclinations. Landslides occurring under this effect often have a certain slope gradient, and the downslope force of the slope must be sufficiently large for sliding to occur.
- **Water sensitivity of loess.** The water sensitivity of loess refers to the various unique hydraulic properties exhibited by loess when interacting with water. It has been observed in engineering construction that loess undergoes phenomena such as disintegration, collapse, and erosion when exposed to water. Under the influence of loads, it can also experience deformation and failure phenomena such as rheology, liquefaction, and sliding. These are all manifestations of the sensitivity of loess to changes in the water environment. The water sensitivity of loess refers to the characteristic of loess that exhibits high strength and low compressibility under low moisture content but undergoes a significant decrease

in strength and a substantial increase in deformation when immersed in water or subjected to increased moisture content (Peng et al. 2020).

When the total stress remains constant, an increase in pore water pressure inevitably leads to a decrease in effective stress, thereby affecting the strength and stability of rock masses. The influence of pore water pressure on the strength of rock–soil masses can be expressed using the Mohr–Coulomb failure criterion (Eq. 2.1):

$$\tau = c' + (\sigma_n - P) \tan \varphi' \quad (2.1)$$

where τ is the shear strength, σ_n is the normal stress, P is the pore water pressure, c' is the effective cohesion force, and φ' is the effective internal friction angle.

The water sensitivity of loess is manifested by a gradual decrease in the structural yield stress with increasing initial moisture content, which can be described by a power function (Fig. 2.6a). The curve, known as the yielding line (LC curve), reaches the point of structural yield on the left side under continuous wetting. Shear strength is another important mechanical property index of loess. Under the softening effect of water, the shear strength of loess decreases under different consolidation pressures. The shear strength of loess consists of both frictional strength and cohesive strength. From Fig. 2.6b, it can be observed that the water sensitivity of loess shear strength is mainly reflected in the logarithmic decrease in the cohesive strength (c') with increasing moisture content, while the internal friction angle (φ') exhibits almost no water sensitivity. According to the expression of the Mohr–Coulomb strength criterion, consolidation pressure is one of the factors influencing the water sensitivity of loess shear strength. In shallowly buried loess layers, the overlying soil layer has a smaller weight, and the cohesive strength becomes the main component of loess shear strength. The cohesive strength of loess is a comprehensive reflection of the molecular attraction between particles, solidification bonding, cementation bonding, and capillary rise of the soil–water contact surface. Among them, the contribution of solidification bonding to cohesive strength is significant, and the dissolution of cementing materials by water is the main factor affecting the water sensitivity of loess cohesion. Therefore, the water sensitivity of the shear strength is higher in shallowly buried loess layers. As the depth of the soil layer increases, the proportion of frictional strength in shear strength gradually increases. However, because the internal friction angle hardly has water sensitivity, the water sensitivity of the soil shear strength decreases.

2.7 Prevention and Control of Loess Landslides

Frequent landslides in loess areas disrupt transportation and destroy water and power facilities essential for basic living, causing severe damage to the lives and properties of people in loess areas. This not only hinders the overall economic development of

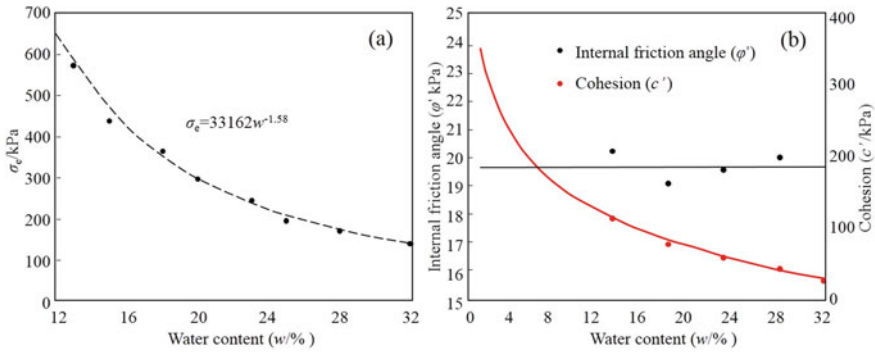


Fig. 2.6 Structure and strength softening line of water-sensitive loess (a variation in yield stress of loess structure with water content; b loess strength parameters changing with water content) (Peng et al. 2020)

loess areas but also affects social harmony and stability. To improve the economic environment and promote economic development in loess areas, it is necessary to study the development laws of landslide disasters in loess areas and seek approaches for their prevention and control. Due to the widespread and severe nature of landslides in loess areas, regional landslide prevention and control should adhere to the principle of prioritizing prevention and complementing it with control. Remedial measures should only be taken for dangerous landslides that pose significant social, economic, and environmental impacts and cannot be effectively prevented. The prevention and control measures for landslides should be determined based on the characteristics of the landslides, as well as financial and material resources and the location of the landslides. If landslides occur in important transportation routes, urban residential areas, factories, etc., significant engineering measures should be implemented. For landslides in remote mountainous areas with sparse populations, simpler preventive measures can be adopted.

2.7.1 Principles for Loess Landslide Prevention and Control

The general principle for landslide mitigation is prioritizing prevention and complementing it with control, aiming to prevent natural landslides caused by changes in the natural environment and human-induced landslides resulting from human activities such as construction, which lead to slope instability. For loess slopes that exhibit regular patterns and characteristic distributions, early detection and timely measures can be taken to avoid unnecessary losses. For unavoidable landslide accidents, real-time surveys should be conducted, closely monitoring their dynamics to minimize the extent of the disaster. The preventive measures include the following:

- Prevent the revival of original landslides. This measure should be implemented throughout the entire construction process, from project planning and design to implementation and usage, to prevent their occurrence.
- Prevent landslides in susceptible areas. Although this step may sound simple and is readily anticipated by many staff members, it is not as easy to implement in practice as imagined. Due to insufficient preliminary data and inaccurate surveys, different opinions exist regarding whether slope failure will occur after the start of the project. Additionally, most loess resource areas in China are located in the northwest, where economic development is relatively lagging, and there is a lack of corresponding funds for landslide control, making it difficult to raise sufficient funds. Consequently, there is often reluctance to invest money and effort in preventive work. Therefore, it is crucial to conduct thorough surveys in the early stages to determine the likelihood of landslides occurring. Simultaneously, comprehensive publicity and mobilization efforts should be made to secure adequate financial support.
- Prevent the exacerbation of ongoing landslides. Whether it is the recurrence of original landslides or landslides currently in progress, measures should be taken to prevent their severity from escalating: real-time monitoring to promptly grasp the dynamics of landslides; timely repair of cracks when they appear to prevent water infiltration into the subsurface, which could worsen the landslide; appropriate excavation of drainage channels near the landslide area to divert surface water away through the channels; strengthening geological exploration to understand the nature and causes of landslides in the local area and design mitigation measures to prevent aggravation; refraining from engaging in any engineering activities without a clear understanding of the causes and nature of the landslide; after obtaining a clear understanding, reducing the load-bearing weight of the easily slidable section on steep slopes and reinforcing the bottom of the slope through pressure measures. Of course, these actions should be carefully planned in advance to avoid potential issues.

2.7.2 Main Control Measurements of Loess Landslides

The measures for landslide prevention and control include two aspects: “prevention” and “treatment.” The “prevention” aspect focuses on reducing the landslide risk and involves relatively simple methods such as diversion, reducing weight and back pressure, strengthening monitoring, and simple support. However, these measures generally cannot fundamentally eliminate the impact of landslides. On the other hand, the “treatment” aspect involves engineering measures taken based on the identification of the causes and mechanisms of landslides. The purpose is to fundamentally eliminate the impact of landslides on human activities. These measures mainly include changing the geometric shape of the slope, intercepting and draining water, and implementing engineering support (Gao et al. 2020).

Interception and Drainage Engineering. Among the factors that trigger loess landslides, water is one of the most significant. On the one hand, it increases the weight of the sliding mass, and on the other hand, water affects landslides through surface water and groundwater. In addition, the infiltration of surface water forms a water-bearing layer with significant pore water pressure on the sliding surface and its vicinity. This pore pressure can cause shear failure in the permeable layer and sliding in the soil mass at the interface between impermeable layers due to softening. Therefore, to prevent the sliding of loess landslides, it is necessary to control the infiltration of surface runoff and orderly discharge of groundwater. Interception and drainage engineering mainly aim to improve the hydrogeological environment of landslides. Effective interception and drainage can better reduce the anti-sliding force, prevent the lubrication of soil particles, maintain the shear strength of the soil mass, and improve landslide resistance. Interception and drainage measures mainly include surface water drainage engineering and groundwater drainage engineering (Peng et al. 2019b).

The exclusion and interception of surface runoff are the primary measures for landslide control. Surface water drainage engineering can be divided into temporary and permanent measures. Permanent surface water drainage measures should be applied to stable landslides with a small traction range. In contrast, when the landslide is in an unstable state, permanent surface water drainage should not be implemented. Instead, temporary measures should be taken with less investment. When temporary drainage is damaged, it should be repaired in a timely manner to prevent surface water from infiltrating the landslide and worsening its movement.

The purpose of groundwater drainage is to lower the groundwater level and eliminate or reduce static water pressure, buoyancy force, and dynamic water pressure on the landslide mass as much as possible. It also eliminates the chemical erosion and physical softening effects of water on the soil mass. There are various methods for groundwater drainage. Depending on factors such as the origin, quantity, flow direction, depth, and relationship with the landslide mass, engineering measures such as water interception trenches (seepage trenches), drainage audits (tunnels), inclined drainage holes, vertical drainage holes, water collection wells, support seepage trenches, and slope seepage trenches can be used to drain groundwater. These measures effectively reduce water pressure in the sliding mass, improve the mechanical properties of the sliding surface, and enhance the stability of the sliding mass.

Mechanical balance engineering. The mechanical equilibrium engineering of landslides primarily focuses on improving the engineering geological environment of landslides. As a special type of slope, landslides possess significant potential energy. Therefore, in landslide prevention and control, rational human intervention is often employed to achieve a “stable state” of the landslide within its design lifespan, meeting different usage purposes. In terms of mechanical equilibrium engineering for landslides, the most effective and relatively economical method is to unload the rear part of the landslide mass and load the front part with back pressure, causing the center of gravity of the landslide mass to shift downward and achieve the purpose of landslide control. When the manipulation of the landslide center of gravity is limited

and cannot be implemented, the most commonly used method in landslide control is through the use of support engineering. This means that by applying support structures, the “strength” of the “resistant sliding segment” of the landslide is increased, making it impossible for the landslide to reach the energy required for shear failure of the “resistant sliding segment” while maintaining the same potential energy, thus preserving the stability of the landslide (Cheng 2013).

When conditions permit, complete excavation of the landslide mass is the most direct and thorough landslide control solution. When it is not possible to completely excavate the landslide mass, for translational landslides with conditions that allow for energy reduction through unloading at the rear edge of the landslide, unloading engineering is the preferred method for landslide control. Especially in emergency situations, when there is insufficient time for other engineering measures to be implemented, reducing the energy of the landslide through unloading can achieve a rapid reduction in the landslide’s energy. In landslide control through unloading engineering, some landslides can achieve stability directly through unloading, while others require a combination of other engineering measures, such as back pressure, drainage, and support structures, for stability.

The pursuit of rational landslide prevention and control solutions has always been a goal of engineering geological research. However, due to the complexity and variability of the geological formations on which landslides depend, as well as the systematic nature of landslide prevention and control engineering, it is often challenging to achieve optimal landslide prevention and control solutions. Nevertheless, regardless of the complexity of the landslide, the determination of prevention and control solutions always relies on the geological conditions, deformation patterns, development stages, and stable states of the landslide. Based on the importance of the protected objects and the requirements for prevention and control, a reasonable landslide prevention and control solution should be determined according to the principles of geological engineering, which is the fundamental principle of rational landslide prevention and control.

References

- Acosta LA, Eugenio EA, Macandog PBM et al (2016) Loss and damage from typhoon-induced floods and landslides in the Philippines: community perceptions on climate impacts and adaptation options. *Int J Glob Warming* 9(1):33–65. <https://doi.org/10.1504/IJGW.2016.074307>
- Cheng Y (2013) Study on regional distribution discipling of landslides and prevention programme. Doctoral Thesis, Southwest Jiaotong University, Chengdu (in Chinese)
- Dolojan NLJ, Moriguchi S, Hashimoto M et al (2023) Hydrologic-geotechnical modelling of shallow landslide and flood hazards caused by heavy rainfall. *Eng Geol* 323:107184. <https://doi.org/10.1016/j.enggeo.2023.107184>
- Gao J, Wang J, Wei Y (2020) Study on treatment of loess landslide based on nanosilica and fly ash composite stabilizer filling fissures. *Adv Civ Eng* 2020:8884981. <https://doi.org/10.1155/2020/8884981>

- Garakani AA, Haeri SM, Khosravi A et al (2015) Hydro-mechanical behavior of undisturbed collapsible loessial soils under different stress state conditions. *Eng Geol* 195:28–41. <https://doi.org/10.1016/j.enggeo.2015.05.026>
- Huang X (2019) Hazard and risk evaluation of fatal landslides in China and the landslides on the Loess Plateau. Master Thesis, Lanzhou University, Lanzhou (in Chinese)
- Leng Y, Peng J, Wang Q et al (2018) A fluidized landslide occurred in the Loess Plateau: a study on loess landslide in South Jingyang tableland. *Eng Geol* 236:129–136. <https://doi.org/10.1016/j.enggeo.2017.05.006>
- Li P, Qian H (2018a) Water in loess. In: Meyers RA (ed) *Encyclopedia of sustainability science and technology*. Springer, New York, pp 1–17. https://doi.org/10.1007/978-1-4939-2493-6_968-1
- Li P, Qian H (2018b) Water resource development and protection in loess areas of the world: a summary to the thematic issue of water in loess. *Environ Earth Sci* 77:796. <https://doi.org/10.1007/s12665-018-7984-3>
- Li W, Zhu J, Zhang H et al (2022a) Geological conditions of saturated soft loess stratum and influence of tunnel excavation and dewatering system on its groundwater environment. *Bull Eng Geol Env* 81(3):128. <https://doi.org/10.1007/s10064-022-02624-z>
- Li B, Tian B, Tong F (2022b) Effect of the water-air coupling on the stability of rainfall-induced landslides using a coupled infiltration and hydromechanical model. *Geofluids* 2022:3036905. <https://doi.org/10.1155/2022/3036905>
- Lian B, Peng J, Zhan H (2020) Formation mechanism analysis of irrigation-induced retrogressive loess landslides. *CATENA* 195:104441. <https://doi.org/10.1016/j.catena.2019.104441>
- Ling X, Ma J, Chen P et al (2022) Isotope implications of groundwater recharge, residence time and hydrogeochemical evolution of the Longdong Loess Basin, Northwest China. *J Arid Land* 14:34–55. <https://doi.org/10.1007/s40333-022-0051-7>
- Liu D (1985) *Loess and environmental*. Science Press, Beijing (in Chinese)
- Ma P (2020) Study on evolution characteristics and transformation mechanism of loess geohazards chain. Doctoral Thesis, Chang'an University, Xian (in Chinese)
- Ma P, Peng J, Wang Q (2019) The mechanisms of a loess landslide triggered by diversion-based irrigation: a case study of the South Jingyang Platform, China. *Bull Eng Geol Env* 78(7):4945–4963. <https://doi.org/10.1007/s10064-019-01467-5>
- Meng Z, Ma P, Peng J (2021) Characteristics of loess landslides triggered by different factors in the Chinese Loess Plateau. *J Mt Sci* 18:3218–3229. <https://doi.org/10.1007/s11629-021-6880-6>
- Pan P, Shang Y, Lyu Q et al (2019) Periodic recurrence and scale-expansion mechanism of loess landslides caused by groundwater seepage and erosion. *Bull Eng Geol Env* 78(2):1143–1155. <https://doi.org/10.1007/s10064-017-1090-8>
- Peng J, Zhang F, Wang G (2017) Rapid loess flow slides in Heifangtai terrace, Gansu, China. *Q J Eng Geol Hydrogeol* 50(2):106–110. <https://doi.org/10.1144/qjegh2016-065>
- Peng J, Wang S, Wang Q et al (2019a) Distribution and genetic types of loess landslides in China. *J Asian Earth Sci* 170:329–350. <https://doi.org/10.1016/j.jseaes.2018.11.015>
- Peng J, Wang Q, Men Y et al (2019b) *Landslide disaster in loess Plateau*. Science Press, Beijing (in Chinese)
- Peng J, Wang Q, Zhuang J (2020) Dynamic formation mechanism of landslide disaster on the Loess Plateau. *J Geomech* 26(5):714–730. <https://doi.org/10.12090/j.issn.1006-6616.2020.26.05.059> (in Chinese)
- Sun J (2005) *Loessology*. Hong Kong Archaeological Society, Hong Kong (in Chinese)
- Sun P, Wang H, Wang G (2021) Field model experiments and numerical analysis of rainfall-induced shallow loess landslides. *Eng Geol* 295:106411. <https://doi.org/10.1016/j.enggeo.2021.106411>
- Tang Y (2014) *Risk assessment and monitoring and early warning of Loess Landslide*. Science Press, Beijing (in Chinese)
- Tang Y, Xue Q, Li Z et al (2015) Three modes of rainfall infiltration inducing loess landslide. *Nat Hazards* 79(1):137–150. <https://doi.org/10.1007/s11069-015-1833-4>
- Wang J, Xi Y (2002) Study on landslide groups induced by irrigation water in loess area. *Science Geographica Sinica* 22(3):305–310 (in Chinese)

- Wang J, Liang Y, Zhang H et al (2015) A loess landslide induced by excavation and rainfall. *Landslides* 11:141–152. <https://doi.org/10.1007/s10346-013-0418-0>
- Wang Y, Yu L, Yin T et al (2018) Stability analysis of partially submerged landslide with the consideration of the relationship between porewater pressure and seepage force. *Geofluids* 2018:9145830. <https://doi.org/10.1155/2018/9145830>
- Wei Y, Fan W, Wang W et al (2017) Identification of nitrate pollution sources of groundwater and analysis of potential pollution paths in loess regions: a case study in Tongchuan region, China. *Environ Earth Sci* 76:423. <https://doi.org/10.1007/s12665-017-6756-9>
- Wu LZ, Zhou Y, Sun P et al (2017) Laboratory characterization of rainfall-induced loess slope failure. *CATENA* 150:1–8. <https://doi.org/10.1016/j.catena.2016.11.002>
- Xu L, Dai F, Tu X (2014) Landslides in a Loess Platform, North-West China. *Landslides* 11(6):993–1005. <https://doi.org/10.1007/s10346-013-0445-x>
- Xu X, Guo W, Liu Y (2017) Landslides on the Loess Plateau of China: a latest statistics together with a close look. *Nat Hazards* 86:1393–1403. <https://doi.org/10.1007/s11069-016-2738-6>
- Xu Q, Zhao K, Liu F et al (2021a) Effects of land use on groundwater recharge of a loess terrace under long-term irrigation. *Sci Total Environ* 751:142340. <https://doi.org/10.1016/j.scitotenv.2020.142340>
- Xu P, Zhang Q, Qian H (2021b) An investigation into the relationship between saturated permeability and microstructure of remolded loess: a case study from Chinese Loess Plateau. *Geoderma* 382:114774. <https://doi.org/10.1016/j.geoderma.2020.114774>
- Zhang M, Li T (2011) Triggering factors and forming mechanism of loess landslides. *J Eng Geol* 19(4):530–540 (in Chinese)
- Zheng M (2017) Database construction and hazard assessment of geological disaster in Loess Plateau of Shan-Gan-Ning Region. Doctoral Thesis, Chang'an University, Xian (in Chinese)
- Zhou W, Tang C, Van Asch TWJ et al (2014) Rainfall-triggering response patterns of post-seismic debris flows in the Wenchuan earthquake area. *Nat Hazards* 70(2):1417–1435. <https://doi.org/10.1007/s11069-013-0883-8>
- Zhu J, Zhu C, Zhang J et al (2002) Landslide disaster in the loess area of China. *J For Res* 13(2):157–161. <https://doi.org/10.1007/BF02857244>
- Zhu Y, Jia X, Shao M (2018) Loess thickness variations across the Loess Plateau of China. *Surv Geophys* 39:715–727. <https://doi.org/10.1007/s10712-018-9462-6>
- Zhuang J, Peng J (2014) A coupled slope cutting-a prolonged rainfall-induced loess landslide: a 17 October 2011 case study. *Bull Eng Geol Env* 73:997–1011. <https://doi.org/10.1007/s10064-014-0645-1>

Chapter 3

Land Subsidence and Groundwater Seepage



3.1 Introduction

Land subsidence is an environmental geological phenomenon characterized by a regional decline in ground elevation due to the compression of unconsolidated soil, influenced by both natural and anthropogenic factors. Natural factors include earthquakes, geological tectonic subsidence, volcanic eruptions, climate change, and natural consolidation of soil. Anthropogenic factors refer to human activities such as the extraction of underground fluid resources (e.g., petroleum, natural gas, water) or solid mineral resources (e.g., metallic minerals, coal mines, salt mines). Land subsidence can cause significant damage to buildings and human lives. Therefore, it is vital to gain adequate knowledge of the causes and mechanisms of land subsidence, and it is also necessary to learn the measures for land subsidence prevention and control.

3.1.1 Causes of Land Subsidence

From a geological perspective, natural land subsidence is primarily attributed to three main causes. First, compaction of loose or semi-loose layers in the Earth's crust under the influence of gravity leads to their transformation into dense, hard, or semi-hard rock layers, resulting in land subsidence due to reduced layer thickness. Second, geological tectonic processes can induce land depression and consequent subsidence. Third, seismic events have the potential to trigger land subsidence (Chen et al. 2020).

The phenomenon of land subsidence is also intricately linked to human activities. Excessive exploitation of underground resources, such as petroleum, natural gas, solid minerals, and groundwater, by humans induces a systematic decline in pore pressure within the sedimentary layers harboring these solid, liquid, and gaseous

substances. This reduction in pore pressure amplifies the effective stress levels and consequently leads to the compaction of geological formations, thereby directly contributing to land subsidence.

- Land subsidence caused by overexploitation of groundwater.** Coastal areas often consist of thick deposits of loose layers with fine particles and complex structures (Galloway and Burbey 2011). Extensive extraction of deep groundwater leads to a decrease in pore water pressure and an increase in effective stress, resulting in the compression of aquifers. This compression increases the contact area between particles, reduces porosity, and induces water release, causing elastic deformation. The subsidence generally corresponds to approximately 15% of the compression rate of cohesive soils. Once the water pressure in the aquifer is restored, the framework rebounds, resulting in temporary land subsidence (Liu et al. 2022). Cohesive soils have a high porosity and tiny pores, primarily containing bound water. When the hydraulic head difference between the aquifer and the cohesive soil layer is sufficient to overcome the bonding forces between water and particles, water is expelled from the cohesive soil layer. During water release, pore compression occurs, increasing the contact area between clay mineral particles and causing relative displacement between particles. This disrupts the pore structure and leads to plastic deformation. When the water pressure in the aquifer is restored, it can only increase the water pressure in the compressed pores of the cohesive soil layer but cannot restore the porosity and storage capacity to their initial states, resulting in permanent land subsidence (Tzampoglou et al. 2023) (Fig. 3.1).
- Land subsidence caused by geothermal extraction.** Some coastal and inland areas harbor geothermal resources, and the extraction of underground geothermal water has been increasing annually. The extraction of geothermal

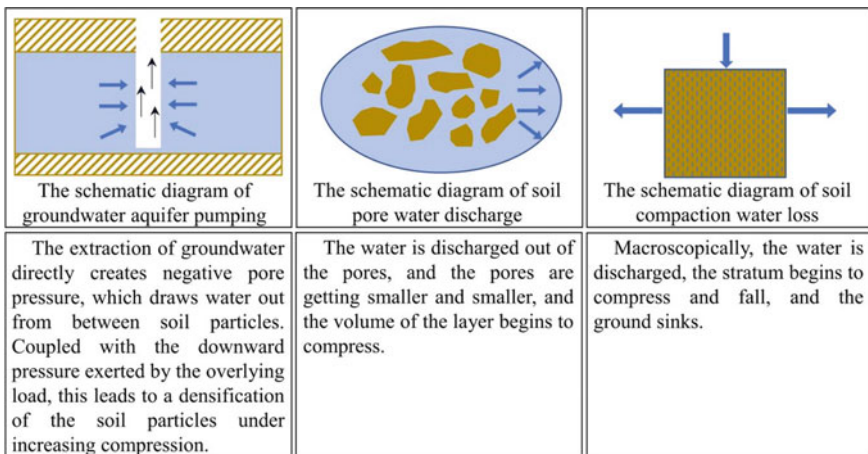


Fig. 3.1 Schematic diagram of land subsidence caused by groundwater exploitation

water leads to a decline in the water table, resulting in a reduction in pore water pressure and an increase in effective stress within the geological strata. This inevitably leads to further consolidation of the strata and subsequent land subsidence.

- **Land subsidence caused by oil and gas extraction.** In oil and gas fields, the extraction of oil and gas resources can also cause land subsidence (Younas et al. 2023). After the development of oil and gas, the decrease in fluid pressure and the increase in effective stress on solid particles further consolidate the geological formations, resulting in land subsidence. Therefore, the extraction of petroleum and natural gas is also one of the factors contributing to land subsidence in oil and gas fields (Tzampoglou et al. 2023).
- **Land subsidence caused by surface loads.** With the expansion of urban areas and the increasing number of tall buildings, as well as the influence of transportation facilities such as railways and bridges, the surface loads have intensified, accelerating land subsidence (Cui 2018).

Land subsidence resulting from crustal movements is possible, but the subsidence rate is generally small. Land subsidence caused by static and dynamic surface loads only exists in localized areas. The main cause of regional subsidence is the depletion of underground fluid resources, leading to a decrease in hydraulic pressure within loose geological formations. However, the majority of land subsidence is caused by excessive extraction of groundwater and other underground resources. Unrestricted groundwater extraction disrupts the balance between water and soil, reduces pore water pressure within the geological strata, increases the effective stress on the soil, and compresses the strata. This compression is manifested as consolidation and compaction of clay and sandy layers, resulting in land subsidence disasters (Zeitoun and Wakshal 2013).

As urbanization continues to expand worldwide and urban populations significantly increase, the demand for water in various sectors, such as residential, industrial, and agricultural industries, has dramatically risen. Excessive groundwater extraction has resulted in severe land subsidence in urban areas (Bagheri-Gavkosh et al. 2021). To date, over 100 countries and regions, including Mexico, Japan, Italy, the United States, and China, have experienced large-scale land subsidence issues. Mexico was the first country to face land subsidence problems, starting in 1891. Initially, the subsidence was minimal and not noticeable, but it later caused significant socioeconomic losses, raising awareness of the severity of land subsidence (Figuroa-Miranda et al. 2018). Accumulated subsidence in Mexico has reached between 8 and 15 m. Serious land subsidence disasters also occurred in Niigata, Japan, affecting cities such as Tokyo, Osaka, and Saga Prefecture. In the nineteenth century, excessive groundwater extraction in the Ravenna region of Italy caused land subsidence. The subsidence rate increased from a few mm per year to several hundred mm per year, resulting in significant land subsidence issues in the area. Similarly, the United States also faced land subsidence issues early on. In the mid-twentieth century, groundwater levels dropped by nearly 100 m, leading to increased land subsidence and widespread impacts. Various states in the United States have experienced land subsidence issues

due to declining groundwater levels (Galloway and Sneed 2013). Since the discovery of land subsidence in Shanghai in 1921, a total of 96 cities and regions in 17 provinces in China have experienced land subsidence. Overall, land subsidence in most cities or regions is still ongoing, with the subsidence area expanding and the associated hazards increasing (Li et al. 2021).

3.1.2 Hazards Caused by Land Subsidence

Land subsidence possesses such characteristics as slow generation, wide-ranging hazards, and severe and irreversible damage. Based on the area of land subsidence and the maximum cumulative subsidence, it can be classified into four levels: catastrophic, large-scale, medium-scale, and small-scale, as shown in Table 3.1. Land subsidence poses various hazards, affecting different aspects.

- **Impact on surveying and mapping data.** Changes in ground elevation render existing surveying results ineffective. Large-scale discrepancies between existing elevation information and available data may arise, and in severe cases, even national-level benchmark elevation data may need to be revised. This discrepancy significantly impacts hydrological, geological, environmental protection, and engineering design and construction data (Higgins 2015).
- **Appearance and hazards of ground fissures.** Uneven land subsidence can induce and result in the formation of ground fissures, leading to more severe disasters. When ground fissures cut through surface structures such as buildings and cultural relics, they cause severe damage to related facilities and even pose a risk of building collapse. When they traverse agricultural fields or other land uses, they cause significant water leakage, further triggering more serious disasters (Guzy and Malinowska 2020).
- **Impact on the transportation industry.** This mainly manifests in long-distance transportation, such as railways and highways. In engineering areas spanning long distances, land subsidence generally exhibits uneven characteristics, leading to phenomena such as roadbed subsidence and rail misalignment, thereby affecting the normal operation of transportation.
- **Uneven land subsidence can cause underground pipelines to bend and, in severe cases, lead to fracture.** If this disaster occurs in the underground laying

Table 3.1 Classification of land subsidence levels

Level	Area (km ²)	Maximum cumulative subsidence (m)
Catastrophic	> 500	2.0–1.0
Large-scale	500–100	1.0–0.5
Medium-scale	100–10	0.5–0.1
Small-scale	< 10	< 0.1

of power transmission lines, gas pipelines, and other utilities, it directly affects industrial production and personal life and can even pose significant risks to life and property. Underground structures, under the influence of uneven land subsidence, develop severe cracks and may experience collapse accidents (Khajehali et al. 2023).

3.2 Compressive Water Seepage Mechanisms in Saturated Porous Media

3.2.1 Principle of Effective Stress

Saturated porous media consist of solid particles and pore water. The stress exerted on the soil is transmitted through contact points between the particles. This inter-particle stress causes displacement of soil particles, resulting in deformation and changes in strength, known as effective stress, denoted as σ' . During natural deposition processes, particle compaction occurs slowly. Due to the extremely small rate of natural compaction, it can be neglected when compared to the rate of land subsidence. Therefore, an undisturbed saturated aquifer can be considered to be in a state of pressure equilibrium.

If the pores of the medium are interconnected and filled with stagnant water, the water in the pores follows the distribution of hydrostatic pressure. The stress transmitted through the pore water is called pore water pressure, denoted as u . Under slow seepage conditions, groundwater can be approximated as being in a static state, and the pore water pressure follows the distribution of hydrostatic pressure, where the pressure in different directions at any point is equal. Therefore, under hydrostatic pressure conditions, pore water pressure does not cause particle displacement but only contributes to particle compression deformation. However, experiments have shown that the compressibility of solid particles is an order of magnitude smaller than that of water. Therefore, in general, the deformation of particles themselves can be neglected.

Under external loading, the stress increment generated at each point in the soil is referred to as additional stress. In saturated soil, the additional stress σ at any point is jointly borne by the effective stress of the particle skeleton σ' and the pore water pressure u , and they satisfy the following relationship (Eq. 3.1):

$$\sigma = \sigma' + u \quad (3.1)$$

This equation represents the principle of effective stress in saturated soils, which states that any increase or decrease in pore water pressure will cause a change in effective stress when the external load remains constant.

The action of additional stress causes the pore water pressure to exceed the hydrostatic pressure, resulting in excess pore water pressure. The relationship between

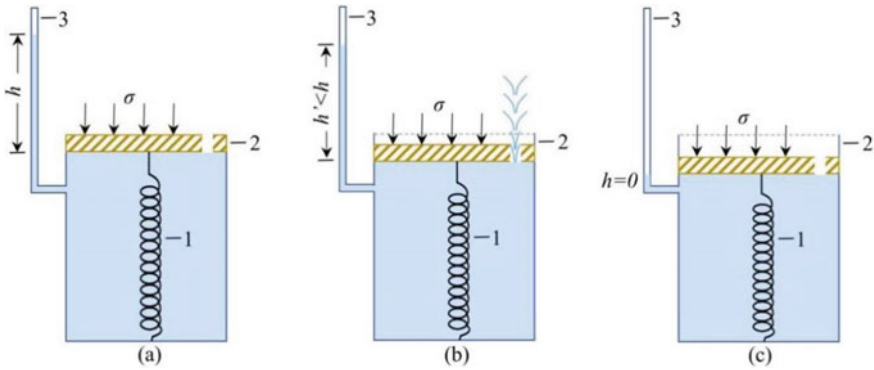


Fig. 3.2 Mechanical model of saturated soil (1-spring, 2-piston with holes, and 3-pressure tube)

excess pore water pressure and effective stress can be illustrated using a simple mechanical simulation model shown in Fig. 3.2.

The model employs a container consisting of a spring and a piston with a hole, filled with water, and equipped with a pressure gauge on the wall to simulate saturated soil. The spring represents the soil particles, and the water in the container represents the free water in the pores.

1. Initially, a uniformly distributed pressure σ' is applied to the piston. At the moment when the pressure is first applied, the height h of the water head in the pressure gauge exceeds the hydrostatic head, and it is equal to the product of the unit weight of water and σ (Fig. 3.2a). At this point, the externally applied pressure is entirely borne by the water below the piston, and the spring is not yet under stress, i.e., $\sigma' = 0$, $u = \sigma$.
2. Under the influence of excess pore water pressure u , the water in the container starts to discharge outward through the small hole, causing the piston to descend and compress the spring. Simultaneously, the water head in the pressure gauge gradually decreases. At this stage, the additional pressure is borne jointly by the spring and the water, i.e., $\sigma = \sigma' + u$ (Fig. 3.2b).
3. As the water continues to discharge and the piston continues to descend, the pressure σ' borne by the spring increases continuously until the entire externally applied pressure σ is transferred to the spring. At this point, the excess water head in the pressure gauge h becomes zero, the water stops flowing, and the piston no longer descends (Fig. 3.2c). This marks the end of the compression process, i.e., $\sigma' = \sigma$, $u = 0$.

It can be observed that for saturated soils, it is necessary for water in the pores to continuously seep outward for the excess pore water pressure to gradually transform into effective stress, compressing the pore volume and causing soil deformation. This compression process induced by the outward seepage of pore water is referred to as consolidation. Therefore, the compression and deformation process of saturated soils essentially involves the dissipation of excess pore water pressure through

continuous seepage and the gradual increase in effective stress. In other words, it is the process of pore water pressure transforming into effective stress, which consistently follows the fundamental principle of effective stress. The time required for this transformation is the time for the soil's compression consolidation to reach its final stability. The duration of consolidation depends on the rate of outward seepage of pore water and the drainage conditions of the soil layer. Sands with high permeability achieve consolidation stability quickly, often completing shortly after the construction of buildings, and the subsidence-time relationship is typically not considered in foundation design. On the other hand, saturated cohesive soils require several years, decades, or even longer to achieve stability due to their characteristics.

3.2.2 Consolidation of Saturated Porous Media Due to Water Loss

Water loss-induced compression of the media is the most common manifestation of land subsidence. The amount of land subsidence can be attributed to two main factors: (1) compression of sandy gravel aquifers and (2) water loss-induced compression of relatively impermeable cohesive soil layers. The former is primarily characterized by elastic deformation, with a rapid rate and small subsidence, and complete rebound upon water level recovery. The latter, on the other hand, involves predominantly plastic deformation, with a slow rate, large subsidence, and minimal rebound after water level recovery, leading to significant ground deformation. Therefore, the compression deformation of relatively impermeable cohesive soil layers is the key focus in the study of land subsidence (El Shinawi et al. 2022).

The mechanism of land subsidence caused by groundwater extraction can be described as follows: the pressure head of the confined aquifer decreases, resulting in the drainage of the overlying impermeable clay layer, reducing the pore pressure. Under nearly constant total stress conditions, the effective stress increases, causing the densification of the cohesive soil and resulting in land subsidence. This consolidation process, closely related to the dissipation of pore water through seepage, is the outcome of consolidation due to permeation. Mathematical models for the permeation consolidation of soil layers can be established based on the principles of effective stress, drainage consolidation characteristics, and Darcy's law. The process of permeation consolidation essentially involves studying the variation in excess pore water pressure with time and depth throughout the compressible soil layer. By applying the principles of effective stress, drainage consolidation characteristics, and Darcy's law, mathematical models for the permeation consolidation of soil layers can be developed.

3.2.2.1 Unidirectional Permeation Consolidation Model

During the process of drainage-induced compression, the additional stress σ_z at any point within the soil always follows the principle of effective stress, which relates to the effective stress σ' and the pore water pressure u , as expressed by Eq. (3.2).

$$\sigma_z = \sigma' + u \tag{3.2}$$

For the entire soil mass, the process of drainage-induced compression can be represented by the physical model shown in Fig. 3.3b. This model consists of a container composed of multiple layers of springs and pistons with small pores filled with water. Pressure-measuring tubes are installed on the walls of each spring layer to observe the variation in excess pore water pressure with depth and time in the soil layers. This model corresponds to the saturated cohesive soil layer depicted in Fig. 3.3a subjected to a uniformly distributed infinite-width load P . In this case, the additional pressure $\sigma_z = P$ is uniformly distributed along the depth of the formation, and the soil layer undergoes only vertical compression deformation, while the pore water can only permeate vertically upward (or downward). This is equivalent to unidirectional permeation consolidation under the condition of no lateral expansion. The process of cohesive soil compression due to groundwater level decline, leading to land subsidence, can generally be abstracted as the mechanical model illustrated in Fig. 3.3.

At the moment of applying the uniformly distributed pressure P , i.e., $t = 0$, the pore water has not had time to drain outwards. At this stage, the excess pore water pressure head in the pressure-measuring tubes at different depths is $\frac{u}{\gamma_w}$ equal to $u = \sigma_z$, $\sigma' = 0$, and the consolidation subsidence of the saturated cohesive soil layer $S_t = 0$. Subsequently, during the stable period $0 < t < \infty$, under the influence of u , the pore

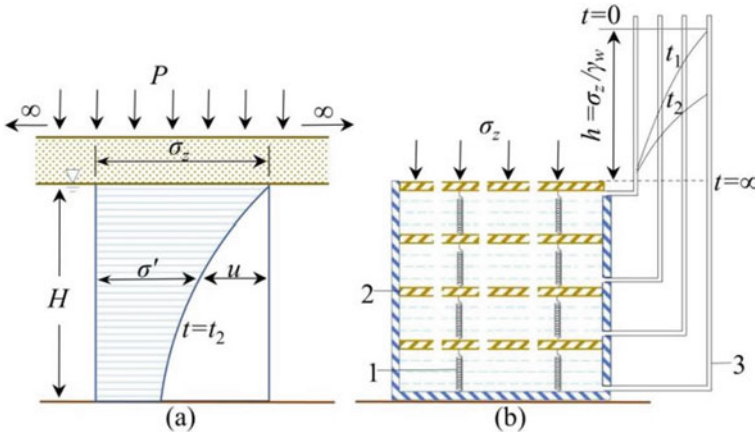


Fig. 3.3 Unidirectional seepage consolidation model of saturated soil (1-spring; 2-piston with holes; 3-pressure tube)

water near the water surface begins to seep outward, resulting in $u = 0$ at that location and $\sigma' = \sigma_z$. As the depth increases, the time required for dissipation of excess pore water pressure increases. At a specified time (t_1), the variation curves of the pore water head with depth in the pressure-measuring tubes are shown in Fig. 3.3b. It can be observed that u and σ' vary with depth, and as time t increases, u gradually decreases at different depths, while σ' increases accordingly, always satisfying the principle of effective stress. At this stage, the consolidation subsidence (S_t) in the saturated soil layer is $0 < S_t < S$ (the final subsidence during consolidation stabilization).

Assumptions:

- The compressible soil layer is a homogeneous and isotropic saturated soil mass.
- The soil particles and water in the saturated soil mass are incompressible.
- During the consolidation process, the permeability coefficient K and the compressibility coefficient α are constant.
- Water and soil particles can only undergo vertical seepage and movement.
- The permeation of water in the soil follows Darcy's law.
- The external load is applied to the soil only once.
- Extremely slow secondary consolidation caused by creep of the water film on the surface of soil particles and rearrangement of the soil particle structure is not considered.

As shown in Fig. 3.4, the additional pressure $\sigma_z = P$ is uniformly distributed along the depth, and since the layer below is impermeable, the pore water can only drain vertically upward.

At any depth z within the saturated cohesive soil layer, consider a differential soil mass with a volume of $1 \times 1 \times dz$. Within this differential mass, the volume of voids V_v and the volume of solid particles V_s are given by Eqs. (3.3) and (3.4), respectively.

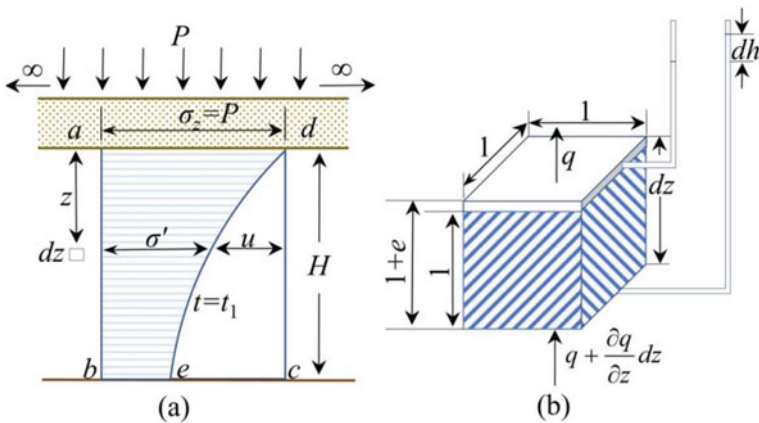


Fig. 3.4 One-way seepage consolidation calculation diagram

$$V_v = \frac{e}{1+e} dz \quad (3.3)$$

$$V_s = \frac{1}{1+e} dz \quad (3.4)$$

During a time interval dt , the amount of water discharged from the differential mass should be equal to the decrease in void volume within the differential soil mass, as expressed by Eq. (3.5)

$$\frac{\partial q}{\partial z} dz dt = \frac{\partial V_v}{\partial t} dt \quad (3.5)$$

where q represents the water quantity passing through a unit area per unit time.

Since $V_v = \frac{e}{1+e} dz$ and the particle volume $\frac{1}{1+e}$ is constant during the consolidation process,

$$\frac{\partial V_v}{\partial t} dt = \frac{1}{1+e} \frac{\partial e}{\partial t} dz dt \quad (3.6)$$

Equation (3.5) can be simplified to Eq. (3.7).

$$\frac{\partial q}{\partial z} = \frac{1}{1+e} \frac{\partial e}{\partial t} \quad (3.7)$$

According to Darcy's law, Eq. (3.8) holds true.

$$q = KI = \frac{K}{\gamma_w} \frac{\partial u}{\partial z} \quad (3.8)$$

Furthermore, based on the law of compression, Eq. (3.9) is derived.

$$a = -\frac{de}{d\sigma'} \quad (3.9)$$

$$de = -a d\sigma' = a du.$$

Substituting Eqs. (3.8) and (3.9) into Eq. (3.7), we obtain Eq. (3.10) or its alternative form.

$$\frac{K}{\gamma_w} \frac{\partial^2 u}{\partial z^2} = \frac{a}{1+e} \frac{\partial u}{\partial t} \quad \text{or} \quad C_v \frac{\partial^2 u}{\partial z^2} = \frac{\partial u}{\partial t} \quad (3.10)$$

where

$$C_v = \frac{K(1+e)}{\gamma_w a}$$

where C_v is the consolidation coefficient, which is equivalent to the pressure conduction coefficient in groundwater dynamics; e is the average void ratio in the process of soil consolidation; γ_w is the density of water; and a is the compression coefficient of soil.

Equation (3.10) represents the differential equation for unidirectional permeation consolidation of saturated soil. For the simplified case depicted in Fig. 3.4, the mathematical model can be written as Eq. (3.11).

$$\left\{ \begin{array}{l} C_v \frac{\partial^2 u}{\partial z^2} = \frac{\partial u}{\partial t} \quad (\text{Differential equation}) \\ u \Big|_{t=0} = \sigma_z \quad (\text{Initial condition}) \\ 0 \leq z \leq H \\ u|_{z=H} = 0 \quad (\text{Upper boundary condition}) \\ \frac{\partial u}{\partial z} \Big|_{z=0} = -1 \quad (\text{Downstream boundary condition}) \end{array} \right. \quad (3.11)$$

The analytical solution to this mathematical model is given by Eq. (3.12)

$$u = \frac{4}{\pi} \sigma_z \sum_{m=1}^{\infty} \frac{1}{m} \sin \frac{m\pi z}{2H} e^{-m^2 \frac{\pi^2}{4} T_v} \quad (3.12)$$

where m is an odd positive integer (1, 3, 5, ...), e is the base of the natural logarithm, T_v is the time factor and $T_v = \frac{C_v t}{H^2}$, H represents the longest flow path of water in the consolidating soil layer (equal to the thickness of the soil layer for single drainage or half the thickness for double drainage), and t denotes time.

When exploiting groundwater resources, if the distribution of aquitards is extensive, their permeability can be approximated as one-dimensional flow. If we further assume that the water level in the aquifer suddenly drops by Δh and remains at that level for a long time, the mathematical model and analytical solution can be identical to the previous discussion by replacing σ_z in Eq. (3.11) with $\Delta h \cdot \gamma_w$.

If the water level in the aquifer continuously changes over time and both the upper and lower boundaries of the saturated cohesive soil layer are drained simultaneously, Eq. (3.11) can be modified into a more general form, as shown in Eq. (3.13).

$$\left\{ \begin{array}{l} C_v \frac{\partial^2 u}{\partial z^2} = \frac{\partial u}{\partial t} \quad (\text{Differential equation}) \\ u(z, t)|_{t=0} = u_0(z) \quad (\text{Initial condition}) \\ u(z, t)|_{z=H} = u_1(t) \quad (\text{Upper boundary condition}) \\ u(z, t)|_{z=0} = u_2(t) \quad (\text{Downstream boundary condition}) \end{array} \right. \quad (3.13)$$

In Eq. (3.13), the initial conditions and upper/lower boundary conditions are generally known functions, and analytical solutions can only be obtained in extremely simplified cases.

3.2.2.2 Two-Dimensional and Three-Dimensional Consolidation Theory

The use of a unidirectional permeation consolidation model is only applicable when the saturated cohesive soil has a large distribution area, gentle inclination, wide and gentle groundwater cones, uniform land subsidence, and negligible lateral flow. However, when lateral flow cannot be ignored, it becomes a two-dimensional or three-dimensional consolidation problem. The differential equations for these cases can be derived by extending the unidirectional permeation consolidation theory. The equations for two-dimensional consolidation are given by Eq. (3.14),

$$\frac{\partial u}{\partial t} = C_{v_x} \frac{\partial^2 u}{\partial x^2} + C_{v_z} \frac{\partial^2 u}{\partial z^2} \quad (3.14)$$

and for three-dimensional consolidation by Eq. (3.15).

$$\frac{\partial u}{\partial t} = C_{v_x} \frac{\partial^2 u}{\partial x^2} + C_{v_y} \frac{\partial^2 u}{\partial y^2} + C_{v_z} \frac{\partial^2 u}{\partial z^2} \quad (3.15)$$

where C_{v_x} , C_{v_y} , and C_{v_z} represent the consolidation coefficients in the X , Y , and Z coordinate directions, respectively. These coefficients are difficult to determine directly from consolidation tests. Typically, the C_v value is obtained from unidirectional consolidation tests, and the following relationships are used to estimate the coefficients for two-dimensional and three-dimensional consolidation:

$$C'_v = \frac{1 + K_0}{2} C_v \quad (3.16)$$

$$C''_v = \frac{1 + K_0}{3} C_v \quad (3.17)$$

In these equations, K_0 represents the coefficient of lateral pressure. Therefore, the formulas for two-dimensional and three-dimensional consolidation can be rewritten as Eq. (3.18) for two-dimensional consolidation and Eq. (3.19) for three-dimensional consolidation.

$$\frac{\partial u}{\partial t} = C'_v \left(\frac{\partial^2 u}{\partial x^2} + \frac{\partial^2 u}{\partial z^2} \right) \quad (3.18)$$

$$\frac{\partial u}{\partial t} = C'_v \left(\frac{\partial^2 u}{\partial x^2} + \frac{\partial^2 u}{\partial y^2} + \frac{\partial^2 u}{\partial z^2} \right) \quad (3.19)$$

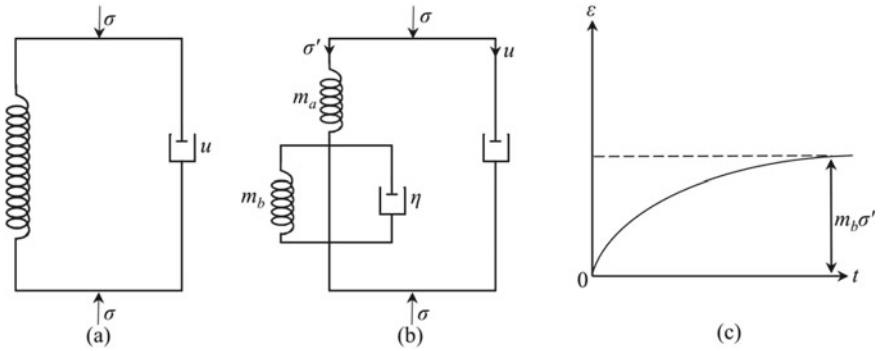


Fig. 3.5 Viscoelastic consolidation model of soil

3.2.2.3 Viscoelastic Consolidation Model

The permeation consolidation models described above consider the soil skeleton as a linear elastic body, using spring elements to simulate it (Fig. 3.5a). These models can only describe the variation in excess pore water pressure with time during the consolidation process and are limited in capturing the time-dependent creep effects caused by soil skeleton deformation. To account for these effects, the soil skeleton is considered a viscoelastic body, and a combined model shown in Fig. 3.5b is adopted, which can simultaneously describe the time-dependent subsidence of both primary and secondary consolidation. This model represents the soil skeleton using a three-element model with compressibility parameters m_a (instantaneous response of the soil), m_b (viscoelastic consolidation response of the soil), and the viscosity coefficient η . Let ε_a represent the instantaneous strain and ε_b represent the viscoelastic consolidation strain; then, the total strain ε of this model is given by Eq. (3.20).

$$\varepsilon = \varepsilon_a + \varepsilon_b \tag{3.20}$$

Taking into account the time-dependent behavior of the viscoelastic consolidation strain ε_b with time t (Fig. 3.5c) and considering secondary consolidation, the permeation consolidation model is modified to incorporate the creep rate caused by viscoelasticity. The resulting viscoelastic consolidation differential equation is given by Eq. (3.21).

$$\frac{K}{\gamma_w} \frac{\partial^2 u}{\partial z^2} = m_a \frac{\partial \sigma'}{\partial t} + \frac{1}{\eta} \sigma'^{prime} - \frac{1}{\eta^2 m_b} \int_0^t \sigma'(\tau) e^{-\frac{1}{\eta m_b}(t-\tau)} d\tau \tag{3.21}$$

In general, numerical methods are employed to solve this differential equation:

3.3 Prediction of Land Subsidence

The study of the mechanisms and patterns of land subsidence caused by groundwater exploitation is fundamental. It is crucial to accurately assess the deformation potential of soil layers in the subsidence area and make predictions about the magnitude and distribution of land subsidence resulting from groundwater exploitation. This is essential for controlling the development of land subsidence and formulating rational groundwater exploitation plans.

The prediction of land subsidence can be divided into several stages (Table 3.2).

Before the 1970s, prediction methods for land subsidence included long-term prediction theories, physical and numerical simulation methods, and theoretical analysis methods. Long-term prediction theories encompassed regression analysis, gray system theory, and artificial neural network methods. Physical and numerical simulation methods included the finite element method (FEM), finite difference method (FDM), and model testing. Theoretical analysis methods encompass empirical approaches, profile function methods, and influence function methods (Ren et al. 2015). The prediction of land subsidence mainly relied on the one-dimensional consolidation theory of the Terzaghi method and related analysis methods to describe the relationship between groundwater extraction and subsidence. For example, the finite element method is based on consolidation theory combined with soil constitutive models. However, due to the complexity of parameter selection and influencing factors, the subsidence values calculated based on consolidation theory often showed significant discrepancies with measured values. Since the 1970s, with the advancement in understanding the mechanisms of land subsidence and the widespread application of computers, mathematical model prediction methods have been employed for land subsidence forecasting. Based on the combination of water flow models and soil deformation models, land subsidence models can be classified into three categories: two-step calculation models, partially coupled models, and fully coupled models.

3.3.1 Two-Step Calculation Model

The basic idea of the two-step calculation model is to first determine the draw-down of groundwater caused by pumping, which leads to changes in hydraulic head within the aquifer system. These changes are then converted into increments of finite stress in the soil. The water exchange between the aquifer and clay layers is handled through seepage flow. Next, the changes in effective stress are calculated based on Terzaghi's principle of effective stress, which determines the deformation of each soil layer. The sum of the deformations of all layers represents the subsidence of the soil (Terzaghi 1925). This model was initially proposed by Gambolati and Freeze (1973) when studying the land subsidence problem caused by groundwater pumping in the multilayered aquifer system with weakly permeable layers in Venice. The

Table 3.2 Prediction method of land subsidence caused by groundwater exploitation

Categories		Features	Merits and demerits
Statistics method	Influence function method	Based on the measured data, the deformation time function is obtained	Requires a large number of statistical data, general applicability is poor
Gray theory method		The correlation between factors is measured according to the similarity of the development trend between factors	There is no too high requirement for sample size
Early numerical calculation methods		Numerical analysis method	Because of the limitation of computer capacity, this method can only analyze simple problems
Quasi three-dimensional calculation method	Two-step calculation model	Horizontal two-dimensional groundwater seepage and one-dimensional consolidation, seepage and deformation analysis are carried out in two steps	The seepage equation is not established for the weak permeable layer, and the seepage flow is treated as the source and sink. Compared with the actual situation, there are still many deficiencies
	Part coupling model	The groundwater seepage and soil deformation are combined into one step calculation	
Calculation method based on true three-dimensional flow model		Considering three-dimensional seepage and one-dimensional consolidation	This method solves the problem that the equation is not established for the weak permeable layer in the quasi three dimensional, and the one dimensional consolidation is still considered for the deformation of the soil
Three-dimensional fully coupled model		Three-dimensional seepage and three-dimensional consolidation are completely coupled	The calculation of this method is complicated, takes up a lot of calculation space, takes a lot of time, and many parameters are difficult to determine

model first employs a generalized axisymmetric quasi three-dimensional groundwater flow model to calculate the changes in hydraulic head H within the aquifer system. Based on the changes in hydraulic head within the aquifer and the weakly permeable layers, the changes in effective stress are calculated, which in turn determine the deformations of each soil layer. The sum of these deformations represents the land subsidence. Mathematically, this can be expressed as follows:

$$\frac{\partial}{\partial r} \left(K_{ri} \frac{\partial H_i}{\partial x} \right) + \frac{K_{ri}}{r} \frac{\partial H_i}{\partial y} + \frac{\partial}{\partial z} \left(K_{zi} \frac{\partial H_i}{\partial z} \right) = \gamma_w (\alpha_i + n_i \beta_w) \frac{\partial H_i}{\partial t} \quad (3.22)$$

The deformation of the i th aquifer is:

$$\eta_i(t) = \gamma_w a_i b_i \Delta H_i(t) \quad (3.23)$$

The deformation of the j th weak permeable aquifer is:

$$\eta_j(t) = \gamma_w a_j b_j \Delta H_j(t) \quad (3.24)$$

The amount of land subsidence is:

$$\eta(t) = \sum_i \eta_i(t) + \sum_j \eta_j(t) \quad (3.25)$$

In the equations, the subscripts i and j represent the i th aquifer and j th weakly permeable layer, respectively. K_{ri} denotes the horizontal permeability coefficient of the i th aquifer, and K_{zi} represents the vertical permeability coefficient of the soil layer. α represents the compressibility coefficient of the soil, n denotes the porosity of the soil, β represents the compressibility coefficient of water, b is the thickness of the soil layer, and η represents the deformation of the soil.

The three-dimensional groundwater flow equation and the one-dimensional consolidation equation conjunctively establish the land subsidence calculation model. The three-dimensional MODFLOW software is used to solve the hydraulic head of each soil layer in the aquifer system, assuming that the total stress of each soil layer remains constant. According to the principle of effective stress, the decrease in pore water pressure in the soil layer is equal to the increase in effective stress of the corresponding soil layer. Mathematically, it can be expressed as:

$$\Delta \sigma' = -\gamma_w \Delta H \quad (3.26)$$

where ΔH represents the change in pore water level. Additionally, Bravo (1990) considered the relationship between soil deformation and variation history of stress and proposed the concept of the pre-consolidation water level. It is believed that within the inelastic range, the unit compressibility of the increase in effective stress is significantly higher than the compressibility within the elastic range.

$$S_{sk}^m = S_{ske}, \quad \text{when } \phi^m > \Phi^{m-1} \quad (3.27)$$

$$S_{sk}^m = S_{skv}, \quad \text{when } \phi^m < \Phi^{m-1} \quad (3.28)$$

In these equations, Φ^{m-1} represents the pre-consolidation water level at time $m-1$ (the pre-consolidation water level is not fixed and changes during the calculation

process with the newly calculated minimum water level); H_m represents the pore water level at time m ; and S_{skv} represents the inelastic specific storage of the soil layer. The specific storage S_{sk} of the semi-saturated clay layer is determined based on the soil's elastic and inelastic properties. If the pore water level φ^m at time m is greater than the pre-consolidation water level Φ^{m-1} at time $m-1$, the coefficient S_{sk} is determined using the elastic specific storage S_{ske} ; otherwise, the inelastic specific storage S_{skv} is used. In a one-dimensional problem, the variation in soil layer thickness Δb is given by:

$$\Delta b = S_{skv} \frac{\Delta \sigma'}{\gamma_w} b_0, \quad \sigma' > \sigma'_c \quad (3.29)$$

$$\Delta b = S_{ske} \frac{\Delta \sigma'}{\gamma_w} b_0, \quad \sigma' \leq \sigma'_c \quad (3.30)$$

where σ'_c represents the pre-consolidation stress (pre-consolidation effective stress) of the soil layer; σ' represents the effective stress; and the remaining symbols have the same meanings as before. Finally, the vertical deformation of each soil layer is calculated based on the above equations, and the magnitude of land subsidence is the sum of the vertical deformations of all soil layers.

3.3.2 Partially Coupled Model

According to the two-step model, when the hydraulic head in adjacent aquifers decreases, groundwater in the weakly permeable layer will flow. Due to the very low hydraulic conductivity of the weakly permeable layer, it takes some time for the groundwater pressure within it to reach a new equilibrium state. Additionally, the deformation of the weakly permeable layer exhibits obvious nonlinear characteristics. As the deformation of the soil increases, the porosity decreases, leading to a reduction in the compressibility and permeability of the soil. Rivera et al. (1991) developed a mathematical model for simulating groundwater flow and total subsidence in a multilayered aquifer system in Mexico on the basis of the two-step model. This model combines groundwater flow equations with Terzaghi's consolidation theory and considers the nonlinear relationship between the permeability and specific storage coefficients of the aquifers. It establishes equations relating the vertical permeability coefficient and elastic specific storage to the porosity. Finally, the total subsidence of the aquifer system is calculated. The mathematical model is as follows:

For the multilayered aquifer system, a quasi three-dimensional groundwater flow model is adopted, and the groundwater flow equation in the aquifers is given by:

$$\frac{\partial}{\partial z} \left(T \frac{\partial H}{\partial x} \right) + \frac{\partial}{\partial z} \left(T \frac{\partial H}{\partial y} \right) = S \frac{\partial H}{\partial t} + Q(x, y) + q_L \quad (3.31)$$

where T represents the hydraulic conductivity, S represents the specific storage, Q represents the source/sink term, and q_L represents the interflow flux from the weakly permeable layer to the aquifer. For groundwater within the weakly permeable layer, it is assumed to flow only vertically. A nonlinear one-dimensional vertical consolidation equation is given as:

$$\frac{\partial}{\partial z} \left(K' \frac{\partial H'}{\partial z} \right) = S'_s(n, \sigma') \frac{\partial H'}{\partial t} \quad (3.32)$$

where H' represents the hydraulic head in the weakly permeable layer and K' represents the vertical permeability coefficient of the weakly permeable layer, which is a function of the porosity n and can be expressed using the following empirical formula:

$$K' = K'_0 \left(\frac{n(1 - n_0)}{n_0(1 - n)} \right)^m \quad (3.33)$$

where K'_0 is the vertical permeability coefficient at porosity n_0 , m is a constant related to the soil, and S'_s represents the elastic specific storage of the weakly permeable layer, which is a function of the porosity n and effective stress.

$$S'_s = \gamma_w \left(0.434 \frac{c}{\sigma'} (1 - n) + n\beta \right) \quad (3.34)$$

where $c = c_c$ ($\sigma' > \sigma'_c$) or $c = c_r$ ($\sigma' < \sigma'_c$), c_c and c_r are dimensionless compression and rebound indices of the soil, and the other symbols have the same meanings as before.

3.3.3 Fully Coupled Model

The theoretical foundation of the fully coupled model is the well-known Biot consolidation theory (Biot 1941). Under the assumptions that the soil is a saturated homogeneous porous medium, its deformation follows the principles of elasticity, the pore water and solid soil particles are considered incompressible, and the flow of water follows Darcy's law, the stress-strain relationship considering effective stress is combined with the groundwater flow equation to establish a coupled control equation that can simultaneously solve pore water pressure and soil deformation. This model unifies the deformation model of the soil and the groundwater flow model in the same physical space. The groundwater flow and soil deformation can be one-dimensional, two-dimensional, or three-dimensional, reflecting not only land subsidence but also the horizontal displacement of the strata. If the stress-strain relationship of the soil satisfies the generalized Hooke's law, the displacement of the soil can be described by the following equation:

$$\begin{cases} -G\nabla^2 u - \frac{G}{1-2\mu} \frac{\partial}{\partial x} \left(\frac{\partial u}{\partial x} + \frac{\partial v}{\partial y} + \frac{\partial w}{\partial z} \right) + \frac{\partial p}{\partial x} = 0 \\ -G\nabla^2 v - \frac{G}{1-2\mu} \frac{\partial}{\partial y} \left(\frac{\partial u}{\partial x} + \frac{\partial v}{\partial y} + \frac{\partial w}{\partial z} \right) + \frac{\partial p}{\partial y} = 0 \\ -G\nabla^2 w - \frac{G}{1-2\mu} \frac{\partial}{\partial z} \left(\frac{\partial u}{\partial x} + \frac{\partial v}{\partial y} + \frac{\partial w}{\partial z} \right) + \frac{\partial p}{\partial z} = 0 \end{cases} \quad (3.35)$$

The groundwater flow equation is given by Eq. (3.36):

$$\begin{aligned} \frac{1}{\gamma_w} \frac{\partial}{\partial x} \left(K_x \frac{\partial p}{\partial x} \right) + \frac{1}{\gamma_w} \frac{\partial}{\partial y} \left(K_y \frac{\partial p}{\partial y} \right) + \frac{1}{\gamma_w} \frac{\partial}{\partial z} \left(K_z \left(\frac{1}{\gamma_w} \frac{\partial p}{\partial z} + 1 \right) \right) \\ + Q(x, y, z, t) = -\frac{\partial}{\partial t} \left(\frac{\partial u}{\partial x} + \frac{\partial v}{\partial y} + \frac{\partial w}{\partial z} \right) - \frac{n}{K_f} \frac{\partial p}{\partial t} \end{aligned} \quad (3.36)$$

where u , v , and w represent the displacements of the soil in the x , y , and z directions, respectively, with positive directions along the coordinate axes. G is the shear modulus of the soil, μ is the Poisson's ratio of the soil, and K_f is the volumetric compressibility modulus of water. The meanings of the other symbols remain the same as before.

The establishment of a true three-dimensional fully coupled model for land subsidence is necessary and represents the development direction of land subsidence models. Land subsidence caused by groundwater extraction is three-dimensional. With the advancement of computational techniques, especially the development of finite element and finite difference numerical methods, as well as continuous improvements in parameter acquisition methods, studying the true three-dimensional model of the fully coupled seepage and deformation has become a key focus for future land subsidence prediction work.

3.4 Land Subsidence Prevention and Control

Whether in the study of land subsidence mechanisms or various prediction models, the ultimate goal is to prevent and control land subsidence. The common methods for preventing and controlling land subsidence are described in the following sections.

3.4.1 Restricting Groundwater Extraction

Reducing or limiting the amount of groundwater extraction. Groundwater extraction is the main factor inducing land subsidence. Therefore, in areas with low research levels on land subsidence and accelerated deformation, the most effective measure to restrain subsidence is to reduce or prohibit groundwater extraction (Pang et al. 2022).

Replacing groundwater sources with surface water sources. The specific measures include (1) replacing groundwater supply sources with tap water from surface water sources; (2) ceasing the extraction of aquifers that cause significant subsidence and instead utilizing deep aquifers or rock fissure water with lower compressibility; (3) limiting groundwater extraction or ceasing it according to the prediction plan (Li et al. 2023); and (4) reducing groundwater extraction while diverting water from distant sources (Tang et al. 2022).

Measures to restrict groundwater extraction have been implemented in Shanghai, Tianjin, Jiangsu, Zhejiang, Xi'an, and other regions in China and have achieved significant control over subsidence (Li et al. 2021). In the Suzhou-Wuxi-Changzhou region of China, due to the pollution of surface water and shallow groundwater, it has been necessary to extract confined water with good quality since the 1980s, resulting in a significant increase in the depth of confined water from 15 to 25 m in the 1970s to below 80 m in the 1990s. Therefore, in 1996, the Jiangsu provincial government implemented measures to restrict extraction, resulting in a significant rise in the groundwater level. Compared to 2002, the groundwater level rose by 2–9 m in 2003, and the regional land subsidence rate slowed down. In Xi'an, excessive groundwater extraction from 1960 to 1975 led to a cumulative land subsidence of nearly 2 m. However, after adjusting the extraction volume and restricting groundwater extraction since 1985, the land subsidence rate has been decreasing year by year, and in recent years, the land subsidence in Xi'an has stabilized (Wang et al. 2018).

3.4.2 *Managed Aquifer Recharge*

Managed aquifer recharge of groundwater involves selecting suitable locations and areas to inject water into the exploited aquifers or oil-bearing layers through artificial injection or pressure, maintaining the pore fluid pressure in the aquifer (oil/gas) at its initial equilibrium state. This helps minimize the incremental effective stress generated by fluid extraction in the subsiding layer, ensuring that the total effective stress remains below the preconsolidation stress of that layer (Spellman 2017). In coastal areas where groundwater extraction causes seawater intrusion and groundwater quality degradation, managed aquifer recharge wells should be located near the interface between seawater and freshwater bodies to prevent the shrinkage or deterioration of freshwater bodies. Adjusting the recharge levels and timing by using water with different temperatures during different recharge seasons can implement underground thermal insulation and energy-saving measures. Low-temperature water can be injected during winter as an industrial cooling water source for the summer, while high-temperature water can be injected during summer as a heat source for winter. Integrating surface water storage with groundwater recharge and establishing joint regulation reservoirs on the surface and underground is an effective approach for the rational utilization of water resources. On the one hand, it effectively supplements groundwater by utilizing surface water storage and expanding managed aquifer recharge sources. On the other hand, it stores surface rainwater in the pore space

of the formation, forming underground reservoirs to increase groundwater storage resources. This technique mainly involves injecting surface water into underground aquifers through deep wells, pits, or ancient river channels to raise the groundwater level and achieve the control of land subsidence and restoration of the aquifer. Since excessive groundwater extraction is the main cause of land subsidence, artificial groundwater recharge promotes the rapid recovery of groundwater levels, increases water pressure, and saturates the easily compressible cohesive soil layers with water. This leads to the rise of pore water levels and increased pore water pressure, resulting in soil expansion. This is reflected on the ground as either no further subsidence or ground uplift. Since 1966, Shanghai, China, has implemented groundwater extraction and recharge schemes. Based on the measured land subsidence data from the previous year, control objectives for the current year are established. Through groundwater dynamics and land subsidence models, the optimal extraction and recharge volumes and their distribution are determined to achieve the annual control objectives. From 1966 to 2003, a total of 600 million m³ of recharge was conducted, with a planned recharge volume of 14 million m³ in 2004. Groundwater recharge not only restores groundwater levels and effectively mitigates land subsidence but also replenishes groundwater resources and improves resource utilization efficiency.

3.4.3 Adjusting Extracted Aquifers

To control land subsidence, many places have adopted measures to adjust aquifers for groundwater extraction. In the early stages, Shanghai, China primarily extracted water from the second and third confined aquifers. Starting in 1968, groundwater extraction was adjusted to increase the exploitation of the fourth and fifth confined aquifers located below a depth of 150 m. By 2003, groundwater extraction below the 150 m depth accounted for 79% of the total extraction volume. In comparison, due to the relatively dense soil layers below 150 m, extracting the same amount of water resulted in less subsidence compared to depths above 150 m. However, adjusting the levels of extraction is only an auxiliary measure that helps control land subsidence during a certain period but does not fundamentally solve the problem. The key lies in reducing groundwater extraction and increasing artificial recharge.

The aforementioned methods are common approaches for preventing and mitigating land subsidence, among which restrictions (or prohibitions) on groundwater extraction and artificial groundwater recharge are the most direct and effective methods. Many cities worldwide have achieved significant results in mitigating land subsidence by employing these two methods (Qin et al. 2018). However, there exists a contradiction between solely restricting extraction, reducing water usage, and the demands of regional economic development. From the perspective of resource development leading to environmental degradation and disaster occurrence, this cannot be considered a proactive solution to resolve the contradiction. This implies that one side of the contradiction (resource development) succumbs to the other side (land subsidence). Therefore, in future land subsidence prevention and control efforts, our

focus will be on using subsidence prediction and scientific experiments to guide mitigation measures.

3.5 Land Subsidence Prediction: A Case Study in Yan'an New District

With the implementation of the Great Western Development strategy in China, urban construction in the northwest loess region has rapidly expanded. “Mountain cutting and land creation” is used to create a large amount of flat land for urban development (Li et al. 2014; Pu et al. 2022). Large-scale “mountain cutting and land creation” projects alter the original topography and landscape and disrupt the structure of the loess, which inevitably affects the infiltration and migration patterns of water in the loess. This changes the conditions for groundwater replenishment, runoff, and drainage in the region, greatly reducing the drainage capacity of the original valleys and causing groundwater levels to rise (Wu et al. 2015). Additionally, during the “mountain cutting and land creation” process, high embankments of tens or even hundreds of meters made of loess need to be constructed. Typical loess exhibits characteristics such as vertical joints and collapsibility. Intense human disturbance significantly alters the structure of the loess, affecting the stability of the foundation. Water is a crucial factor that influences the stability of collapsible loess. Particularly in areas with collapsible loess, large-scale “mountain cutting and land creation” projects can trigger environmental geological issues such as land subsidence in embankment areas.

For the land subsidence caused by high embankments of loess, there is a lack of engineering examples and relevant research in this area. The “mountain cutting and land creation” project in Yan'an New District, China, is currently the largest-scale geotechnical engineering project conducted in an area with collapsible loess, and it is also the first of its kind in the history of urban construction worldwide. After the completion of the project, the embankment area's soil will experience certain subsidence and deformation over time due to the infiltration of surface water and the rise in groundwater levels. For calculating the subsidence amount, it is necessary to study the dynamic changes in groundwater under the influence of the “mountain cutting and land creation” project and investigate the dynamic changes in compaction, compression, and moisture content of the embankment loess using experimental analysis and numerical simulation methods. Based on this, this chapter takes the construction of Yan'an New District in China as an example and conducts predictive research on the subsidence and deformation of the embankment soil. The distribution patterns of subsidence and deformation in terms of time and space are analyzed.

3.5.1 Prediction Method

Due to the stable structure of the excavated soil in the cut area and the minimal water level fluctuations, as well as the reduction in overlying soil thickness resulting from excavation, subsidence and deformation are unlikely to occur. Therefore, this calculation only considers the subsidence and deformation of the embankment soil in the fill area. Based on the distribution pattern of moisture content in the high embankment loess, the distribution of groundwater levels, and their compression deformation characteristics, a preliminary prediction of the subsidence and deformation of the high embankment loess in the northern area of Yan'an after the completion of the project was conducted using Visual Basic programming. The algorithm is shown in Fig. 3.6, and the specific prediction steps are as follows:

1. Divide the calculation area into sections on a plane. The calculation area in this study is the same as the aforementioned research area. A 40×40 m orthogonal grid is used for discretization of the plane, and the fill area is selected.
2. Perform interpolation on the original terrain and the postconstruction terrain to obtain the elevation of each sectioned grid in the original terrain, the height after filling, and the fill height. Divide each grid into several unequal quantities of cells vertically, with each layer being 2 m apart, and create multiple cells.
3. Based on the distribution pattern of moisture content in the fill soil and the variation in groundwater levels, calculate the volumetric moisture content at the center points of each cell at different time intervals for the different layers, intermediate layers, capillary fringe, and saturated zone. The volumetric moisture content was converted to mass moisture content to represent the moisture content of the entire cell.

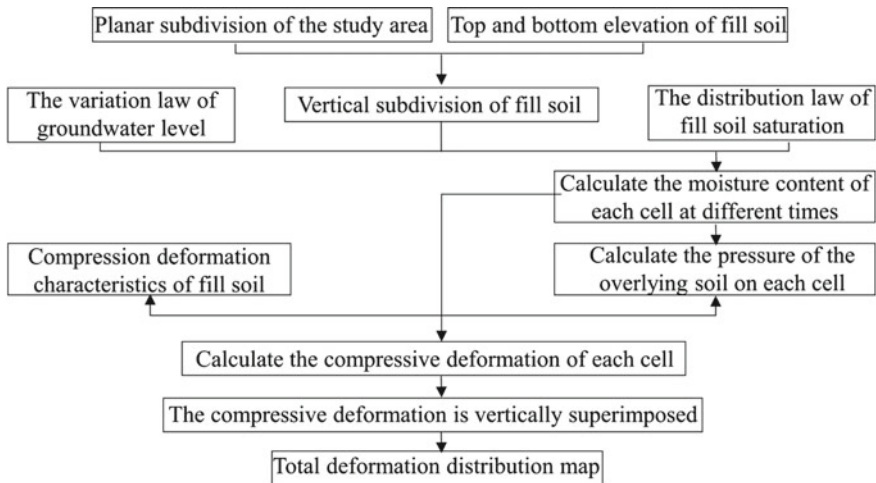


Fig. 3.6 Roadmap for subsidence prediction

4. Calculate the pressure exerted by the overlying soil at the center of each cell using Eq. (3.37). It is combined with the mass moisture content and the compression deformation coefficient of the soil under different pressures corresponding to different moisture contents obtained in Sect. 4.1. Calculate the subsidence and deformation of the soil in each cell using Eq. (3.38).
5. The subsidence and deformation values of each cell in the vertical direction of each grid are summed to obtain the subsidence amount of the entire area at different time intervals.

$$P = \rho_d(1 + \omega)gD \quad (3.37)$$

$$h_i = \delta_p \cdot H_{i0} \quad (3.38)$$

where P represents pressure (kPa); g is the gravitational constant, equal to 9.8 N/kg; D is the thickness of the overlying soil (m); h_i is the compression deformation of the soil (m); H_{i0} is the initial height of the soil before compression (m); and the other parameters are the same as mentioned above.

3.5.2 Accuracy Analysis

To validate the reliability of the proposed subsidence calculation method, a comparative analysis was conducted between the measured subsidence results and the calculated results from the previous stage of the project. Based on the measured subsidence results during the initial stage of the project, the maximum subsidence rate was recorded as 10.8 mm/month immediately after completion and 2.9 mm/month after 15 months. From these data, it can be estimated that the average maximum subsidence rate between 3 and 15 months after construction should range between 3 and 6 mm. The subsidence amounts for the first 3 months and 15 months after the completion of the fill were calculated, and the distributions of average monthly subsidence for the first 3 months and the period of 3–15 months were analyzed, as shown in Fig. 3.7a, b.

From the figures, it can be observed that during the initial stage of the project, the subsidence amounts in the region with the fastest subsidence rate in the first 3 months generally ranged from 10 to 16 mm/month, while the subsidence amounts between 3 and 15 months ranged from 2 to 4.5 mm/month. These results are consistent with the maximum subsidence rates observed through actual monitoring, indicating the reliability of the calculation method. Therefore, this method can be used to analyze the distribution of subsidence amounts in the area at different times in the future.

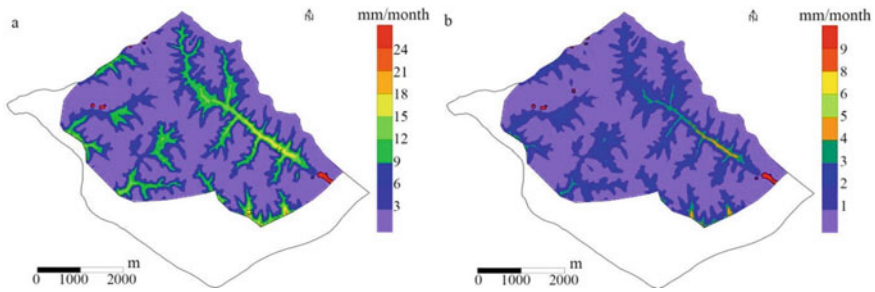


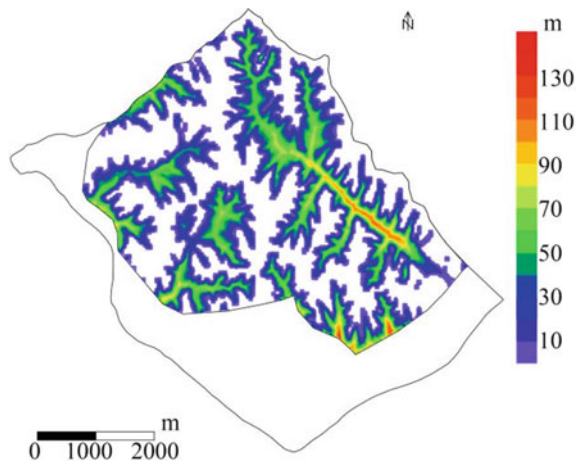
Fig. 3.7 Distribution of average monthly subsidence of filled soil in 0–3 months (a) and 3–15 months (b) after construction

3.5.3 Analysis of Prediction Results

The distribution of fill thickness in the study area is shown in Fig. 3.8. The figure shows that the fill area in the study area has a wide distribution range, covering an area of approximately 11 km², with a maximum fill thickness of approximately 134 m. The thickness of the fill material is smaller at the edges of the valleys and gradually increases toward the valleys. The areas with fill thicknesses greater than 30 m, 60 m, and 90 m are approximately 6.0 km², 1.8 km², and 0.23 km², respectively.

To predict the subsidence of the fill material at different times in the study area, representative points were selected to analyze the variation in subsidence with time for different thicknesses of fill material, as shown in Fig. 3.9. Additionally, the distribution of subsidence at different times in the study area was also analyzed and is presented in Fig. 3.10. From Fig. 3.9, it can be observed that the representative point with a fill thickness of 32 m exhibits high compressibility due to the influence of the saturated zone. In the first 50 years, the subsidence increases rapidly with the rise of

Fig. 3.8 Distribution of filled soil thickness in the study area



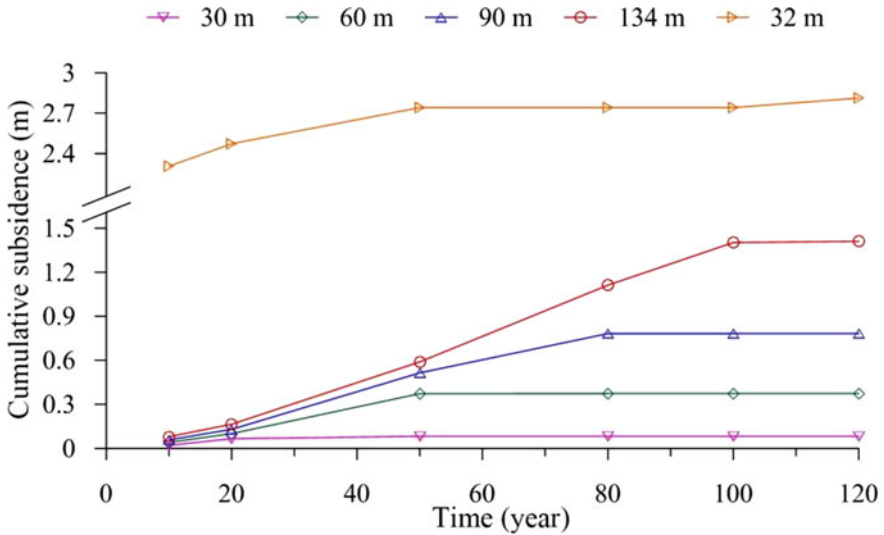


Fig. 3.9 Variation in subsidence of landfill soil with different thicknesses with time

the water table. After 10, 20, and 50 years of construction, the subsidence amounts are 2.30 m, 2.47 m, and 2.74 m, respectively. The subsidence growth slows down after 50 years, and after 120 years of construction, the subsidence reaches 2.81 m, with an average subsidence rate of approximately 1 mm/year. Other representative points, which were not influenced by the saturated zone in a short period of time, show relatively smaller subsidence amounts. The subsidence gradually increases with time and fill thickness until it reaches a relatively stable state. The time required to reach a relatively stable state for fill thicknesses of 30 m, 60 m, 90 m, and 134 m is approximately 20 years, 50 years, 80 years, and 100 years, respectively. The subsidence amounts at the relatively stable state are approximately 0.083 m, 0.37 m, 0.78 m, and 1.40 m, respectively.

From the distribution maps of subsidence amounts at different times, it can be observed that within 120 years after construction, except for a few areas with significant subsidence due to the influence of the saturated zone, the subsidence amounts in other areas generally remain within 1.3 m. Additionally, the subsidence amounts at the edges of the valleys are relatively smaller and gradually increase toward the center. The subsidence amounts show a trend of gradual increase and approaching relative stability over time.

After 10 years of construction, in the areas influenced by the groundwater level, the subsidence amount at the center is between 1 and 2 m. In other areas, the average subsidence amount at the edges of the tributaries is 0.01 m, that in the middle of the tributaries and the upper reaches of the main channel is 0.04 m, and that in the lower reaches of the main channel is 0.06 m.

After 20 years of construction, in the areas influenced by the groundwater level, the subsidence amount at the center is between 1.2 and 2.3 m. In other areas, the

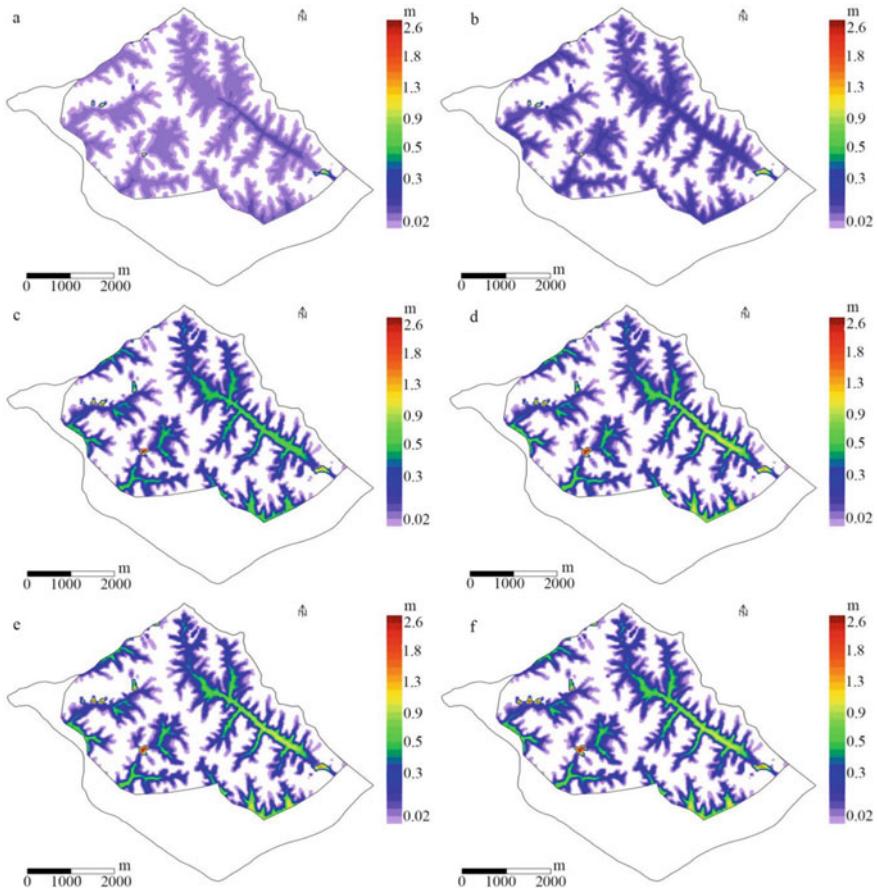


Fig. 3.10 Distribution map of the subsidence of filled soil in the study area at 10 years (a), 20 years (b), 50 years (c), 80 years (d), 100 years (e), and 120 years (f) after construction

subsidence amount at the edges of the tributaries is within 0.03 m, the average subsidence amount in the middle of the tributaries and at the edges of the main channel is 0.08 m, the subsidence amount in the upper reaches of the main channel is 0.11 m, and the subsidence amount in the lower reaches of the main channel is 0.14 m.

After 50 years of construction, in the areas influenced by the groundwater level, the subsidence amount at the center ranges from 1.4 to 2.7 m. In other areas, the subsidence amount at the edges of the tributaries generally remains within 0.1 m, the average subsidence amount in the middle of the tributaries and at the edges of the main channel is 0.25 m, the subsidence amount in the upper reaches of the main channel is 0.45 m, and the subsidence amount in the lower reaches of the main channel is 0.50 m.

Table 3.3 Statistical results of the subsidence area in the study area (unit: km²)

Time (years)	Subsidence					
	0.05–0.1 m	0.1–0.2 m	0.2–0.5 m	0.5–0.8 m	0.8–1.2 m	> 1.2 m
10	0.637	0.01	0.021	0.012	0.012	0.006
20	4.942	2.055	0.033	0.007	0.024	0.011
50	1.241	1.584	3.839	0.372	0.036	0.03
80	1.243	1.585	3.311	0.677	0.265	0.045
100	1.239	1.585	3.314	0.675	0.261	0.056
120	1.228	1.585	3.325	0.680	0.264	0.064

After 80 years of construction, in the areas influenced by the groundwater level, the subsidence amount at the center ranges from 1.2 to 2.75 m. In other areas, the subsidence amount at the edges of the tributaries generally remains within 0.1 m, the average subsidence amount in the middle of the tributaries is 0.60 m, the subsidence amount in the upper reaches of the main channel is 0.75 m, and the subsidence amount in the lower reaches of the main channel is 1.0 m.

There is not much difference in subsidence amounts between 100 and 120 years after construction. In the areas influenced by the groundwater level, the subsidence amount at the center ranges from 1.55 to 2.8 m. In other areas, the subsidence amount at the edges of the tributaries generally remains within 0.1 m, the average subsidence amount in the middle of the tributaries is 0.65 m, the subsidence amount in the upper reaches of the main channel is 0.80 m, and the subsidence amount in the lower reaches of the main channel is 1.0 m.

The areas with subsidence amounts of 0.05–0.1, 0.1–0.2, 0.2–0.5, 0.5–0.8, 0.8–1.2, and > 1.2 m were statistically analyzed based on the data in the graph. The results are presented in Table 3.3 and Fig. 3.11. It can be observed that the areas with subsidence amounts of 0.05–0.1 m and 0.1–0.2 m show a rapid increase in the initial stage, reaching their maximum values at 20 years after construction, approximately 4.942 km² and 2.055 km², respectively. After 30 years, these areas decrease to a relatively stable state, with areas of 1.24 km² and 1.584 km², respectively. The area with subsidence amounts of 0.2–0.5 m exhibits rapid growth from 20 to 50 years after construction, increasing from 0.033 km² to 3.839 km². After a slight decrease at 80 years, it shows a slow upward trend, reaching an area of 3.325 km² at 120 years. The area with subsidence amounts of 0.5–0.8 m shows a significant upward trend from 20 to 80 years after construction, increasing from 0.007 to 0.677 km², and then remains relatively stable. The area with subsidence amounts of 0.8–1.2 m experiences a noticeable increase from 50 to 80 years after construction, growing from 0.036 to 0.265 km², and then stabilizes. The area with subsidence amounts exceeding 1.2 m shows a continuous growth trend within 120 years after construction, with an average increase of 0.004–0.006 km² every 10 years. At 120 years after construction, the area reached 0.064 km². However, the growth rate shows a declining trend, with an average decrease of approximately 300 m² every 10 years.

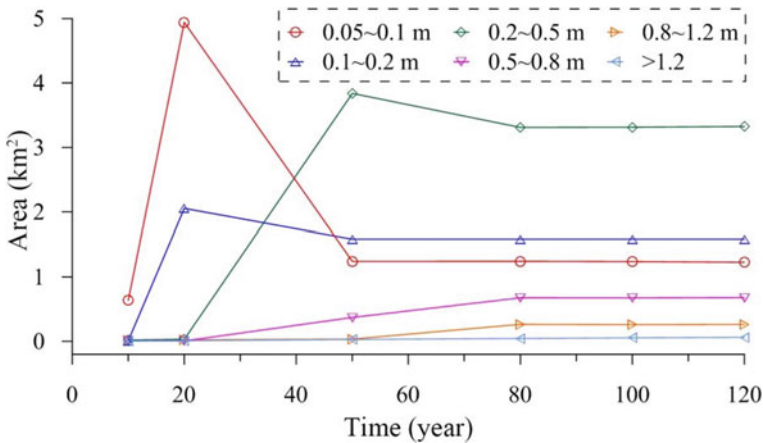


Fig. 3.11 Temporal changes in area in each subsidence range

References

- Bagheri-Gavkosh M, Hosseini SM, Ataie-Ashtiani B, Sohani Y, Ebrahimian H, Morovat F, Ashrafi S (2021) Land subsidence: a global challenge. *Sci Total Environ* 778:146193
- Biot MA (1941) General theory of three dimensional consolidation. *J Appl Phys* 12(2):155–164
- Bravo R (1990) Prediction of Houston ground-water heads and land subsidence using three-dimensional finite differences. Ph. D. Thesis, University of Houston
- Chen B, Gong H, Chen Y, Li X, Zhou C, Lei K, Zhu L, Duan L, Zhao X (2020) Land subsidence and its relation with groundwater aquifers in Beijing Plain of China. *Sci Total Environ* 735:139111
- Cui ZD (2018) Land subsidence induced by the engineering-environmental effect. Springer Singapore Pte. Limited, Singapore.
- El Shinawi A, Kuriqi A, Zelenakova M, Vranayova Z, Abd-Elaty I (2022) Land subsidence and environmental threats in coastal aquifers under sea level rise and over-pumping stress. *J Hydrol* 608:127607
- Figueroa-Miranda S, Tuxpan-Vargas J, Ramos-Leal JA, Hernández-Madrugal VM, Villaseñor-Reyes CI (2018) Land subsidence by groundwater over-exploitation from aquifers in tectonic valleys of Central Mexico: a review. *Eng Geol* 246:91–106
- Galloway DL, Burbey TJ (2011) Review: regional land subsidence accompanying groundwater extraction. *Hydrogeol J* 19:1459–1486
- Galloway DL, Sneed M (2013) Analysis and simulation of regional subsidence accompanying groundwater abstraction and compaction of susceptible aquifer systems in the USA. *Boletín Soc Geol Mex* 65:123–136
- Gambolati G, Freeze AR (1973) Mathematical simulation of the subsidence of Venice theory. *Water Resour Res* 9(3):721–733
- Guzy A, Malinowska A (2020) State of the art and recent advancements in the modelling of land subsidence induced by groundwater withdrawal. *Water* 12(7):2051
- Higgins SA (2015) Review: advances in delta-subsidence research using satellite methods. *Hydrogeol J* 24:587–600
- Khajehali M, Safavi HR, Pour SI (2023) Evaluation of management scenarios for land subsidence reduction and groundwater rehabilitation in Damane-Daran plain, Iran. *Groundwater Sustain Dev* 23:100995. <https://doi.org/10.1016/j.gsd.2023.100995>

- Li P, Qian H, Wu J (2014) Accelerate research on land creation. *Nature* 510(7503):29–31. <https://doi.org/10.1038/510029a>
- Li MG, Chen JJ, Xu YS, Tong DG, Cao WW, Shi YJ (2021) Effects of groundwater exploitation and recharge on land subsidence and infrastructure settlement patterns in Shanghai. *Eng Geol* 282:105995
- Li Z, Chen Q, Xue Y, Qiu D, Chen H, Kong F, Liu Q (2023) Numerical investigation of processes, features, and control of land subsidence caused by groundwater extraction and coal mining: a case study from eastern China. *Environ Earth Sci* 82:82
- Liu R, Zhao Y, Cao G, Wang Q, Ma M, Li E, Deng H (2022) Threat of land subsidence to the groundwater supply capacity of a multi-layer aquifer system. *J Hydrol: Reg Stud* 44:101240
- Pang M, Du E, Shoemaker CA, Zheng C (2022) Efficient, parallelized global optimization of groundwater pumping in a regional aquifer with land subsidence constraints. *J Environ Manage* 310:114753
- Pu C, Xu Q, Zhao K, Chen W, Wang X, Li H, Liu J, Kou P (2022) Spatiotemporal evolution and surface response of land subsidence over a large-scale land creation area on the Chinese Loess Plateau. *Int J Appl Earth Obs Geoinf* 111:102835
- Qin H, Andrews CB, Tian F, Cao G, Luo Y, Liu J, Zheng C (2018) Groundwater pumping optimization for land-subsidence control in Beijing plain, China. *Hydrogeol J* 26:1061–1081
- Ren G, Buckeridge J, Li J (2015) Estimating land subsidence induced by groundwater extraction in unconfined aquifers using an influence function method. *J Water Resour Plan Manag* 141(7):04014084
- Rivera A, Ledoux E, Marsily GD (1991) Nonlinear modeling of groundwater flow and total subsidence of the Mexico city aquifer-aquitard system. In: *Proceedings of the 4th international conference on land subsidence, Houston, 12–17 May 1991*, pp 45–58
- Spellman FR (2017) *Land subsidence mitigation: aquifer recharge using treated wastewater injection*, 1st edn. CRC Press
- Tang W, Zhao X, Motagh M, Bi G, Li J, Chen M, Chen H, Liao M (2022) Land subsidence and rebound in the Taiyuan basin, northern China, in the context of inter-basin water transfer and groundwater management. *Remote Sens Environ* 269:112792
- Terzaghi K (1925) Principles of soil mechanics, IV—settlement and consolidation of clay. *Eng News-Rec* 95(3):874–878
- Tzampoglou P, Ilija I, Karalis K, Tsangaratos P, Zhao X, Chen W (2023) Selected worldwide cases of land subsidence due to groundwater withdrawal. *Water* 15(6):1094
- Wang YQ, Wang ZF, Cheng WC (2018) A review on land subsidence caused by groundwater withdrawal in Xi'an, China. *Bull Eng Geol Env* 78:2851–2863
- Wu JH, Li PY, Qian H (2015) Opportunities and challenges associated with the world's largest geotechnical engineering project for land creation on the Loess Plateau. In: *Proceeding of the international conference on computer science and environmental engineering (CSEE2015)*, DESTech Publications, Inc., pp 141–147
- Younas M, Khan SD, Tirmizi O, Hamed Y (2023) Geospatial analytics of driving mechanism of land subsidence in Gulf Coast of Texas, United States. *Sci Total Environ* 902:166102
- Zeitoun DG, Wakshal E (2013) *Land subsidence analysis in Urban Areas: the Bangkok metropolitan area case study*. Springer, Netherlands, Dordrecht, Netherlands

Chapter 4

Earth Fissures and Natural Resources

Mining



4.1 Introduction

Earth fissures are a macroscopic surface phenomenon where surface rock layers and soil formations crack and form fractures of a certain length and width due to natural factors such as tectonic activity and water action, or human factors such as groundwater extraction, irrigation, and excavation. Under external and internal forces, rocks and soil layers undergo deformation. When the applied force exceeds the tensile strength of the rock and internal cohesion of soil layers, they fracture, resulting in the disruption of continuity and the formation of fissures (including joints and faults). Due to the confinement of surrounding rock and soil layers and the pressure from the overlying layers, the fissures become smaller with depth. However, at the surface, the pressure decreases, creating some free space, resulting in wider fissures, which are referred to as earth fissures or ground fissures (Wang 2000).

As a special type of geological hazard, earth fissure disasters directly or indirectly deteriorate the geological environment, posing a serious threat to human life and property safety, and causing significant economic losses (Pacheco-Martínez et al. 2013; Youssef et al. 2014). The frequency and severity of modern earth fissure disasters have been increasing worldwide, occurring in many countries (Burbey 2002; Hjartardóttir et al. 2012; Filippis et al. 2013). Earth fissure disasters are globally distributed, and China is one of the countries that is most severely affected by earth fissures, and the earth fissures are mainly distributed in the North China Plain, Fen-Wei Basin, and the Suzhou-Wuxi-Changzhou region (Li 2003; Wang et al. 2010, 2019; Peng et al. 2017, 2018).

China is one of the countries with the earliest and most extensive records of research on earth fissures. In ancient times, surface cracking phenomena were often considered secondary disasters accompanying earthquakes and did not receive much attention. With the significant increase in demand for resources such as oil and groundwater, uncontrolled exploitation of underground resources has accelerated the process of earth fissures rupturing to the surface. At the same time, the rapid growth

of the global population and the contradiction between engineering development and earth fissure hazards have become apparent. In the mid-twentieth century, earth fissures gradually attracted the attention of scholars globally. However, by that time, many countries had already experienced large-scale earth fissure disasters, resulting in significant economic losses.

The study of earth fissure disasters in the United States began in the 1920s, starting with the earth fissures in the Goose Creek oil field in Texas between 1918 and 1926 (Minor 1925; Pratt and Johnson 1926). In the following decades until the 1970s, numerous earth fissures appeared in many regions (Jachens and Holzer 1982). During this period, Feth (1951) conducted research on earth fissures in the central and southern regions of Arizona, proposing that the tensile stress caused by uneven subsidence due to localized changes in aquifer thickness was the primary cause of earth fissure formation. The influence of groundwater changes on earth fissure formation was emphasized. After more than half a century of research, three main viewpoints regarding the formation mechanisms of the Doña Ana earth fissures in the southwestern United States have emerged: the tectonic origin theory (Kreitler et al. 1977; Holzer and Gabrysch 2010), the groundwater exploitation theory (Bouwer 1977; Lofgren 1978), and the combined tectonic and groundwater activity theory (Holzer and Pampeyan 1979).

Systematic research on earth fissures in China began in the mid-1970s. After the 1976 Tangshan earthquake, earth fissures appeared successively in various regions, attracting the attention of scholars. Subsequently, starting with the study of the formation mechanisms of earth fissures in Xi'an, Yi (1984) compared the spatiotemporal correlation between changes in groundwater levels, ground subsidence, and earth fissure activity. It was proposed that significant ground subsidence caused by over-exploitation of confined groundwater was the main cause of earth fissure formation and development in the Xi'an area, while being controlled by local geological structural conditions. Xia (1990) further studied the formation mechanisms of earth fissures in the Xi'an area, emphasizing the significant role of modern tectonic activity and human engineering activities in the process of earth fissure formation. With the expansion of the investigation scope and in-depth research, more than 500 earth fissures have been discovered in various areas of the Fenwei Basin. Scholars such as Peng Jianbing have comprehensively summarized the formation mechanisms of typical earth fissures in the region, including the coupling effects of tectonic fissures, pumping-induced fissures, and rainfall-induced fissure expansion (Peng et al. 2016, 2019; Jia et al. 2020).

4.2 Classifications of Earth Fissures

Earth fissures are geological phenomena characterized by the release of energy, movement of materials, or deformation and displacement of rock and soil masses. They are a result of the coupling of multiple scales, dynamics, and factors. Earth fissures can be triggered by regional stress fields, fault structures, groundwater exploitation,

rainfall, underground mineral resource extraction, collapses, and landslides (Wang et al. 2020). They exhibit different spatial manifestations. Considering the diverse types of earth fissures, this chapter classifies them based on their formation causes, mechanical properties, and spatial forms.

4.2.1 Classification Based on Formation Causes

The Earth's crust and surface are constantly undergoing dynamic changes driven by natural forces, which geologists refer to as geological forces. These forces encompass the natural dynamics (internal and external) that cause movements and changes in the composition of the Earth's crust, internal structure, and surface morphology. Therefore, scholars have classified these forces into internal forces and external forces (Xie 1988). Common types of internal force-induced fissures include earthquake fissures, volcanic fissures, and tectonic creep fissures. Common types of external force-induced fissures include expansive soil fissures, collapse fissures, landslide fissures, subsidence fissures, slump fissures, erosion fissures, drought fissures, freeze–thaw fissures, salt dome fissures, and mud volcano fissures. Due to the increasing impact of human activities on the natural environment, many experts and scholars believe that human activities should be separately classified in terms of fissure formation, such as ground subsidence fissures caused by excessive groundwater extraction. The following provides specific descriptions of each type of fissure.

4.2.1.1 Earthquake Fissures

It is generally believed that the development of earthquake fissures is closely related to the magnitude of the earthquake. Higher magnitude of earthquakes can usually produce wider, longer and deeper earth fissures. The development of earthquake fissures is most concentrated in the seismically active zones, where they tend to be larger in scale. As the distance from the epicenter increases, the number of fissures gradually decreases. However, in some localized areas far from the seismic zone, due to variations and influences of structural conditions, rock and soil properties, landforms, and groundwater, these areas may exhibit a high density of fissures. Overall, earthquake fissures are characterized by their large scale, extensive distribution, and clear directional patterns. They exhibit good continuity in the horizontal plane, with distinct horizontal and vertical displacements. In cross-section, multiple secondary fissures are present, showing overall displacement and multiple stages, and may even exhibit water and sand ejections.

4.2.1.2 Volcanic Fissures

Volcanic fissures triggered by volcanic activity include volcanic inflation cracks and lava extrusion cracks. Volcanic inflation cracks are characterized by their small scale, exhibiting a circular or radial distribution in the horizontal plane, with no significant vertical displacement. In cross-section, the fissure walls are rough, showing clear tensile characteristics and displaying multiple stages and periodicity. On the other hand, lava extrusion cracks are larger in scale, extending over a greater distance, and exhibiting a zigzag pattern in the horizontal plane. They do not show significant vertical displacement but display pronounced horizontal tension.

4.2.1.3 Tectonic Creep Fissures

In addition to the rapid fracturing of structural fissures during earthquakes, tectonic creep fissures can also form due to the slow and steady changes in tectonic stress. In the same tectonic stress field, areas most prone to tectonic creep fissures include zones of strain accumulation, areas with brittle rocks, and regions experiencing intense changes in active structures, such as active fault zones, the axial parts of active folds, and the transitional areas of uplift and subsidence in active structures. Tectonic creep fissures generated during intense crustal movements often have a widespread distribution, ranging from several thousand square kilometers to several hundred thousand square kilometers in size. In extensive regions, tectonic creep fissures do not develop along a single direction but may exhibit multiple sets of fissures with different orientations.

4.2.1.4 Expansive Soil Fissures

Expansive soil, also known as shrink-swell soil or fissured soil, is a special type of cohesive soil. Due to its characteristics of swelling when wet and shrinking when dry, expansive soil often experiences severe shrinkage and generates numerous fissures during dry seasons, especially during years of extreme drought. Although expansive soil rapidly expands after absorbing water during the rainy season, this swelling-shrinking deformation is irreversible. The opening width of the cracks during shrinkage is greater than the closure width during wet expansion, resulting in increasing differences with each cycle of swelling and shrinking. Additionally, local microclimatic influences, such as sun-facing slopes versus shaded slopes or variations in ventilation conditions, can affect the degree of development of expansive soil fissures. Generally, fissures are more developed in the former conditions and less developed in the latter.

4.2.1.5 Collapse and Landslide Fissures

Collapse and landslide fissures often occur together in similar terrain conditions, primarily influenced by gravitational forces. They are initially formed by the development of fissures. Generally, slopes with collapse fissures are steep, with the upper part protruding and the lower part concave. When the fissures extend to a certain extent, rock blocks and soil will fall freely and accumulate at the foot of the slope, forming a talus deposit. Slopes with landslide fissures are relatively gentle, often exhibiting an arc-shaped or straight-line form. The upper part of the slope is concave, while the lower part is convex. Rock blocks and soil slide along the slope surface, maintaining their original structural characteristics. The surface of the landslide body exhibits a stepped morphology, and a series of new fissures are formed during the sliding process.

4.2.1.6 Subsidence and Collapse Fissures

Subsidence and collapse are common phenomena caused by various factors. Prior to subsidence and collapse, the ground often develops fissures, known as subsidence fissures and collapse fissures, respectively. Generally, large-scale caves with a significant height difference between the cave floor and ceiling and shallow burial depth are prone to subsidence and the formation of subsidence fissures. Conversely, collapse and collapse fissures occur in cases where the cave collapses.

4.2.1.7 Swelling, Erosion, and Drought Fissures

The morphological characteristics of swelling fissures are influenced by the landforms formed by loess swelling. Due to the formation of circular depressions during loess swelling, fissures often surround these depressions. The density of fissures around the depressions is influenced by the scale and depth of the swelling and the columnar joints in the loess. Generally, in areas with well-developed columnar joints in loess, the fissures around the edges of the swelling depressions are denser when swelling occurs. The cutting depth of swelling fissures is generally shallow and mostly within the swelling loess layer.

Erosion fissures generally occur in unconsolidated sandy soil and gravel layers. When rainwater falls on the surface of the sandy soil layer, it permeates underground through the pores between the sand particles. During the infiltration, flowing water has two effects: it carries away extremely small particles filling the gaps between coarse particles, increasing the porosity of the sandy soil layer; and under the influence of gravity, loose sandy soil gradually becomes compacted. When these two effects occur simultaneously in the same soil mass after a certain period of accumulation, the surface of the soil layer suddenly collapses in a linear pattern, forming fissures.

Drought fissures mainly occur due to the loss of moisture in the soil layer under arid climatic conditions. These fissures primarily develop on the surface of the soil layer and are not only controlled by dry weather but also closely related to the composition of the soil. In general, silty clay soils are most prone to drought fissures.

4.2.1.8 Thaw-Freezing Earth Fissures

Changes in the moisture content of soil can cause surface cracks in the ground. In cold climates, the water in the soil freezes into ice during the cold season and then thaws back into water after a certain period. The earth fissures that form under these conditions are called thaw-freezing earth fissures. Thaw-freezing fissures are closely associated with cold climate regions and are mostly found in the permafrost zones near glaciers. In these frozen soil areas, the repeated cycles of freezing and thawing can lead to earth fissure formation. Additionally, during the summer, the thawing of the surface layer can induce creep and contribute to earth fissures development. Thaw-freezing earth fissures primarily occur in sloping areas or small valleys.

4.2.1.9 Salt Dome Fissures and Mud Volcano Fissures

Salt dome fissures are mainly caused by the plasticity of rock salt, petroleum, and the overlying rock layers' weight. Sometimes, the compressive forces from crustal movements also play a role. The characteristics of salt dome fissures are influenced by the shape and size of the salt dome. Generally, shallowly buried salt domes exhibit more developed earth fissures, while deeply buried ones have less pronounced earth fissure development and a smaller distribution range. The earth fissures formed prior to mud volcano eruptions have a similar shape to the mud volcano itself, often radiating outward. The scale and density of these earth fissures are controlled by the extent and magnitude of the mud volcano dome's rise. The development of earth fissures is most active when a mud volcano is nearing eruption.

4.2.1.10 Ground Subsidence Fissures

Ground subsidence fissures are typically caused by uneven subsidence resulting from excessive groundwater extraction. The extraction of groundwater causes a loss of water in the aquifer, leading to a decrease in hydraulic head and a reduction in pore water pressure. This increase in effective stress causes a decrease in intergranular pore space, disruption of particle structures, and particle movement and rearrangement, resulting in macroscopic surface subsidence. The formation process of these earth fissures involves the accumulation and dissipation of stress and strain due to differential subsidence. In this process, hidden fractures form in the shallow soil layers at locations of stress concentration, providing a structural basis for the subsequent formation of earth fissures.

4.2.2 Classification Based on Mechanical Properties

4.2.2.1 Compressive Earth Fissures

Under the influence of compressive stress, a group of compressive earth fissures can be formed perpendicular to the direction of maximum principal stress. These earth fissures are relatively small, exhibiting a smooth and wave-like linear shape with limited extent. Local bulging or sinking may be observed in the vicinity of these earth fissures. In the natural environment, compressive earth fissures are highly uncommon, making it difficult to locate a representative example of such earth fissures in the field.

4.2.2.2 Tensile Earth Fissures

Tensile earth fissures have a strike parallel or perpendicular to the direction of maximum principal stress or maximum principal tensile stress. These tensile earth fissures are characterized by their wide width and rough, uneven fracture surfaces, often exhibiting a serrated or jagged pattern. They have limited linear extensions, with each segment transitioning into another extension direction. However, the overall extension direction of the entire fracture remains relatively stable. Adjacent to a large-scale tensile earth fissure, there is often a series of smaller fractures parallel to it. Tensile earth fissures are the most commonly observed type of earth fissures.

4.2.2.3 Shear Earth Fissures

Shear earth fissures have a well-defined linear extension, stable orientation, and straight shape, sometimes resembling neatly cut lines. Some shear earth fissures exhibit a series of feather-like small fissures intersecting obliquely with them on one or both sides. Shear earth fissures often appear in zones, with a harmonious relationship between their beginnings and ends. In the plane, some areas have a higher density of shear earth fissures, while others have a lower density. The widths and spacing of dense and sparse zones are approximately similar, resulting in a rhythmic variation in density.

4.2.2.4 Compressive Shear Earth Fissures

When the angle between the strike of a fracture and the direction of maximum principal compressive stress is less than 90° but greater than 45° , it is classified as a compressive shear earth fissure. Compressive shear fractures exhibit a combination of characteristics from both compressive and shear earth fissures. The earth fissure line takes on a gentle “S” or reverse “S” shape and is often composed of several fissures arranged in a staggered pattern. The width of compressive shear fissures varies, and their surfaces are relatively smooth and flat.

4.2.2.5 Tensile Shear Earth Fissures

When the angle between the strike of a fracture and the direction of maximum principal compressive stress is less than 45° but greater than 0° , it is classified as a tensile shear fracture. Tensile shear fractures exhibit a combination of characteristics from both tensile and shear fissures. The fissure line appears relatively straight, but in certain local sections, it often adjusts to accommodate another set of shear fissures, leading to a change in direction.

4.2.3 Classification Based on Morphology

Earth fissures can also be classified based on their morphology. They are classified primarily based on their geometric patterns observed on a plane. In the classification of earth fissures, it is important to consider both the morphology of an individual earth fissure and the combination of multiple earth fissures. The integration of these two aspects is crucial for a logical and comprehensive classification (Table 4.1).

Table 4.1 Earth fissure classification based on morphology

Common morphology	Main features
Straight-line shape	The earth fissure is flat and straight, with a stable direction of extension, and no turning occurs throughout the crack
Arcuate shape	Under certain natural conditions or influences, the fissure bends to form an arc, resembling a curved line
“S” and inverted “S” shape	The middle section is straight while both ends curve in opposite directions, giving it a back-and-forth bend
Sawtooth shape	Fissure zigzags like the teeth of a saw but extends in a specific direction overall
“Z” or “N” shape	The middle and both ends of the fissure are straight, but there’s a sudden deviation between them, resembling either a “Z” or “N”
Ring shape	The fissure circumscribes a ringed structure, geological entity, or topographical feature, looking almost circular or shaped by several arcuate lines forming a near-circular image
Geese-row shape	Several roughly parallel fissures appear in succession, mimicking a line of geese in flight
“入” or “人” shape	On one side of the main fissure, a branch meets it at a certain angle but doesn’t cut through, resulting in a “入” or “人” shape
“X” and grid shape	Two sets of fissures with different orientations intersect in an “X” form. Each set often consists of multiple parallel fissures that frequently weave with the other set, forming a grid-like pattern

(continued)

Table 4.1 (continued)

Common morphology	Main features
Broom shape	On one end of the main fissure, a series of smaller fissures develop with varying angles of intersection, looking like the bristles of a broom splaying out
Radiating shape	Fissures radiate outwards from the center, akin to the spokes of a bike wheel. The center typically is more elevated than its surroundings, and the fissure width narrows from the center to the edges
Centripetal shape	Fissures converge towards the center. Its appearance is similar to the radiating form, but the center manifests as a depression, with the fissure width narrowing from the edges to the center

4.3 Hazards of Earth Fissures

Earth fissures induce deformation and stress fields within a certain range of the surrounding geological body, subsequently impacting buildings through their foundations and bases. The consequences of various earth fissures on human populations primarily manifest as the destruction of surface structures and other artificial facilities, posing a significant threat to human life and property safety. Earth fissure disasters are widespread in China, with the main distribution areas including the Fen-Wei Basin, the North China Plain, and the Suzhou-Wuxi-Changzhou region. These areas are characterized by intense tectonic activity and high population density, which have contributed to the occurrence of large-scale earth fissure disasters. The specific hazards of earth fissures can be summarized as follows.

4.3.1 Road Surface Damage

Earth fissures primarily disrupt road surfaces by causing misalignment, resulting in uneven surfaces or even complete fractures that hinder normal traffic flow. Additionally, the rupture of road surfaces can lead to significant infiltration of surface water during the rainy season. This water infiltration not only erodes the underlying gravel layer but also triggers surface subsidence. When combined with earth fissure activity, these factors exacerbate the extent of road surface damage. The characteristics of earth fissure disasters on road structures are closely related to the development and movement patterns of the fissures. For both flexible road structures, such as asphalt roads and unpaved dirt roads, and rigid road structures, such as concrete roads, their damage characteristics and disaster modes differ due to their distinct mechanical properties when exposed to the same earth fissure environment. These disaster modes can be categorized into four types: slope type (flexible road structures), steep slope type (rigid road structures), tension type, and fragmentation type (Peng et al. 2017).

The slope-type road surface damage is primarily observed when roads with flexible structures, like asphalt gravel, intersect earth fissures. In these cases, there is a significant relative vertical displacement between the upper and lower sections of the fissure, resulting in the damage pattern depicted in Fig. 4.1. It can be observed that the fundamental cause of this type of damage is the relative subsidence of the upper section, which leads to the settling of the road structure above under the influence of gravity. Thanks to the excellent deformation adaptability of flexible road surfaces, a slope that slightly tilts towards the upper section or even a steep slope is formed in the vicinity of the earth fissure. Additionally, small transverse tension cracks may appear in areas with high convex curvature on the slope.

Figure 4.2 illustrates the disaster mode of slope-type road surface damage when roads with rigid structures, such as concrete, intersect earth fissures. In this scenario, if there is a significant relative vertical displacement between the upper and lower sections of the fissure, a steep slope-type road surface damage pattern will occur, as shown in Fig. 4.2a. The fundamental cause of this type of damage is also the relative subsidence of the upper section, resulting in the settlement of the road structure under the influence of gravity. Due to the limited deformation adaptability and low tensile strength of concrete materials, areas with concentrated tensile and shear stresses near the earth fissure can lead to the fracturing of the concrete road surface, forming a steep slope. If the earth fissure is well-developed and has a certain width, it is possible to form a double-section or even multiple-section steep slope damage (Fig. 4.2b).

For nearly vertical tensional earth fissures, regardless of whether the road surface structure is flexible or rigid, tensional cracks generally form parallel to the fissure. As

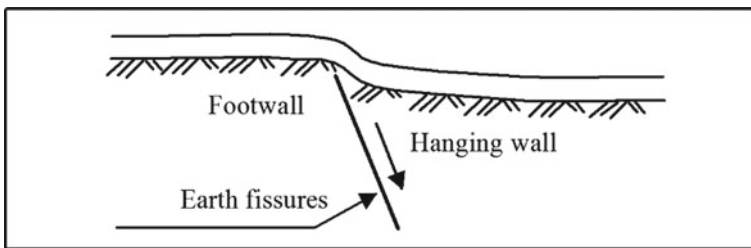


Fig. 4.1 Illustration of slope-type road surface damage modes (Peng et al. 2017)

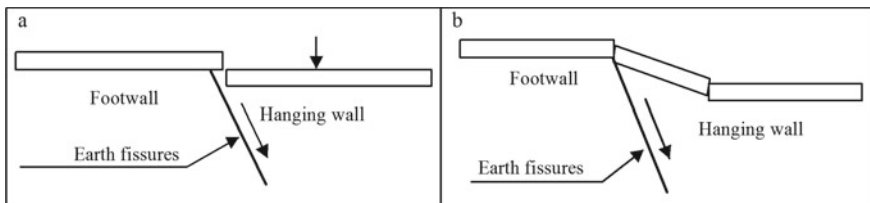


Fig. 4.2 Illustration of disaster modes for a steep slope type road surface damages and b double-section steep slope type road surface damages (Peng et al. 2017)

flexible materials have better deformation adaptability, a group of parallel tensional cracks usually forms within a certain range near the earth fissure, although the crack opening width is generally small. In contrast, for rigid road surface structures such as concrete, the opening deformation tends to concentrate on a main crack, resulting in a larger opening width, but fewer cracks compared to flexible road surfaces. The damage mode is shown in Fig. 4.3.

The fragmentation-type road surface damage caused by earth fissures is similar to the mode of rupture observed in the formation of figure-eight-shaped wall cracks. Specifically, when the earth fissures are well-developed, a subsidence trough with a certain width is formed due to the combined effects of fissure creep and surface erosion. This leads to severe damage to the road structure above, especially under repeated vehicular loads, resulting in a fragmented zone on the road surface. The disaster mode is illustrated in Fig. 4.4.

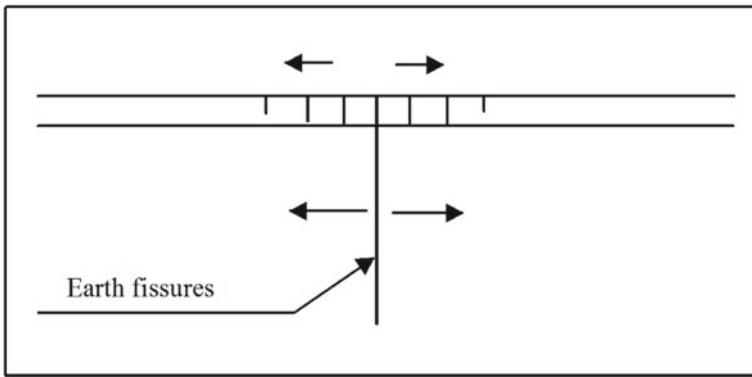


Fig. 4.3 Illustration of disaster mode for tension type road surface damages (Peng et al. 2017)

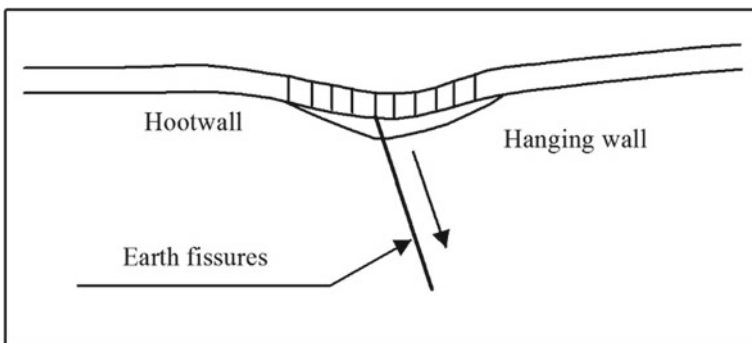


Fig. 4.4 Illustration of disaster mode for fragmentation-type road surface damages (Peng et al. 2017)

4.3.2 Hazards to High-Speed Railway Projects

The hazards posed by earth fissures can severely constrain local urban planning and utilization. They also pose a significant threat to the safety of local high-speed railways. For example, there are 21 earth fissures or fissure clusters that intersect or covertly intersect with the Datong-Yuncheng high-speed railway. Some of these fissures have branch fissures or secondary fissures, with a total of 36 intersections or covert intersections with the high-speed railway. They are primarily distributed in the Taiyuan Basin, Linfen Basin, and Yuncheng Basin. The causes of these fissures can be categorized into the following types: structural (controlled or influenced by fault creep or hidden faults), subsidence-induced, and paleo-geomorphologically (topographical) controlled.

Peng et al. (2017) studied the earth fissures along the Datong-Yuncheng North high-speed railway. Through physical model testing and numerical simulation of the impacts of fissure activities on the high-speed rail embankment and bridge, they concluded that when the high-speed railway embankment crosses the fissure zone at a small angle, the deformation and failure mode of the concrete base plate of the embankment under the action of the fissures is tension-shear failure caused by torsion and bending deformation. Cracks primarily concentrate in the middle of the plate, with a nearly parallel distribution and intersecting at a small angle with the fissures, with more severe deformation and failure in the lower structure than in the upper structure. However, when the high-speed railway embankment crosses the fissure zone at a large angle, the pressure at the pile end of the cement fly ash gravel piles under the action of the fissures mainly shows a decreasing trend in the upper structure and an increasing trend in the lower structure. When the vertical displacement of the fissure reaches 4 cm, cracks begin to appear near the location of the trackbed board close to the fissure. The failure mode of the cement fly ash gravel piles is bending failure, and the failure surface is approximately horizontal.

4.3.3 Impacts on Buildings

Earth fissures can be a slow deformation geological hazard. The fundamental cause of their occurrence lies in the formation of fissures that reach or approach the surface of the earth, followed by uneven deformation or uneven settlement on the surface due to tectonic creep, groundwater extraction, and surface water erosion. When buildings are situated above or within the uneven deformation zone of the upper and lower plates of an earth fissure, additional internal forces and deformations occur, leading to structural damage or even complete destruction. Therefore, the characteristics of engineering structures and their disaster patterns are closely related to the activity features of earth fissures, meaning that the deformation and destruction patterns of engineering structures are determined by the activity features or patterns of the earth fissures.

Among all forms of structural damages to ground buildings, the most common and typical form is the destruction of the wall. Walls situated above or within the uneven settlement and deformation zone of an active earth fissure will experience varying degrees of damages, characterized primarily by wall cracking. The cracking and destruction of building walls can be classified into four types: inclined type, vertical type, splayed type, and irregular type.

The inclined type is the most common form of wall cracking when the wall crosses over a geological fissure with a significant vertical displacement between the upper and lower plates. The disaster pattern of the inclined type is shown in Fig. 4.5.

The vertical type earth fissure is a horizontal tension crack that typically occurs in the upper wall of shallow earth fissures experiencing horizontal tension. The disaster pattern is shown in Fig. 4.6. The horizontal relative movement is mainly observed on both sides of the fracture surface, with the degree of opening determined by the extent of horizontal relative movement between the upper and lower plates of the earth fissures.

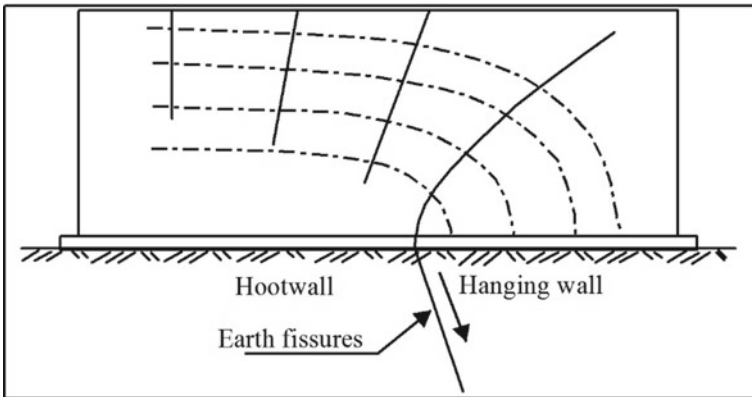


Fig. 4.5 Illustration of disaster mode for counter-tilting wall fracture (Peng et al. 2017)

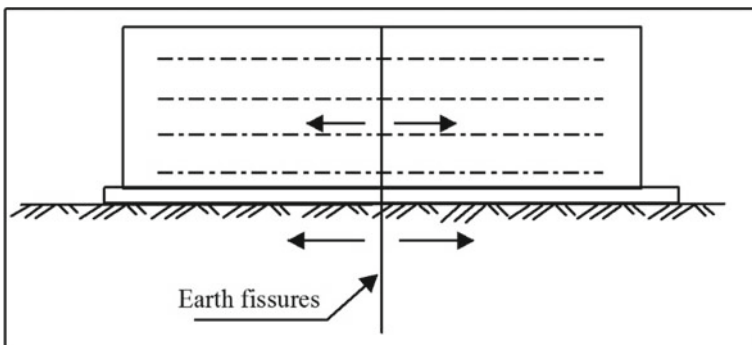


Fig. 4.6 Illustration of disaster mode for upright wall fracture (Peng et al. 2017)

The splayed type of wall cracking is not commonly observed and only occurs when a wall spans a large-scale and highly active earth fissure. The disaster pattern is shown in Fig. 4.7. From Fig. 4.7, it can be observed that when the earth fissure develops to a large scale, it can create an influence zone several meters to tens of meters wide. Under the combined effects of creep and subsurface water erosion of the earth fissure, the soil in the influence zone forms a funnel-shaped settlement trough. Consequently, two nearly symmetrical sets of principal tensile stress traces, as indicated by the dotted lines in Fig. 4.7, are formed in the upper wall. This results in inclined fractures perpendicular to the principal stress traces at the edges of the settlement trough, forming a splayed type earth fissures.

Irregular earth fissures generally occur when walls are not directly positioned above a earth fissure but are within the influence zone of uneven deformation between the upper and lower plates of the fissure. The disaster pattern is illustrated in Fig. 4.8. Generally, the scale of irregular earth fissures is smaller compared to the aforementioned types of earth fissures, and the relative displacement on both sides of the crack is relatively small.

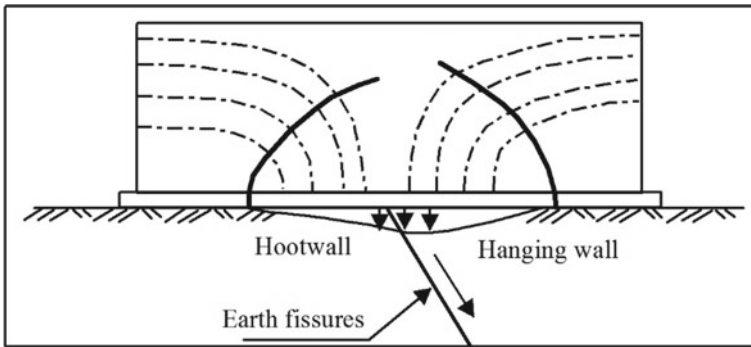


Fig. 4.7 Illustration of disaster mode for figure-eight wall fracture (Peng et al. 2017)

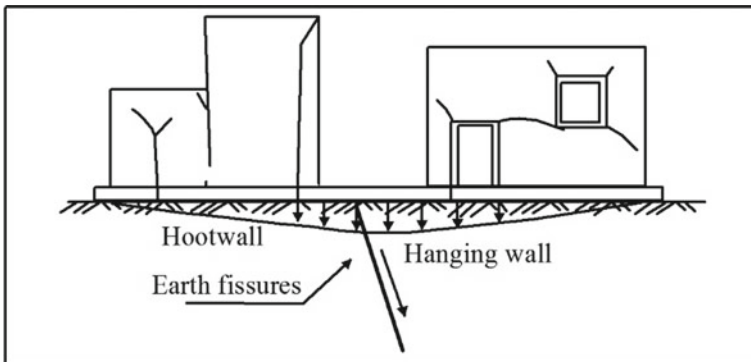


Fig. 4.8 Illustration of disaster mode for irregular wall fracture (Peng et al. 2017)

These findings contribute to a better understanding of the characteristics and disaster patterns of building structures in relation to the activity features of earth fissures, which are essential for mitigating the risks and improving the resilience of buildings in areas prone to such hazards.

4.4 Formation Mechanisms of Earth Fissures

Earth fissures are complex surface geological phenomena formed in specific geological environments. The process of their incubation, formation, and development is a non-equilibrium and nonlinear process. There are various types of earth fissures. The formation mechanisms of some common earth fissures are described below.

4.4.1 *Formation Mechanisms of Earthquake-Induced Earth Fissures*

The formation of earthquake-induced earth fissures is closely related to the magnitude of earthquakes. The larger the magnitude, the more earth fissures are generated. Based on their causes, earthquake-induced earth fissures can be further classified into tectonic earth fissures and secondary gravity-induced earth fissures.

Tectonic earth fissures are surface destruction phenomena formed in the epicentral region and surrounding areas during seismic activity. They are caused by the rupture of rock layers in the seismic source area, resulting in shallow surface displacement of rock and soil materials (Wang 2000). Tectonic earth fissures mainly extend along fault zones, with large scale and far-reaching distribution. They exhibit obvious directional characteristics. Different seismic fault zones often show regular combinations, reflecting the main structural directions of the seismic region and the regional stress field or local stress field controlling the geological structure. They exhibit significant displacement in both horizontal and vertical directions and can occur in different geomorphic units and lithological positions (Yi and Liang 2010).

Secondary gravity-induced earth fissures are surface cracks formed by the creeping and sliding deformation of shallow rock and soil materials in local zones due to the vibration effects of earthquakes. They can be categorized into three types based on their causes: (1) Intense ground shaking causes inclined surfaces or slopes to become unstable, resulting in rock and soil collapse and tensile earth fissures at the edges of the sliding zone. (2) Various forms of cracks appear in artificial fill structures (such as earth dams, gravel roads, and embankments) due to strong ground motion, with their orientations aligning with the long axis of the fill structures and exhibiting certain distribution patterns. (3) Flat and horizontal overlying layers slide along the underlying inclined layers, leading to the occurrence of tensile earth fissures on the ground. These fissures mostly occur in areas with artificial fill soil.

Overall, the formation mechanisms of earth fissures are complex and involve various geological and geotechnical factors. Understanding these mechanisms is crucial for predicting and mitigating the hazards associated with earth fissures.

4.4.2 Mechanism of Formation for Landslide Earth Fissures

Common types of earth fissures caused by landslides can be divided into collapse-type and landslide creep-type. Collapse-type fissures are mainly formed by the development of joint fissures or unloading fissures and are often a precursor to landslide activity. Collapse-type fissures are mainly induced by activities such as excavation at the foot of slopes, open-pit mining, and slope cutting during road construction. The inclination angle of collapse-type fissures is steep, and their spatial distribution density, fissure opening width, and extension length gradually decrease from near the slope surface towards the slope interior. Collapse-type fissures can be formed by tension zones created by stress concentration in local sections of slopes, or by sliding deformation of slope rock and soil materials along unloading fissure zones. For example, in the Yuen Long area of Shenzhen City, Guangdong Province, due to excavation at the foot of slopes, the slope experienced significant unloading deformation, and under the long-term effect of rainfall infiltration, several arc-shaped collapse fissures were formed in the artificial slope zone.

Long-term creep deformation of landslides often leads to the formation of different-shaped landslide fissures. Landslide fissures are the evolution of stress states in slope zones that give rise to landslides, causing changes in the original stress equilibrium state and resulting in the concentration of stresses in local sections that gradually exceed the strength of the rock and soil materials at that site, leading to shear and tensile fractures and the formation of surface cracks. Landslide fissures are both the product of landslide activity and a precursor to landslides, closely related to rainfall infiltration conditions and other triggering factors. Generally, landslide fissures can be divided into the following four categories:

1. Arc-shaped tensile fissures are mainly distributed at the rear of the landslide body, with lengths ranging from a few meters to several hundred meters. They usually take the form of arcs and are roughly parallel to the direction of the landslide rear wall. These fissures are mainly formed by the downward creeping and tearing of the landslide body.
2. Feather-shaped shear fissures are mainly distributed on both sides of the middle part of the landslide body. Due to the sliding deformation of the landslide body, relative displacement occurs between the landslide body and the stationary material in the surrounding area, forming a shear deformation zone at the boundary between the landslide body and the stationary material, which results in shear fissures. Feather-shaped fissures often accompany both sides of the shear fissures.
3. Bulging fissures are mainly distributed at the front of the landslide body. These are tensile fissures formed by the uplift of the landslide body due to being obstructed

during downhill movement, with their directions mostly perpendicular to the direction of landslide movement.

4. Fan-shaped fissures are a common type of fissure in landslide terrain, mainly distributed in the middle and front parts of the sliding body, especially in the area of the landslide tongue. These fissures typically have an open shape, similar to that of a fan. The direction of the fissures is approximately parallel to the sliding direction in the middle part of the landslide body, while in the area of the landslide tongue, they are radially distributed, resembling the radiation lines of a fan. These fissures are primarily formed due to the sliding body sliding to the bottom and spreading to both sides. During the sliding process, the soil in the middle part of the landslide body experiences significant stress and shear forces, leading to the formation of fissures. The direction of these fissures is close to the sliding direction, showing the characteristics of sliding. At the same time, in the area of the landslide tongue, the cracks exhibit a radial distribution, consistent with the trajectory of the outward spreading of the collapse point.

4.4.3 Mechanism of Formation for Collapse Earth Fissures

The formation mechanisms of collapse earth fissures can be divided into karst collapse earth fissures and goaf collapse earth fissures.

Karst collapse is a slow process. Prolonged drought and groundwater pumping activities increase the groundwater seepage velocity and hydraulic gradient, resulting in hydraulic erosion on the overlying soil layer caused by the seepage of groundwater. As the dynamic hydraulic environment of karst further evolves, the covering soil layer on the top of the open karst cave is continuously eroded and excavated, and fine particles are gradually carried away by the groundwater flow, causing the soil structure to relax. At the contact between the top of the karst cave and the overlying soil layer, the soil starts to collapse and form initial soil caves. This process is a slow progressive process. During this evolution process, the stress state of the covering soil layer is disrupted, and local tensile stresses concentrate, leading to settlement and tensile deformation of the shallow soil layer, eventually forming a series of earth fissures. Karst collapse earth fissures are common deformation signs before ground subsidence disasters occur and often occur around collapse pits.

Goaf collapse earth fissures mainly occur in the goaf area, and the process of their formation is an extremely complex dynamic process. From the perspective of the mechanical mechanism of formation, before being affected by mining activities, the overlying soil layer in the goaf area is in a state of natural dynamic equilibrium. After the goaf is formed, the stability of the overlying rock and soil mass is supported by mining pillars. In the long-term bearing process, due to the heterogeneity of the rock structure of a few mining pillars with weak structures, progressive damage occurs, leading to deformation, cracking, and collapse of the underlying rock layers, and the bending deformation and further collapse of the overlying soil layer. As the underlying rock mass deforms and collapses, the overlying soil layer undergoes

creep. Coupled with the influence of groundwater seepage into the goaf area, earth fissures gradually form on the surface of the goaf.

Overall, both karst collapse earth fissures and goaf collapse earth fissures are complex processes involving the interaction of geological, hydrological, and mining factors. Understanding the formation mechanisms of these earth fissures is crucial for early warning and prevention of ground subsidence disasters.

4.4.4 Mechanism of Formation for Expansive Soil Fissures

The formation of fissures in expansive soils is the result of swell-shrink deformations caused by seasonal wetting and drying of the soil. The primary development depth of these cracks is typically located within the near-surface expansive soil layers or within the non-expansive soil layers situated above the shallow expansive soil strata. Common types of cracks in expansive soils are categorized into plane fracture-type earth fissures of swelling soil and underground fracture traction-type earth fissures of swelling soil induced by tensile forces.

Plane fracture-type earth fissures of swelling soil often evolve from weathering fissures. Densely developed weathering fissures on the surface of expansive soils are, in essence, a type of swell-shrink crack. These fissures represent the cumulative effect of countless seasonal wetting and drying cycles over extensive geological periods, and their opening and closing are entirely controlled by climatic moisture fluctuations. During seasons with ample rainfall, the surface of the expansive soil receives infiltrated rainwater, increasing its moisture content. Consequently, as the soil swells due to water absorption, these swell-shrink cracks gradually close, endowing the soil with a high shrinkage potential. As the environment transitions into the subsequent dry season characterized by scarce rainfall and high evaporation rates, this soil with its high latent shrinkage potential begins to lose its moisture content under the effects of solar heat and atmospheric evaporation. Cracks that had previously closed now gradually reopen in response to the soil's shrinking. With the progression of the dry season and intensifying atmospheric evaporation, the soil continues to lose moisture, leading to the continuous development and expansion of the shrinkage cracks. As the number and size of these cracks increase, a crack expansion cycle system gradually emerges. On one hand, these fissures contribute to the overall structural breakdown of the expansive soil. On the other, their development results in an increased evaporation surface area and depth, leading to more significant soil dehydration, greater soil shrinkage, and thus, rapid enlargement of the cracks. Over time, amidst numerous fissures, one or more dominant cracks may interconnect along their expansion paths to form significant earth fissures.

Underground fracture traction-type earth fissures of swelling soil induced by tensile forces emerge primarily in prolonged dry climatic conditions. Initially triggered by the drying effects of tree root water uptake, these cause "deep" areas of the expansive soil to shrink, resulting in underground concealed cracks. Following this, evaporation from the tree canopy further dries out the soil layers near the tree roots,

leading to additional soil shrinkage and further development of the concealed cracks. This process can culminate in the sudden tearing apart of the upper and lower soil layers, giving rise to visible earth fissures. Once these concealed underground fissures appear, if the dry conditions persist, the shrinkage force within the soil can intensify. After an extended dry spell, if a heavy downpour follows, rainwater rapidly infiltrates the surface cracks, penetrating deeper layers. This results in substantial water absorption by the soil within the crack development zone, causing the soil to swell, soften, and decrease in strength. At this juncture, the shrinkage force within the expansive soil's "shrinkage field" greatly surpasses the cohesive force between the soils located above the concealed crack boundary. The intense tensile forces then rapidly pull apart the concealed cracks at the edges of the forested area, severing the tree roots. Consequently, the upper and lower soil strata suddenly tear apart, leading to the formation of pronounced earth fissures.

4.4.5 Mechanism of Formation for Collapsible Loess Earth Fissures

Such types of earth fissures are caused by the collapsibility of loess soil and can form under long-term water saturation conditions, typically being of smaller scale. Due to the development of vertical joints in the loess, its vertical permeability often significantly surpasses its horizontal permeability. When this soil becomes saturated, it primarily undergoes deep vertical infiltration until it encounters the groundwater table or a soil layer with strong water-barrier properties. Only then does lateral saturation become pronounced. Following underground water-induced deformation, annular cracks form around the saturated soil mass, extending to the surface and resulting in earth fissures (Fig. 4.9).

4.4.6 Mechanism of Formation for Ground Subsidence Fissures

A potential cause for the formation of such earth fissures is the excessive extraction of groundwater leading to the creation of subsidence funnels. In the funnel's central region, significant groundwater level decline results in considerable soil compression. This, in turn, leads to a pronounced surface subsidence. The tensile stresses are relatively concentrated, and when the regional tensile stress surpasses the tensile strength of the soil layer, it induces cracking and deformation in the upper soil strata, giving rise to earth fissures (Fig. 4.10). Typically, these kinds of earth fissures do not follow a fixed direction and are generally smaller in scale.

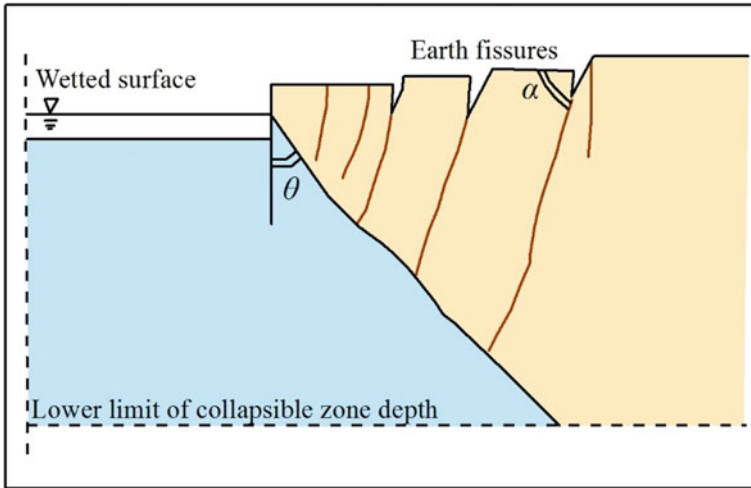


Fig. 4.9 Patterns of collapsible loess earth fissures (He 2011)

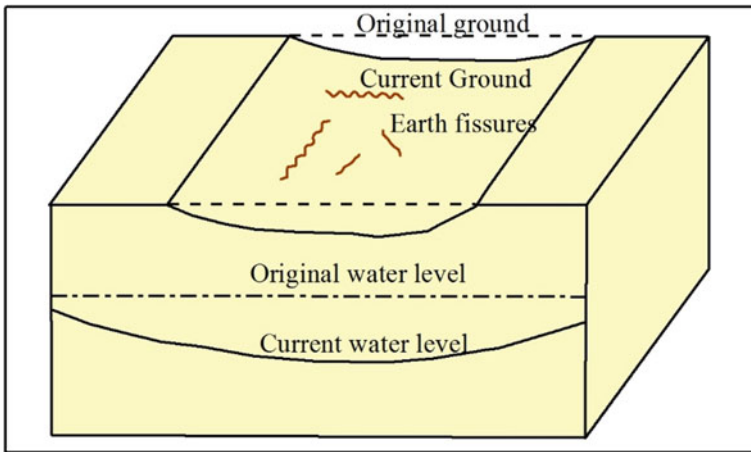


Fig. 4.10 Patterns of ground subsidence fissures (He 2011)

4.5 Groundwater Development and Earth Fissures

With the rapid socio-economic development of cities, the demand for water in agriculture, industry, and daily life has surged dramatically. This has resulted in the over-extraction of groundwater. The extraction of groundwater leads to a decline in the groundwater table, causing compression of the compressible soil layers, which in turn results in land subsidence. As groundwater continues to be extracted, earth fissures may first appear in areas where the land subsidence initially occurs. The

exploitation of groundwater is a crucial triggering factor for the formation of earth fissures, a viewpoint accepted by the majority of researchers studying these fissures. However, how groundwater extraction leads to the formation of earth fissures has long been a subject of substantial debate. Numerous scholars have proposed various causative mechanisms over time. In summary, there are primarily five main theories.

1. **Permeation Deformation Mechanism.** During the groundwater extraction process, earth fissures form due to the permeation deformation mechanism. Once a subsidence pit forms, the groundwater infiltration rate increases, the hydraulic gradient increases, and the dynamic water pressure formed by groundwater seepage produces latent erosion on the soil layer and gradually develops to pipe surge, which relaxes the structure of the soil layer, thus causing the tensile stress of the overlying soil layer to be concentrated and occurring tensile fissure deformation at the surface.
2. **Soil Layer Dehydration Shrinkage Deformation Mechanism.** Neal (1968) proposed that the shrinkage deformation of soil layers due to dehydration was a cause of earth fissures during groundwater development. As the groundwater level drops, the upper soil layer loses moisture and shrinks in the horizontal direction, leading to surface cracking. Some researchers have validated Neal’s causative mechanism through model experiments. The experimental results showed that the aquifer body strain caused by aquifer dewatering is obvious and can cause the contraction deformation of the soil layer in the horizontal direction.
3. **Permeation Stress Drag Mechanism** (Lofgren 1969). During the seepage of groundwater from the periphery to the center of the landfall funnel, a strong dynamic water pressure is formed along the seepage direction. The kinetic energy generated by the dynamic water pressure on the solid particles will produce an obvious viscous drag effect on the aquifer skeleton, and the accumulation of this viscous drag effect in the whole aquifer will form a tensile strain concentration in the overburden soil layer, thus causing it to crack.
4. **Differential Subsidence Deformation Mechanism** (Schumann and Poland 1970). Abrupt changes in the bedrock surface morphology or noticeable differences in the thickness of compressible soil layers will result in differential subsidence in loose soil layers, this will lead to a concentration of tensile stresses at the ground surface where compaction subsidence differences are the greatest, resulting in tensile deformation and cracking (Fig. 4.11).

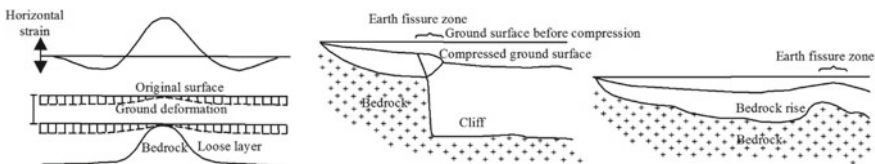


Fig. 4.11 Differences in pressures (Peng et al. 2012)

- 5. Rigid Fracture Mechanism. As the groundwater table decreases, the loose soil layer continuously undergoes consolidation deformation. Compared to the consolidation deformation of the underlying soil layer, the surface soil layer's consolidation is almost negligible. Therefore, during the subsidence process, a rigid inversion occurs, leading to fractures forming along the edges of the subsidence basin, as illustrated in Fig. 4.12.

The differential subsidence deformation mechanism has been more widely accepted and is considered the primary factor for the formation of earth fissures. The other mechanisms play dominant roles only in certain specific environments. Earth fissures resulting from differential subsidence due to groundwater extraction are widespread and have significant impacts. For instance, the bedrock undulation-induced earth fissures in the Suzhou-Wuxi-Changzhou region and the ancient river channel earth fissures in the North China Plain both fall under this category. Both have been caused by uneven subsidence due to over-extraction of groundwater. The extraction of groundwater causes the aquifer to lose water, leading to a decrease in hydraulic head, a reduction in pore water pressure, and an increase in effective stress. This, in turn, leads to a reduction in inter-particle voids. The granular structure gets disrupted, particles move and rearrange, which macroscopically manifests as ground subsidence. This process precisely serves as the driving force and the fundamental reason for earth fissures caused by differential subsidence. The formation process of such earth fissures is the evolution of stress and strain from accumulation to dissipation. In this process, the superficial soil undergoes concealed fractures at stress concentration points, laying the structural foundation for the eventual formation of fissures.

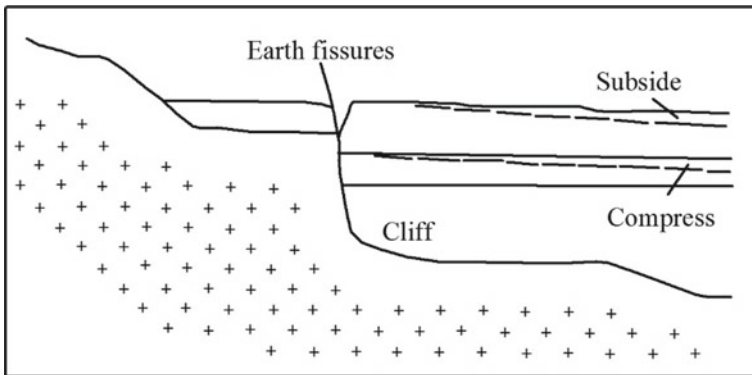


Fig. 4.12 Brittle fracture mechanisms (Peng et al. 2012)

4.6 Coal Development and Earth Fissures

Many regions are endowed with rich coal reserves, primarily extracted through underground mining. As a result of prolonged and extensive coal extraction, numerous voids or “mined-out” areas are created, often leading to the formation of earth fissures. After the coal is extracted, an underground cavity emerges. In an attempt to reestablish a geological equilibrium, the subterranean strata undergo repositioning and redistribution. This realignment process induces various physical and chemical alterations. When the coal beneath the surface is depleted and these voids form, the overlying rock layers, influenced by gravitational forces, descend and move. This movement compresses and bends the rock strata, causing surface deformations, subsequently resulting in earth fissures. Fissures arising from coal extraction are categorized as non-tectonic origin fissures. Their occurrence has posed severe threats to the safety of mining operations. Underground coal seam mining, the formation of the air-mining zone is the main reason for the formation of earth fissures in coal mines, and the geometric characteristics of the earth fissures, such as the scale, width and depth of the cracks, depend on the depth and area of the air-mining zone, topography and geomorphology, stratigraphy, lithology, and other geologic and mine mining conditions.

Following coal extraction, the structural integrity of the mined-out voids primarily relies on their inherent strength and the support provided by safety pillars (often referred to as barrier pillars). When the void spans a substantial area and these safety pillars are subsequently mined, the overlying rock strata, under the influence of their own weight, will descend as a whole. This results in a progression from bottom to top characterized by a caving zone, a fissure zone, and a subsidence zone. Due to variances in subsidence speed and magnitude, surface depression basins are formed. Based on the stress conditions within these depression basins, they can be categorized into three zones: the central zone, the inner edge zone, and the outer edge zone (Fig. 4.13).

1. Central Zone (Intermediate zone in Fig. 4.13). The surface sinks uniformly, with the maximum rate and amplitude of subsidence, and there are no obvious earth fissures.
2. Inner Edge Zone. The surface sinks unevenly, tilts to the center of the basin, is concave, produces compressive deformation, the surface is squeezed, and there are no mechanical conditions for the generation of earth fissures.
3. Outer Edge Zone (Outer marginal zone in Fig. 4.13). The surface subsidence is uneven, tilted toward the center of the basin, but convex, producing tensile stress and forming tensile earth fissures.

Mining-induced collapse cracks are another form of earth fissure in the coal mine area, which are developed immediately above the mining area and are in the form of wide below and narrow above. Its development conditions are shallow burial of coal seams, small thickness of overlying rock body in the mining area, and the formation

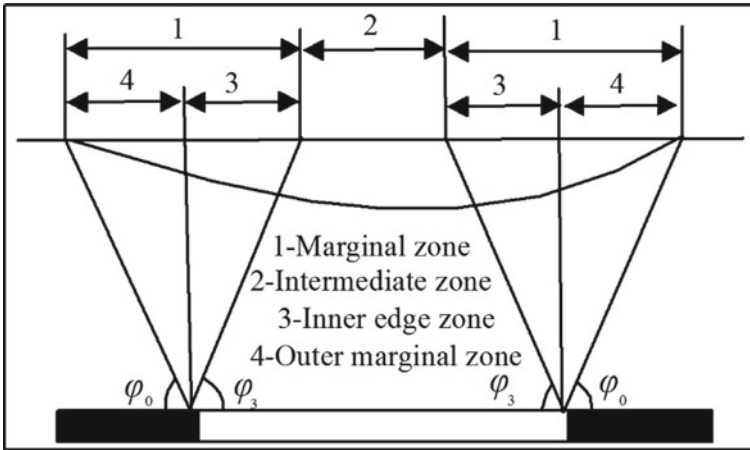


Fig. 4.13 Diagram of sedimentary basin zoning (China Institute of Hydrogeology and Engineering Geology 1996)

of rift zones reaching the surface, and the spatial relationship with the earth fissures in the subsidence basin is shown in Fig. 4.14.

A common feature of both types of earth fissures is that they are tensile cracks formed under the influence of self-weight stress in the rock mass. Their distinctions lie in their morphological characteristics and the damages they cause. The latter's harm is primarily manifested in the changes to the geological environment, while the

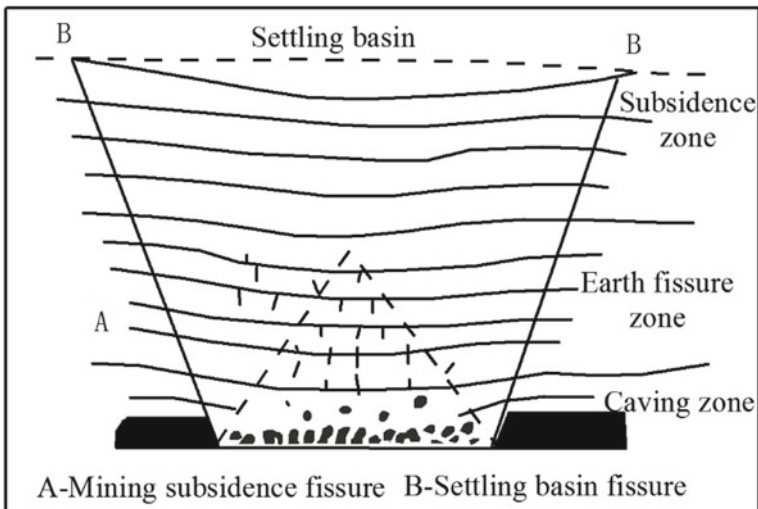


Fig. 4.14 Diagram of overlying rock failure in goaf area (China Institute of Hydrogeology and Engineering Geology 1996)

former primarily affects and damages surface structures. These two types of earth fissures coexist and are often found together within coal mining areas.

4.7 Prevention and Control of Earth Fissures

4.7.1 Preventive Measures

Earth fissure disasters predominantly occur within zones comprised of major fissures. All engineering projects and buildings that span these main fissures are at risk of damage. Investigations and research should be strengthened for naturally occurring earth fissures. Regional evaluations of areas prone to fissure occurrences should be conducted, prioritizing avoidance to either prevent or mitigate disaster losses. For earth fissures caused by human activities, the key lies in prevention, rational planning, and strict prohibition of unreasonable engineering activities near the fissures. The preventive measures that can be adopted are.

4.7.1.1 Avoidance Measures

When carrying out development and construction in areas where tectonic earth fissures are prevalent, a detailed engineering geological survey should be the first step. This entails investigating the regional tectonics and the history of fault activities. It's essential to ascertain the fissure development zones and potential hazard areas in the proposed construction site. Urban development plans and rational layout of buildings should be crafted to ensure that engineering facilities avoid the earth fissure hazard zones as much as possible. It is especially crucial to strictly limit the construction of permanent facilities across these fissures.

For engineering facilities already constructed within the earth fissure hazard zones, reinforcement measures should be adopted based on the specific circumstances. For example, underground pipeline projects that span earth fissures can adopt measures such as external corridor isolation, internally suspended pipeline supports combined with active flexible joint connections to prevent damage from fissures. Facilities that have already suffered significant damage from earth fissures might require partial or complete demolition to prevent further extensive damage to the entire structure or neighboring buildings.

4.7.1.2 Controlling the Inducing Effects of Human Factors

For non-tectonic earth fissures, measures can be taken to prevent or reduce their occurrence based on the reasons for their formation. For instance, engineering measures can be adopted to prevent collapses and landslides. The extraction of groundwater

can be controlled to prevent and mitigate ground subsidence; for loess wet-collapse fissures, it's essential to prevent the infiltration and erosion caused by precipitation and the use of industrial and domestic water. During underground mining in mining areas, depending on the actual conditions, one should control the scope of mining, increase the number and size of reserved protective pillars to prevent mine collapses that may induce earth fissures.

4.7.1.3 Monitoring and Forecasting Measures

Earth fissure activities can be monitored using methods such as surface exploration, ground deformation measurement, fault position measurement, audio-frequency magnetotelluric measurements, and high-resolution P-wave reflection measurements. This aids in predicting and forecasting the direction of fissure development, its rate, and the potential range of its impact.

4.7.2 Remedial Measures

When designing specific remedial measures, different treatments should be applied to different types of earth fissures. With the current level of technology, it is impossible to completely prevent the occurrence of tectonic earth fissures. Therefore, the remediation of tectonic earth fissures mainly includes the fissure displacement method, partial demolition method, foundation reinforcement measures, and structural strengthening of the upper sections. Non-tectonic earth fissures, on the other hand, have various causes. Different remedial measures need to be adopted for non-tectonic earth fissures with different causes to achieve better disaster mitigation effects. The leading factors in the formation of non-tectonic earth fissures are surface soil conditions and the water environment, which are subject to local condition changes. Thus, the preventive and control strategies for non-tectonic earth fissures also have commonalities, primarily focused on eliminating the impacts of these local conditions. Measures that can be adopted for non-tectonic earth fissures include removing the weak foundation, localized inundation method, and compaction filling method. Detailed introductions are as follows.

4.7.2.1 Fissure Displacement Method

The displacement method, as a special treatment for foundational soil, adopts the approach of using fissures to remedy fissures. The theoretical basis for this method lies in the principle that the extension of earth fissures also follows the path of least energy. By this approach, a trench can be excavated at the location where the earth fissure passes through or is predicted to pass, avoiding structures. This trench connects with the earth fissure, forming an “artificial fissure.” This induces the tectonic fissure to

develop along the “artificial fissure,” severing the connection between the damaged building foundation and the tectonic earth fissure, thereby preventing further damage to the building.

4.7.2.2 Partial Demolition Method

Zhang (1990) proposed the principle of “demolish part, retain the whole.” For buildings situated directly across a tectonic earth fissure, the damaged parts can be demolished, effectively dividing one structure into two, thereby safeguarding the entire building from the influences or damages caused by the earth fissure. If it’s a multi-story building and only the ground floor is damaged, the affected ground floor can be demolished, disconnecting its foundation from the earth fissure. Reinforcement and support measures can then be applied to the upper levels, achieving a satisfactory disaster mitigation effect.

4.7.2.3 Foundation Reinforcement and Structural Strengthening Measures

These measures are primarily designed for buildings that, due to site constraints, are situated within protective zones or cannot be relocated. For instance, for frame structures within the protective belts, their foundations can be designed with crossed foundational beams. If considering treatment for collapsible soil and using loess as the foundation, it’s prudent to design it as a ribbed raft slab foundation. For standard residential buildings, a shallow embedded reinforced concrete ring beam foundation can be adopted. Along the direction parallel to the earth fissure, settlement (or contraction) joints can be installed to divide larger structures into simpler independent units.

4.7.2.4 Removal of Unsuitable Foundations

This measure is a fundamental solution for mitigating non-tectonic earth fissures. Techniques such as excavation and soil replacement can be employed to completely remove problematic components from the building foundation, like expansive clays, soft soils, and backfilled soils. For broader and thicker layers of soft soil (like marine silt layers), other treatments such as dynamic compaction slurry displacement, sand well consolidation, and vacuum preloading drainage consolidation can be adopted.

4.7.2.5 Localized Water Immersion Method

This method is suitable for collapsible loess foundations. By controlling localized water immersion, structures tilted due to earth fissures or surface subsidence can be realigned.

4.7.2.6 Tamping Fill Method

This approach is applicable in areas where the development of earth fissures has stabilized. Backfilling and compaction are done along the direction of the earth fissure's propagation, followed by waterproofing treatments.

References

- Bouwer H (1977) Land subsidence and cracking due to groundwater depletion. *Ground Water* 15(5):358–364
- Burbey TJ (2002) The influence of faults in basin-fill deposits on land subsidence, Las Vegas Valley, Nevada, USA. *Hydrogeol J* 10:525–538
- China Institute of Hydrogeology and Engineering Geology (1996) Environmental geology research series 3. Seismological Press, Beijing
- Feth JH (1951) Structural reconnaissance of the Red Rock quadrangle, Arizona. Open-file report 51-199, United States Geological Survey, Arizona. <https://doi.org/10.3133/ofr51199>
- Filippis LD, Anzalone E, Billi A, Faccenna C, Poncia PP, Sella P (2013) The origin and growth of a recently-active fissure ridge travertine over a seismic fault, Tivoli, Italy. *Geomorphology* 195:13–26
- He HQ (2011) Study on the formation mechanism of ground fissures in Weihe Basin. Chang'an University, Xi'an
- Hjartardóttir ÁR, Einarsson P, Bramham E, Wright TJ (2012) The Krafla fissure swarm, Iceland, and its formation by rifting events. *Bull Volcanol* 74(9):2139–2153
- Holzer TL, Gabrysch RK (2010) Effect of water-level recoveries on fault creep, Houston, Texas. *Groundwater* 25:392–397
- Holzer TL, Pampeyan EH (1979) Earth fissures and localized differential subsidence. *Water Resour Res* 17:223–227
- Jachens RC, Holzer TL (1982) Differential compaction mechanism for earth fissures near Casa Grande, Arizona. *Geol Soc America Bull* 93(10):998–1012. [https://doi.org/10.1130/0016-7606\(1982\)93%3c998:DCMFEF%3e2.0.CO;2](https://doi.org/10.1130/0016-7606(1982)93%3c998:DCMFEF%3e2.0.CO;2)
- Jia Z, Peng JB, Lu QZ, Meng LC, Meng ZJ, Qiao JW, Wang FY, Zhao JY (2020) Characteristics and genesis mechanism of ground fissures in Taiyuan Basin, northern China. *Eng Geol* 275(3):105783
- Kreitler CW, Guevara E, Gramata G et al (1977) Hydrogeology of gulf coast aquifers, Houston-Galveston area, Texas. *Gulf Coast Assoc Geol Soc Trans* 27:72–89
- Li CC (2003) Study on the ground fissures in Hebei Plain. China University of Geosciences (Beijing), Beijing
- Lofgren BE (1969) Land subsidence due to the application of water. *Rev Eng Geol* 2:271–303
- Lofgren BE (1978) Hydraulic stresses cause ground movement and fissures, Picacho, Arizona. *Geol Soc Am Abstra Programs* 10:113
- Minor HE (1925) Goose Creek oil field, Harris County, Texas. *AAPG Bull* 9:286–297

- Neal JT (1968) Playa surface morphology: miscellaneous investigations. Air force Cambridge research laboratories, environmental research Papers vol 238, p 150
- Pacheco-Martínez J, Hernandez-Marín M, Burbey TJ, Gonzalez-Cervantes N, Ortiz-Lozano JA, Zermeno-De-Leon ME, Solis-Pinto A (2013) Land subsidence and ground failure associated to groundwater exploitation in the Aguascalientes Valley. *México Eng Geol* 164(18):172–186
- Peng JB et al (2012) Earth crack disaster in Xi'an. Seismological Press, Beijing
- Peng JB, Qiao JW, Leng YQ, Wang FY, Xue SZ (2016) Distribution and mechanism of the ground fissures in Wei River Basin, the origin of the Silk Road. *Environ Earth Sci* 75(8):718
- Peng JB, Lu QZ, Huang QB (2017) Fenwei basin geosyncline disaster. Science Press, Beijing
- Peng JB, Wang FY, Cheng YX, Lu QZ (2018) Characteristics and mechanism of Sanyuan ground fissures in the WeiHe Basin, China. *Eng Geol* 247:48–57
- Peng JB, Sun XH, Lu QZ, Meng LC, He HQ, Qiao JW, Wang FY (2019) Characteristics and mechanisms for origin of earth fissures in Fenwei Basin, China. *Eng Geol* 266(3):105445
- Pratt WE, Johnson DW (1926) Local subsidence of the Goose Creek oil field. *J Geol* 34(9):557–590
- Schumann HH, Poland JF (1970) Land subsidence, earth fissures, and groundwater withdrawal in south central Arizona. *Tokyo Int Assoc Sci Hydrol Publ* 1:295–302
- Wang JM (2000) Theory and application of ground fissures and their hazards. Shaanxi Science and Technology Press, Xi'an
- Wang GY, You GG, Shi B, Wu SL, Wu JQ (2010) Large differential land subsidence and earth fissures in Jiangyin, China. *Environ Earth Sci* 61(5):1085–1093
- Wang GY, Xu MX, Gong XL (2019) Formation mechanism and warning of earth fissures in Suzhou-Wuxi-Changzhou area. *Jiangsu Technol Inf* 36(6):74–77
- Wang FY, Xun SZ, Peng JB, Huang QB, Lu QZ, Meng ZJ, Qiao JW, Liu Y, Jia Z, Zhao JY (2020) A study of the symbiotic relationship between tectonic fissures and faults in the Fenwei Graben System, China. *Environ Earth Sci* 70(10):212. <https://doi.org/10.1007/s12665-020-08966-9>
- Xia QF (1990) Forecast and control of geological hazard caused by exogenic process. *J Geol Hazard and Control* 1:27–32
- Xie GL (1988) Surface crack. Seismological Press, Beijing
- Yi XF (1984) A discussion on the ground subsidence and the genesis of ground fissure in Xi'an city. *Earthquake* 6:52–56
- Yi SM, Liang CS (2010) Geological disasters and prevention in Guangdong province. Science Press, Beijing
- Youssef AM, Sabtan AA, Maerz NH, Zabramawi YA (2014) Earth fissures in Wadi Najran, Kingdom of Saudi Arabia. *Nat Hazards* 71(3):2013–2027
- Zhang JM (1990) Research on ground fissure in Xi'an. Northwestern University Press, Xi'an

Chapter 5

Karst Collapse and Its Management



5.1 Introduction

Karst collapse refers to the phenomenon where caves in the soluble bedrock layer or soil voids in the overlying layer collapse or subside due to the enlargement of the cavities themselves or the combined effects of natural and human factors. It is a common dynamic geological hazard in karst areas. Karst collapse occurs primarily in carbonate rock distribution areas. The presence of numerous karst landforms, particularly the karst landforms that are shallowly buried and directly covered by loose Quaternary sediments, render the overlying layers unstable, resulting in downward subsidence. This type of geological hazard is widely observed in carbonate rock regions and is often characterized by sudden onset, rapid development, large scale, and severe consequences (De Waele et al. 2011). Consequently, it has attracted significant attention from researchers and professionals in the field of karst science and technology.

To better understand the concept and scope of karst collapse, Fig. 5.1 illustrates the interrelationships among the material conditions, triggering factors, forces, and collapse mechanisms involved. For karst collapse, the material conditions leading to collapse include the overlying layer, soluble bedrock, and their spatial relationships (referred to as karst geological structures). Some researchers consider water as one of the material conditions for collapse, but this is not appropriate, as water should be classified as a triggering factor. The overlying layer is the main component of collapse, and the movement of soil particles under external forces determines the collapse mechanism. The movement of soil particles is closely related to the lithology, particle composition, soil properties, and physical and mechanical characteristics of the overlying layer.

Karst processes refer to the geological processes in which water primarily chemically dissolves soluble bedrock, supplemented by mechanical processes such as erosion, subsurface erosion, and collapse caused by flowing water. It is a long-term and gradual geological process. During geological history, karst processes form a

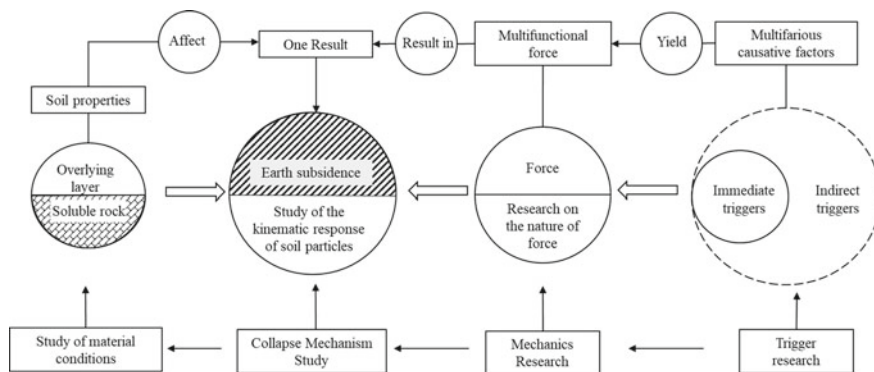


Fig. 5.1 Relationship among the material condition, inducement, force and mechanism of karst collapse

system of karst conduits or caves. Karst conduits provide pathways for the transfer of soil particles within the overlying layer, creating space for subsequent particle loss. Caves directly provide storage space for soil particle loss. Together, they provide natural conditions for karst collapse. Karst geological structures refer to the superposition relationships between different types of overlying layers and underlying soluble bedrock. Different karst geological structures have different collapse mechanisms and require correspondingly different methods for prediction, monitoring, and prevention.

The overlying soil above the soluble bedrock is formed through sedimentation and consolidation processes over geological history. After undergoing long-term geological processes during this period, most of the underlying soluble conduits are blocked. The soluble bedrock and its overlying layer have reached a state of mechanical equilibrium. Without external forces to disrupt this equilibrium, karst collapse phenomena should not occur, especially within the relatively short lifespan of engineering projects compared to geological history. Therefore, the forces generated by external triggering factors are the driving force behind karst collapse and are crucial sources of energy.

Karst collapse can be attributed to various factors, categorized as direct and indirect inducers based on their interaction with the soil. Direct inducers directly apply forces on the soil. For instance, during the process of groundwater seepage, the seepage exerts pressure on soil particles, inducing kinematic responses. This phenomenon is referred to as “groundwater seepage” and is considered a direct inducer. Other factors, such as overburden loads, construction loads, vehicular vibrations, and seismic loads, all directly exert forces on the soil, falling into the category of direct inducers. Indirect inducers, on the other hand, do not directly apply forces to the soil but rather indirectly induce external forces on the soil through various mechanisms. For example, “large-scale karst water emergence” does not directly apply force to the soil. Instead, it results in a rapid drop in water levels within enclosed karstic spaces, creating negative pressure, which, in turn, leads to the influence of

atmospheric pressure on the soil. In this case, “large-scale karst water emergence” is considered an indirect inducer. Other examples of indirect inducers include extensive drainage in karst mining areas and significant excavation of karst water during construction. Regardless of whether they are direct or indirect inducers, their role is to generate forces, either directly or indirectly, and apply them to the soil, potentially leading to ground collapse, although not necessarily causing it. The purpose of studying these inducing factors is to identify the sources of external forces acting on the soil, the processes involved in force generation, and the characteristics, magnitude, direction, location, and mode of action of these forces. This information serves as a foundation for researching the effects of external forces on karst collapse. The properties of forces generated by external inducing factors share similarities, but they also exhibit several differences. They can be equivalently classified based on their effects and subjected to detailed analysis, facilitating the development of a unified physical mechanics model. For instance, the vacuum load induced by large-scale underground water emergence, when acting on the surface of a cave roof, exerts a downward area load, which shares similar characteristics with the action of overburden loads on the cave roof. When constructing a physical mechanical model, it can be considered alongside overburden loads and subjected to force synthesis. However, the manifestation of vacuum loads differs for sandy soils, where it directly acts as pore pressure on fluid (groundwater). In this case, it takes the form of volumetric forces, equivalent to the groundwater head. These can be combined with the groundwater head, leading to the establishment of a unified hydromechanical model.

The study of soil subsidence mechanisms focuses on the kinematic response of soil particles to external forces, specifically investigating the behavior of soil particles during the process of soil failure. Different types of soil exhibit different kinematic responses when subjected to external forces. For example, cohesive soils, represented by clay, have high cohesion and close interparticle bonding, often forming “clay clusters”. Under external forces, these “clay clusters” move as a whole, or multiple clusters may be connected and undergo block movement, resulting in the collapse of the soil mass in a “block-by-block” manner. Loose soils, represented by fine sand, undergo particle-by-particle leakage under the combined action of gravity and groundwater. Weak soils, on the other hand, experience plastic flow under the influence of gravity and suction, flowing into karst cavities or conduits.

The kinematic response characteristics of cohesive soils, sandy soils, and weak soils in the collapse process determine three types of collapse mechanisms: soil cavity-type collapse, hourglass-type collapse, and mudflow-type collapse (Luo 2017). In summary, in karst areas with soil cover, karst cavities and conduits provide channels or storage space for the loss of soil particles. Various inducing factors (including direct and indirect factors) generate one or more types of forces that act on the soil individually or in combination, ultimately leading to the collapse of cohesive soil masses, particle leakage in sandy soils, or soil flow in weak soils, resulting in macroscopic deformation of the ground, namely, ground collapse. Therefore, in karst collapse, the main subject is not the inducing factors or the karst itself but the soil itself. The inducing factors and karst provide the forces and spatial conditions for soil collapse, respectively. Based on this, karst collapse can be defined as follows:

in karst areas with soil cover, the presence of karst cavities, conduits, etc., provides channels and storage space for the movement of soil particles. The forces generated directly or indirectly by external inducing factors lead to the collapse of cohesive soil clusters, particle leakage, or soil flow in weak soils, resulting in surface settlement and deformation. This definition highlights that the core of ground collapse is the collapse of the soil, not other factors, and that karst phenomena provide sufficient but not necessary conditions for soil collapse (as other underground spaces can also lead to similar soil collapse). The inducing factors provide the driving force required for collapse. This concept clarifies the relationship between the main subject, conditions, and forces involved in karst collapse, indicating the research focus and direction for studying karst collapse.

5.2 Types of Karst Collapse

Karst collapse is a natural consequence of karst processes, which result from the interaction of water, gas, and rock–soil formations. However, it is also an indication of the interference and disruption of the equilibrium state of the karst environment caused by human activities. With the increasing interference and disruption caused by human activities, the frequency and scale of modern subsidence have surpassed those of historical periods. A significant portion of recent collapse incidents can be attributed to human-induced factors.

5.2.1 *Classification of Karst Collapse*

To reflect that karst collapse is a dynamic geological phenomenon in karst regions, representing a stage in the development of karst processes and influenced by various forces, a classification system based on the dominant factors causing collapse and the main stress states is adopted here. This classification system allows for multilevel categorization, as well as further subdivision into subtypes and combination types (Kang 1984). Based on this approach, karst collapse can be divided into two major categories, seven subtypes, and eight basic types, as shown in Table 5.1.

5.2.1.1 Natural Collapse

Natural collapse refers to collapse that occurs under the combined influence of internal and external forces in natural conditions, typically unrelated to human economic activities.

Ancient Collapse. It is related to ancient karst in various regions and refers to the collapse formed by the subsidence of the overlying sedimentary layers on karstified formations during the period of ancient karstification. The collapse mass has been

Table 5.1 Classification of karst collapse

Categories	Subtypes	Basic types									
		Submerged erosion collapse	Gravity collapse	Suffosion collapse	Hydraulic blasting collapse	Vibration-induced collapse	Load-induced collapse	Root-induced collapse	Dissolution-induced collapse		
Natural collapse	1. Ancient collapse	<input type="checkbox"/>	<input type="checkbox"/>	<input type="checkbox"/>					<input type="checkbox"/>		
	2. Modern collapse	<input type="checkbox"/>	<input type="checkbox"/>	<input type="checkbox"/>	<input type="checkbox"/>		<input type="checkbox"/>		<input type="checkbox"/>		
Anthropogenic collapse	3. Mining-induced collapse	<input type="checkbox"/>	<input type="checkbox"/>	<input type="checkbox"/>							
	4. Water extraction-induced collapse	<input type="checkbox"/>	<input type="checkbox"/>				<input type="checkbox"/>				
	5. Reservoir filling and water release-induced collapse	<input type="checkbox"/>		<input type="checkbox"/>	<input type="checkbox"/>	<input type="checkbox"/>		<input type="checkbox"/>			
	6. Collapse caused by blasting vibrations and increased loads					<input type="checkbox"/>			<input type="checkbox"/>		
	7. Collapse caused by improper water accumulation or drainage	<input type="checkbox"/>	<input type="checkbox"/>							<input type="checkbox"/>	

compacted and cemented, and the collapse cavities are generally difficult to preserve. They are often filled, covered, or eroded by subsequent sedimentation. In terms of landforms, they are referred to as basin-shaped depressions or mound-like protrusions. Currently, there are few documented studies on this type of ancient collapse, and further subdivision and classification have yet to be established. However, its existence poses challenges to underground mining operations or water conservancy projects. In the North China region, specifically in the Ordovician limestone distribution area, the presence of exposed coalless columns and collapsed columns serves as evidence of ancient collapse.

Modern collapse. It refers to the collapse caused by the collapse of rock and soil along concealed dissolution cavities or soil cavities during the period of modern karstification, primarily due to natural fluctuations in precipitation and groundwater levels. The subsided mass in this type of collapse is not compacted or cemented and is often carried away by underground water flow. Surface sinkholes are generally well preserved, and some collapsed cavities develop into significant landforms of modern surface karst, such as swallow holes, shafts, funnels, depressions, and karst ponds. They can be further classified based on their stress conditions.

5.2.1.2 Anthropogenic Collapse

Anthropogenic collapse is the result of human economic and engineering activities that disrupt the stable equilibrium state of karst areas under natural conditions, accelerating the process of karstification and leading to collapse. They can be classified into five subcategories based on their impacts on karst collapse.

Mining-Induced Collapse. In karst areas, mining operations and tunnel engineering projects that involve deep dewatering or intense drainage to control groundwater or deal with underground water inrush can cause a significant drop in groundwater levels by tens to several hundred meters. This process gradually expands the cone of depression, which can extend to the confined or recharge boundaries, affecting an area several kilometers to tens of kilometers away. After dewatering, the groundwater level generally does not recover significantly, except for localized seasonal fluctuations due to rainfall or surface water recharge. The collapse that occurs in this situation is rapid, with numerous occurrences, large-scale effects, and a wide range of impacts, posing severe hazards. After the main collapse period, with proper management and remediation, the collapse will tend to stabilize, with only localized collapses or further development.

Water extraction-induced collapse. In karst areas, pumping groundwater or utilizing underground water for water supply can cause a general drop in water levels by several meters to twenty or even thirty meters, with an impact range of several hundred meters to one or two kilometers. Intermittent pumping or the rainy season can lead to groundwater level recovery. The collapse that occurs in this situation is often centered around wells, with small-scale effects and a limited impact range. However, due to the fluctuation of water levels, collapse occurs intermittently, making it difficult

to stabilize. Sometimes, collapse directly forms near pumping wells, posing a risk to well and pump safety.

Reservoir filling and water release-induced collapse. In karst areas, reservoir filling and water release in water conservancy projects can cause a rapid change in groundwater levels, with a variation range of generally more than twenty meters. The impoundment of reservoirs also significantly increases the load on the karst cover layer. The collapse that occurs as a result of this process has various types and is mainly distributed in the reservoir area, directly affecting reservoir operations and dam safety. At the same time, due to the impoundment of reservoirs, the remediation of collapse is often challenging.

Collapse caused by blasting vibrations and increased loads. In karst areas, blasting operations and vibrations from vehicles or machinery can potentially cause liquefaction of saturated sandy soils or damage the structure of rock and soil, resulting in collapse. When the increased load exceeds the allowable strength of the karst cover layer and underlying hidden cavities, it can cause the collapse of cave roofs or the development of soil cavities, leading to collapse. The collapse formed in such cases is generally not numerous and of small scale. However, it directly endangers the safety of buildings and roads, often resulting in significant economic losses.

Collapse caused by improper water accumulation or drainage. In covered karst areas, improper water management leading to water accumulation, as well as leakage and improper discharge in drainage routes, can potentially result in ground collapse. This type of collapse is typically localized and occurs in limited quantities. However, with the implementation of appropriate measures, it can be easily managed and mitigated.

5.2.2 Main Characteristics of Different Types of Karst Collapse

There is no fundamental distinction between the basic types of anthropogenic collapse and natural collapse in terms of their underlying causes and stress conditions. However, anthropogenic collapse often exhibits faster rates, larger scales, and more severe consequences compared to natural collapse. Although research on the formation mechanisms of various types of collapse is still limited, the following provides a general overview of their main conditions and characteristics.

5.2.2.1 Submerged Erosion Collapse

Submerged erosion collapse refers to the collapse caused by the erosion of underground water flow. In karst areas, as the groundwater level drops, the hydraulic gradient increases, resulting in increased hydraulic pressure and gradually increasing pore water pressure in the soil. When the hydraulic gradient reaches a value that

allows the migration of fine particles in karst fillings or soil layers, hidden erosion occurs, which we refer to as “pipe flow erosion” or piping. Initially, small voids form in the soil layer, gradually developing into soil cavities that expand from bottom to top, eventually leading to surface collapse. The hydraulic gradient value at which soil particles can migrate is called the critical hydraulic gradient, and the collapse resulting from it is called “pipe flow erosion collapse”. Pipe flow erosion collapse occurs when there is a sufficiently large hydraulic gradient and continuous water flow. At the contact between the soil layer and the top of the dissolution cave, although the water level has dropped below the soil layer, which no longer exhibits characteristics of underground water flow, the saturated soil layer still exerts significant pore water pressure. When this pore water pressure is large enough to cause soil erosion along the dissolution cave, soil cavities form, expand, and eventually lead to collapse. We refer to the phenomenon of soil erosion caused by this pore water pressure as “seepage erosion”. The resulting collapse is called “seepage erosion collapse”. Pipe flow erosion collapse and seepage erosion collapse are collectively referred to as hidden erosion collapse. Generally, multiple cycles of water level changes and hidden erosion occur before surface collapse occurs. The soil cavities that develop before collapse primarily occur in the zone of water level fluctuation and at the contact between the bedrock and the soil layer, often providing conditions for the occurrence of other types of collapse. Therefore, it can be said that hidden soil cavities are potential triggers for collapse in karst areas. The morphological characteristics of hidden erosion collapse typically exhibit a large bell-shaped cavity with a small entrance diameter, often less than one meter. Submerged erosion collapse is one of the main types of natural soil collapse in shallow-covered karst areas. Many instances of soil collapse in karst basins, peak-cluster valleys, and peak-forest plains belong to this type. In mining dewatering, hidden erosion collapse mainly occurs in low-lying areas and near rivers, especially where open dissolution caves are present. Submerged erosion collapse in pumping and water supply sources mainly occurs near wells. Submerged erosion collapse in water conservancy projects is directly related to the leakage caused by reservoir storage, ensuring a continuous water supply for the required pipe flow erosion. Additionally, due to the higher water level in reservoirs, a larger hydraulic gradient is generated, leading to a faster occurrence of hidden erosion collapse. This type of collapse often occurs in sections of improper drainage or water diversion projects where leakage occurs.

5.2.2.2 Gravity Collapse

Gravity collapse can occur in various karst areas. In shallow-covered karst regions, when a temporarily stable soil cavity becomes saturated again, the mechanical strength of the soil decreases. If the depressurization arch formed by the cavity cannot resist the overlying soil’s self-weight, the cavity will expand, and the soil layer will undergo intermittent stripping or instantaneous collapse from the bottom up, resulting in surface collapse. In the shallow karst development of bedrock mountainous areas, surface collapse occurs when the top rock mass of a dissolution cavity

suddenly collapses under its own weight due to the expansion of the cavity space. This type of collapse caused by the self-weight of the rock–soil mass is called gravity collapse. Accompanying the occurrence of gravity collapse, varying degrees of sound can often be heard, and the intensity of the sound is directly related to the size and height of the collapsed mass. The collapsed cavities formed by gravity collapse are generally steep, and their planar morphology is mainly determined by the shape of the lower dissolution or soil cavities. Gravity collapse in the soil layer sometimes exhibits a bell-shaped morphology with a small entrance and a large cavity. Gravity collapse is an important type of karst surface collapse. Many sinkholes, shafts, swallow holes, and depressions are formed through this stage of gravity collapse. Gravity collapse is also a major type of ancient collapse. In mining dewatering, it often occurs and appears in large quantities during the initial stage of dewatering, with a patchy distribution. Especially when there are large open dissolution caves below the soil layer, irregular and large-scale collapses can occur in the soil layer, accompanied by audible sounds. Gravity collapse is sometimes difficult to distinguish from hidden erosion collapse and can be collectively referred to as hidden erosion-gravity collapse.

5.2.2.3 Suffosion Collapse

Suffosion collapse refers to the collapse that occurs in relatively sealed karst voids under negative pressure. Negative pressure refers to a pressure lower than standard atmospheric pressure. The negative pressure state in karst voids can be generated under the following conditions: (1) The groundwater level in karst decreases from the Quaternary sedimentary layer to below the bedrock surface under the influence of gravity in groundwater flow. This results in the loss of water from previously water-filled karst voids. (2) High-velocity water flow in underground karst conduits creates a suction effect (water flow suction) on the connected karst voids. (3) Changes in groundwater flow velocity (alteration of cross-sections) can also lead to negative pressure states. In this negative pressure state, loose sediments and fractured rock masses first experience the bursting of “high-pressure” gas voids (pores) as they rupture toward the low-pressure space. This causes the gradual stripping of rock and soil layers, forming soil cavities (karst caves) or overall collapse. At the same time, the negative pressure state generates a suction force on the walls of the karst voids. When this suction force becomes excessive, it can cause the destruction of the rock and soil mass, leading to the enlargement of the karst voids (or soil cavities) and subsequent collapse. The magnitude of this suction force is directly proportional to the extent and rate of groundwater level decline, as well as the velocity and flow.

The ground collapse caused by the bursting of rock and soil masses under negative pressure and the collapse resulting from the “suffosion effect” in karst voids is referred to as suffosion collapse. Suffosion collapse occurs under specific conditions. The planar morphology of suffosion collapse is often circular, while the profile morphology is predominantly well-shaped or bowl-shaped. Audible sounds are sometimes associated with suffosion collapse.

Under natural conditions, a sudden drop in water level or the occurrence of high-velocity water flow in karst caves and conduits can lead to the formation of negative pressure conditions and subsequent suffosion collapse. Causes of suffosion collapse are commonly observed in features such as air-intake caves and vertical shafts. Instances of sudden water inflow or breakthrough accidents in karst mineral deposits, as well as deep drainage and dewatering operations, can also result in this type of suffosion collapse due to a significant and rapid decrease in groundwater levels.

5.2.2.4 Hydraulic Blasting Collapse

Hydraulic blasting collapse refers to the collapse that occurs when the groundwater level rapidly rises under natural or human-induced factors, leading to the formation of high-pressure gas pockets and significant hydrostatic pressure in well-sealed karst voids. When the pressure from these gas pockets and hydrostatic pressure exceeds the allowable strength of the roof of the karst void, it can cause the rupture of the overlying rock and soil mass, followed by ground collapse under the influence of gravity and water flow. This type of collapse, caused by the rupture resulting from high-pressure gas pockets and hydrostatic pressure, is referred to as hydraulic blasting collapse.

Accompanying hydraulic blasting collapse, there are often explosive sounds or whistling sounds caused by the discharge of water and gas. The morphology of the resulting sinkholes primarily depends on the characteristics of the underlying karst caves and conduits, as well as the thickness of the soil layer. In areas with a thick soil layer, circular pits are predominant. The surroundings of sinkholes are often covered with ejected solid materials such as mud and sand. This type of hydraulic blasting collapse is commonly observed in small- to medium-sized water conservancy projects in karst areas. Insufficient understanding of this phenomenon often leads to reservoir accidents or severe leakage issues.

5.2.2.5 Vibration-Induced Collapse

Vibration-induced collapse refers to the phenomenon in karst areas where saturated sandy soil experiences a reduction in effective stress between particles to zero due to actions such as blasting and mechanical vibrations. The shear strength of the sandy soil also decreases to zero, and a certain residual pore water pressure is generated, leading to liquefaction of the soil. When this liquefied soil is present with underground soil or dissolution cavities, it can cause the expansion of the soil cavity or induce subsurface erosion, resulting in ground collapse. Vibration can also cause structural damage to the rock and soil mass, reducing its mechanical strength and causing the collapse of the rock and soil mass along the underlying karst voids, leading to ground subsidence. Vibration-induced collapses caused by human activities have

limited influence and are characterized by small-scale collapses and low occurrence rates.

5.2.2.6 Load-Induced Collapse

Load-induced collapse refers to the collapse of the roof of an underlying dissolution cavity or soil cavity in karst areas when the additional load exceeds its allowable strength. This type of collapse is known as load-induced collapse. Load-induced collapses often occur on the basis of preexisting caves or cavities formed by other factors. They are typically localized in distribution, with a small number of sinkholes. However, they can cause significant economic losses due to the direct threat to the safety of buildings. Load-induced collapses are sometimes difficult to distinguish from gravity-induced collapses and can be referred to as gravity-load collapses.

5.2.2.7 Root-Induced Collapse

Root-induced collapse refers to the collapse that occurs in certain karst depressions or small- to medium-sized reservoirs when plant roots and stems are buried underground. When these organic materials decompose and form voids, they can connect with underlying karst voids or soil cavities, becoming pathways for groundwater flow and inducing subsurface erosion, ultimately resulting in collapse. This type of collapse is known as root-induced collapse.

5.2.2.8 Dissolution-Induced Collapse

There are two cases of dissolution-induced collapse. The first case involves the dissolution of evaporite rocks by water flow, forming voids. As these voids expand, they may not be able to withstand the weight of the overlying layers, resulting in subsidence and collapse. The second case involves the dissolution of soluble salt components in the overlying soil layer by acidic or alkaline wastewater, which alters the structure and properties of the soil. This leads to the formation of soil cavities and subsequent collapse. This type of collapse caused by the chemical dissolution of water flow is known as dissolution-induced collapse.

5.3 Mechanisms of Karst Collapse

The mechanisms underlying karst ground collapse are complex. Understanding these mechanisms is not only a theoretical issue but also crucial for implementing targeted prevention and control measures. Currently, there are various viewpoints regarding the mechanisms of karst collapse, among which the most representative ones include

the subsurface erosion theory, the vacuum suction erosion theory, and the “three mechanism” theory.

5.3.1 Subsurface Erosion Theory

The “subsurface erosion theory” of karst collapse was first proposed by Academician Bapulov of the Soviet Academy of Sciences in 1898. Its core concept suggests that karst collapse is formed by the subsurface erosion of groundwater and can be effectively managed through backfilling methods. According to this viewpoint, the continuous erosion and scouring of underground water flow on the fillings of dissolution cavities and overlying loose soil layers lead to the enlargement of voids within soluble rock formations and the formation of concealed soil cavities within the loose cover layer. As these soil cavities further develop, the overlying soil loses its stability and collapses. The process of subsurface erosion by groundwater involves both physical and chemical erosion. Physical erosion includes seepage erosion and scouring erosion, which occur during the movement of groundwater. Seepage erosion refers to the gradual dissolution and removal of soluble components in the rock or soil due to the flow of water through the pore spaces. Scouring erosion, on the other hand, involves the mechanical removal of particles from the rock or soil surfaces by the force of flowing water.

Physical erosion, also known as mechanical erosion, refers to all underground erosion phenomena primarily driven by various physical actions of water. It includes two main scenarios: (1) Seepage erosion that occurs in porous media under the influence of groundwater flow, where the main driving force is the hydraulic force. This concept of seepage erosion is widely accepted by most researchers. (2) Scouring erosion refers to erosion dominated by the dynamic scouring action of water carrying sediment, including underground conduit flow, cavity flow, pipe flow, cave flow, and even underground river flow. Here, the author collectively refers to these processes as scouring erosion, with the primary driving force being the scouring force of underground runoff.

Chemical erosion refers to all underground erosion phenomena primarily driven by various chemical actions. It involves the dissolution and filtration of water through rocks and soils, carrying away soluble salts and weakening the internal cohesion of rocks and soils, resulting in their loosening. This phenomenon often creates favorable conditions for mechanical erosion. Chemical erosion includes both chemical weathering erosion and chemical dissolution, with chemical dissolution being the dominant process. Chemical dissolution commonly occurs in soluble rock layers, and its concept is relatively well defined.

The occurrence and development of subsidence require certain conditions. First, the soil layer should have a structure and particle composition conducive to subsidence. Second, the groundwater flow velocity and hydraulic gradient in the soil layer need to reach a certain critical value. The latter is the dominant factor, while the

former is a necessary condition under certain hydraulic conditions. The subsidence mechanisms of different types of soils vary during the process of ground collapse.

5.3.2 *Vacuum Erosion Theory*

For a long time, research on the causes and prevention of karst collapse at home and abroad has been influenced and constrained by the “subsurface erosion theory” of groundwater. Xu and Zhao (1979) found that the subsurface erosion theory cannot explain all karst collapses, especially in cases where residual soil or clay with good impermeability or gravel layers are covered or filled at the top under natural conditions. These conditions generally do not meet the basic requirements for subsurface erosion-induced collapse. Therefore, the vacuum erosion theory for karst collapse was proposed. Vacuum erosion refers to the microscopic emptying and macroscopic deformation and destruction that occur inside and on the surface of karst vacuum cavities. The essence of this process is that the karst vacuum erodes the bottom soil of the overlying layer, forming cavities. When the vacuum accumulation inside the cavity reaches the critical value of destruction, the overlying layer loses equilibrium. The instantaneous vacuum pressure difference and the suction force of the water surface inside the cavity, known as the internal suction and external pressure effect, rapidly collapse the overlying layer, resulting in ground subsidence. This process is often accompanied by a loud noise generated when the vacuum is released.

Erosion suction occurs in a harmonious structural system under specific karst geological and hydrogeological conditions, which are as follows:

Karst network conditions. Karst areas generally have well-developed caves, fractures, and karst conduits, collectively referred to as karst cavities. Many karst cavities are interconnected in a spatial network structure known as the karst network. The openings of karst cavities are generally oriented toward the surface, while the lower parts of the cavities extend deep underground. The shallow spatial network structure forms the spatial field where karst vacuum formation and collapse occur.

Karst cover conditions. The surface or top of the karst network is covered or filled with residual clayey soil with good impermeability. Additionally, sediment deposition carried by overlying water flow further covers the karst network. These coverings are collectively referred to as the karst cover layer or “cover layer”, which seals the lower part of the karst network in a relatively closed state. This creates the necessary conditions for the formation of karst vacuum and the material conditions for collapse.

Groundwater conditions of the karst network. The middle or lower parts of the karst network cavities contain abundant confined or unconfined groundwater. When mining drainage or exploiting karst water, the groundwater is discharged under the influence of gravity. This provides the dynamic conditions for groundwater to descend and create a vacuum in the karst cavities.

Close connection between structures and karst network. The spatial structure of the karst network is primarily controlled by geological structures. Faults, fractured

zones, major fissures, etc., strictly define the conditions mentioned in (1) and (3) and serve as the link connecting the spatial structure of the karst network with deep mine water and water sources. Therefore, collapse phenomena regularly occur near faults, in the axial parts affected by faults, on the limbs of anticlines, at coal outcrops, at the boundaries of mineral deposits, as well as in spring groups, lakes, along riverbanks near groundwater outflows, and in low-lying areas with thinner Quaternary sediment layers.

The above four fundamental conditions constitute the specific geological and hydrogeological conditions for the development and formation of collapses in karst areas, collectively referred to as the karst vacuum geological environment. The force driving the erosion suction originates within the karst vacuum cavities rather than within the cover layer, as shown in Table 5.2.

5.3.3 Three-Mechanism Theory for Karst Collapse

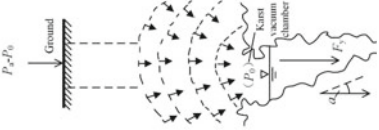
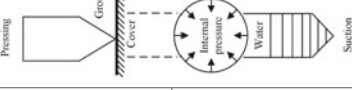
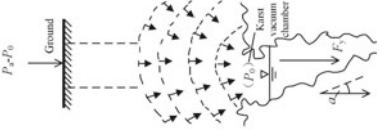
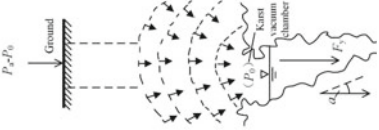
Luo (2017) proposed that research on collapses should include the study of collapsing soil, soluble rocks, and triggering factors. The essence of karst collapse lies in the collapse of soil. Therefore, research should focus on the composition of the soil, its physical and mechanical properties, the deformation process under external forces, and the kinematic response of soil particles or “clayey aggregates”. Based on the movement of soil particles during the collapse process, including block collapse of clayey aggregates, sand particle loss, and erosion of weak soil, a new theory called the “Three-Mechanism Theory (TMT)” for karst collapse was proposed. This theory consists of three collapse mechanisms: cavity collapse, hourglass collapse, and mudflow collapse (Luo and Luo 2021).

5.3.3.1 Cavity Collapse Mechanism

In cohesive and dense sandy soils, various-sized cavities may exist due to geological processes, human activities, or biological activities. This is because in such soil layers, small clay particles and compacted sand particles do not have the same degree of freedom as loose sandy soils to freely displace under the influence of gravity, resulting in the formation of an arch effect at the top of the cavity. When the arch effect is present, the cavity remains stable. However, for various reasons, such as continuous enlargement of the cavity diameter, reduction in the thickness of the cavity roof, external loading, and structural damage to the cavity roof soil, the arch effect may fail, leading to collapse and, in severe cases, ground subsidence.

The ground collapse phenomenon that occurs in cohesive and dense sandy soil layers due to the failure of the arch effect at the top of cavities is referred to as cavity collapse. In areas where the overlying layer consists of cohesive soil on soluble rocks, the process of cavity collapse can be divided into two stages: cavity formation and evolution and ground collapse. The formation and evolution of cavities is a gradual

Table 5.2 Analysis of the effect of various forces on the collapse mechanism induced by vacuum corrosion

Force	Force effect	Illustration of the location of the force	The basic principle of force	The mode of action of the force
Press pressure ($P_a - P_0$)	1. Stamping shaping-macroscopic shaping action applied from the surface of karst cover; 2. Self-sealing action, whereby the shaped body is self-sealed on the karst vacuum cavity opening or at a certain depth		The force is instantaneous and conforms to the principle of impulse; The greater the vacuum pressure difference, the thinner the cover layer, the faster the press molding; The steeper the wall, the rounder the opening	
Volume-expanding forces (P_0)	Microscopic physico-mechanical suction hollowing damage within karst cover-microscopic suction volume expansion		Rapid or slow equivalent expansion of the action force, resulting in a spherical space body inside the cover layer to the surrounding expansion, in line with the principle of gas pressure conduction; The higher the vacuum in the cavity, the stronger the expansion effect	The gravitational drop of groundwater draws a vacuum—instantaneous pumping—in accordance with the principle of gravity; The higher the gravity of the water, the stronger the pumping effect and the higher the vacuum level
Suction force (F_y)	Applying suction to the soil at the bottom of the cap below the bottom surface of the karst cap to make it bubble down and accelerate the microexpansion-macroformation-macroabsorption action, the internal dynamics of karst vacuum formation		The higher the vacuum in the cavity, the stronger the expansion effect	The gravitational drop of groundwater draws a vacuum—instantaneous pumping—in accordance with the principle of gravity; The higher the gravity of the water, the stronger the pumping effect and the higher the vacuum level

process that takes a considerable amount of time. The cavity collapse stage is a sudden occurrence of ground collapse triggered by external factors and is relatively short-lived. The characteristics of cavity collapse are as follows: (1) Due to karst providing pathways and storage space for cavity formation and evolution, cavities are often closely related to karst features. The development of karst voids and caves, including their locations and sizes, is random, resulting in the spatial distribution of cavities also being random. (2) The ground is typically stable during the natural formation and evolution of cavities, making them often concealed and not easily discovered by people, thus possessing a high degree of concealment. (3) The ground collapse triggered by cavities is a result of the failure of the arch effect at the top of the cavities. When the arch effect fails, ground collapse occurs suddenly, exhibiting an abrupt nature. The randomness, concealment, and suddenness of cavity collapse often pose significant hazards.

Cavity collapse can be summarized by the following geological processes: (1) Initial formation of the cavity: The collapse of the cavity roof soil occurs, and the cavity gradually develops and increases in size while the thickness of the cavity roof decreases. (2) Accumulation or preservation of collapsed soil: The collapsed soil accumulates at the bottom of the cavity, either preserved or transported into dissolution cavities by groundwater. The cavity expands and migrates upwards, while the cavity roof remains in equilibrium due to the upward frictional forces exerted by the surrounding soil. (3) Triggering factors and further thinning of the cavity roof: External factors induce the failure of the frictional forces around the cavity roof or the continued thinning of the cavity roof. As a result, the cavity roof rapidly collapses into the cavity, and the collapsed soil accumulates within the cavity, eventually forming a collapse sinkhole. (4) Formation of the collapse surface: After the collapse forms an open cavity, the walls of the sinkhole slide or collapse toward the center, causing ground tilting and the formation of ring-shaped ground fissures.

5.3.3.2 Hourglass-Type Collapse Mechanism

The hourglass shape serves as a physical model for loose sand collapse. In natural environments, there are often thick layers of loose sandy soil, beneath which there exist numerous and large cavities, such as karst voids and caves in karst areas or defective shield tunnels. Under the influence of external factors, sand particles will leak downward through channels, resulting in ground settlement and deformation. This type of ground collapse caused by the leakage of sand particles is referred to as hourglass-type collapse. Its fundamental characteristics are as follows: (1) Gravity is a necessary condition for the occurrence of hourglass-type collapse. Even without the presence of groundwater, collapse can still occur. The involvement of groundwater accelerates the collapse rate and shortens the collapse duration. (2) Hourglass-type collapse requires channels and storage space for the leakage of sand particles. This is another essential condition for collapse to occur. Without these conditions, collapse will not occur. (3) External factors are necessary to trigger hourglass-type ground collapse. (4) Hourglass-type collapse is caused by the loss of sand particles and does

not result in the formation of cavities in the overburden. Therefore, it is not caused by the failure of arching effects. (5) The collapse process is continuous until the conditions for collapse are no longer present.

In covered karst areas, when the covering layer consists of loose sandy soil, dissolution fissures and sinkholes provide channels for the leakage of sand particles, while various-sized caves and underground river systems serve as storage spaces for these particles. It is similar to a gigantic natural hourglass, where under the influence of external factors, sand particles gradually leak, causing surface deformations. As the amount of sand particle loss increases, larger-scale sinkholes gradually form on the surface, resulting in karst collapse.

5.3.3.3 Mudflow-Type Collapse Mechanism

Soft soil has a high water content, large porosity, and low dry density and exhibits a soft-plastic to fluid-plastic state with low shear strength. As a result, it possesses strong thixotropic and rheological properties. In areas where the upper layer consists of soft soil and the lower layer is karstified, under the influence of external factors, when the dissolution fissures and karst funnels in the underlying karst region are unobstructed, the soft soil can undergo flow deformation along these channels, gradually causing surface deformations. As the deformation of the soft soil increases, macroscale sinkholes form on the surface. This type of ground collapse, caused by the loss of soft soil, is referred to as mudflow-type ground collapse.

The development of cohesive soil occurs between the soft soil and soluble rock. Human activities, such as drilling and pile foundation construction, can penetrate the middle cohesive soil layer, creating a connection between the upper soft soil and the lower soluble rock's karstic voids. This can also lead to mudflow-type karst collapse.

Due to the low shear strength of the soft soil, with a generally cohesive strength of 3–8 kPa and an angle of internal friction less than 8° , the resulting sinkholes are shallow in depth but have a large impact area. The slope angle of these sinkholes is minimal. Therefore, mudflow-type collapses often form saucer-shaped sinkholes.

5.4 Influencing Factors of Karst Collapse

Karst collapse occurs in carbonate rock distribution areas due to the presence of karst voids in the geological strata. Under certain conditions, the overlying rock and soil mass migrates downward toward the underlying karst voids due to the effects of water and gas. However, human activities altering natural conditions are the primary causes and triggering factors for recent large-scale collapses. Therefore, the formation of karst collapse is influenced by both environmental factors and human activities (Parise and Gunn 2007).

5.4.1 Fundamental Conditions for the Formation of Karst Collapse

The formation of karst collapse requires three fundamental conditions: karst cavities, a certain thickness of overlying strata, and groundwater activity. These can be referred to as the three essential elements for karst collapse formation, as shown in Fig. 5.2. The presence of karst cavities serves as the foundation for collapse occurrence, while loose and fragmented overlying strata constitute the main components of the subsided mass. Groundwater activity plays a crucial role as the primary driving force behind collapse generation (Kang 1988).

5.4.1.1 Foundation of Karst Collapse Formation

The presence of karst cavities serves as the foundation for collapse formation, providing a place for the subsided material to accommodate and space for its migration.

Most karst cavities were formed during long geological periods in the past. Only in areas with easily soluble rocks such as gypsum and salt formations can intense dissolution processes resulting from human economic and engineering activities such as reservoir construction, mining development, and transportation development promote the development of new karst and provide necessary spatial conditions for karst collapse. The distribution and development of karst cavities are controlled by the conditions for karst development. They are typically found along fault zones, fold axes, relatively soluble lithological sections, or areas in contact with insoluble rocks. In these areas, surface karst development often forms negative landforms in karst regions, such as sinkholes, valleys, troughs, karst plains, and lower river terraces. Moreover, karst cavities mainly develop in the shallow part of the subsurface, and their development weakens rapidly with increasing depth. Shallow karst cavities, due to frequent and intense groundwater activity, generally have good connectivity,

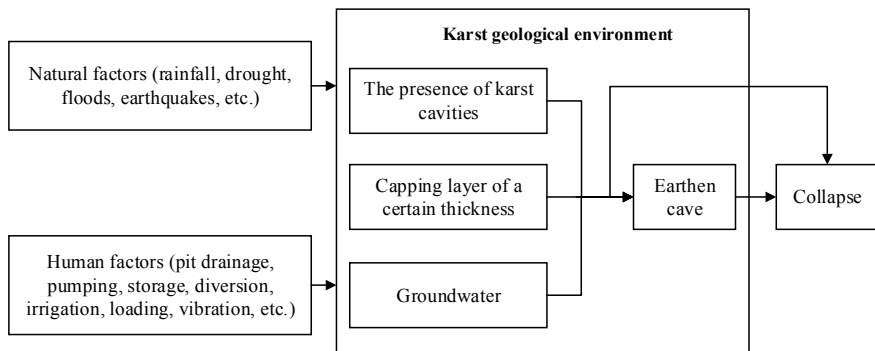


Fig. 5.2 Block diagram showing the formation conditions of karst collapse

forming intricate and complex networks of underground cavities. These characteristics of karst cavities not only provide necessary storage space and migration pathways for subsided material but also control the distribution of karst collapse, leading to its predominant occurrence in areas with intense karst development. Furthermore, due to the heterogeneity of karst development, subsidence exhibits characteristics of zonal, sporadic, and areal distributions.

The degree of opening of karst cavities is an important factor in collapse generation. Upward-opening dissolution fractures and caves serve as gateways and windows for subsided material. Cavities without upward openings generally do not cause ground collapse. Abundant empirical data confirm a clear vertical correspondence between sinkholes and caves, with larger caves often leading to major collapses, smaller caves resulting in minor collapses, and fissure-like caves leading to elongated collapses. The degree of karst development in soluble rock formations affects the scale and intensity of karst collapse. Areas with strong karst development experience a greater number and higher intensity of collapse, while areas with weaker karst development exhibit smaller-scale collapse.

5.4.1.2 Main Components of Subsided Mass

Unconsolidated and fragmented overlying strata are the main components of the subsided mass, with most collapses consisting of soil layers. The material of the karst subsided mass can be various types of soluble or nonsoluble rocks, as well as loose Quaternary sediments. The bedrock mainly constitutes the subsided mass due to tectonic and weathering dissolution processes, making the rock layers become fragmented and weak. When the block size is relatively small compared to the cave opening, collapses are often directly caused by the collapse of cave roofs or conduits under the influence of gravity. This type of collapse is known as bedrock collapse, and it is prevalent in the karst collapse columns in northern China. Loose Quaternary sediments are the main components of reported collapses, resulting in soil collapse. Statistics from southern China show that soil collapse accounts for 97% of the total collapses. Loose sediments can consist of sand, gravel, rubble, and clay, forming different types, such as homogeneous structures, double-layer structures, or multilayer structures.

In karst regions, the prevalent soils often consist of homogeneous clay or clay with gravel deposits due to residual accumulation from dissolution processes. Along a typical vertical profile, the clay's moisture content gradually increases from top to bottom. The soil transitions from a firm vertical state to a progressively softer, plastic, and ultimately flowing state. This type of soft soil is prone to erosion during groundwater activity, leading to the early formation of soil cavities on the bedrock surface. In areas with limestone formations, weathered limestone residues, typically ranging from a few centimeters to several millimeters thick, are frequently found on the bedrock surface. These residues are susceptible to removal during groundwater activity, contributing to the creation of cavities at the rock–soil interface, thus providing conditions conducive to subsidence. In regions covered by clayey soils in

karst areas, the development of soil cavities is common. Soil cavities are primarily distributed in two areas: near the rock–soil interface and within the seasonal groundwater level fluctuation zone. When soil layers are relatively thin and the groundwater table is shallow, these two zones often overlap, making soil cavity development more likely. Soil cavities underground typically take the form of spherical or semispherical voids with diameters ranging from tens of centimeters to several meters, with diameters less than one meter being the most common. These soil cavities can remain concealed underground for several months to several years, gradually expanding until surface collapse occurs. Occasionally, the time interval between the formation of soil cavities and the appearance of surface collapse is very short, ranging from a few hours to several minutes. Generally, soil collapse undergoes a process from dissolution cavities to soil cavities and finally to surface collapse. Therefore, it can be said that soil cavities represent latent collapse hazards.

The lithological structure of the soil layer has a significant influence on the formation of collapse. Under the same conditions, homogeneous sandy soil is prone to collapse, followed by layered heterogeneous soil with sand and gravel. The collapse of homogeneous clay soil occurs relatively more slowly, and newly formed clay in cohesive soil is more prone to collapse than older clay. In areas with a dual-layer or multilayer distribution of cohesive soil at the bottom, the occurrence of collapse is much less common. It should be noted that in karst areas covered by loose soil layers, there are significant differences in the water characteristics, hydraulic properties, and permeability between the upper porous aquifer and the lower karst aquifer with fissures. When the water level decreases, the upper porous aquifer lags behind in dewatering compared to the lower karst aquifer. In the areas where fissures are distributed in the porous aquifer, concentrated leakage points are formed, leading to the formation of sinking centers along these leakage points. This increases the permeation pressure in the soil layer and promotes the development of hidden erosion, facilitating the formation of soil cavities.

5.4.1.3 Main Driving Forces Behind Collapse Formation

Groundwater activity is the primary driving force behind collapse formation. Changes in groundwater level, flow velocity, and discharge will exert various mechanical effects and actions on the soil layer's pore space, leading to the failure of the rock and soil mass and resulting in collapse.

Groundwater is the most active and influential factor in the formation of karst collapse. Fluctuations in groundwater level and lateral flow activities not only change the bulk density and state of the soil mass due to variations in water content, but also generate pore pressure through seepage flow, inducing hidden erosion and the migration of soil particles or masses, leading to piping or soil flow phenomena (Lei et al. 2023). Fluctuations in groundwater level can also alter the buoyant force acting on the soil mass below the groundwater level, causing gas in relatively sealed karst cavities to experience upward pressure (positive pressure) or form negative pressure cavities, resulting in hydraulic burst or suction erosion and causing damage to the

rock and soil mass. In addition to its dissolution effect and its role as a crucial factor in the development of karst cavities, groundwater itself possesses erosion and transport capabilities, which further alter the size and shape of the karst space. It can also relocate fill materials within the cavities from one place to another, reopening filled cavities or blocking them with fill material, thus changing the flow dynamics of groundwater.

The effects of groundwater can lead to various mechanical phenomena in the rock and soil mass, including the loss of buoyancy and increased load effect, seepage erosion effect, negative pressure suction effect, hydraulic burst effect, thixotropic liquefaction effect, dissolution effect, and fluctuation dissolution effect. These effects can cause damage to the rock and soil mass, resulting in the formation of soil cavities (karst cavities) or directly leading to collapse (Lei et al. 2016).

Although groundwater activity is widespread in karst areas, it is most intense and concentrated in the preferential flow zones. These zones are the primary contributors to collapse formation and the concentrated distribution of collapses. They include the main flow or discharge zones of karst groundwater, areas where the groundwater table is shallow or fluctuates near the bedrock surface, areas within the range of sinkhole funnels, and zones with rapid changes in groundwater level.

In its natural state, groundwater activity is typically influenced by rainfall, drought, or interannual climate variations, with relatively small fluctuations in water level and changes in flow velocity and discharge. However, in human-induced economic and engineering activities such as groundwater pumping, mine dewatering, and reservoir impoundment, the changes in groundwater level, flow velocity, and discharge can be severe and rapid. Consequently, the effects and mechanical phenomena caused by groundwater are more intense in these cases. Therefore, it is known that most collapses are caused by human factors. Large-scale collapses with significant impact and extensive coverage are often attributed to mine dewatering and water extraction for water supply sources.

5.4.2 Factors Inducing Karst Collapse

In addition to the three fundamental conditions mentioned above, various natural or human-induced factors can influence or induce the occurrence of karst collapses. These factors include topographic conditions, precipitation and water storage, drought and pumping, earthquakes and vibrations, loads and gravity, and the dissolution of acidic or alkaline solutions.

5.4.2.1 Terrain Conditions

Certain topographic features reflect the combination of specific lithological and structural conditions. Depressions, valleys, basins, and river valleys in karst areas often correspond to locations with developed structural fractures or relatively soluble

lithology. These areas exhibit well-developed karst features and often serve as convergence points for water or as flow or discharge zones for groundwater, making them highly conducive to karst collapse formation. Currently, most collapses are distributed in such karst-negative landforms, especially in low-lying areas within these landforms.

5.4.2.2 Rainfall and Water Storage

Rainfall and water storage (including surface water infiltration) are the primary sources of groundwater recharge and significant factors causing groundwater activity. They increase the bulk density and decrease the strength of the saturated or partially saturated rock and soil mass. They generate seepage flow, promote the development of seepage erosion, cause water levels to rise, create positive pressure within karst cavities, and increase the static water pressure and load on reservoirs, all of which contribute to the occurrence of collapses. Among these factors, rainfall has a particularly significant impact on collapses. Many areas experience a higher frequency of collapses during the rainy season or periods with increased rainfall, especially after prolonged droughts followed by heavy rainfall.

5.4.2.3 Drought and Artificial Pumping and Drainage

Climate drought and human activities such as groundwater pumping and mine dewatering are the main factors causing a decline in groundwater levels. Natural droughts occur interannually, with generally slow water level changes and small fluctuations. However, human-induced changes in groundwater levels can reach tens to hundreds of meters, particularly in underground engineering projects where sudden karst water inrushes can result in a rapid and substantial drop in groundwater levels. This has a significant impact on karst voids, causing the rock and soil mass to lose buoyancy, increasing the permeation pressure of groundwater, and inducing seepage erosion or hydraulic impact. In well-sealed areas, vacuum negative pressure can occur, leading to negative pressure erosion and resulting in the liquefaction of covering soil layers or filling materials in caves. This ultimately damages the structure of the rock and soil mass, facilitating collapse. Drought often leads to surface soil cracking and a decrease in soil strength. Natural droughts frequently trigger collapses in karst valleys and depressions.

5.4.2.4 Earthquakes and Vibrations

Both earthquakes and human-induced vibrations exert a dynamic force on rock and soil masses through the generation of vibration waves, causing various destructive effects. These effects include the rupture of fault earthquake fissures, deformation and damage to slopes, consolidation settlement of soil, vibration-induced liquefaction,

and plastic deformation. Consequently, rock and soil masses are damaged, and in areas with distributed caves, this often leads to surface collapses. Clearly, the destructive force of earthquakes is much greater than that caused by artificial blasting or mechanical vehicle vibrations.

5.4.2.5 Gravity and Load

Gravity is an inherent force within rock and soil masses, while load is an external force applied to them. Both forces act on the cave or soil roof in a static manner, leading to their destruction and subsequent collapse. Gravity is a force that operates throughout the entire process of collapse formation. During the expansion of caves or soil voids, gravity can induce collapses. The additional force generated by the load is related to the weight of the loaded object. Through stress transfer, it can cause collapses by penetrating the cave or soil roof. Most natural collapses in bedrock formations are caused by the force of gravity. Collapses induced by loads are often associated with modern economic development.

5.4.2.6 Dissolution by Acidic and Alkaline Liquids

In modern human economic and engineering activities, the discharge of waste acidic and alkaline liquids is increasing. These liquids have a strong corrosive effect on the rock and soil masses in karst areas. They can dissolve a large number of soluble substances, alter the structure of the rock and soil mass, reduce its strength, create soil voids, and ultimately lead to collapse.

In conclusion, the formation of karst collapses is the result of the combined influence of multiple factors. In-depth research into the formation conditions of collapses will contribute to a better understanding of their mechanisms and provide a scientific basis for their prediction and prevention. Apart from the three basic conditions required for their formation, various natural and human-induced factors can induce or contribute to collapses. These factors interact and constrain each other during the process of collapse formation, shaping the conditions for karst collapses.

5.5 Prediction of Karst Collapse

The prediction of karst collapse involves assessing the stability of the overlying layers in soluble rock areas based on the engineering and hydrogeological conditions of the karst region. By considering potential external influencing factors and employing appropriate prediction methods, the occurrence time, location, and likelihood of karst collapse can be determined. This provides a basis for assessing the hazard potential of karst collapse and offers technical guidance for disaster prevention and mitigation. The evaluation of karst collapse involves assessing the degree of threat to

the surrounding population and the extent of damage to the surrounding environment based on the results of karst collapse prediction. This assessment serves as a basis for decision-making regarding the prevention, control, and risk management of karst collapse (Papadopoulou-Vrynioti et al. 2013).

The prediction methods for karst collapse can be broadly categorized into two main types: geological methods and mathematical-physical methods, which include comprehensive geological prediction models and mathematical-physical prediction models, respectively. Comprehensive geological prediction models are established based on the fundamental principles of geology and the mechanisms of karst collapse. These models utilize geological theories and employ geological scientific methods and techniques guided by an understanding of collapse mechanisms. These prediction models have a solid geological theoretical foundation and consider a comprehensive range of inducing factors (with irrelevant factors eliminated based on geological conditions). The conclusions drawn from these models are relatively objective and reliable, making them the only prediction methods currently applicable in engineering practice. They fall under qualitative prediction. On the other hand, mathematical-physical prediction models are based on fundamental geological theories and utilize the characteristics of geological formations. After analyzing various influencing factors, deterministic and probabilistic prediction models are established. These models employ mathematical and/or physical methods and techniques to quantitatively or semi-quantitatively predict karst collapse. Although mathematical-physical methods exhibit logical rigor, the complex and variable nature of geological conditions makes it challenging to capture the intricate geological evolutions and features at microscopic and macroscopic levels. Consequently, it is difficult to establish mathematical-physical models for karst collapse that fully align with geological formations, leading to limitations in the predictive results.

5.5.1 Comprehensive Geological Model

Karst collapse is a geological hazard, and comprehensive geological prediction is the preferred method. Therefore, Luo (2017) proposed a geological model prediction method. The core idea is to investigate the engineering geological and hydrogeological conditions of the study area, delineate the karst geological structures and their spatial distribution, assess the degree of karst development, identify collapse-inducing factors, define the regions for each type of karst collapse based on the collapse mechanism, and predict the likelihood of corresponding types of ground collapse in each region. The prediction consists of the following five steps.

5.5.1.1 Determining the Karst Collapse Mechanism

Before conducting comprehensive geological prediction of karst collapse, it is necessary to investigate the engineering and hydrogeological conditions of the study

area, delineate the karst geological structures, clarify the spatial distribution of various collapse mechanisms in the study area, and, if necessary, divide the collapse mechanism types into different zones.

The basis for dividing collapse mechanism types into zones is the karst geological structure. Based on the superposition relationship between sandy soil, clayey soil, and weak soil above soluble rock, the karst geological structure is divided into three categories and nine types (Table 5.3).

Table 5.3 provides a comprehensive compilation of various potential geological structure types. In a specific study area, only a subset of these karst geological structure types may exist. Before dividing the zones based on collapse mechanism types, it is necessary to first delineate the karst geological structures of the study area and determine the potential soil collapse mechanisms based on regional geology, engineering surveys, and ground investigations, following the approach outlined in Table 5.4.

Within the same geomorphic unit, cover layers of the same origin generally exhibit similar geological structures. Therefore, the zoning of collapse mechanism types can often be combined with local topography and geomorphology. The zoning of collapse mechanism types can be initially divided into three regions based on the geological structure of the study area: funnel-type collapse zone, soil cavity-type collapse zone, and mudflow-type collapse zone. If necessary, further subdivision into potential subregions can be based on the geological structure type, allowing for more detailed zoning and stronger guidance in predictive results.

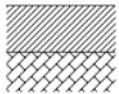
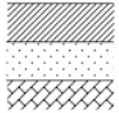
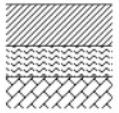
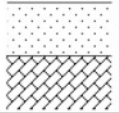
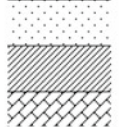
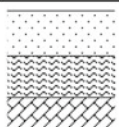
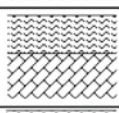
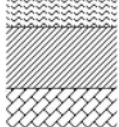
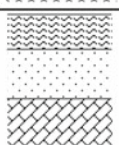
5.5.1.2 Assessing the Degree of Karst Development

In soil collapse, karst plays a role in providing storage space or pathways for the collapse of soil particles. It is the result of karst processes rather than the processes themselves. Therefore, prior to conducting comprehensive geological prediction, it is necessary to determine the characteristics of the local stratigraphy, lithology, and geological structures, as well as their controlling effect on the degree of karst development and the spatial distribution patterns of karst. In areas with covered karst, the borehole encountering cavity rate and the linear karst rate are important parameters for reflecting the degree of karst development. The borehole encountering cavity rate represents the percentage of boreholes that encounter cavities out of the total number of boreholes drilled in soluble rock. The linear karst rate represents the percentage of borehole cavity length relative to the total length of boreholes drilled in soluble rock. The linear karst rate provides a relatively good reflection of the degree of karst development.

5.5.1.3 Identifying Triggers

There are many triggering factors for collapse, which can be broadly categorized into three types: water action, external loads, and soil weakening. In a specific area, not all

Table 5.3 Karst geological structure types and characteristics of ground collapse in the covered karst area

Class	Subclass	Model diagram	Structural characteristics and collapse mechanism	The main predisposing factor
I	I ₁		Clayey soil in the upper part and soluble rock in the lower part. Soil-hole type of collapse can occur.	Applied loads, weakening of the roof of the soil cavity.
	I ₂		Upper part is clayey soil. Sandy soil (thickness > 3 m) in the middle and soluble rock in the lower part. Soil-hole type collapse can occur.	Applied loads, weakening of the roof of the earth cavern and groundwater activity.
	I ₃		The upper part is clayey soil, the middle part is weak soil (thickness > 3 m), and the lower part is soluble rock. Soil-hole type collapse can occur.	Applied loads, weakening of the roof of the soil cavity.
II	II ₁		Sandy soil in the upper part and soluble rock in the lower part. Hourglass-type collapse occurred.	Groundwater activities, such as large-scale pumping, karst outbursts, etc., plus dynamic loads.
	II ₂		The upper part is sandy soil, the middle part is clayey soil (thickness > 3 m), and the lower part is soluble rock. Hourglass-type collapse can occur when the clayey soil is damaged.	Destruction of the integrity of clayey soil layers and groundwater activities by human activities.
	II ₃		The upper part is sandy soil, the middle part is weak soil (thickness > 3 m), and the lower part is soluble rock. Mudflow-hourglass type compound collapse can occur.	Applied dynamic load.
III	III ₁		Weak soil in the upper part and soluble rock in the lower part. Mudflow-type collapse can occur.	External dynamic loads, negative pressure loads.
	III ₂		The upper part is weak soil, the middle part is clayey soil (thickness > 3 m), and the lower part is soluble rock. Mudflow-type collapse can occur when the clayey soil is damaged.	Destruction of the central clay layer by human activities and imposed dynamic loads.
	III ₃		The upper part is weak soil, the middle part is sandy soil (thickness > 3 m), and the lower part is soluble rock. Compound collapse of hourglass-mudflow can occur.	Groundwater activity and applied dynamic loads.

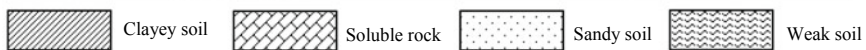


Table 5.4 Relation between TMT and karst geological structure types and triggering factors in the covered karst areas

Collapse mechanism	Karst geologic structure	Main predisposing factors
Cavity collapse	I ₁ , I ₂ , I ₃	Imposed loads, weakening of soil cavity roof resistance, groundwater activity
Hourglass-type collapse	II ₁ , II ₂ , III ₃	Groundwater activities (e.g., large-scale pumping, karst outbursts, etc.), applied dynamic loads, and human activities that disrupt the integrity of clayey soil layers
Mudflow-type collapse	III ₁ , III ₂ , II ₃	Imposed dynamic loads, groundwater activity, and anthropogenic damage to central clayey soil layers

triggering factors necessarily coexist. In most cases, one primary triggering factor or a combination of several factors plays a key role. Prior to conducting comprehensive prediction, it is important to understand and determine the main triggering factors in the local area. Based on the impact of these triggering factors on the three types of collapse mechanisms and considering the actual conditions of karst collapse in the area, the likelihood of collapse occurrence and the areas where different causes may appear can be assessed.

5.5.1.4 Comprehensive Geological Prediction

Comprehensive geological prediction of karst collapse involves assessing the susceptibility zones based on collapse mechanisms, degree of karst development, and main triggering factors.

Before delineating susceptibility zones, it is necessary to determine the susceptibility levels. If the susceptibility is divided into too many levels, it reduces practicality and increases the difficulty of the work, making it challenging to achieve high precision. In contrast, inadequate levels result in limitations in guiding prevention and control measures. Generally, the susceptibility of karst collapse is divided into three levels: high, medium, and low susceptibility zones.

5.5.1.5 Collapse Hazard Assessment

Based on susceptibility zoning, combined with the degree of impact on engineering facilities and human activities, the collapse hazard levels are determined to provide a basis for collapse disaster prevention and control.

The hazard levels can be divided into three categories: high, medium, and low. High hazard zones are designated for areas with high susceptibility that are densely populated, with significant infrastructure, and where the consequences of collapse would be severe. Low hazard zones are designated for areas in the outskirts, far from

urban areas, where there is no threat to human habitation, such as open agricultural fields. Other areas with a significant impact on engineering facilities and human activities are classified as medium hazard zones.

5.5.2 *Mathematical and Physical Prediction Models*

5.5.2.1 **Deterministic Model Prediction**

Regardless of the factors leading to karst collapse, it ultimately results from the action of forces. In other words, external factors provide forces to karst collapse in different ways. Therefore, all karst collapses can be generalized into their physical–mechanical models (Luo and Luo 2016). The basic idea of deterministic model prediction is as follows: conduct research and analysis on the geological conditions of the study area, apply the TMT to determine the karst collapse mechanism based on the karst geological structure; study the potential influencing factors and the forces they generate; determine the types of forces and classify them according to their attributes; generalize the physical–mechanical model and analyze the forces acting on it; establish equilibrium equations using appropriate mechanical theories based on certain boundary condition assumptions; and deduce general mathematical expressions. The specific methods are as follows:

Conduct geological analysis to determine the collapse mechanism. Collect relevant data on various karst collapses that have occurred, including engineering geology, hydrogeological data, information on the collapse process, ground deformation, and building damage. The state and physical–mechanical properties of the soil layers are determined, and the karst geological structure is identified. Based on the TMT, the types of collapse mechanisms (soil cavity collapse, hourglass collapse, and mudflow collapse) were determined.

Conduct causative analysis to determine the attributes and types of collapse forces. Various historical and ongoing karst collapses are studied, various influencing factors are identified, the forces that various causes may generate are determined, and the nature of these forces is analyzed and classified.

Conduct mechanical analysis to determine the physical–mechanical model of collapse. Based on the determined collapse mechanism and considering the types of forces, a representative physical–mechanical model is generalized by making appropriate boundary condition assumptions. For example, for the roof of a soil cavity, although it is composed of loose soil particles, when establishing the physical–mechanical model of soil cavity collapse, it is generally idealized as a rigid block to facilitate analysis and calculation using the theory of limit equilibrium of blocks.

Conduct force analysis and select appropriate mechanical theories. Analyze the forces provided by various influencing factors and their nature. Based on the determined physical–mechanical model, the physical processes and effects resulting from the force action are studied, force analysis is conducted, and forces of the same type are synthesized.

Select suitable mechanical theories to establish equations. For example, for the stability analysis of the roof of a soil cavity collapse, rigid body limit equilibrium theory is used to establish equilibrium equations. For hourglass-type collapses, establish equilibrium equations based on hydraulic and fluid mechanics theories. For mudflow-type collapses, Newton’s law of internal friction is utilized to establish equilibrium equations. Then, perform calculations on the established equilibrium equations to obtain the general mathematical expression of the prediction model.

5.5.2.2 Stochastic Model Prediction

Stochastic model prediction refers to obtaining predictive conclusions directly through uncertainty calculation based on the influencing factors of collapse. In the prediction process, apart from considering geological factors when determining the influencing factors and their weights, the other steps involve purely mathematical calculations based on characteristics such as probability, fuzziness, and grayness. As a result, uncertainty prediction models lack rigorous geological and physical mechanisms and processes. Some models strictly rely on mathematical calculations of uncertainty, and their predicted results often deviate from geological processes and actual conditions to some extent. Therefore, they are semiquantitative prediction methods. Common stochastic models include probability statistics, fuzzy mathematics, gray system theory, and artificial neural network models, among others.

In the prediction of karst collapse, the fundamental approach of stochastic model prediction is as follows: for a specific site, study various factors that influence ground collapse and determine the contributions of each factor (i.e., determine the weights of each factor). Then, employ a selected uncertainty prediction model (such as a probability prediction model, fuzzy prediction model, gray prediction model, or other uncertainty prediction models) to evaluate collapse according to the calculation methods and steps specified by each model. The typical methods and steps are as follows:

1. Determination of evaluation categories (levels)

Evaluation categories represent the conclusions of the assessment of karst collapse. Determining the evaluation categories involves classifying the likelihood of collapse in different levels. In karst collapse assessment, commonly used descriptors include “stability”, “susceptibility”, or “hazard”, typically divided into 3–5 levels. Too few levels would result in an insufficient characterization of collapse phenomena, while too many levels, although theoretically detailed, would be impractical. For complex collapse processes, overly detailed descriptions do not align with actual conditions and are therefore unnecessary.

If we consider 5 evaluation levels, namely, stable, relatively stable, moderately stable, unstable, and extremely unstable, denoted as v_1 , v_2 , v_3 , v_4 , and v_5 , respectively, the evaluation categories for karst collapse can be selected as Eq. (5.1):

$$V = (v_1, v_2, v_3, v_4, v_5) \quad (5.1)$$

2. Selection of influencing factors

Before conducting formal predictions, start by studying existing collapse phenomena in the site area and analyzing the process of karst collapse. Identify the causes of collapse and determine the set of influencing factors, denoted as U . Research indicates that karst collapse is mainly influenced by the following six major factors:

- (1) Cover layer factors include lithology, thickness, structure, and physical–mechanical properties.
- (2) Karst factors include the lithology of strata, degree of karst development, distribution types of karst, linear karst rate, rock mass structure, and characteristics of the bedrock surface.
- (3) Structural factors include the degree of structural influence, distance to faults, distance to folds, structural properties, and recent tectonic movements.
- (4) Water factors include the following: ① Groundwater. It is mainly related to water level fluctuations, vertical distance between the water level and the soil–rock interface, frequency and duration of water fluctuations, chemical properties of water, runoff intensity, seepage intensity, water richness, connection between pore water and karst water, distance to the center of a sinkhole, water inflow from boreholes in karst water wells, and depth of the water table. ② Surface water. It is mainly related to infiltration intensity, distance to surface water bodies, runoff intensity, and atmospheric precipitation.
- (5) Topography factors include geomorphic units and changes in topography.
- (6) Environmental factors include distance to pumping wells, reservoir storage capacity, discharge intensity, properties of discharged water, pumping intensity, additional loads from human activities, and others.

In engineering practice, not all factors mentioned above are applicable to every study area. When determining the specific set of factors, it is necessary to select a representative set U of m factors based on the specific engineering and hydrogeological conditions of the study area (Eq. 5.2).

$$U = (u_1, u_2, \dots, u_m) \quad (5.2)$$

where, m represents the number of selected factors.

Once the influencing factors are determined, they can be classified and merged based on certain characteristics to establish a hierarchical structure. The hierarchical structure can consist of multiple levels, with three levels being commonly used, namely, the objective level, indicator level, and factor level (Fig. 5.3). This hierarchical structure is simple, facilitates weight calculation, and provides a clear and intuitive logic. In contrast, too many levels would complicate the calculations and are unnecessary.

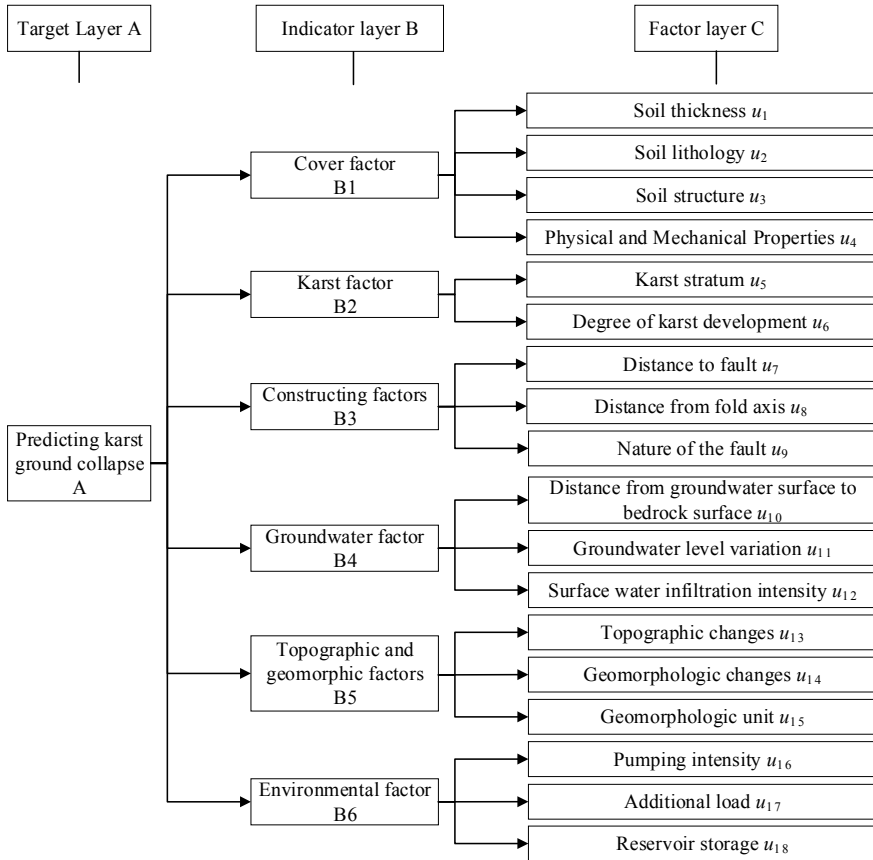


Fig. 5.3 Hierarchy model of the prediction factor for karst collapse

3. Determination of weights for each influencing factor

Determining the weights of each influencing factor involves assessing their contributions to collapse. There are various methods to determine weights, such as expert estimation, the Delphi method (expert survey), the eigenvalue method, the analytic hierarchy process (AHP), and artificial neural network models. In artificial neural network models, weights can be automatically adjusted and determined through training. AHP is a commonly used method for weight determination (Wei et al. 2021).

4. Selection of a predictive mathematical model and calculation according to the corresponding rules

Considering the characteristics of karst collapse, predictive mathematical models for collapse prediction can be categorized into three main types: statistical models, fuzzy models, and gray models. They are based on the randomness, fuzziness, and

gray nature of collapse, respectively. Additionally, other predictive models can be applied to karst collapse prediction, such as scoring methods and artificial neural network models. These models approach the problem of karst collapse from different perspectives.

Each predictive mathematical model has its own mathematical operations and processing procedures. Once a predictive mathematical model is selected, the corresponding mathematical operations and processing procedures are applied.

5. Determination of evaluation criteria and drawing conclusions

Based on the rules adopted by each mathematical predictive model, evaluation criteria are determined to select evaluation conclusions within the evaluation set.

6. Model testing and revision

After establishing the predictive model, it is generally necessary to test its conformity using existing collapse instances. Only models that pass the test and align with the actual situation can be used for prediction. Otherwise, the model requires further revision.

5.6 Prevention and Control of Karst Collapse

The purpose of prediction is to achieve effective prevention and control. The prevention and control of karst collapse can be broadly divided into two aspects: prevention and control. Prevention aims to prevent collapse from occurring or minimize its occurrence, while control focuses on limiting the expansion and depth of collapse areas and mitigating their hazards.

5.6.1 Prevention of Karst Collapse

5.6.1.1 Regional Prevention and Anti-Collapse Structural Design of Building Foundations

In the planning and construction of karst development areas, it is necessary to implement regional prevention and anti-collapse design. Prior to construction, comprehensive studies on geology, karst geology, cover layer characteristics, groundwater, and other aspects should be conducted in potential collapse areas to identify or eliminate factors that may cause collapse. Measures such as diverting surface rivers, removing thin cover soil layers, filling sinkholes in riverbeds, minimizing the connection between surface water and groundwater, conducting necessary pumping tests, and developing overall designs for preventive drainage systems should be implemented. Based on the prediction data, important buildings should be located in stable

areas away from potential collapse zones. For buildings that must be constructed within collapse areas, anti-collapse measures should be incorporated into the design or temporary structures should be used.

Anti-collapse structural designs for building foundations in potential collapse areas may include strip foundations, raft foundations, elongated box foundations, and large-scale foundations. These structures can span soil cavities or karst voids and reduce the stress on the foundations in the event of collapse. Deep foundation reinforcement methods such as drilled pile foundations, driven piles, caissons, and pier foundations can also be employed to ensure that the foundations are placed on deep and stable bedrock. The selection of preventive methods should be based on the actual conditions and may involve one or a combination of the abovementioned anti-collapse structures.

5.6.1.2 Prevention of Collapse in Water Source Areas

1. Reasonable well drilling and control of pumping intensity: Wells in water source areas should be located as far away as possible from residential and production areas to minimize damage to buildings and ensure personal safety. In cases where multiple wells are used, they should be dispersed to reduce mutual interference and cumulative drawdown effects. For areas with concentrated well pumping, the pumping rate and drawdown should be controlled to maintain the groundwater level above the bedrock surface, avoiding simultaneous intensive pumping or sudden drawdown from a single well and gradually lowering the water level to reduce the destructive effects of sudden hydraulic gradients on the soil. Prior to the development of new water sources, large-scale pumping tests with significant drawdown and high flow rates should be conducted to predict and evaluate collapse.
2. A reasonable filter should be installed in the well casing to prevent sand from flowing out of the well casing.
3. For areas with deep karst development, deep-seated karst groundwater should be extracted while sealing off shallow karst water. Alternatively, pumping should be conducted in areas with thick soil layers and deep groundwater levels.

5.6.1.3 Prevention of Mining Collapse

The key to preventing karst collapse in mining areas lies in addressing the intensity of pit dewatering, underground water inflow, and surface water backflow. Generally, strong dewatering methods are not recommended for mining operations in karst areas to prevent sudden drops in the groundwater level. Measures such as sealing water inflow points or consciously controlling and diverting water should be taken to transform the water inflow into controlled discharge. Surface measures such as

channeling (rivers and streams), filling (sinkholes), intercepting (floods), and modifying (river channels) should be implemented to reduce the amount of surface water entering the mining pit.

In addition to controlling drainage and preventing surface water infiltration, it is also possible to select narrower cross-sections for groundwater flow paths, install grouting curtains to intercept groundwater sources, and limit the expansion of groundwater level decline funnels within a certain range, thereby avoiding large-scale collapse. The successful example of using grouting curtains to protect the water source of Jinan City in the Zhangmatun Iron Mine in Shandong, China, demonstrates the effectiveness of this approach.

5.6.1.4 Monitoring of Karst Collapse

Monitoring related to karst collapse aims to provide timely warnings of collapse (Lei et al. 2023). Monitoring work includes long-term observations of the ground, buildings, and water points (wells, springs, mine water inflows, and reservoir leakages), as well as monitoring of precursory phenomena of collapse. Long-term observations are generally conducted during the first 1–3 years before dewatering and impoundment. The observation frequency varies depending on different stages: in the early stage of dewatering, observations are usually carried out every 5–10 days, while in the later stage, monthly observations are acceptable. Before dewatering, observations may be conducted every 1–3 months. The primary focus of long-term observations is to monitor the cracking, displacement, and settlement changes in the adjacent ground and buildings caused by dewatering of karst water or the construction of reservoirs for water storage, as well as the dynamics of water points and changes in sediment content. Precursory phenomena of collapse, which serve as the prelude to collapse, are intuitive manifestations that require particular attention and early detection due to their short time interval before collapse occurs. The monitoring content includes groundwater-induced surface waterlogging and spring drying, gas or water exhalation from the ground caused by artificial impoundment, changes in vegetation status, structural noises or tilting of buildings, circular ground cracks, collapsing sounds in underground soil layers, sudden changes in water quantity, water level, and sediment content at water points, abnormal behavior of frightened animals, and so on.

5.6.2 Management of Karst Collapse

The management of collapse should primarily target the fundamental environmental factors that contribute to collapse formation, including water, soil, and karst voids. It should be approached from three aspects: intercepting water flow, strengthening soil layers and sediment in gullies and cavities, and sealing karst channels. The specific methods employed should be tailored to the local conditions and may involve the use of individual or integrated approaches.

5.6.2.1 Sealing Method

This method is commonly used for treating shallow and small collapse sinkholes. The choice of sealing materials and the structure of the seal depend on the actual situation. If bedrock is exposed in the sinkhole, it is first filled with large rocks or crushed stones to create an anti-filter layer. Alternatively, underground rock blasting can be used for backfilling, followed by compacted clay. If the sinkhole does not expose bedrock and the hazard is relatively minor, it can be backfilled with rocks or clay directly. If the hazard is significant, the loose subsided soil should be removed first, followed by the placement of large rocks or crushed stones as an anti-filter layer and finally the compaction of backfill soil. For subsidence treatment with special requirements, such as sinkholes and caves beneath railways or building foundations, steel plate reinforcement should be installed at the bottom. Additionally, to enhance the strength of the backfill, cement slurry can be injected during the placement of crushed stones or aggregates.

5.6.2.2 Spanning Method

This method is used for deep and large sinkholes where backfilling is challenging. It involves constructing a solid and stable spanning structure that allows the load on the sinkhole to be transferred to a reliable soil or rock mass through the spanning structure. The advantage of this method is that it transforms complex underground engineering into a more manageable surface engineering project.

5.6.2.3 Dynamic Compaction Method

This method aims to improve the strength of the soft soil layers after collapse and the backfilled soil in the sinkhole. It can also eliminate hidden voids and weak layers. It combines both remediation and prevention measures.

5.6.2.4 Injection Method

This method involves injecting grout through boreholes or cave entrances to strengthen soil layers and fill voids, aiming to intercept groundwater sources and reinforce building foundations. The injection materials mainly consist of cement, aggregates (sand, slag, etc.), and accelerators (sodium silicate, calcium chloride). The preferred injection method is low-pressure intermittent quantitative injection or cyclic injection.

5.6.2.5 Deep Foundation Method

For large and deep sinkholes where spanning structures are ineffective, strengthening the foundation of buildings through deep foundations is an ideal approach. Typically, methods such as driven piles, drilled shafts, caissons, and pier foundations are used to place the building's foundation on the bedrock. The jet grouting method is a relatively new technique in pile foundation applications, characterized by rapid construction, simple processing, and effective reinforcement of cave deposits.

5.6.2.6 Controlled Dewatering Method

Rational control of dewatering intensity is an important approach to reducing collapse in mining areas and water source areas.

5.6.2.7 Clearing, Diverting, Enclosing, and Channel Modification Method

Sinkholes in collapse areas often become inlets for surface water. Therefore, diversion methods should be employed to redirect surface water away from the collapse area. Flood control measures should be implemented to enclose sinkholes in flood-prone areas. In cases where collapse occurs extensively on both sides of a river channel or within the riverbed, channel modification should be considered to divert the river. In areas with thin covering layers on the riverbed, even if collapse occurs in small amounts, thorough cleaning and bottom protection should be carried out to prevent leakage and water intrusion.

5.6.2.8 Balancing Groundwater and Air Pressure Method

For subsidence at the bottom of karst reservoirs in rocky karst mountain areas, after identifying the underground karst channels, devices for ventilating various karst conduits should be installed to balance groundwater and air pressure. This can help eliminate the effects of water and air pressure and achieve the goal of preventing collapse.

5.6.2.9 Integrated Management

For large-scale collapse areas with a high number of sinkholes, a single method may not achieve satisfactory results. Therefore, comprehensive management should be implemented. Based on different conditions, two or more methods should be employed to eliminate or mitigate the main causes of collapse, leading to better outcomes.

Karst collapse is a unique and complex anthropogenic environmental issue and geological hazard. Human activities in karst environments are inevitable, and collapse occurrences cannot be completely avoided. Currently, there is a lack of highly effective prediction methods, so comprehensive prevention and control measures are necessary to limit the intensity and impact of collapse. As karst areas continue to be developed and utilized, the issue of ground collapse will become increasingly prominent, highlighting the need for strengthened research on this environmental hazard.

References

- De Waele J, Gutiérrez F, Parise M, Plan L (2011) Geomorphology and natural hazards in karst areas: a review. *Geomorphology* 134:1–8. <https://doi.org/10.1016/j.geomorph.2011.08.001>
- Kang Y (1984) Classification of land collapses in karst regions. *Carsologica Sinica* 2:146–155
- Kang Y (1988) Forming condition of land collapse in karst regions. *Carsologica Sinica* 7(1):9–18
- Lei M, Gao Y, Jiang X, Guan Z (2016) Mechanism analysis of sinkhole formation at Maohe village, Liuzhou city, Guangxi province, China. *Environ Earth Sci* 75:542. <https://doi.org/10.1007/s12665-015-5100-5>
- Lei M, Zhou W, Jiang X, Dai J, Yan M (2023) *Atlas of Karst collapses*. Springer, Cham, Switzerland. <https://doi.org/10.1007/978-3-030-92912-1>
- Luo X (2017) *Theory and practice of karst ground collapse*. China University of Geosciences Press, Wuhan
- Luo X, Luo C (2016) Physical model of soil-cave type karst ground collapse. *J Eng Geol* 24:1229–1237. <https://doi.org/10.13544/j.cnki.jeg.2016.s1.179>
- Luo X, Luo C (2021) Three-Mechanism Theory (TMT) of karst ground collapse and its application. *Carsologica Sinica* 2:171–188. <https://doi.org/10.11932/karst2021y001>
- Papadopoulou-Vrynioti K, Bathrellos GD, Skilodimou HD, Kaviris G, Makropoulos K (2013) Karst collapse susceptibility mapping considering peak ground acceleration in a rapidly growing urban area. *Eng Geol* 158:77–88. <https://doi.org/10.1016/j.enggeo.2013.02.009>
- Parise M, Gunn J (2007) Natural and anthropogenic hazards in karst areas: an introduction. *Geol Soc London SP 279*(1):1–3. <https://doi.org/10.1144/SP279.1>
- Wei A, Li D, Zhou Y, Deng Q, Yan L (2021) A novel combination approach for karst collapse susceptibility assessment using the analytic hierarchy process, catastrophe, and entropy model. *Nat Hazards* 105:405–430. <https://doi.org/10.1007/s11069-020-04317-w>
- Xu W, Zhao G (1979) Causes of ground deformation in karst mining areas and their prevention and control methods. *Hydrogeol Eng Geol* 06:47–65

Chapter 6

Mine Water Inrush and Its Prediction



6.1 Introduction

Under natural conditions, ore bodies, especially in the surrounding rocks, are often filled with groundwater of a certain quantity and composition. During the construction and production of mines, surface water and groundwater flow into the mine shaft through various mining channels. This phenomenon is known as ore deposit water filling or pit water inflow. The volume of this inflow is described as the inflow intensity. When the volume of water entering the mine exceeds its normal drainage capacity, it results in a mine flood, referred to as a mine water inrush. Water hazards caused by water inrushes in coal mines are one of the major safety disasters in the coal mining process, alongside gas and coal dust (Dong et al., 2021). A water inrush not only affects normal mining operations, but in severe cases, it can also flood the mine shaft and extraction areas, leading to potential fatalities and causing serious harm. The frequent occurrence of sudden water accidents in coal mines serves as a stark warning and reminds us to pay close attention to the dynamics of pit water inflow at all stages of coal mining, emphasizing the importance of accurately predicting mine water inflow.

The term ‘water yield of mine’ typically refers to the amount of water seeping into mine passages from surrounding rock layers per unit of time during the excavation of mine fields and coal seams. The magnitude of the inflow is one of the crucial indicators in determining the complexity of hydrogeological conditions in a mineral deposit. It not only pertains to the safety and construction costs of the mine but also significantly impacts the economic and technical evaluation of the mineral deposit. The volume of inflow serves as the primary basis for the design and mining departments in selecting appropriate mining plans and methods, formulating drainage measures, and determining drainage equipment. Hence, during the hydrogeological survey of mineral deposits, it is imperative to accurately evaluate and forecast the inflow volume at each stage of future mine development. Currently, commonly used methods for predicting the water yield of mines on a global scale

include analytical methods (Capta & Chen, 1984), the water balance method, the hydrological analogy method, numerical methods (Kihm et al., 2007; Yin et al., 2016), the correlation analysis method (Li et al., 2022), and the Q-S curve equation method. In addressing practical issues, several methods are often coupled together in hopes of more accurately forecasting the water yield of mine or groundwater levels.

During coal mining operations, it is essential to promptly drain the water that floods the mines, as well as any groundwater that could potentially turn into mine inflow or threaten the safety of mine tunnels. Consequently, a significant amount of mine water is discharged, leading to a broad and pronounced decline in groundwater levels. This decline can cause existing water supply wells to reduce their output or even lose their ability to provide water altogether (Odintsev & Miletenko, 2015). Additionally, this process might alter surface infiltration conditions, change or disrupt the original surface water flow patterns, and may even lead to substantial surface water flowing into mines, resulting in sudden mine inflows. Furthermore, under certain conditions, the boundary conditions of the aquifer in which the mine operates can be altered. For instance, originally impermeable boundaries may become permeable; natural discharge areas might transform into recharge zones; underground water divides could shift outward; water-blocking faults may turn into water-conducting faults; and there might even be instances of seawater intrusion (Slesarev, 1983). Therefore, it is imperative to study the factors and mechanisms affecting mine inflow during coal mining processes.

Research into the analysis of hydrogeological conditions in ore deposits, the determination of mine inflow mechanisms, and the prediction of mine inflows encompasses virtually all methodologies of hydrogeological exploration, research, and evaluation. Given the varying objectives and focal points of these studies, the selection and application of different technical methods also diverge. The basic hydrogeological characteristics under distinct geological conditions dictate that for different types of water-infused ore bodies, the chosen methods for analyzing hydrogeological conditions and discerning inflow mechanisms are not uniform (Li et al., 2018a, b; Zhang et al., 2023). Predicting the water yield of mines is also a process of analyzing hydrogeological conditions, with calculations potentially employing various methodologies used in underground water resource assessments. Consequently, this section, with a backdrop of the hazards associated with mine inflows, delves into the mechanisms of mine inflow under different scenarios. It introduces various computational methodologies for determining the water yield of mines from perspectives such as factors influencing the inflow. The chapter culminates in a predictive analysis of mine inflow using real-world case studies from mining regions.

6.2 Hazards of Mine Water Inrush

Mine inflow incidents that impact normal production activities, pose threats to mine safety, or result in partial or complete flooding of the mine are collectively termed ‘mine water hazards’ (Gui & Lin, 2016; Wu et al., 2022). Not only do they severely

disrupt the regular construction and production activities within the mine, but they also endanger the lives of underground personnel. Due to the intricate hydrogeological conditions in coal fields and deep mining in older mining areas, the likelihood of such water hazard incidents is on the rise (Zhang et al., 2020). To date, mine water hazards have led to substantial human, material, and economic losses (Sun et al., 2016). The primary manifestations of water hazards caused by water discharge into mines include the following:

- **Deterioration of the working environment:** Mine water disasters can lead to water accumulation in the underground passageways of coal mines and create dripping phenomena from the roof of coal seams. This results in a relatively humid atmosphere in the workspace and nearby corridors, hindering proper air circulation. Such conditions can lead to the proliferation of pathogenic microorganisms, deteriorating the entire working environment and endangering the physical and mental health of the workforce.
- **Increased cost per ton of coal:** The occurrence of mine water disasters, especially during significant inflow events, requires the installation of specialized pipelines, water pumps, and other equipment for drainage. This elevates the overall drainage costs, raising the production cost per ton of coal and impacting the overall business operations of coal mining enterprises.
- **Shortened equipment lifespan:** Water inflow hazards in mines can cause varying degrees of corrosion to metallic equipment, support structures, and tracks. This affects the normal operation of machinery, shortens its service life, escalates maintenance costs, and significantly reduces coal extraction efficiency.
- **Threat to life and property:** In instances of stagnant water accumulation from old mining voids, accumulated gases such as methane and hydrogen sulfide can be released with the water flow. When the released methane reaches its explosive limit and encounters a source of ignition, an explosion can occur. In poorly ventilated corridors, miners inhaling highly toxic hydrogen sulfide gas can suffer from poisoning or even death. Additionally, sudden water inflows or volumes exceeding drainage capacity can result in minor issues such as partial mine shut-downs or localized flooding. In severe cases, it can lead to the complete flooding of mines, casualties, enforced shutdowns, and even mine closures. This not only leads to financial losses for the nation but also poses grave threats to the lives of underground workers.
- **Impact on coal resource recovery and quality:** Due to the threat posed by water in mines, it is often necessary to leave behind safety pillars for water prevention. This inevitably hinders the full utilization of coal resources, with some even becoming challenging or impossible to mine. This severely affects the development and utilization of coal resources.
- **Complications in disaster relief and rescue:** Accompanying sudden water inflow incidents, there is bound to be considerable accumulation of coal slurry and rock sediments obstructing the passageways. This creates barriers for rescue personnel, prolonging and delaying rescue and relief efforts.

6.3 Types of Mine Water Hazards

In mining areas, atmospheric precipitation, surface water, and groundwater enter the mines through various channels, a phenomenon termed “mine water inrush”. When the volume of this inflow surpasses the mine’s normal drainage capacity, water-related hazards or inundations can occur. These water hazards not only severely disrupt the standard construction and production within the mine but also pose significant threats to the safety of underground workers. Clarifying the mechanisms behind mine water inflow can help prevent such hazards (Liu et al., 2022; Wang et al., 2022). This ensures the safety of mine construction and production, reduces regular water inflow, lowers production costs, and facilitates the efficient and rational utilization of coal resources.

6.3.1 Hazards Caused by Surface Water

In regions with surface water bodies (such as perennial rivers, lakes, reservoirs, ponds, dams, etc.), mining hazards can arise due to improper allocation of protective coal pillars underground. When underground mining activities lead to roof collapses or fault zones cracking and becoming water conduits, surface water can rapidly and massively inundate the mines. Such inundation accidents have occurred multiple times. Particularly in some normally or even long-term dry riverbeds or low-lying water collection areas, which have been incident-free for years, they have not drawn significant attention or concern. When flash floods occur and waters overflow, elements such as ancient concealed mine shafts, hidden karst funnels, shallow mining holes with collapsed cracks, or even poorly sealed boreholes may suddenly collapse due to the erosive flow of floodwaters. This makes it easy for ground floods to extensively backfill into mines. Additionally, floods can intensely seep through the exposed areas of certain water-bearing strata with strong water inrush, thereby causing inundation accidents. Under specific conditions, floods can sometimes wash away industrial plazas, directly filling mines and preventing underground workers from evacuating. These water-related hazards often arrive abruptly and ferociously, posing an immediate and overwhelming threat and frequently resulting in significant losses.

Therefore, an essential principle in coal mining production is that water prevention is more critical than drainage, emphasizing both preventive and remedial measures. Only through comprehensive prior surveys and analyses, preparing for the worst scenarios, and ensuring thorough preventive measures can the safety of mine production be genuinely assured.

6.3.2 Hazards Caused by Abandoned Mine Pools

Abandoned mine pool refers to the accumulated water in abandoned or closed mines whose excavation extent is unknown, in haphazardly dug pits surrounding mines without accurate mapping data, or even in abandoned mine tunnels that were intentionally excavated by the mine itself (Polak et al., 2016). This water accumulates in mined-out areas or coal or rock tunnels connected to these voids. The geometric shapes of such water bodies are highly irregular. The spatial relationships between ongoing mining activities and these water bodies are intricate and challenging to analyze and predict. Moreover, these water bodies are concentrated, transmitting pressure rapidly. Their flow mimics surface water, distinct from the infiltration of groundwater within aquifers. If mining activities inadvertently approach these abandoned mine pools, they can suddenly burst out, leading to what is commonly known as a water inrush accident. Evidence suggests that even a few cubic meters of such accumulated water, if released suddenly, can cause fatalities. Large volumes of water from abandoned mine pools can devastate mines and injure miners. These water bodies are not only present in regions with abundant groundwater resources but can also be found in arid and water-poor coal mining areas. They represent a ubiquitous water source in coal mining production, with several unexpected incidents historically reported.

6.3.3 Hazards Caused by Pore Water

During the coal mining process, water hazards are also manifested in terms of pore water. Given that the geological structure of the mining area tends to be loose and is extensively overlain with layers such as quicksand, pebbles, and clayey sand, it directly absorbs atmospheric precipitation and infiltration from surface water bodies such as rivers, lakes, and reservoirs located above it. This results in the formation of water-filled bodies with an extremely complex structure in both cross-section and plan views. Over time, these water-filled bodies consistently replenish the underlying coal seams, the water-filled aquifer at the top and bottom of the coal seams, and the fault fracture zones. The hydraulic connection varies due to different contact relationships, the thickness and distribution range of the aquiclude thickness, and the quality of borehole sealing (Yin et al., 2019). These variations often make it difficult to accurately determine the permeability of the water-filled aquifer and the hydraulic strength of the hydraulic fracture zones in the goaf. This unpredictability can lead to sudden increases in the amount of inflowing water at the mining face. In severe cases, this can result in sudden inrushes of water, flooding the mine. Under certain conditions, this could even lead to catastrophic incidents where both water and quicksand simultaneously breach into the mine. Moreover, during the mining process, issues such as long-term infiltration or collapse of upper structures can cause

anomalies in soil layers with high water content, leading to blockages in the tunnels or flooding of the mine.

6.3.4 Hazards Caused by Coal Seam Roof Water

Coal-bearing strata typically consist of multiple extractable coal seams, some of which are quite thick. Above these coal seams, there are often multilayer water-filled aquifers, with some even being strong karst aquifers. Due to the differential subsidence and fault fracturing associated with the extraction of thick coal seams and multiple seams, the height and location of the induced water-conducting fracture zones change. This can cause unidentified water-rich zones in the overlying water-bearing strata to suddenly release groundwater into the excavation face, resulting in significant water-related accidents. At times, this can flood the entire mining area, the working face, or even the entire production level. If such water-filled aquifers receive intense replenishment from Quaternary porous water-filled strata groundwater in concealed outcrop areas or from surface water or atmospheric precipitation in outcrop areas and fall within the impact range of coal seam-induced water-conducting fracture zones, water hazards are inevitable during coal extraction. Preventing and mitigating such hazards becomes even more complex and challenging. In specific instances, this might render vast coal resources unminable or make their extraction economically unjustifiable (Xu et al., 2022; Zeng et al., 2018).

6.3.5 Hazards Caused by Coal Seam Bottom Water

Water hazards from water-filled aquifers under pressure in the coal seam floor are the most frequent and hazardous disasters in coal mines. Such disasters have frequently resulted in sudden water inrushes, inundating the entire production level, with even more instances of flooding specific mining areas or coal extraction faces. The primary reason for this is the extensive deposition of thick carbonate rock karst water-filled aquifers at the base of coal mine deposits. These carbonate rocks have a widespread distribution, with large areas both exposed and concealed beneath porous aquifer layers, capable of receiving intense replenishment from atmospheric precipitation, surface water, or pore groundwater. A single significant precipitation event can nearly replenish the groundwater deficit caused by long-term drainage, refilling the groundwater drawdown funnel (Li et al., 2018a, b). Due to the inclination of the coal seams, as mining extends deeper, the hydrostatic pressure acting on the coal seam floor from the water-filled aquifer increases. The relative thickness of the impermeable layer above the coal seam floor and its lithological combinations vary across sections, and the extent of fracture and fissure development differs. The mining-induced stress acting on the coal seam floor and its consequent impacts and damage to production also vary from place to place. Hence, the conditions for sudden water inrushes

from the coal seam floor are challenging to anticipate and analyze. Even with thorough investigation, analysis, and judgment, unexpected scenarios frequently arise, making the probability of water inrushes from the coal seam floor relatively high. Any oversight can lead to serious water-related accidents.

6.3.6 Hazards Caused by Karst Water

In such water-related hazards, the roof and floor of the coal seam are typically composed of limestone aquifers. During the mining process, it is inevitable that these aquifers will be exposed and drained (Cao et al., 2021; Zhang et al., 2017a). Under general circumstances, these aquifers can be successfully drained. However, when these aquifers are hydraulically connected to surface water bodies or groundwater, when they are intersected by geological structures, or when coal sequences continuously collapse into caverns throughout geological history, forming karst collapse pillars and creating water-conducting channels connected to thick limestone aquifers, the water-rich nature of these aquifers significantly increases. Consequently, in areas with strong water source replenishment and proximity to water-conducting channels, major disastrous water inrush accidents often occur. This type of water hazard is isolated and concealed in its occurrence conditions, making it challenging to prospect and detect in advance and thus difficult to prevent and mitigate.

6.3.7 Hazards Caused by the Fracture Zone

Water inrush hazards from fractured and broken zones can be associated with old mine water pools, aquifers in the roof of the coal seam, pressurized aquifers in the floor, or even surface water bodies, making them the most common type of water hazards in coal mines. They can cause water-related hazards over an extended range along the fault direction or can be localized to a small section or even a single point, causing water inrush. In some cases, these zones might originally be dry but can become water-conducting faults due to mining-induced roof fractures unexpectedly increasing their upper limits or floor rock fractures becoming activated (Ma et al., 2020). When such water hazards occur, they can lead to severe consequences. For instance, if aquifers surround a fault, it poses a significant risk of water hazards to the mine. If the amount of conductive water in the aquifer is large, it will even increase the level of harm. Furthermore, if there is a substantial drop across the fault and it becomes water-conducting, a significant safety hazard is embedded. If this is exposed during subsequent mining operations, a sudden water inrush can occur, posing significant dangers to the surrounding workers.

6.3.8 Hazards Caused by Acidic Mine Water

In addition to the aforementioned typical types of water hazards encountered in mine excavation, due to regional variations and differences in the soil quality within the mine, there are often other more severe water hazard issues. For instance, the threat of acidic mine water is a significant concern that cannot be overlooked. This is because mines contain components such as pyrite, which, over prolonged mining processes, are gradually oxidized. This oxidation can lead to the formation of acidic substances. With the infiltration of water, acidic mine water is easily produced, posing a serious threat to mine excavation. Acidic mine water not only poses a direct threat to workers but can also affect mining equipment, necessitating heightened vigilance from mine operators and workers.

6.4 Prediction Methods of Mine Water Inrush

The water yield of a mine refers to the volume of water flowing into the mine (including the well, tunnels, and tunnel systems) per unit of time from the initial excavation to the mining process. It serves as one of the vital indicators for determining the hydrogeological type of the ore deposit and the complexity of its hydrogeological conditions and for evaluating the technical conditions of the mine's development. Furthermore, it provides the primary foundation for designing mine drainage systems and determining production capacity. Not only is the water yield of a mine a significant benchmark for technical and economic evaluations of coalfield construction, but it is also the main basis for the coal mining design department when formulating excavation plans, determining mine drainage capacity, and implementing drainage measures. Therefore, accurately predicting the water yield of mines is one of the essential tasks in mine hydrogeological work.

6.4.1 Overview of Mine Inrush Prediction Methods

Predicting the water yield of mines is at the heart of hydrogeological surveys of mineral deposits and is a complex task. Therefore, at every survey stage, there is a demand for accurate forecasting of the water inflow under various mining conditions with appropriate precision. The forecasting encompasses:

- Predicting the normal water yield of a mine: This refers to the relatively stable total amount of water inflow when the mining system reaches a specific elevation under normal conditions, typically denoted as the annual average water yield.
- Predicting the maximum water yield of the mine: This denotes the peak water inflow under normal conditions during the rainy season of a wet year. For certain exposed deposits and those controlled by flash floods or subterranean rivers,

it is also necessary to consider the local meteorological cycle characteristics. Using the historical maximum rainfall intensity data, predictions should be made for potential maximum mine water inflow values during once-in-several-decades intense rainstorms. This aids in forecasting sudden water inflows and formulating contingency measures.

- Predicting the water yield during shaft and tunnel development: This points to the volume of water encountered during the excavation of various shafts and tunnels.
- Predicting the drainage volume of dewatering projects: This refers to the volume of water drained during the designated dewatering period to lower the water table to a specified elevation.

The prediction of the water yield of mines is progressively refined as geological exploration of the mineral deposit advances and as the understanding of the hydrogeological conditions deepens. This process can be divided into three steps:

- Step one: Establish a hydrogeological conceptual model. This step requires ① generalizing the hydrogeological conditions of the mining area under known conditions, ② defining the internal boundary conditions for future mine shafts and tunnels, and ③ predicting external boundaries under future mining conditions. For large mineral deposits with complex conditions, establishing a reliable conceptual model usually goes through three stages. First stage (preliminary exploration): Based on the data obtained during preliminary exploration, a rudimentary model of the deposit's hydrogeological conditions is proposed, which can serve as a basis for designing large-scale water extraction (or injection) tests. Second stage (detailed exploration): Using various information provided by the exploration project, especially data from large-scale water extraction (or injection) tests, the preliminary model is adjusted, and a "corrected" hydrogeological model is established. Third Stage: Based on the "corrected" hydrogeological model, changes in the boundaries under future mining conditions are predicted according to the mining plan, leading to the establishment of a "predictive" hydrogeological model.
- Step two: Choose a calculation method and establish the corresponding mathematical model. Based on commonly used mathematical models in current mine water yield predictions, water yield forecasts can be categorized into different types. The selection of a model for calculation should be based on local conditions and available data.
- Step three: Solve the mathematical model and evaluate the prediction results. The solution of the mathematical model should not be viewed merely as a mathematical operation. Instead, it should be seen as the earlier identification and validation of both the hydrogeological and mathematical models. It also represents the process of deepening the understanding of various conditions in the mining area, transitioning from qualitative to quantitative knowledge.

The accurate assessment of water yield in mines is a critical task in mine hydrogeology. Different mines have varied water recharge conditions, and the factors affecting the water yield can vary significantly. The precision of hydrogeological

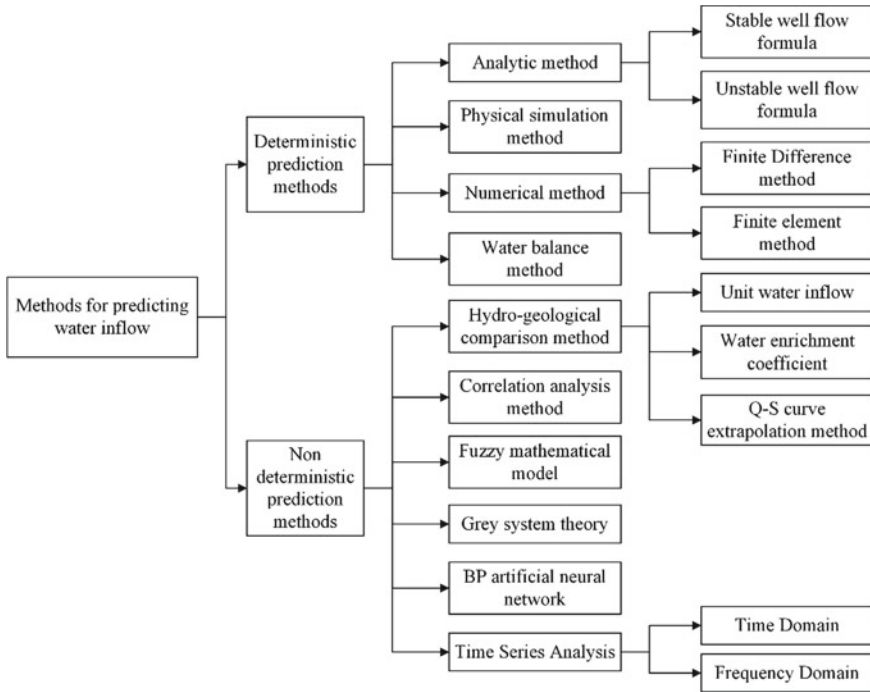


Fig. 6.1 Classification of methods for mine water inrush prediction

surveys differs from one mine to another, as does the detail of the available hydro-geological data. Therefore, it is challenging to directly apply a singular prediction method for mine water yield across the board. To make accurate predictions on water yield, it is essential to consider the mine's specific geological and hydro-geological conditions, maximizing the use of related data available for that mine. Different methods of predicting mine water yield need to be studied and chosen, as depicted in Fig. 6.1. The most common methods for predicting mine water yield include the hydrological analogy method, Q-S curve equation method, correlation analysis, analytical methods, numerical methods, and water balance methods, among others. This chapter primarily focuses on analytical methods (Peng et al., 2022) and numerical methods (Wu et al., 2019; Zhang et al., 2017b).

6.4.2 Analytic Method

In groundwater dynamics, the theories of steady-state flow and transient flow are introduced, along with formulas for calculating the water yield of various types of catchment structures. When predicting the water yield of mines, the mine shafts,

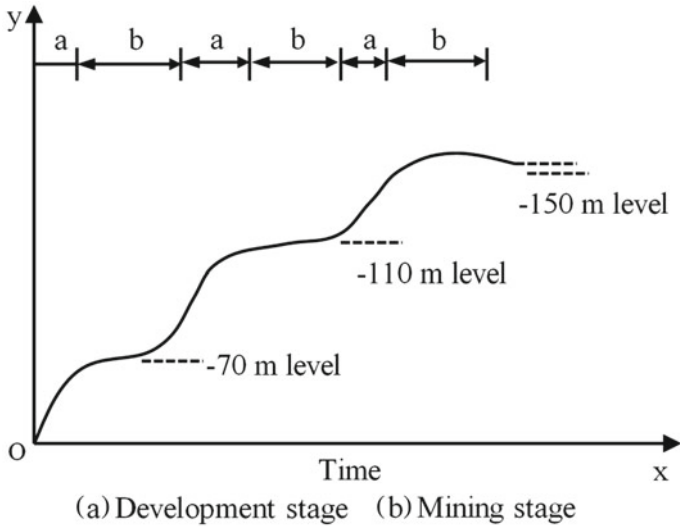


Fig. 6.2 Schematic curve of the mine water inrush process (x axis: time; y axis: water flow rate)

galleries, or even the entire mine can similarly be viewed as different types of catchment structures. As observed in Fig. 6.2, the curve illustrating the process of water influx in mines indicates the transition from unstable movement to the steady state of groundwater at various mining stages in multilevel mines. Therefore, either steady-state or transient flow formulas can be used to predict mine water yield. Additionally, when using the analytical method to forecast the water yield in mines, the key is to clarify the hydrogeological conditions. Given the features of the analytical model, complex hydrogeological conditions are then generalized. The actual issues are abstracted into mathematical problems through the establishment of a physical model.

6.4.2.1 Analyzing the Hydraulic Characteristics of the Dewatering Flow Field

The dewatering flow field of a mineral deposit evolves under natural flow field conditions, superimposed with the effects of artificial mining activities. Therefore, when analyzing various hydraulic characteristics of the dewatering flow field, one should base the analyses on natural conditions, taking into full account the impact of mining. It is crucial to discern and determine to which state it belongs.

- Distinguishing between steady-state and unsteady-state flows. In the early stages of mine excavation (during the development phase), the position of the tunnel line and its peripheral contour are constantly changing. The dewatering funnel rapidly extends outward, and the water influx in the mine is primarily driven by

the depletion of the aquifer's storage. This influx grows proportionally with the expansion of the development area. Therefore, during this phase, the dewatering flow field is primarily controlled by the development of mining operations, representing unsteady-state flow. In the later stages of mining (during the backfilling phase), since most of the mining development work is essentially complete and the tunnel contour is largely fixed, the dewatering flow rate is mainly controlled by the recharge conditions of the external boundaries of the flow field. In mining areas with insufficient recharge conditions, the dewatering flow field mainly consumes the aquifer's storage. The external boundary of the flow field continuously expands over time until it reaches the impermeable boundary, with the water influx in the mine gradually decreasing, and the flow characteristics still represent unsteady-state flow. However, in mines with ample recharge conditions, i.e., mines with fixed hydraulic head boundaries, the external boundary of the flow field quickly stabilizes due to the fixed tunnel contour. At this time, the mine's water influx is balanced by the recharge amount of the flow field's fixed hydraulic head boundary. Apart from the effects of seasonal climate changes, a relatively steady-state flow appears in the flow field characteristics.

- Differentiating between Darcy and non-Darcy flows. When significant dewatering occurs in the mining area, non-Darcy flows often appear near the dewatering project. According to studies, the range of this complex flow state is limited, and in a broader area, Darcy's law is still applicable. Therefore, the linear permeability law remains the theoretical foundation for establishing deterministic models for seepage flow.
- Distinguishing between plane flow and spatial flow. The form of groundwater movement in the dewatering flow field is controlled by the type of tunnel. At a macro level, it can be generalized as plane flow directed toward complete tunnels and spatial flow directed toward incomplete tunnels. The water influx in vertical shafts can be generalized as a radial plane flow problem, expressed using shaft flow formulas. When calculating the water influx in horizontal tunnels, it is approximated as a sectional plane flow. The single-width flow analytical formula can be used, but radiation flows also occur at both ends. The radial plane flow formula can be used to supplement calculations for water ingress at the ends of the tunnel. The tunnel system is much more complex. Although it is generally an approximate radial flow, when its distribution approaches a narrow, elongated belt shape, sectional plane flow can also occur. For inclined tunnels, based on Abramov's research on hydroelectric analogy methods, it is proven that the inclination of the tunnel has little effect on the water influx. Depending on the degree of tunnel inclination, calculations can be made approximately as per the type of vertical or horizontal tunnels.
- Differentiating between phreatic and confined water. During depressurization dewatering, there is often a transition from confined water to unconfined water or a combination of both confined and unconfined water. Moreover, in some mining areas with steeply inclined rock layers, one side may retain its original confined water state, while the other side transitions from confined water to unconfined

water or a combination of both. When establishing a computational model, it is essential to fully consider the abovementioned characteristics.

6.4.2.2 Determine the Type of Boundary

The dewatering flow field of a mineral deposit evolves within the context of natural flow conditions, compounded by the impacts of human mining activities. Therefore, when analyzing various hydraulic characteristics of the dewatering flow field, one should always base analyses on natural conditions while fully considering the influence of mining activities. It is crucial to differentiate and determine its specific state.

- Lateral boundary type generalization. ① In classifying the types of boundary inflow, boundaries should be broadly categorized into impermeable (barrier) and rechargeable types. It is important to note that postmining, an impermeable boundary may be compromised, transitioning into a rechargeable boundary, or the original discharge boundary could similarly become rechargeable. ② For the sake of computational models using analytical methods, irregularly shaped boundaries should be simplified into ideal geometric forms. Examples include semi-infinite straight boundaries, orthogonal boundaries, oblique intersections, and parallel boundaries. ③ Under various boundary conditions, calculation methods typically employ mapping techniques or partitioning methods, such as the Kaminsky plane radiative flow method. Based on the state of the groundwater flow field during dewatering, it is divided along the flow plane or equal water pressure surfaces into several fan-shaped flow sectors. Each sector commonly uses the Kaminsky plane radiative flow formula to compute its water inflow. The aggregate inflow from these sectors gives the total inflow for the entire mining area.
- Determination of vertical cross-flow recharge boundary type. When the top and bottom of the dewatered aquifer layer are weakly permeable, the vertically adjacent aquifers will provide cross-flow recharge to the dewatered layer through these weak layers, leading to the emergence of what is termed a cross-flow recharge boundary. Typically, cross-flow recharge boundaries are assumed to have a fixed water head, and the chosen calculation formulas are those that account for cross-flow recharge in groundwater dynamics.

6.4.2.3 Determination of Parameters

The calculation parameters directly affect the accuracy of predicting water inflow into the mine pit. Therefore, it is essential to determine various parameters sensibly, based on the characteristics of the analytical calculation model, combined with the hydrogeological conditions of the mining area and future mining plans. These parameters include the hydraulic conductivity of the rock layers (K), the yield value of the aquifer (μ), the thickness value (M), the radius of large diameter wells (r_0), the

impact radius (R), the width of the impact zone (L), and the maximum water level drop value (S_{\max}).

The hydraulic conductivity of rock layers (K). The hydraulic conductivity is an extremely important parameter in analytical calculations. However, due to the complexities of natural and mining conditions and the shortcomings of test calculation methods, it is not easily measured accurately, making it one of the main reasons for inaccuracies in water inflow predictions. The analytical method is mainly suitable for homogeneous aquifers. Therefore, the first step should be to determine whether the aquifer is homogeneous or heterogeneous. Commonly used methods include the weighted average method and the flow field analysis method. The weighted average method can be further divided into thickness averaged method, area averaged method, and directional averaged method. For instance, the formula of calculating hydraulic conductivity using the thickness averaged method is Eq. 6.1:

$$K_{cp} = \frac{\sum_{i=1}^n M_i K_i}{\sum_{i=1}^n M_i} \quad (6.1)$$

where M_i represents the thickness of each vertical segment of the confined (unconfined) aquifer and K_i represents the hydraulic conductivity of the corresponding segment.

For the flow field analysis method, when there is a contour map of equal water levels available, the closed contour method can be employed. The formula of calculating hydraulic conductivity is Eq. 6.2:

$$K_{cp} = -\frac{2Q\Delta r}{M_{cp}(L_1 + L_2)\Delta h} \quad (6.2)$$

Or, according to the characteristics of the flow field, the zoning method can be used to calculate the hydraulic conductivity:

$$K_{cp} = -\frac{Q}{\sum_{i=1}^n \left(\frac{b_1 - b_2}{\ln b_1 - \ln b_2} \cdot \frac{h_1^2 - h_2^2}{2L} \right)} \quad (6.3)$$

where,

- L_1, L_2 The lengths of any two closed contour lines of equal water levels.
- Δr The average distance between the two closed contour lines of equal water levels.
- Δh The difference in water levels between the two closed contour lines.
- M_{cp} The average thickness of the aquifer.
- Q The inflow volume of the mine.
- b_1, b_2 The width of the upstream and downstream cross-sections in a radial flow, respectively.
- h_1, h_2 The height of the water head above the water-separating bottom plate on the b_1, b_2 cross-sections, respectively.

L The distance between the b_1 and b_2 cross-sections.

- Aquifer thickness (M) in analytical methods: In analytical methods, the thickness of the aquifer is assumed to be uniform, necessitating the use of an overall average value. During calculations, one should first delineate the mining area into several computational zones based on lithological and structural characteristics, with each zone having an area of F_i . Subsequently, based on the variations in fractures and karst development with depth, one should identify the dominant and minor water-bearing segments, calculating the average thickness M_i (H_i) for each zone. Ultimately, the overall average thickness for the mining area can be determined using an area-weighted average approach.
- Calculation of the equivalent radius (r_0) for a “large diameter well”: The configuration of a tunnel system is considerably more complex than that of a water supply well. Its distribution is highly irregular, spanning a vast range, and is constantly undergoing changes, forming a sophisticated inner boundary. Analytical methods require idealizing this system. As such, this complex tunnel system is often treated as a single “large diameter well”. The area defined by the tunnel system or the area confined by the water table contour closest to the tunnel (F) is considered the area of this large diameter well. In this context, the total water inflow of the entire tunnel system is equated to the inflow of the large diameter well, allowing the use of various tunnel formulas to calculate the mine water inflow. This is referred to as the “large diameter well” method. The calculation formula for the equivalent radius r_0 of a nearly circular large diameter well is:

$$r_0 = \sqrt{\frac{F}{\pi}} = 0.564\sqrt{F} \quad (6.4)$$

- Calculation of the influence radius (R) for the “large diameter well” in drainage: When predicting the water inflow of a mine using the “large diameter well” method, the influence radius of the drawdown funnel (R_0) should be calculated from the center of the large diameter well. It is the sum of the equivalent radius of the large diameter well (r_0) and the drainage influence radius (R). Specifically:

$$R_0 = R + r_0 \quad (6.5)$$

6.4.3 Numerical Simulation Method

The numerical simulation method involves solving mathematical models using discretization techniques on electronic computers, commonly referred to as numerical methods. The solution obtained is a numerical solution, which is a collection of values and serves as an approximate solution to the mathematical model. Generally, an analytical solution can only be derived when the geometry of the seepage area is

relatively simple and the aquifer is homogeneous. For a complex groundwater basin, achieving large-scale equilibrium is essential for understanding the total amount of groundwater resources. It is undoubtedly very effective. However, its calculation results cannot reflect the distribution of the groundwater basin's flow field or the variations in water head at any given point over time.

6.4.3.1 Principle and Application Conditions

The principle of approximation in numerical computation overcomes the strict idealization requirements of the analytical method when addressing practical problems, making the solutions more aligned with actual scenarios. As a result, it is primarily used for large water deposits with complex hydrogeological conditions. This method exposes the overall hydrogeological conditions based on high-flow pumping tests and provides a plethora of information for modeling, model identification, and deep desaturation predictions.

While the fundamental methodology for predicting mine inflow rates numerically aligns perfectly with water resource evaluations, the conditions of the mining environment present unique challenges. Mining areas are situated in complex natural environments with ever-changing mining conditions and numerous uncertainties. Further complicating matters are the need to forecast under substantial depth reductions. Consequently, the most distinguishing feature of numerical computation for mine inflow rates is its challenging model identification process. The conditions for this are adverse, the tasks are laborious, and the difficulties are immense. Not only is there a need for the identification and rectification of all unknown and uncertain factors in the hydrogeological model under its original state, but there is also a requirement to establish an interaction mechanism for the internal boundary during deep numerical predictions. That is, with changes in the internal boundary (in terms of area and depth), one must decipher the external boundary's downward trajectory and its water equilibrium conditions.

6.4.3.2 Computational Procedure

Selection of the Mathematical Model

When constructing mathematical models, one must not only consider the requirements but also analyze their potential effectiveness. This involves assessing whether the complexity of the actual problem matches the data offered by the chosen model. Generally, a two-dimensional planar mathematical model can satisfy the fundamental requirements for addressing practical issues. However, for multilayered aquifer structures interconnected by weak permeable layers, a quasithree-dimensional model can be pragmatically selected. This means depicting the basic characteristics of the aquifer with a two-dimensional planar problem and using a vertical one-dimensional flow to describe the interactions between aquifers. For aquifers that exhibit distinct

heterogeneity in the vertical direction, especially thick aquifers, it becomes essential to consider the depth of mining and water level predictions. In such cases, to avoid misrepresentation, it is best to employ a three-dimensional flow mathematical model. This ensures a more accurate representation of the intricacies involved in heterogeneous and deep aquifers.

Generalization of Hydrogeological Conditions

The generalization of hydrogeological conditions is a crucial step in numerical computations. This process demands that actual problem characteristics be generalized using numerical methods based on available exploration data. This generalization reflects the utilization and assurance rate of exploration information as well as the depth of research into hydrogeological conditions. Importantly, it directly impacts the accuracy of the calculations. Proper generalization ensures that the complexity of real-world conditions is faithfully represented in the numerical model while also balancing the need for computational efficiency and precision.

Spatial morphology and structural parameter zoning of the aquifer: The spatial morphology of the aquifer is derived using contour maps of the top and bottom elevations of the aquifer. By providing the elevation of the aquifer's top and bottom at every discretized node or point with coordinates, the model automatically identifies the thickness of the aquifer, completing the generalization of its geometric shape. The heterogeneous structural parameter zoning of the aquifer is based on the hydrogeological zoning foundation. This means considering the distribution characteristics of T and S, in conjunction with lithology, the genesis type of loose sediments, the structural conditions of bedrock, and the hydrodynamic conditions in karst regions. According to the macroscopic laws of hydrogeological conditions and the characteristics of seepage movement, parameters are zoned and graded spatially in a gradient manner. The average values of the parameters for each zone, along with their upper and lower limits, are provided as the basis for model debugging.

Interaction generalization between the extraction layer and adjacent aquifers: The geological model typically provides the connection locations and coordinates with adjacent aquifers. The modes of connection can be faults, "skylights", or overflows supplied through weakly permeable layers. Recognizing these interactions is crucial because it determines the flow dynamics and interactions between various layers, which can have significant implications for water extraction and management strategies.

Generalization of boundary conditions: Numerical methods can realistically simulate complex boundary conditions. When combined with mathematical statistical models, they can handle various indeterminate boundary issues that analytical methods cannot address. During generalization, it is necessary to identify the spatial morphology of the boundary distribution, providing coordinates for these boundaries. The nature of boundary effects should be determined, including whether there is a water exchange and the method of this exchange. Relying on dynamic observations or pumping test data, the water level or flow rate variation rules should be

generalized using mathematical statistical methods. Depending on the time segment, water levels or unit-width flow rates at boundary nodes should be provided.

Generalization of initial conditions: Based on the contour map drawn from the water level data measured at the control nodes at the initial moment, the water level at each node should be provided as the initial condition. Given the limited number of control nodes, the creation of contour maps might inevitably have some level of arbitrariness. In cases where the aquifer structure or boundary conditions are more complex, it is advisable to use the model's short step length for correction. This generalization helps ensure that simulations begin from a realistic starting point and respect the conditions observed in the field, ensuring the accuracy of subsequent predictions and analyses.

Discretization of the Computational Region

Based on the principle of partitioned approximation, numerical methods transform a smooth, continuous head surface, which represents an actual seepage field, into a continuous but nonsmooth head surface pieced together by seamlessly interconnected, nonoverlapping triangles (Finite Element Method) or squares/rectangles (Finite Difference Method). This approach simplifies nonlinear problems, rendering them solvable as linear ones. When discretizing the domain, key control nodes must be initially selected, which are observation points with complete water level data. Given the limited number of these observation points, numerous interpolation points are needed to ensure a comprehensive discretization of the entire computational domain. To maintain the accuracy of model identification, each parameterized zone and hydrological boundary should contain at least one control node with a known pattern of water level variation. Interpolation points should be strategically placed where there are significant water level changes, boundaries of parameterized zones, and demarcations between confined and unconfined waters. Aligning with the principle of elemental partitioning, the positioning of these interpolation points should be judiciously adjusted.

Principle of elemental partitioning: The primary objective is to control the overarching trends of hydrogeological conditions. Generally, the approach is to start from the central area where there is ample data and gradually become sparser as we move toward more remote areas. In areas with significant hydraulic gradient variations, densification should be appropriately applied. However, abrupt transitions should be avoided. The lengths of the three sides of a triangular element should not vary too drastically. The ratio of the longest to shortest side should not exceed 3:1. The interior angles of the triangle should ideally range between 30° and 90° ; otherwise, the convergence of the numerical solution might be affected. Once partitioned, the nodal grid should be systematically numbered in a specific sequence, and data for each node should be prepared.

Temporal discretization: Depending on the characteristics of the groundwater level decline (or rise) speed field, an appropriate time step should be chosen to control the head variation pattern. This ensures both computational accuracy and efficient

calculation time. For instance, when simulating a pumping test, the initial drop in water level is rapid, necessitating the use of minute-based short time steps for control. As the rate of decline slows, the time step can be progressively extended to hourly or daily intervals. For simulations of steady-state extraction, larger time steps, such as monthly, quarterly, or even annually, might be suitable.

Model Calibration and Verification

Model calibration involves using observed groundwater head values and other known conditions to adjust and correct certain uncertain elements in the model equations, structural parameters, and boundary conditions. In mathematical computations, this is termed solving the inverse problem. Calibration relies on hydrological data from dynamic observations over one hydrological year, providing natural flow field data for dry, average, and wet seasons, as well as artificial flow field data from pumping tests. Appropriate software tools are either chosen or custom-developed for this purpose. As the groundwater head function is a multivariate function, it reflects the combined effects of all factors within the groundwater model. Thus, the geological implication of model calibration can be understood as a comprehensive assessment of the hydrogeological conditions of the study area. Where possible, the model should be further validated using historical groundwater levels from long-term observations.

Given the diverse practical situations, it is challenging to set a universal standard for fitting errors. Generally, a relative error less than 5–10% of the water level variation within a given period is considered acceptable. This, combined with the synchronicity and consistency of the groundwater head fitting curve trends, as well as the reasonability of the hydrogeological conditions and water balance conditions, serves as the basis for comprehensive assessment.

The outcomes of model calibration and verification are typically presented as comparative tables of calculated groundwater heads at control nodes versus observed values. Moreover, groundwater head spatial–temporal fitting maps are used to illustrate these findings. The latter showcases the fitting of groundwater head decline (or rise) rates at each control node and the head gradient fields at different times. This reflects the overall fitting precision in terms of point and area, as well as time and space.

Numerical Prediction of Mine Water Inrush

Model forecasting: Typically, forecasting is based on the quantification of the hydrogeological model. By considering the extraction plan (i.e., the known internal boundary conditions of the drainage project), one can predict how the external boundary will change under future extraction conditions, achieving the purpose of forecasting. As mining progresses with intense dewatering, the drainage funnel continues to expand, which may alter the original model's boundary conditions. Therefore, predicting the changing trends under extraction conditions becomes

crucial for calculating the inflow volume into the mine. Using numerical methods to forecast the inflow volume into the mine, one can generally determine:

- **Effective drainage volume:** This refers to the optimal drainage intensity or drainage plan required to lower the groundwater in the drainage area to a specific design elevation within a designated drainage time frame. It is essential to differentiate between this and the inflow volume into the mine pit. The latter is an objective phenomenon, while the former is man-made. Since the effective drainage volume is contingent upon the drainage time, it is determined by comparing the economic and technical conditions of data sets from various drainage plans, each with its associated drainage time and volume, before making the final selection.
- **Stable inflow volume:** After determining the effective drainage volume, the drainage tunnel is demarcated using a type-I constant head boundary. A steady-state flow field is then established, and the stable flow entering the tunnel is calculated.
- **Maximum inflow volume:** Based on the dynamic analysis of groundwater, the rate of groundwater level rise during the rainy season is identified. During the calculations, the drainage tunnel is still processed with a type-I constant head boundary. Building upon the steady-state flow field, the boundary and nodal heads are demarcated according to the rate of groundwater level rise during the rainy season. The inflow volume into the drainage tunnel is then determined for the end of the rainy season or the period when the rate of groundwater level rise is at its maximum.

6.5 Numerical Prediction of Mine Water Inrush: A Case Study in Liuyuanzi Coal Mine, China

Using the Liu Yuanzi coal mine in Gansu Province, China, as an example (Song, 2013), a comprehensive understanding of various hydrogeological conditions in the mining area was established. MODFLOW software was employed to set up a numerical groundwater flow model for the mining region (Fernández-Álvarez et al., 2016). Utilizing the monitored data of inflow volume from the already developed sections of the mine, the model parameters were directly identified and calibrated. Numerical simulations and analytical calculations were then carried out to determine the inflow volumes during both the tunnel development phase and the coal mine extraction period.

6.5.1 Overview of the Mining Area

6.5.1.1 Location and Hydrometeorology

The Liu Yuanzi coal mine is located to the east of the Shajingzi mining area in the western part of Huan County, Qingyang City, Gansu Province. Its geographical coordinates are $106^{\circ} 48' 45''\text{E}$ – $106^{\circ} 50' 45''\text{E}$ longitude and $36^{\circ} 28' 30''\text{N}$ – $36^{\circ} 31' 15''\text{N}$ latitude, with an elevation of 1523–1823 m. The mine spans an area of 9.9 km². Positioned on the western part of the Loess Plateau in eastern Longdong, the mine's topography is characterized by hilly and gully terrains of the Loess Plateau. Over 90% of the area within the mining region is covered by Quaternary loess, with a loess thickness varying from 60 to 240 m. The mountain ranges primarily run in a northwest direction, turning east–west in the northern part. The topography is dramatically dissected with well-developed gullies between mountains. The region's average annual temperature is 8.9 °C. Precipitation is primarily concentrated between July and September, often in the form of heavy downpours, with an average annual rainfall of 408.9 mm. The annual average evaporation rate is 1681.7 mm, indicating that the region is typically arid to semiarid. The main river developed in the study area is the Mafuchuan River, a first-level tributary of the Huanjiang River. It is a seasonal stream with observed flow rates of 0–33.74 m³/d.

6.5.1.2 Geology

The mining area hosts a stratigraphic development that includes, from oldest to youngest, the Triassic, Jurassic, Cretaceous, and Quaternary series. As illustrated in Fig. 6.3, the Jurassic Yan'an Formation (J2y) is the only coal-bearing stratum within the mining area. From the syncline center outward, the middle and upper parts of the Yan'an Formation are eroded to varying extents. Based on lithology, facies, coal content, and sedimentation, there are four identifiable coal seams (Coal 4–1, Coal 5–1, Coal 7–1, and Coal 8–3). The prospective mining face is located in the 51 mining area of the Liu Yuanzi coal mine and consists of the Coal 4–1 and Coal 5–1 seams. The mining face length in the extraction area is 180 m, with the primary mining height averaging 2.0 m. Specifically, Coal 4–1 spans 1 km east–west and 2.5 km north–south, taking an elliptical shape with a total area of 1.80 km². Within the extractable area, the coal seam thickness ranges from 1.83 to 2.56 m, averaging 2.15 m, exhibiting a pattern where the center is slightly thicker and the wings are thinner, with a south-thin to north-thick trend. Coal 5–1, centered around the axial part of the Liu Yuanzi syncline, spans 1.4 km east–west and 4.1 km north–south, also forming a closed elliptical coal distribution area with a size of 4.25 km². Within this coal-rich area, the coal seam thickness ranges between 5.12 and 8.83 m, with an average of 6.98 m. This makes it the thickest coal seam in the Liu Yuanzi mining area and the one with a significant resource volume. The working face of this mine is complex. During shaft sinking and drift construction, some faults were exposed.

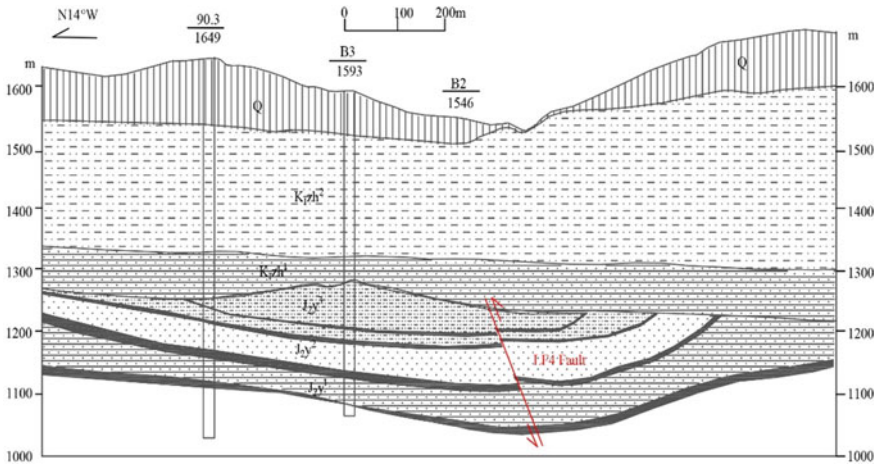


Fig. 6.3 Hydrogeologic profile of the mine site (Song, 2013)

Among them, the LF4 normal fault provides a connection to the waters from the Cretaceous series and the roofs of the Coal 4–1 and Coal 5–1 seams.

6.5.1.3 Hydrogeology

Based on the aquifer characteristics of the geological strata, the groundwater in the study area can be categorized into three main types: Quaternary unconsolidated rock fracture-pore phreatic water, bedrock surface weathered fracture phreatic water, and bedrock fracture-pore confined water.

- **Quaternary Unconsolidated Rock Fracture-Pore Phreatic Water:** The sole recharge source for the groundwater is vertical infiltration from atmospheric precipitation. Due to the local topography consisting of beams, mounds, and hills with a significant slope, most atmospheric precipitation forms surface runoff in valleys, limiting infiltration recharge to groundwater. Once the groundwater is recharged, it drains along the gullies, resulting in short flow paths. Consequently, the loess phreatic water content in this area is minimal.
- **Bedrock Surface Weathered Fracture Phreatic Water:** Located within the surface weathered fractures of the Upper Cretaceous Zhidan Group bedrock. There are no natural groundwater outcrops within the mining field. The spring flow rate in the surrounding areas ranges from 0.008 to 0.186 L/s, typically less than 0.10 L/s, indicating extremely weak aquifer characteristics. The water chemistry is diverse, with a mineralization degree ranging from 1712.0 to 2581.3 mg/L. Groundwater mainly receives recharges from atmospheric precipitation and surface water, flowing from higher terrains to lower ones. The general flow trend

is from northwest to southeast, draining out of the area through lateral groundwater flow.

- **Bedrock Fracture-Pore Confined Water:** This represents a fully independent and closed confined aquifer, with the aquifer rock type being sandstone of various grain sizes, creating a composite aquifer. Sandstones are 27–140 m thick, accounting for 44–86% of the total strata thickness, averaging 64%. Sandstones are generally well cemented with poorly developed pores and fractures. There are no outcrops of this aquifer on the surface around the mining area. It mainly receives overflow recharge from the “Cretaceous water” in the northern and northwestern sections, having poor recharge conditions and very weak aquifer characteristics. Considering mine flooding due to coal mining, the extraction of coal seams will form bursting zones, and the overlying sandstones of each coal layer will become independent closed confined aquifers. Those posing significant flooding threats to coal mining mainly include the following: ① Sandstones over the coal 4–1 layer have a smaller thickness, poorer cementation and are more porous. Their thickness varies from 0.79–18.55 m, averaging approximately 8 m, with an increasing trend from north to south. ② Sandstones over the coal 5–1 layer have a larger thickness, poor cementation and are loose. Their thickness ranges from 2.3–36.6 m, averaging approximately 20 m, also with an increasing trend from north to south.

6.5.1.4 Characterization of Groundwater Dynamics

Based on existing records of the aquifer’s dynamics within the region, groundwater behavior is directly influenced by meteorological and hydrological factors. After rainfall events, there is a general rise in groundwater levels and a decrease in mineralization levels. Throughout the year, groundwater levels fluctuate between 0.3 and 0.5 m, while mineralization variations range from 0.3 to 0.5 mg/L. The lowest groundwater levels typically occur between March and May, while the highest levels are usually observed between July and October. The annual variation in artesian water levels is less pronounced than that in groundwater levels. Influenced by mine drainage, there has been a slight decline in groundwater levels across the research area, with some exploratory boreholes showing drops exceeding 40 m from their initial levels at the time of well construction.

In the mining area, “Cretaceous water” serves as the primary source of recharge. A distinctive feature of the mining pit is the water from the “Coal 5–1 cap,” which represents the main direct recharge aquifer layer. Observations over a five-month period indicate that the inflow rates under artificial drainage conditions have shown a declining trend, although the magnitude of the decrease is generally minimal, with the exception of a more significant reduction in fault water. The inflow in the mine is predominantly concentrated in the “Coal 5–1 cap” with a steady rate of 104 m³/h. Following this, fault water shows an inflow rate of 80 m³/h, which is relatively consistent.

6.5.2 Model Setup

6.5.2.1 Conceptual Hydrogeological Model

- **Modeling area scope:** Due to the difficulty in generalizing the boundary conditions surrounding the research area, to eliminate the influence of these boundary conditions, the modeling area was expanded by 3 km on all sides from the target research scope. Consequently, the final simulation area spans 12 km from north to south and 10 km from east to west, covering a total of 120 km². Vertically, it extends from the Quaternary strata above to the upper part of the Triassic below.
- **Generalization of boundary conditions:** Based on the hydrogeological conditions of the research area and the analysis of water level records from observation wells near the boundaries, it is observed that water level changes over time in these wells are minimal. Hence, the boundaries were generalized as fixed-head boundaries. For the Mafuchuan valley, since the valley has cut into the Cretaceous layer and has seasonal flows during the flood season and considering its hydraulic connection with groundwater, it is generalized as an intermittent third-type river boundary. The top boundary of the simulation area is exposed to the atmosphere, where vertical water exchanges such as atmospheric precipitation infiltration and groundwater evaporation occur, making the use of a phreatic surface boundary appropriate. The base boundary of the simulation area is Triassic, characterized by sands of various grain sizes. Due to the good cementation and poorly developed pores and fissures in the sandstone, its recharge conditions are unfavorable, and its water-bearing capacity is very weak; hence, it can be generalized as an impermeable boundary.
- **Recharge, runoff, and discharge conditions:** The main groundwater recharges within the modeling area are infiltration from atmospheric precipitation, seepage recharge from parts of the Mafuchuan area, and lateral groundwater runoff from surrounding boundaries. The principal groundwater discharges are mine tunnel drainage, artificial extraction, groundwater evaporation, and lateral groundwater runoff to surrounding areas. In the water-bearing layers of the modeling area, groundwater generally flows from west to east. In some areas influenced by mine tunnel drainage, localized groundwater flow systems are evident. In areas with intense mine inflow and human extraction activities, funnel-shaped depressions form, directing groundwater flow from the surrounding areas toward the center of these depressions.

In summary, the three-dimensional flow characteristics of the groundwater in the region are significant. The medium is generalized as a heterogeneous isotropic medium, and the movement of groundwater conforms to Darcy's law.

6.5.2.2 Mathematical Model

Based on the aforementioned hydrogeological conceptual model, the three-dimensional seepage issue of the groundwater in the research area can be described using the following three-dimensional unsteady flow mathematical model:

$$\left\{ \begin{array}{l} \frac{\partial}{\partial x} (K \frac{\partial H}{\partial x} + \frac{\partial}{\partial y} (K \frac{\partial H}{\partial y})) + \frac{\partial}{\partial z} (K \frac{\partial H}{\partial z}) = S_s \frac{\partial H}{\partial t} \quad (x, y, z) \in \Omega, t > 0 \\ H(x, y, z, 0) = H_0(x, y, z) \quad (x, y, z) \in \Omega \\ \left. \begin{array}{l} H = z \\ -(K + W) \frac{\partial H}{\partial z} + W = \mu \frac{\partial H}{\partial t} \end{array} \right\} \quad \text{Water table boundary} \\ H(x, y, z, t)|_{\Gamma_1} = H_1(x, y, z) \quad t > 0 \\ \left. \begin{array}{l} \frac{\partial H}{\partial x} |_{\Gamma_2} = 0 \\ \lim_{r \rightarrow r_w} \left[r \int_0^{2\pi} K M \frac{\partial H}{\partial r} d\theta \right] = Q_i \end{array} \right\} \quad t > 0, \text{ Well} \\ \left. \begin{array}{l} K' \frac{H_r - H}{M'} A = Q_r \\ K' \frac{H_d - H}{M'} A = Q_d \end{array} \right\} \quad \begin{array}{l} t > 0, \text{ Mafuchuan} \\ H_d < H, t > 0, \text{ Mine tunnel} \end{array} \end{array} \right. \quad (6.6)$$

where,

- H_0 is the initial groundwater head (m);
- H is the elevation of the groundwater table (m);
- K is the hydraulic conductivity (m/d);
- S_s is the specific storage (1/m);
- M is the thickness of the aquifer (m);
- $x, y,$ and z are coordinate variables (m);
- H_1 is the elevation of the first type (fixed head) boundary groundwater (m);
- W is the vertical water exchange intensity ($\text{m}^3/\text{d m}^2$);
- Q_i is the extraction rate of the i th well (m^3/d);
- R is the radial distance from the pumping well (m);
- K' is the vertical permeability of the sediment layer at the bottom of the Mafuchuan River and mine tunnel (m/d);
- M' is the thickness of the sediment layer at the bottom of the Mafuchuan River and mine tunnel (m);
- A is the area of the Mafuchuan River and mine tunnel (m^2);
- Q_r is the water exchange volume between the Mafuchuan River and groundwater (m^3/d);
- Q_d is the volume of groundwater drained by the mine tunnel (m^3/d);
- H_r is the water elevation in the Mafuchuan River (m);
- H_d is the drainage elevation in the mine tunnel (m);
- Γ_1 is the type I boundary;
- Ω is the computational domain;
- Γ_2 is the bottom boundary;
- N is the normal direction to the bottom surface of the Jurassic system.

The numerical simulation model of groundwater flow in this study area was established by using MODFLOW, a finite difference software developed by the U.S. Geological Survey (USGS), and the parameters of the model were assigned on the basis of organizing and analyzing a large amount of basic information.

6.5.2.3 Three-Dimensional Hydrogeologic Modeling

The hydrogeological three-dimensional model of the study area incorporates various hydrogeological data into a 3D geometric framework. Specifically, this model encompasses boundary conditions around and beneath the study area, groundwater evaporation, mine tunnel drainage, atmospheric precipitation infiltration, seasonal river recharge, initial flow field, human-induced extraction, and initial values of hydrogeological parameters.

- Initial selection of model parameters. The various parameters required to solve the model include the hydraulic conductivity (K) of different aquifers, the drainage coefficient of the tunnels, and the specific storage coefficient (S). After a thorough analysis of the hydrogeological conditions of the study area and based on the collected data from previous pumping tests conducted in the area, the initial values of the parameters for this model were determined.
- Boundary conditions on the periphery and bottom. Based on the hydrogeological conceptual model of the research area, the water levels on the surrounding boundaries generally do not vary significantly. Therefore, in the model, these are set as constant head boundaries based on the initial water level. The bottom boundary of the calculation area corresponds to the Triassic strata. As analyzed above, this stratum has good cementation, low permeability, and weak water enrichment, and the groundwater is in a stagnant state. Its impact on the mine tunnels is negligible; hence, it is treated as a no-flow boundary.
- Atmospheric precipitation infiltration recharge. Based on the collected meteorological data, there are minimal differences in the precipitation recorded at different meteorological stations within Huan County. After multiplying by the coefficient of effective precipitation, these differences become even smaller. To simplify the calculations, the average precipitation value from all meteorological stations within Huan County is used as the input for the model. This recharge is applied to the topmost active layer of the model.
- Groundwater evaporation. Along the valley segment of the Mafu River, the groundwater level is relatively shallow, making subsurface evaporation a potential pathway for groundwater discharge. The evaporation rate used in this study, derived from meteorological station data in Huan County, is multiplied by a factor of 0.62 to convert the observed evaporation rate to the open water surface evaporation, as indicated in Eqs. (6.7) and (6.8). The maximum depth for potential groundwater evaporation is set at 5 m.

$$E_{0i} = E_i \times 0.62 \quad (6.7)$$

$$Q_{\text{蒸}} = \sum_i E_{0i} \left(1 - \frac{s_i}{\Delta S_i}\right)^n A_i \quad s_i < \Delta s \quad (6.8)$$

where,

Q is the groundwater evaporation volume in the research area (m^3);

E_i is the observed evaporation rate at the meteorological station (m).

E_{0i} is the open water surface evaporation rate (m).

s_i is the burial depth of the groundwater (m).

ΔS is the maximum evaporation depth of the groundwater (m).

A_i is the area of the unit cell (m^2).

n is a control factor, set at 2.

- **Artificial extraction:** Artificial extraction is one of the primary discharge amounts in the study area. According to the hydrogeological exploration report for water supply in the study area, the artificially extracted wells mainly serve residential water needs, requiring $1000 \text{ m}^3/\text{day}$.
- **Mafu River (or Mafuchuan):** Within the study area, the Mafu River flows from southwest to northeast. In some segments, it has eroded deeply, reaching the top of the Cretaceous strata. The exchange volume between the Mafu River and the local groundwater is calculated using Eq. (6.9).

$$Q_r = K' A \frac{H_r - H}{M'} = C(H_r - H) \quad (6.9)$$

where,

Q_r is the seepage recharge volume of the Mafu River (m^3/day);

H is the groundwater level of the cell (or node) where the Mafu River is located (m);

H_r is the water level elevation of the Mafu River (m);

K' is the vertical permeability of the Mafu River's sediment (m/day);

M is the thickness of the sediment in the Mafu River (m);

A is the area of the Mafu River in the corresponding cell (m^2);

C is the hydraulic conductivity of the Mafu River's sediment (m^2/day).

- **Mine tunnel drainage performance.** From the tunnel drainage (spring flow) calculation Eq. (6.10), it is evident that the permeability performance of tunnel drainage is related to grid partitioning, tunnel size, surrounding rock parameters, etc. The following formula can be used for the calculation:

$$C = \frac{K}{\Delta l} \cdot \pi D \cdot L \quad (6.10)$$

where,

C is the permeability performance of the mine tunnel (m^2/d).

K is the hydraulic conductivity of the surrounding rock in the unit where the mine tunnel is located (m/d).

Δl is the distance from the center point of the mine tunnel to the center of the unit (m).

D is the diameter of the mine tunnel (m).

L is the length of the tunnel within the unit where the mine tunnel is located (m).

- Initial flow field: To depict the general flow field characteristics of the computation zone, the initial flow field utilized is based on long-term average precipitation data. This was derived through the establishment of a stable flow model under the long-term average conditions of the computation zone before the excavation of the mine tunnels. Figures 6.4 and 6.5 depict the groundwater flow field and water level drop after the completion of the tunnel construction, respectively, as well as the contour map of the groundwater flow field and water level drop in the main aquifers of the mining area 20 years later.
- Model solution method: The preconditioned conjugate gradient (PCG) method is adopted for solving the model. In this computation process, the maximum number of external iterations is set at 500, while the maximum number for internal iterations is capped at 250. The convergence criterion for water level change is set at 0.001 m, and the residual convergence standard is also 0.001 m. The damping coefficient is set at 0.8.

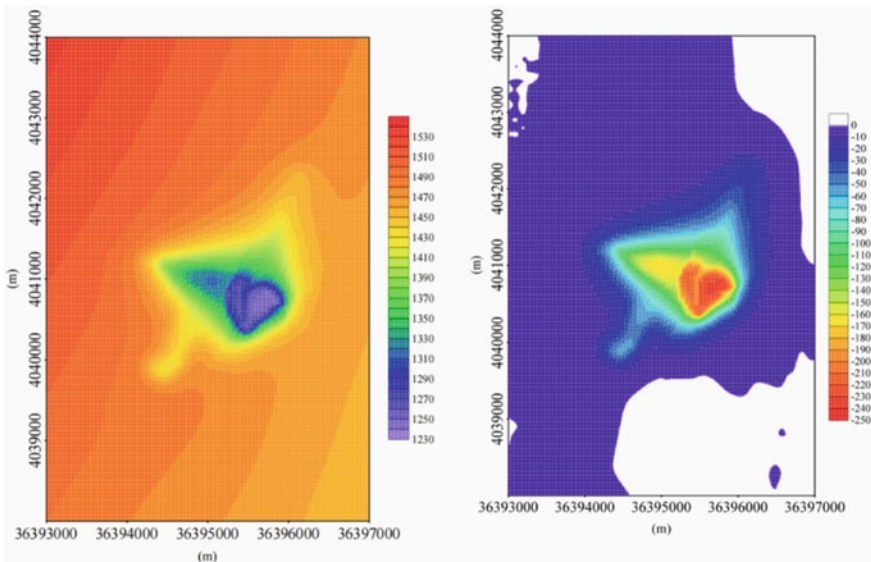


Fig. 6.4 Groundwater flow field and drawdown field after construction of the mine tunnel (Song, 2013)

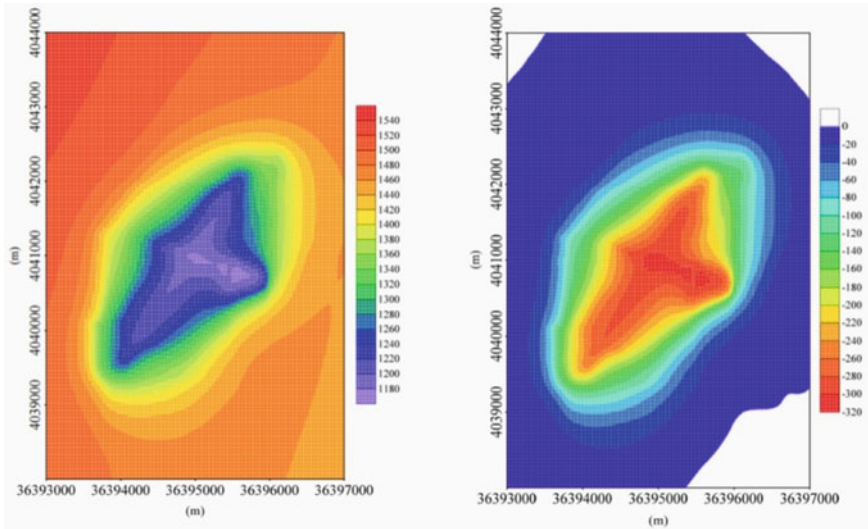


Fig. 6.5 Groundwater flow field and drawdown field in the study area 20 years after completion of the mine tunnel construction (Song, 2013)

6.5.3 Prediction of Mine Water Inrush

6.5.3.1 Water Inrush During Shaft Development

Based on the tunnel development construction plan, under long-term average hydrological and meteorological conditions, the corresponding model is used to predict the inflow volume of the mine tunnel. The settings of the tunnel boundary in the model are arranged monthly based on the selected construction plan schedule, taking each construction month as a unit. For the construction section in progress, its drainage elevation is the floor elevation of that section, and the permeability of the tunnel corresponds to its construction period. After inputting relevant data into the model, the inflow volume during mine tunnel development can be calculated. According to the results, due to differences in traversed rock layers, faults, drainage elevation differences, tunnel lengths, etc., the inflow volume during mine tunnel development varies, as shown in Fig. 6.6. The variations in inflow volume during the construction period are mainly characterized by the following features:

- Peak in inflow volume when a fault is exposed during construction: At the beginning of the exposure, the water gushing from the fault is mainly due to the depletion of the stored water within the fault. As time progresses, the storage in the fault gradually depletes, and the water gush becomes dominated by the water-conducting channels within the fault, stabilizing the inflow volume.
- Inflow volume is significantly affected by tunnel length and drainage elevation difference during construction: If there is a longer construction length in

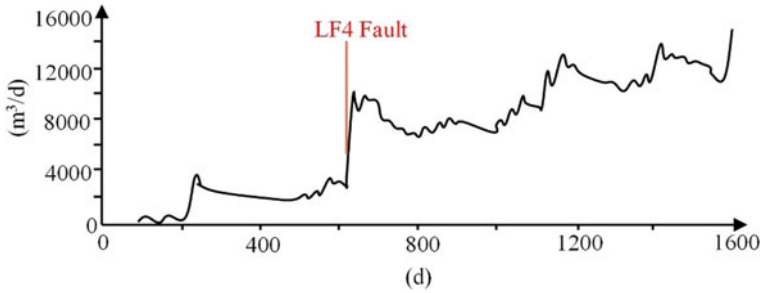


Fig. 6.6 Predicted water inflow in the mine tunnel during development (Song, 2013)

a short period or a larger drainage elevation difference, a smaller peak in the inflow volume can also occur. Thus, during development, the inflow volume often fluctuates in a sawtooth pattern.

- As the length of the tunnel extends, the inflow volume also gradually increases, eventually reaching $629 \text{ m}^3/\text{h}$.

6.5.3.2 Water Inrush During Wellfield Mining

The design proposes a combined mining approach for the Coal 4–1 and Coal 5–1 seams. The mining layout for the upward inclined section is situated within the Coal 5–1 seam. Within this seam, three inclinations are planned following the dip direction. These are the rail incline, the conveyor belt incline, and the return air incline. The distance between each passage is set at 30 m. It is recommended to adopt a descending mining approach for the design. Specifically, mining should begin with the Coal 4–1 seam within the 51 mining zone. The coal flow from the working face of the Coal 4–1 seam will be transferred to the Coal 5–1 seam conveyor belt inclined through chutes in each section (the coal from the primary working face will be directly fed to the conveyor belt via the chutes). The auxiliary transportation and ventilation from the Coal 4–1 working face will be connected through the auxiliary transport inclines, ventilation inclines, and the main rail and air inclines in the mining zone. The design confirms that the working face length in the 51 mining zone is 180 m. The average mining height for the initial mining face is 2.0 m.

Based on the aforementioned establishment of the numerical model for groundwater flow in the research area, by utilizing multiyear average data on precipitation, evaporation, and river flow, a predictive model for mine water inflow during the mining period in the research area can be established.

Figure 6.7 depicts the relationship between mine water inflow and time under the mining conditions of the research area. It reveals that:

- In the early stages of mining, as the mining area expands, the inflow of water increases continuously, peaking at $912 \text{ m}^3/\text{h}$. The surrounding groundwater in the

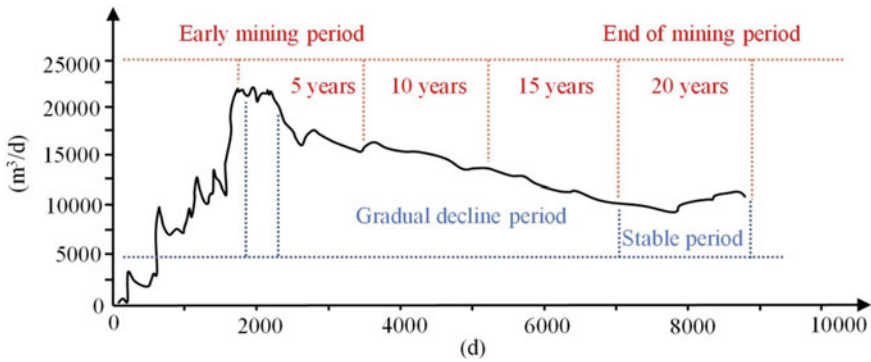


Fig. 6.7 Projected water volumes in response to mining progress (Song, 2013)

mining area gradually drains into the tunnels, leading to a brief period where the runoff achieves a balance with drainage.

- During the mining process, water from the aquifer consistently flows into the tunnels. However, due to the high-intensity drainage within the tunnels, the aquifer can no longer meet the drainage demands, resulting in a decreasing trend in the amount of water inflow to the tunnels.
- In the later stages of mining, the groundwater funnel continues to develop, leading to a gradual stabilization of the tunnel's water inflow. The inflow stabilizes at approximately 10,000 m³/day.

6.5.3.3 Comparison of Different Prediction Methods

A comparative analysis of mine water inflow was conducted by juxtaposing the results from analytical methods with those from numerical methods. The analytical method, grounded in the principles of groundwater dynamics, employs mathematical analysis tailored to specific hydrogeological conditions. This method idealizes scenarios under steady-flow conditions to estimate the mine water inflow. The results reflect a consistent replenishment rate, thereby eliminating the influence of storage volume.

Calculation of Mine Water Influx by the Steady Flow Analysis Method

- Explanation of the calculation of water inflow volume: After mining the Coal 4–1 and Coal 5–1 seams, the filling of water in the mine pit will mainly originate from the storage and replenishment of “① Cretaceous water” located above the coal seam roof, storage from “② Coal 4–1 roof water”, and storage from “③ Coal 5–1 roof water”. Once the mine pit is established and under steady-flow conditions, the inflow of water into the mine is primarily facilitated by water-conducting

Table 6.1 Calculation results of mine water inrush from the roof aquifer

Selected parameter					Q_1 (m ³ /h)
K (m/d)	M (m)	H_0 (m)	a:b	r_w (m)	
0.041	111	264	3.4	1040	598.9

fissure zones. Water from the “① Cretaceous aquifer” flows into the pit. The immediate rock strata beneath the coal seam primarily consist of silty sandstone, sandy mudstone, and mudstone. Moreover, the water-conducting fissure zones formed at the base of the coal seam are weak. Therefore, the water inflow from the base of the coal seam is not calculated here.

- Inflow volume from roof aquifers into the mine system: The calculation of the inflow volume from roof aquifers into the mine system adopts Eq. (6.11), which is the formula for transitioning from confined to unconfined conditions in a complete well.

$$\begin{cases} Q = \frac{\pi K (2H_0M - M^2 - h_w^2)}{\ln\left(\frac{R}{r_w}\right)} \\ R = 10s_w\sqrt{K} + r \\ h_w = H_0 - s_w \end{cases} \quad (6.11)$$

where,

Q is the volume of water entering the mine system (m³/d);

K is the hydraulic conductivity (m/d);

H_0 is the height of the confined water head (m);

M is the thickness of the aquifer (m);

h_w is the height of the water column during maximum drainage (m). It is taken as 0.

s_w is the drop in height during maximum drainage (m). It is taken as H_0 ;

R is the influenced radius of the mine system (m);

r_w is the reference radius of the mine system (m).

Based on Eq. (6.11) and utilizing borehole data collected from the research area through stratified analysis, the necessary parameters for the formula were determined. The final calculated inflow volume from the roof is 598.9 m³/h. For further details, refer to Table 6.1.

- Accounting for other water inflow sources. Apart from the inflow from the roof aquifer into the mine pit, there is also the contribution of water from the wellbore, fault zones, and other aquifers filling the mine, as detailed in Table 6.2. The combined water inflow from fault zones, wellbore, and other aquifers to the mine pit is 231.9 m³/h.
- Total water inflow into the mine system. The overall inflow volume to the mine system is the sum of the inflow from the roof aquifer and other sources. From

Table 6.2 Water inrush from other sources (m³/h)

Shaft	Fault	Other aquifers	Total inrush
34.4	180.5	17.0	231.9

the calculations mentioned above, the maximum water inflow into the mine is determined to be 792 m³/h.

Analogical Analysis of Mine Water Inrush

Compared to the results obtained using numerical methods, the analytical method results are slightly smaller. The primary reason for this discrepancy is that the steady-flow analytical method only considers the contribution of the Cretaceous system and other water inflow factors under stable conditions while overlooking the dynamic effects of aquifer storage and replenishment on the mine water inflow. However, in numerical terms, the difference between the two is less than 15%. This demonstrates the appropriateness of establishing and parameter identification and correction processes for the groundwater flow numerical model in this study. This proves its capability to effectively predict mine water inflow changes. Hence, the standard mine water inflow calculations adopt the results from the numerical method.

From the aforementioned calculation process, it is evident that when determining mine water inflow using the analytical method, a steady-state water inflow model is established by idealizing hydrogeological conditions. The calculation process is relatively simple and requires fewer parameters and hydrogeological data. Despite continuous advancements in computer technology and numerical simulation techniques, the analytical method, due to its simplicity and practicality in operation, remains a predominant method for calculating mine water inflow today. However, it is most suitable for predicting mine water inflow in mines with simpler hydrogeological conditions. Additionally, the model overlooks a series of complex hydrogeological conditions, including aquifer storage, faults, fissures, etc. Thus, it is challenging to present the dynamic changes in water inflow under complex conditions and cannot explicate the intricate hydraulic relationships between multiple aquifers.

Compared to the analytical method, the numerical method, although reliant on extensive hydrogeological data and featuring a more complex modeling and solution process, is adept at predicting mine water inflow under intricate conditions. It can depict the dynamic changes in mine water inflow under various conditions, representing the leading direction in the evolution of mine water inflow prediction.

In summary, although the analytical method has a lower prediction accuracy compared to the numerical approach, its straightforward operation and cost-effective processing make it the preferred method for calculating mine water inflow under simpler conditions. However, for complex natural hydrogeological conditions, where boundary conditions and aquifer characteristics are difficult to generalize into ideal scenarios, the numerical method emerges as an effective tool for mine water inflow calculations. With the rapid advancement of computer technology, the prospects for applying numerical methods are becoming even more promising.

References

- Cao ZZ, Ren YL, Wang QT, Yao BH, Zhang XC (2021) Evolution mechanism of water-conducting channel of collapse column in Karst mining area of southwest China. *Geofluids* 2021:8
- Capta SK, Chen HC (1984) Finite analytic numerical method for unsteady two-dimensional Navier-Stokes equations. *J Comput Phys* 53:209–226
- Dong S, Wang H, Guo X, Zhou Z (2021) Characteristics of water hazards in China's coal mines: a review. *Mine Water Environ* 40(2):325–333
- Fernández-Álvarez JP, Álvarez-Álvarez L, Díaz-Noriega R (2016) Groundwater numerical simulation in an open pit mine in a limestone formation using MODFLOW. *Mine Water Environ* 35(2):145–155
- Gui HR, Lin ML (2016) Types of water hazards in China coalmines and regional characteristics. *Nat Hazards* 84(2):1501–1512
- Kihm JH, Kim JM, Song SH (2007) Three-dimensional numerical simulation of fully coupled groundwater flow and land deformation due to groundwater pumping in an unsaturated fluvial aquifer system. *J Hydrol* 335:1–14
- Li P, Wu J, Tian R et al (2018a) Geochemistry, hydraulic connectivity and quality appraisal of multilayered groundwater in the Hongdunzi Coal Mine, Northwest China. *Mine Water Environ* 37:222–237
- Li W, Liu Y, Qiao W et al (2018b) An improved vulnerability assessment model for floor water bursting from a confined aquifer based on the water inrush coefficient method. *Mine Water Environ* 37:196–204
- Li B, Zhang H, Luo Y et al (2022) Mine inflow prediction model based on unbiased Grey-Markov theory and its application. *Earth Sci Inf* 15:855–862
- Liu JH, Zhao YL, Tan T, Zhang LY, Zhu ST, Xu FY (2022) Evolution and modeling of mine water inflow and hazard characteristics in southern coalfields of China: a case of Meitanba mine. *Int J Min Sci Technol* 32(3):513–524
- Ma D, Duan H, Li W et al (2020) Prediction of water inflow from fault by particle swarm optimization-based modified grey models. *Environ Sci Pollut Res* 27:42051–42063
- Odintsev VN, Miletenko NA (2015) Water inrush in mines as a consequence of spontaneous hydrofracture. *J Min Sci* 51:423–434
- Peng H, Frenelus W, Zhang JG (2022) Key factors influencing analytical solutions for predicting groundwater inflows in rock tunnels. *Water Supply* 22(11):7982–8013
- Polak K, Rózkowski K, Czaja P (2016) Causes and effects of uncontrolled water inrush into a decommissioned mine shaft. *Mine Water Environ* 35:128–135
- Slesarev B (1983) Conditions for safe coal mining under water (development and practice of foreign mine water control technology). Metallurgical Mine Design Institute
- Song B (2013) Forecasting research of mine inflow of Liuyuanzi coal zone in Gansu Province. Master's thesis, Chang'an University (in Chinese)
- Sun W, Zhou W, Jiao J (2016) Hydrogeological classification and water inrush accidents in China's coal mines. *Mine Water Environ* 35:214–220
- Wang D, Sui W, Ranville JF (2022) Hazard identification and risk assessment of groundwater inrush from a coal mine: a review. *Bull Eng Geol Env* 81:421
- Wu C, Wu X, Zhu G et al (2019) Predicting mine water inflow and groundwater levels for coal mining operations in the Pangpangta coalfield, China. *Environ Earth Sci* 78:130
- Wu M, Ye Y, Hu N et al (2022) Visualization analysis and progress of mine water inrush disaster-related research. *Mine Water Environ* 41:599–613
- Xu LL, Mf C, Dong SN, Yin SX et al (2022) An upscaling approach to predict mine water inflow from roof sandstone aquifers. *J Hydrol* 612:128314
- Yin H, Wei J, Leticariu L et al (2016) Numerical simulation of water flow from the coal seam floor in a deep longwall mine in China. *Mine Water Environ* 35:243–252

- Yin H, Zhao H, Xie D et al (2019) Mechanism of mine water inrush from overlying porous aquifer in Quaternary: a case study in Xinhe Coal Mine of Shandong Province, China. *Arab J Geosci* 12:163
- Zeng Y, Wu Q, Liu S et al (2018) Evaluation of a coal seam roof water inrush: case study in the Wangjialing coal mine, China. *Mine Water Environ* 37:174–184
- Zhang HM, Zhai XR, Wu JW, Shen SH (2017a) Study on water inrush mechanism of subsided column under deep coal seam mining fluid-solid coupling effect. *Coal Min* 22(5):102–105
- Zhang K, Cao B, Lin G et al (2017b) Using Multiple methods to predict mine water inflow in the Pingdingshan no. 10 coal mine, China. *Mine Water Environ* 36:154–160
- Zhang JJ, Xu KL, Reniers G, Greg Y (2020) Statistical analysis the characteristics of extraordinarily severe coal mine accidents (ESCMA) in China from 1950 to 2018. *Process Saf Environ Prot* 133:332–340
- Zhang C, Bai Q, Han P (2023) A review of water rock interaction in underground coal mining: problems and analysis. *Bull Eng Geol Env* 82:157

Chapter 7

Groundwater Contamination and Induced Risk and Hazard in a Karst Aquifer



Studying and rehabilitating groundwater in hydrogeologic settings such as karst, fractured rock, and deep alluvial aquifer systems presents significant challenges. The process of restoring aquifers and developing accurate conceptual site models becomes even more complex due to various factors associated with contaminants. The coexistence of light non-aqueous phase liquids (LNAPLs) and dense non-aqueous phase liquids (DNAPLs) further complicates the selection of appropriate remedial response strategies. In order to assess the feasibility of restoration efforts, the National Research Council (NRC 1994) has categorized sites into different classes, as illustrated in Table 7.1.

The intricate nature of hydrogeologic conditions in karst terranes poses challenges for aquifer restoration efforts. The variations in porosity and hydraulic conductivity within these terranes make it difficult to predict changes in hydraulic head, groundwater flow, and contaminant transport. Typically, a small percentage of the aquifer volume accounts for the majority of water flow and contaminant migration. Therefore, targeting remedial actions towards these permeable pathways may enhance restoration effectiveness. However, identifying these significant transport zones in karst hydrogeologic settings can be challenging. Furthermore, complexities arise from vertical hydraulic connections that exist within multiple water-bearing formations, as well as the influence of groundwater production wells on the movement and direction of groundwater and contaminants.

Characterizing the distribution of contaminants, groundwater flow paths, and potential receptors in karst environments with open conduit flow poses significant challenges. Contaminants exhibit distinct behavior in karst aquifers compared to granular or fractured rock aquifers. Within karst aquifers, contaminants can be stored in the vadose zone and the contact zone between bedrock and overburden, known as the epikarst zone. Periodic recharge events, such as seasonal or storm-related influxes, can flush a part of the contaminants into the bedrock aquifer. Groundwater flow within the bedrock converges towards conduits, such as subterranean caverns, resulting in rapid flow over long distances towards receptors. It is important

Table 7.1 Feasibility and relative ease of contaminated groundwater investigation and remediation (NRC 1994)

Hydrogeological properties	Properties of contaminants					
	Mobile and dissolved	Mobile and dissolved	Strongly sorbed and dissolved	Strongly sorbed and dissolved	Separate phase of LNAPLs	Separate phase of DNAPLs
Homogeneous, and single layers	1	1-2	2	2-3	2-3	3
Homogeneous, and multiple layers	1	1-2	2	2-3	2-3	3
Heterogeneous, and single layers	2	2	3	3	3	4
Heterogeneous, and multiple layers	2	2	3	3	3	4
Fractured and Karst	3	3	3	3	4	4
1 and 1-2	Achieving a full cleanup of aquifers to meet health-based standards is considered feasible based on current knowledge.					
2, 2-3, and 3	The feasibility of achieving a complete technical cleanup is likely to be uncertain.					
4	Currently, there are no available technologies capable of fully cleaning up aquifers.					

to acknowledge that conventional groundwater flow equations may not accurately capture the turbulent flow dynamics present in karst environments. The presence of DNAPLs further complicates aquifer restoration, as specialized techniques are required to assess associated risks and hazards. To address these intricate challenges, this chapter presents a compelling case study that showcases the implementation of specialized techniques and innovative approaches for the assessment and mitigation of contaminated groundwater.

7.1 Investigation Approaches

The geological characteristics of the study area, which included karst-type lithologies, presented significant challenges in gathering the necessary data for hydrogeological characterization. Compared to aquifers in other hydrogeologic settings, the investigation in karst areas required tailored approaches that were typically conducted in phases (Teutsch and Sauter 1991). Figure 7.1 illustrates the various techniques employed in the remedial investigation of the specific karst site. A three-phase approach was utilized to characterize the site, and this section provides detailed descriptions of several techniques that were unique to this site-specific investigation. The presence of karst is indicated by the formation of distinct physiographic features that develop due to the dissolution of soluble limestone or dolomite beneath the surface. These features may include sinkholes, sinking streams, caves, and springs. The hydrological characteristics associated with karst environments are also unique and typically involve the following: (1) Internal drainage of surface runoff through sinkholes. (2) Diversion or partial subsurface flow of surface streams, known as sinking streams or losing streams. (3) Vertical structure comprising three zones: overburden, epikarst, and bedrock. (4) Bedrock aquifer characterized by triple-porosity, including pores, fractures, and conduits. (5) Release of subsurface water from conduits through one or more large and continuous springs. Karst aquifers

exhibit heterogeneity and possess hydraulic properties that vary depending on the scale of observation and may also change over time.

In areas with karst features, it is crucial to acknowledge that conventional hydrogeologic techniques alone, such as potentiometric mapping, hydraulic testing of monitoring wells, or numerical modeling, may not fully characterize the flow system. Gathering the necessary data often requires a phased and multidisciplinary approach that integrates specialized investigation methods. Some of these methods include:

Water-tracing tests: These tests involve introducing a tracer substance into the groundwater system and monitoring its movement to understand the flow paths and connections between different parts of the aquifer. Tracers can be dyes, fluorescent substances, or isotopes that can be detected and traced back to their source.

Digital geophysical mapping: Geophysical methods, such as electrical resistivity tomography (ERT) or ground-penetrating radar (GPR), can be used to map subsurface features and identify potential conduits, fractures, or voids within the karst aquifer. These techniques provide valuable information about the subsurface structure and can aid in understanding groundwater flow patterns.

Packer testing: Packer tests involve isolating specific sections of a borehole using inflatable packers and conducting aquifer tests to evaluate the hydraulic properties of the surrounding rock or aquifer. This method helps in characterizing the permeability and flow characteristics of different zones within the karst aquifer.

Multi-level groundwater monitoring: Installing multiple monitoring wells at different depths within the karst aquifer allows for the collection of data on water levels, water quality parameters, and flow velocities at various locations. This approach provides insights into the vertical and horizontal variations in groundwater flow and helps in understanding the complex hydrogeologic behavior of the karst system.

By incorporating these specialized investigation methods into the phased approach, a more comprehensive understanding of the karst aquifer can be achieved, enabling better characterization of the flow system and more effective management of groundwater resources in karst environments.

7.1.1 On-Site Mobile Laboratory Application to Investigating Contamination Distributions

Seventeen soil borings were advanced using direct-push technology (DPT). These borings were placed in the presumed hydrogeologically downgradient direction from the suspected contamination source. The objective of the soil boring activities was to obtain screening-level field groundwater data from an on-site mobile laboratory for preliminary assessment of the contamination plume and to determine locations for additional monitoring wells. A track mounted geoprobe rig was utilized to advance

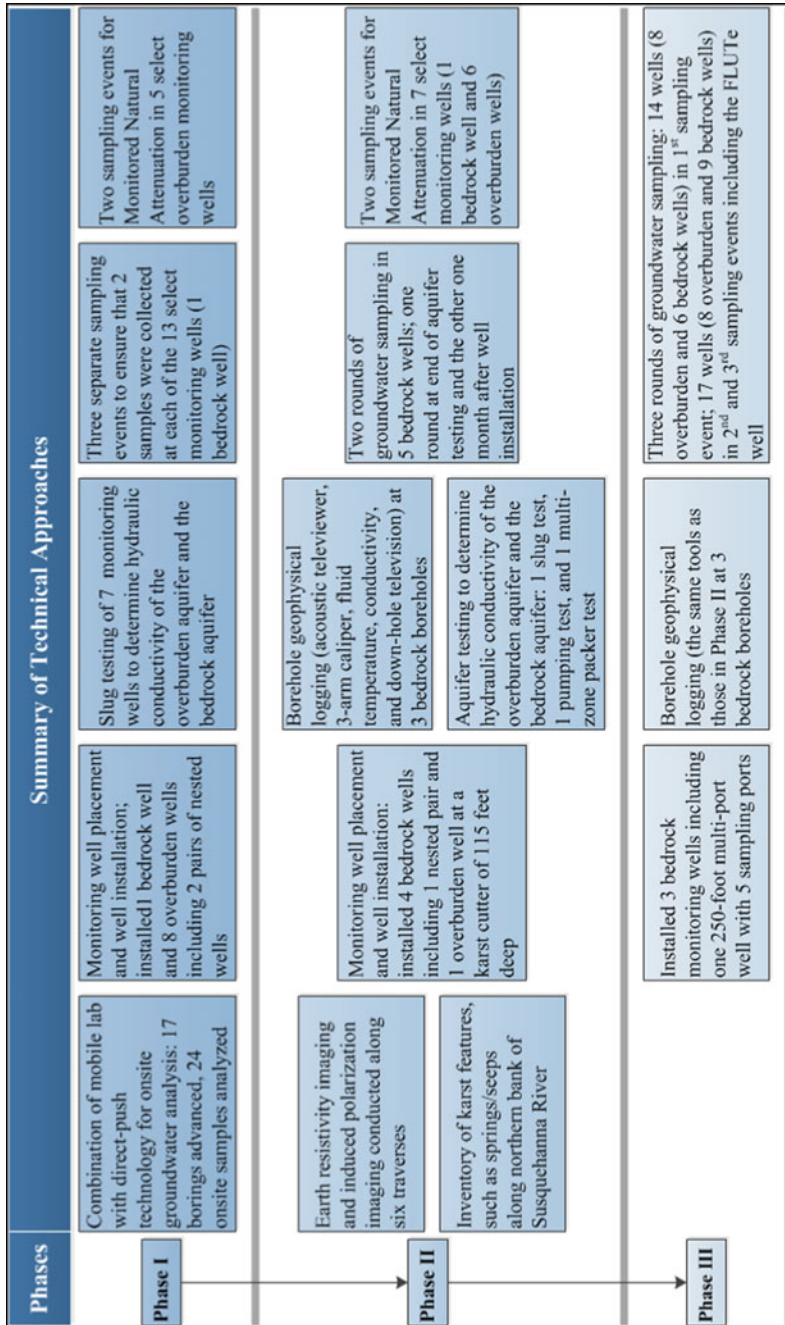


Fig. 7.1 Phased approach used in groundwater contamination investigation

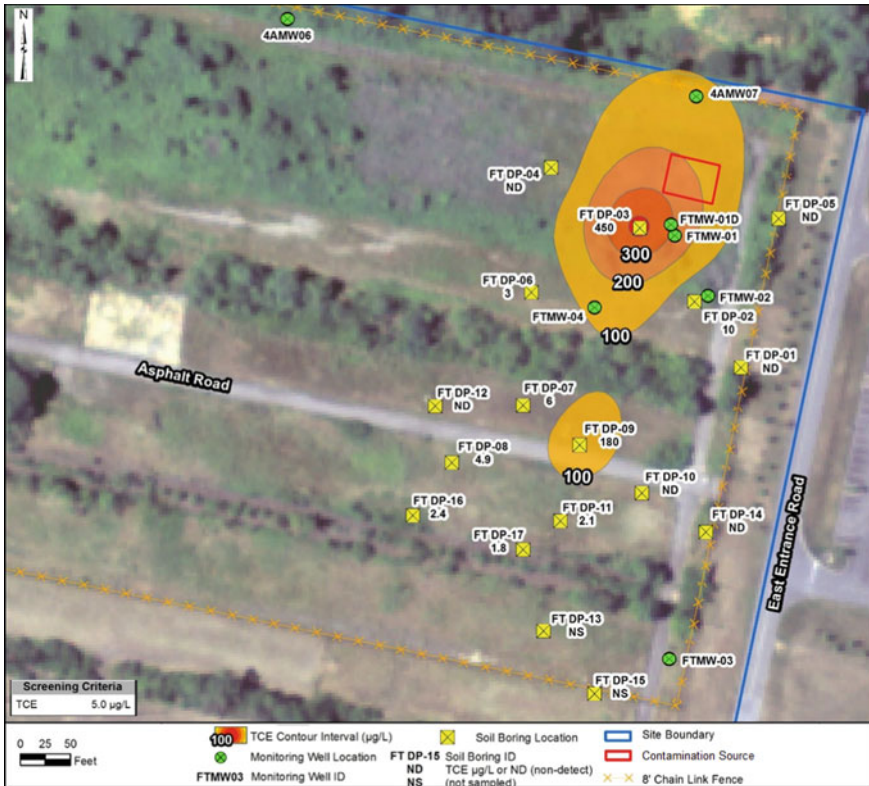


Fig. 7.2 TCE concentration distribution from on-site mobile laboratory analysis

each boring to refusal. Figure 7.2 shows the soil borings and the contours of the depth to refusal. The depth to refusal varied from 11 to 31 feet.

Groundwater was encountered above the refusal level at each boring. Upon advancement to refusal, the DPT tooling was extracted from the boring and offset to the side of the completed boring. The DPT macrocore sampler was exchanged for a discrete-depth groundwater sampler, and this was advanced next to the boring to just below the encountered groundwater. When this depth was reached, the discrete-depth groundwater sampler was partially retracted exposing the screened section. Single-use high density polyethylene tubing was inserted into the center of the Geoprobe rods and groundwater samples were collected by a peristaltic pump. The sample stream was collected in a laboratory-provided clean 20-milliliter (mL) volatile organic analysis vial. The sample was then transferred to the on-site mobile laboratory technician for analysis.

A mobile laboratory was set up for on-site screening level analysis of groundwater samples. Analysis was performed by direct injection gas chromatography analyses of the heated headspace of groundwater samples and target compounds were identified with the gas chromatograph’s photoionization detector (PID) and

electron capture detectors. Tetrachloroethylene (PCE) and its degradation products including trichloroethylene (TCE) and cis-1,2-dichloroethene (cis-DCE) were targeted for detection. Table 7.2 presents the results from mobile laboratory analysis at geoprobe locations. Figure 7.2 also shows the TCE concentration distributions based on the on-site analysis data.

Table 7.3 compares the on-site analysis results with those by an in-house laboratory for two groundwater samples for quality assurance. Data in this table indicate that the TCE or cis-DCE results analyzed from the mobile laboratory may have underestimated the contamination concentrations. The on-site analysis results provide essential information on placing additional monitoring wells.

Table 7.2 Results of mobile laboratory analysis at geoprobe locations

Soil boring	Depth to refusal (feet below ground surface [bgs])	Results of mobile laboratory ($\mu\text{g/L}$)		
		TCE	cis-DCE	PCE
FTDP1	15.3	Non-detect (ND)	ND	0.1
FTDP2	31.0	10	67	0.087
FTDP3	17.0	450	450	0.46
FTDP4	16.5	ND	ND	0.13
FTDP5	15.0	ND	ND	0.075
FTDP6	20.0	3	0	0.075
FTDP7	30.0	6	2.9	0.093
FTDP8	23.0	4.9	3	0.1
FTDP9	27.3	180	620	0.49
FTDP10	34.8	ND	5.6	0.12
FTDP11	15.0	2.1	38	ND
FTDP12	20.0	ND	ND	ND
FTDP13	11.0	ND	ND	ND
FTDP14	18.5	ND	ND	0.15
FTDP15	11.8	ND	ND	ND
FTDP16	20.0	2.4	ND	ND
FTDP17	13.0	1.8	18	ND

Table 7.3 Quality assurance of on-site analysis

Analyte	FTMW-01		FTMW-04	
	On-site mobile laboratory ($\mu\text{g/L}$)	In-house laboratory ($\mu\text{g/L}$)	On-site mobile laboratory ($\mu\text{g/L}$)	In-house laboratory ($\mu\text{g/L}$)
TCE	150	850	65	120
cis-DCE	250	1700	53	120

7.1.2 Earth Resistivity Imaging and Induced Polarization Imaging

ERI (Earth resistivity imaging) and induced IP (polarization imaging) were conducted along six traverses. The objective of this geophysical survey was to investigate any subsurface fracturing and preferential groundwater flow pathways in the underlying dolomite to facilitate location of four new monitoring wells in bedrock. Figure 7.3 presents the location of the six ERI/IP traverses. The dipole–dipole array was used for the apparent resistivity and apparent IP data collection. The unit electrode spacing was 10 feet for all traverses. Fifty-six electrodes were used in all traverses, so the total length of each traverse was 550 feet.

Resistivity is a material property, and different materials, geological or otherwise, have different resistivity. The fundamental science behind application of ERI is the empirical Archie’s law, which is often expressed by Eq. 7.1:

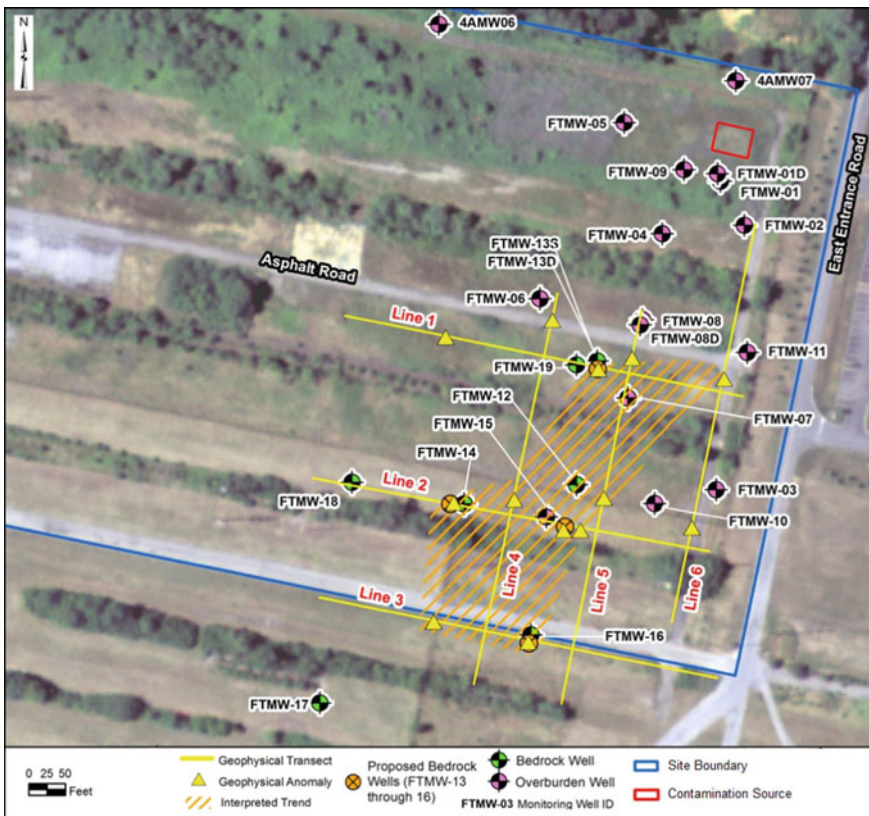


Fig. 7.3 Geophysical transects, interpretations, and proposed bedrock monitoring wells

$$\rho_0 = a\rho_w\phi^{-m} \tag{7.1}$$

where ρ_0 is the bulk resistivity for the soil/rock; ρ_w is the water resistivity; a is an empirical constant ($0.6 < a < 1$); m is the cementation factor ($m = 1.3$ for unconsolidated and $m = 2.2$ for cemented or crystalline), and ϕ is the fractional porosity, a ratio between water volume and soil/rock volume.

Both electrical resistivity and fractional volume of water in the earth materials are the main factors affecting the bulk resistivity. Large fractional volumes of water with low resistivity tend to correspond to overall resistivity lows, whereas dried materials tend to correspond to resistivity highs. Although bedrock such as limestone or dolomite may have high resistivity value, the bulk resistivity can be significantly decreased if the bedrock consists of large fractional volume of water. The resistivity of natural groundwater is typically low, and even lower if contaminated. Therefore, clay or water-filled fractures or conduits tend to have much lower resistivity values, while air-filled fractures or competent rock tend to have higher resistivity values. Table 7.4 lists possible resistivity values for materials encountered at the site.

The IP data were collected in conjunction with the ERI data. IP surveys involve measuring the polarization voltage magnitude that arises from injecting pulsed current into the ground, using the same instrument as electrical resistivity imaging (ERI). The integration of IP data aims to enhance the resolution and analysis of resistivity data in the following manners:

- Resolving thin stratigraphic layers can be improved by analyzing IP data, reducing some of the uncertainties encountered during electrical resistivity data modeling.
- IP data can aid in distinguishing geologic layers that may exhibit poor response in an electrical resistivity survey. The measurement of electrical chargeability, which is another physical property, can be utilized to augment hydrogeologic interpretations in various ways, such as distinguishing between equally electrically conductive targets like saline, hydrocarbon, or metallic-ion contaminant

Table 7.4 Possible interpretation of measured resistivity values

Value (ohm meter)	Interpretation
< 5	Possible interference from man-made objects (utilities) or artifacts from too many iterations in data processing
5–50	Clay dominated materials with high water content, saturated clay, clay-filled, or water-filled fractures or conduits
50–200	Moist silt, fine sand, weathered bedrock (dolomite) below water table
200–1000	Competent bedrock (dolomite), dry silty materials, possible small air-filled voids above water table
> 1000	Very competent rock (dolomite), dry sandy materials, possible large air-filled void above water table or artifacts from too many iterations in data processing

plumes and clay layers. This additional information can enhance the accuracy and effectiveness of the hydrogeologic interpretation.

There are two primary mechanisms attributed to the electrical chargeability or IP effect, although the exact causes are not yet fully understood. The first mechanism, known as electrode polarization or overvoltage effect, is predominant in rocks that contain metallic minerals. It occurs when conductive grains within the rock matrix hinder the flow of current, leading to the accumulation of charge on either side of these grains. When the current is removed, the ions responsible for the charge gradually diffuse back into the electrolyte (groundwater), causing the potential difference across each grain to decay slowly until it reaches zero. The second mechanism, known as membrane polarization, arises from the restriction of ion flow through narrow pore channels. It can also occur due to an excessive buildup of positive ions around clay particles. Exactly, the presence of a cloud of positive ions obstructs the movement of negative ions through the pores in the rock. When the applied voltage is removed, the concentration of ions gradually returns to its original state, resulting in the observed IP response. This phenomenon contributes to the electrical chargeability and is a key factor in understanding the IP effect.

During an IP survey, a square waveform is used to apply the current, and the polarization voltage is measured at short time intervals after each current cut-off. There is typically a brief delay of approximately 0.5 s before taking these measurements. These voltage readings are integrated to determine the area under the decay curve, which is used to define the voltage. To calculate the apparent chargeability, the integrated voltage is divided by the observed steady voltage. The observed steady voltage encompasses both the voltage resulting from the applied current and the polarization voltage. The apparent chargeability is expressed in milliseconds. By analyzing the measured apparent chargeability for a given charging period and integration time, qualitative information about the subsurface geology can be obtained.

Different minerals are distinguished by characteristic chargeabilities. However, it is challenging to use laboratory measurements to directly characterize the response of materials in the field because the IP response come from the processes of membrane polarizations caused by earth materials consisting of many minerals, and from electrode polarization caused by the presence of metallic grains. Both effects tend to be non-linear and depend on the surface area between the grains and fluids in the rock. Because minerals in groundwater can affect this interface, which may result in detectable changes in chargeability, the IP measurements can be applied to groundwater investigations. Table 7.5 lists typical chargeability of various earth materials.

Figure 7.4 shows the processed profiles on one of the geophysical lines (Line 2). Three graphs are presented. The top graph shows the modeled resistivity profile of the ERI; the middle graph shows the chargeability profile, and the bottom graph shows the normalized chargeability, which was obtained by dividing the chargeability by the resistivity. Fractures with groundwater flow and/or groundwater contamination typically have low resistivity and high chargeability. The interpreted anomalies

Table 7.5 Chargeability of various earth materials

Chargeability (milliseconds)	Materials
2000–3000	20% sulfides
1000–2000	8–20% sulfides
100–500	Sandstone, siltstone
50–100	Shale, clay
10–20	Limestone, dolomite
1–9	Sand, silt, gravel
0	Pure water
Variable, but can be in the thousands	Contaminated groundwater

are also plotted in Fig. 7.3. Based on the interpretation of resistivity and chargeability anomalies, the existing monitoring wells and the data gap in delineating the extent of bedrock contamination offsite, recommendations were made on additional monitoring wells.

The true resistivity/IP distributions along each traverse result from the measured apparent resistivity/IP data that are average values representing a volume of geologic material. The volume-averaged inherent in resistivity/IP methods tends to obscure small-scale irregularities in the geologic interfaces, except in very shallow subsurface. The data are more generalized at greater depths because of lower resolution due to averaging and/or smearing. Like other geophysical techniques, interpretation of resistivity/chargeability anomalies is not unique, especially in areas with complex geology such as the site. For example, isolated, near-surface areas of high resistivity may be caused by less moist silt, oxide nodules, or bedrock fragments. An apparent resistivity low may be caused by the presence of a clay- or water-filled fracture, cavity, or highly fractured but water-saturated rocks. A large void or multiple small voids may produce the same resistivity anomalies. Although the resistivity/IP imaging is two-dimensional, significant variations in subsurface resistivity in a direction perpendicular to the survey can cause distortions in the lower sections of the model (out-of-plane effects). This effect is most pronounced when the resistivity line is near a localized feature with different electrical properties than the material along the line (such as the railroad tracks at the site). Some of the resistivity/chargeability highs or lows shown on individual profiles may be caused by features that are actually laterally offset from the profile. As a result, when survey lines cross each other, the resistivity/chargeability profiles should be similar but may not be exactly the same at their intersections. The different results at the intersections may be indicative of the heterogeneous and anisotropic subsurface conditions.

When resistivity/IP data are interpreted, it is also important to understand how the image is created. The algorithm used in modeling is a “smoothing algorithm” meaning that a target is delineated by a number of equi-resistivity/chargeability lines. The lines describe the transition from one material to the other. However, if a target is too small, the equi-resistivity/chargeability lines will not reach the target values.

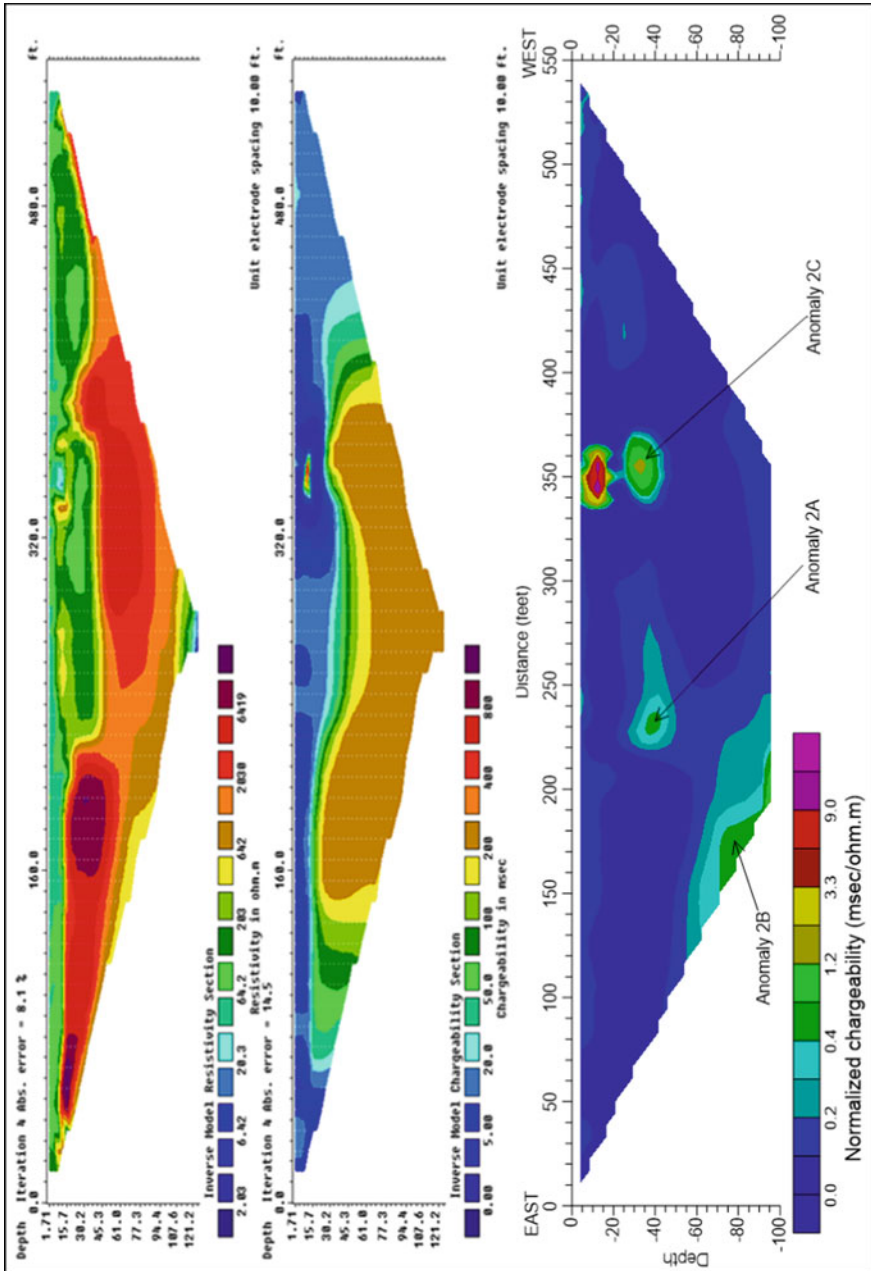


Fig. 7.4 Example image of normalized chargeability

Because the profiles are presented by resistivity/chargeability contours, the size of an anomaly over a geologic feature may be larger than the actual size of the feature.

7.1.3 Monitoring Well Installation and Aquifer Testing

Table 7.6 summarizes the monitoring wells installed during three phases and the associated investigation methods. Placement of these monitoring wells is based on location of suspected contamination area, on-site mobile laboratory analysis, and geophysical surveys. Monitoring well installation started with wells in the overburden and shifted to those in the bedrock. The boreholes were drilled using a combination of DPT, hollow stem auger (HSA) and air rotary drill. DPT or HSA was utilized to advance the boring through the alluvium overburden down to bedrock. The bedrock was then drilled using an air rotary drill rig. The formation characteristics were studied by the drilling logs, examining the cuttings, and a subsequent down-hole geophysical investigation in bedrock wells. The cuttings of each borehole were logged to the extent practicable to produce the drilling log. Visual observations such as depth of encountering water, voids, loss of circulation and changes in drill rig performance (i.e., rate of penetration) were recorded during the drilling process. The cuttings retrieved from the drilling were screened by a PID for volatile organic compounds (VOCs).

Aquifer characterization was conducted with slug test, pump test, and packer test. The slug used to perform the slug tests was made of polyvinyl chloride (PVC) cylinders and weighted internally with sand and concrete, with epoxy end caps and vinyl rope attached to each end. The slug has an outer diameter of 1.55 inches and 36 inches in length. The water level data were collected after lowering the slug into and pulling out of the water column. Prior to beginning the slug test, an initial water level measurement was collected. Initially, a pressure transducer was installed in the well to a depth below the target drawdown estimated for the test. Groundwater level data were collected for approximately 3 h prior to beginning the slug test. The transducer was set to collect data at one-minute intervals.

In packer testing, specific intervals within each borehole are isolated from the rest of the open bedrock borehole using straddle packer assemblies. These packers consist of external bladders coated with natural rubber, which are inflated with nitrogen to expand and create a seal against the borehole wall. By isolating these intervals, measurements of hydraulic head potential (water pressure) and yield (water flow) can be taken. The packer testing system typically includes a straddle packer assembly, a submersible pump, and a data collection system. Within each borehole, three pressure transducers calibrated to measure the depth to water are inserted as part of the straddle packer system. These transducers allow for continuous monitoring of water levels above, within, and below each isolated interval being tested. This comprehensive monitoring helps assess the hydraulic behavior and characteristics of the subsurface formations. The signals from the pressure transducers are transmitted through the top packer to a digital data logger. The data logger collects and records the measurements

Table 7.6 Summary of monitoring wells and associated investigations

Location ID	Screen interval (feet bgs)	Lithology	Total depth (feet)	Diameter (inches)	Aquifer testing	Borehole logging	Sampling and analysis	Groundwater level monitoring
4AM-07	5.9-24	Overburden	24	2			✓	✓
FTMW-01	5.9-20.9	Overburden	20.9	2	Slug test		✓	✓
FTMW-01D	79.6-99.6	Overburden	99.6	2			✓	✓
FTMW-02	5.8-20.8	Overburden	20.8	2			✓	✓
FTMW-03	7-22	Overburden	22	2			✓	✓
FTMW-04	4.6-19.6	Overburden	19.6	2			✓	✓
FTMW-05	11.5-16.5	Overburden	16.5	4			✓	✓
FTMW-06	15-25	Overburden	25	4	Slug test		✓	✓
FTMW-07	14-19	Overburden	19	4			✓	✓
FTMW-08	13-23	Overburden	23	4	Slug test		✓	✓
FTMW-08D	28-33	Overburden	33	4	Slug test		✓	✓
FTMW-09	15-25	Overburden	25	4	Slug test		✓	✓
FTMW-10	23.5-33.5	Overburden	33.5	4	Slug test		✓	✓

(continued)

Table 7.6 (continued)

Location ID	Screen interval (feet bgs)	Lithology	Total depth (feet)	Diameter (inches)	Aquifer testing	Borehole logging	Sampling and analysis	Groundwater level monitoring
FTMW-11	14-19	Overburden	19	4			✓	✓
FTMW-12	35-45	Bedrock	45	4	Slug test		✓	✓
FTMW-13S	19-34	Bedrock	34	2	Straddle packer test	ATV, 3-arm caliper, fluid temperature and conductivity, and down-hole television	✓	✓
FTMW-13D	55-70	Bedrock	70	2	Straddle packer test	ATV, 3-arm caliper, fluid temperature and conductivity, and down-hole television	✓	✓
FTMW-14	40-55	Bedrock	55	2	Pump test	ATV, 3-arm caliper, fluid temperature and conductivity, and down-hole television	✓	✓
FTMW-15	108-128	Overburden	128	2	Slug test		✓	✓
FTMW-16	16-40 open hole, 40-47 gravel pack	Bedrock	47	6	Straddle packer test	ATV, 3-arm caliper, fluid temperature and conductivity, and down-hole television	✓	✓
FTMW-17	38-68	Bedrock	68	6			✓	✓
FTMW-18	18-48	Bedrock	48	6			✓	✓

(continued)

Table 7.6 (continued)

Location ID	Screen interval (feet bgs)	Lithology	Total depth (feet)	Diameter (inches)	Aquifer testing	Borehole logging	Sampling and analysis	Groundwater level monitoring
FTMW-19 Zone 1	96.4–106.4	Bedrock	106.4	6		ATV, 3-arm caliper, fluid temperature and conductivity, and down-hole television	✓	✓
FTMW-19 Zone 2	124.9–130.9	Bedrock	130.9	6			✓	✓
FTMW-19 Zone 3	137.9–143.9	Bedrock	143.9	6			✓	✓
FTMW-19 Zone 4	188.9–193.9	Bedrock	193.9	6			✓	✓
FTMW-19 Zone 5	226.9–231.9	Bedrock	231.9	6			✓	✓

of water levels from the transducers. The output from the data logger is then directed to a field laptop computer, where the data can be analyzed and further processed. A pump test was conducted at FTMW-14 in which a highly permeable zone was encountered approximately 20 feet into the bedrock after auger refusal and drilling was difficult because of high water production in the formation. Monitoring well FTMW-14 was pumped at a constant rate of 11.5 gallons per minute (gpm) for approximately 2.6 h for the pump test. Prior to the pumping test, pressure transducers were installed in the pumped well and in three existing monitoring wells (FTMW-13, FTMW-15, and FTMW-16), which were used as observation wells during the pumping test.

Borehole geophysical logging, including acoustic televiewer (ATV), 3-arm caliper, fluid temperature and conductivity, and down-hole television, was performed at bedrock wells to identify relevant characteristics of the boreholes and determine fracture intervals and water production zones.

7.1.4 Borehole Logging and Design of Multi-port Monitoring Well

Borehole geophysical logging, including ATV, 3-arm caliper, fluid temperature and conductivity, and down-hole television, was performed at bedrock boreholes including the multi-port monitoring well FTMW-19. The purpose of this investigation was to identify relevant characteristics of the boreholes and determine the appropriate spread interval for the packer testing. The total depth of the well is approximately 260 feet below the top of the casing. The measurement from the top of the casing to the land surface is 1.10 feet. The well is constructed with a 5-inch diameter steel casing, which is set to a depth of approximately 91.5 feet below the top of the casing. This means that the open borehole interval, where the packer testing is conducted, spans from 91.5 feet below the ground surface (bgs) to approximately 260 feet bgs. At the time of the survey, the depth-to-water level in the well was approximately 18.3 feet below the top of the casing. Figure 7.5 displays a portion of the logging data obtained from the borehole at FTMW-19.

Caliper (3-arm): The caliper log is a tool used to measure and record the average diameter of a borehole. It provides information about changes in borehole diameter that are associated with well construction, such as the depth of the well casing or the location of a screened interval. Additionally, the caliper log is valuable in identifying potential fracture zones in open bedrock wells. The caliper log consists of three spring-loaded feeler arms that work together to determine the average diameter of the borehole. Before collecting the caliper logs, the tool is calibrated at the surface using measuring templates. It is then lowered into the borehole to the desired depth, and the feeler arms are remotely opened. The logging process involves moving the caliper tool in an upward direction within the borehole. Ten (10) inflections representing an increase in the average borehole diameter were identified. The top of the inflections

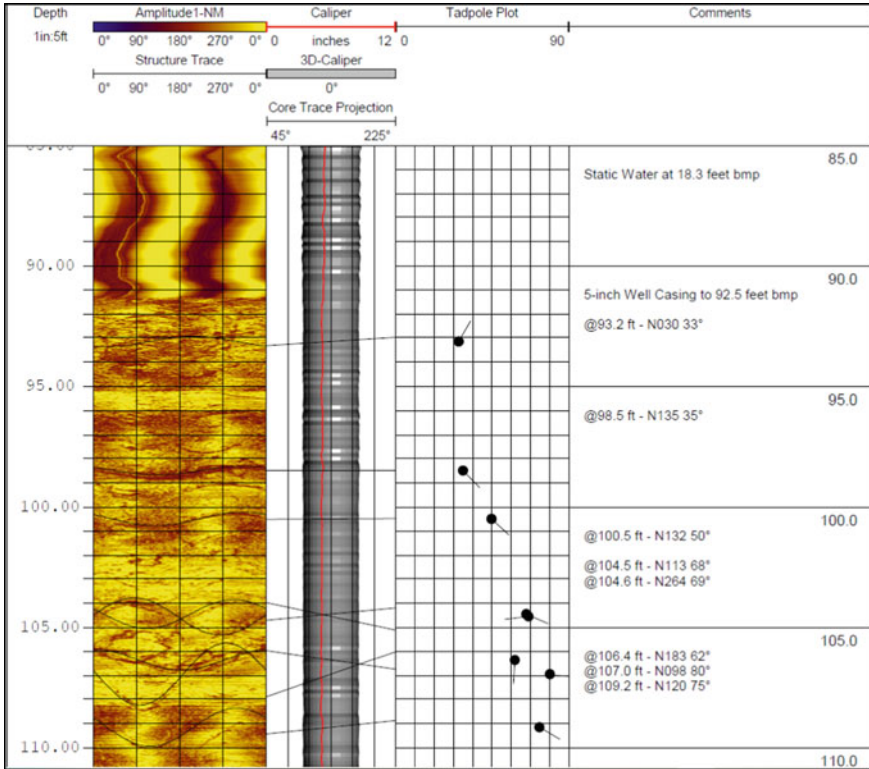


Fig. 7.5 Part of geophysical logs for FTMW-19

was found at 98, 109, 115, 126, 132, 145, 149, 178, 195, and 248 feet bgs. Based on the size of the inflections in the caliper log all these features represent minor increases in the average borehole diameter.

Acoustic televiewer: The acoustic televiewer (ATV) is a tool used for borehole imaging that functions similarly to a borehole television survey. It generates a 360° image of the borehole, but instead of relying on light, it uses a focused beam of ultrasound to produce the image. It is important to note that the ATV can only provide data in the fluid-filled portion of the borehole. It is unable to produce images in dry or partially filled sections of the borehole. The ATV records both the amplitude and the delay in transit of the reflected ultrasound signal, also known as travel time. These measurements provide valuable information about the borehole conditions, including the reflectivity of the surrounding rock and the size of the borehole.

The ATV printout contains information obtained from the survey of the borehole using the acoustic televiewer. It includes several graphics and a comments field that provide important details about the borehole features. The first graphic on the ATV printout is the borehole televiewer amplitude log, which is represented as an

“unwrapped core” displayed from North to North. The N45°-N225° graphic represents the apparent angle of the borehole through a “3-D” representation. The borehole image is viewed from a position that is rotated counter-clockwise by 45°. The arrow plot in the ATV printout displays the feature angle (ranging from 0 to 90°) and the direction of dip. It uses a “tadpole” symbol to indicate the features, with the angle of the feature represented by the position of the tadpole’s head, and the tail pointing in the direction of dip. The comments field in the ATV printout lists additional information about the identified features. A diagonal pattern wrapping from the north side of the image appears on the ATV log starting at a depth of 119 feet bgs. Based on the down-hole television survey and the caliper log it appears that a slight change in the size and smoothness of the borehole also occurs at this depth. This change may be due to a possible drill bit change and/or the combination with a facies change in the characteristics of the bedrock below the depth of 119 feet bgs. The ATV log produced for the well was analyzed and twenty-one (21) features were identified based on correlation with inflections in the caliper log. Table 7.7 lists the characteristics for each feature identified in the ATV log.

Fluid temperature and conductivity/resistivity: The fluid temperature log is used to measure the temperature of the surrounding air, water, or formation within the borehole. Abrupt changes in the slope of the temperature log can indicate the presence of water with different temperatures and/or quality entering or exiting the borehole. The fluid conductivity log, on the other hand, measures the borehole fluid’s electrolytic conductivity, typically reported in microSiemens per centimeter ($\mu\text{s}/\text{cm}$). In general, water with lower concentrations of TDS will result in lower fluid conductivity values, while water with higher amounts of total dissolved solids will exhibit higher conductivity values. Water quality can have an impact on fluid conductivity, and if sufficient details about specific contaminants in a well are available, the fluid conductivity log can provide valuable insights. By analyzing the fluid conductivity values alongside knowledge of certain contaminants, it becomes possible to draw conclusions about the composition of the borehole fluid. Changes observed in the fluid conductivity log can indicate variations in the borehole fluid when water-producing fractures or formations are transmitting fluid with different compositions into or out of the well. Fluid conductivity is the inverse of fluid resistivity. Typically, the fluid conductivity log is the initial parameter to be measured and is collected concurrently with the temperature log. Ten (10) inflections representing a change in temperature and/or resistivity were identified. The inflections are found at 98, 117, 128, 132, 157, 188, 200, 220, 240, and 248 feet bgs. The inflection depths correlate well with the caliper and ATV logs indicating possible zones of secondary porosity.

Down-hole television survey: During the down-hole television survey it was noted that the water clarity was fair (slightly cloudy) down to the bottom of the borehole at a depth of 260.5 feet. The open borehole consisted primarily of competent rock with calcite veins throughout. A fracture/weather zones that correlate well with the caliper, ATV, and fluid temperature/resistivity logs are visible at the depths of approximately 92–98 feet, 106–109 feet, 115–117 feet, 126 feet, 132 feet, 139 feet, 144 feet, 147 feet, 149.5 feet, 162 feet, and 178 feet.

Table 7.7 Acoustic televiewer features for well FTMW-19

Depth (feet bgs)	Feature		
	Strike azimuth (0–360°)	Feature dip azimuth (0–360°)	Dip angle (degree from horizontal)
93.2	300	30	33
98.5	45	135	35
100.5	42	132	50
104.5	23	113	68
104.6	174	264	69
106.4	93	183	62
107.0	8	98	80
109.2	30	120	75
115.9	68	158	62
126.5	53	143	68
128.9	51	141	59
131.8	52	142	66
139.0	54	144	70
144.0	41	131	76
149.3	177	267	59
153.4	192	282	47
161.8	54	144	77
177.8	86	176	65
191.0	56	146	65
194.8	33	123	71
230.5	141	231	59

FLUTE monitoring well design and installation: Unlike traditional groundwater monitoring wells, a FLUTE well uses flexible liner underground technologies to facilitate construction of multiple sampling ports in one well. A total of five sample ports were installed in the FLUTE monitoring well and were custom designed based upon field observations, and borehole logging, to align each port in fracture zones within the bedrock. The depths of the intervals for the five discrete sampling zones are:

- Zone 1 (FTMW-19-Z1), 96.4–106.419 feet
- Zone 2 (FTMW-19-Z2), 124.9–130.9 feet
- Zone 3 (FTMW-19-Z3), 137.9–143.9 feet
- Zone 4 (FTMW-19-Z4), 188.9–193.9 feet
- Zone 5 (FTMW-19-Z5), 226.9–231.9 feet

Upon determining the discrete sampling zones, a unique FLUTE sample liner was fabricated, to include the desired discrete sampling zones and a tubing bundle.

The installation of the FLUTE consisted of placing the unique form-fitting urethane coated nylon fabric liner within the borehole; the main component of the FLUTE monitoring well is the liner. The sample liner supports and seals the borehole. This method of installation allows for controlled installation whether horizontal, vertical, constricted, or curved. Typically, the sample liner descends by filling the inner portion of the liner with potable water provided by an off-site source, unrolling the sample liner from its shipped condition, and allowing the inherent water pressure securing the sample liner firmly into place against the borehole wall. A tether was attached to the sample liner to allow for controlled installation, but also for potential future removal of the sample liner. Figure 7.6 shows the installation and completion processes of the FLUTE well.

7.2 Hydrogeological Characterization

The formation of karst in carbonate rocks is predominantly linked to the dissolution of calcite in limestone and dolomite in dolostone. Various factors contribute to the karstification process, including the lithology of the bedrock, hydrogeology, bedrock structure, topography, climate, vegetation cover, time, and geological history. The initial step in the dissolution of carbonate rock involves the formation of carbonic acid, a mild acid formed when CO_2 dissolves in pore water. When rainfall descends and infiltrates the soil, it absorbs CO_2 from the atmosphere and the soil itself, which can contain elevated levels of CO_2 generated by the decomposition of organic matter. Consequently, the recharge water undergoes a transformation, becoming a diluted solution of carbonic acid. This acidified water permeates through the soil and eventually reaches the carbonate rocks. Guided by gravity, it continues its downward trajectory, traversing interconnected pores, fractures, or bedding planes within the rock. As the mild carbonic acid descends, it gradually dissolves and enlarges the preexisting pores or cracks, commonly known as “joints,” through which it passes. Most near-surface rocks exhibit a dense network of joints, forming a complex pattern of intersecting cracks. While these joints can be widened through the process of dissolution, the majority of them do not extend to significant depths, typically only penetrating a few layers of rock or reaching depths of a few tens of feet. Once solution widening occurs, these joints have the ability to facilitate the movement of water. However, due to their limited vertical extent, the water cannot continue its downward flow. Solutionally widened fractures or joints are known as karren. These karren can vary in size, ranging from small seams to large, cavernous openings found at greater depths. On the irregular surfaces of the rock, undissolved rock formations, known as pinnacles, alternate with deep fractures that have been widened through solution. These widened fractures are often filled with clay, and they are commonly referred to as “cutters.” Terzaghi and others (1996) state that, “the weathering products of limestone, dolomite and marble consist almost entirely of the insoluble portion of the parent rock. They usually form a nearly structureless residuum, generally clayey

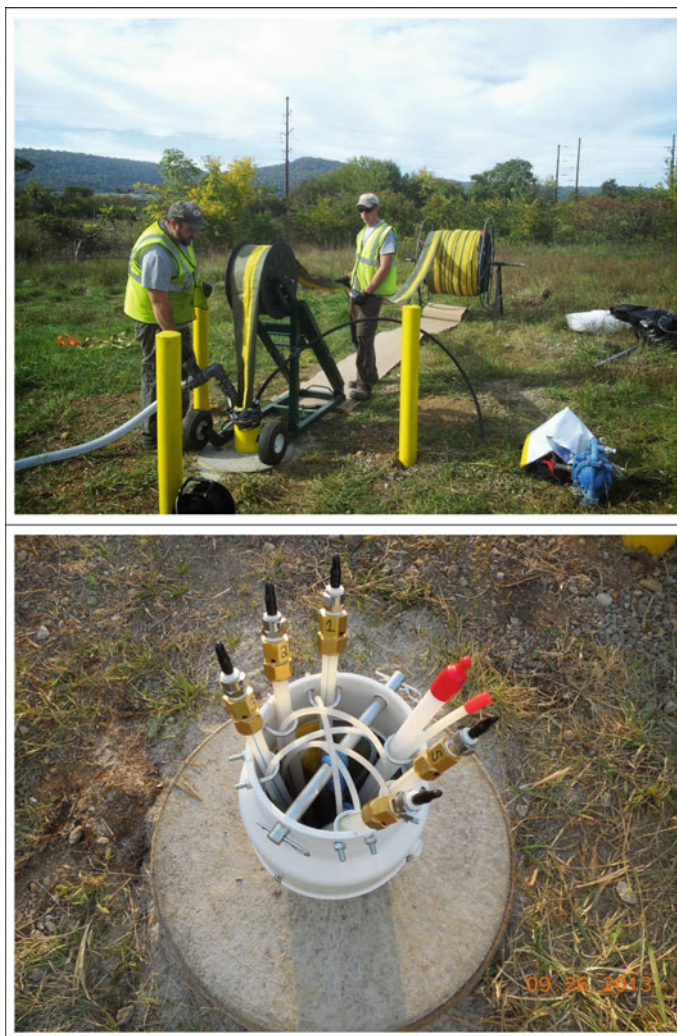


Fig. 7.6 FLUTe well installation and completion

but sometimes sandy or pebbly, with no transition to the undissolved, unweathered rock. However, although sharp, the contact may be extremely irregular.”

In contrast to the majority of joints, there are certain prominent cracks known as master joints that extend continuously through multiple layers of rock. These master joints play a crucial role in facilitating the downward movement of water to greater depths. When two master joints intersect vertically, they create a favorable pathway for water flow. This specific linear zone experiences faster dissolution compared to the surrounding areas due to the increased water volume it carries. As this zone enlarges, it becomes capable of transmitting larger quantities of water, diverting drainage from

the surrounding rock mass. This self-amplifying process leads to the formation of a few significantly enlarged tubes or pipes that penetrate through the carbonate rock, with minimal dissolution occurring between them, except in the upper portion of the carbonate rock.

The dissolution of carbonate rock is most rapid at the surface, where the water initially contacts the rock, as it is at its highest acidity during this stage. However, as the water infiltrates deeper into the bedrock, its acidity gradually diminishes, leading to a decrease in the dissolution rate. As a result, the upper portion of the carbonate rock undergoes extensive weathering and dissolution, particularly along joints and bedding planes (the horizontal surfaces between rock layers). This process gives rise to a complex network of interconnected planar features in three dimensions. This highly weathered and permeable zone, known as the epikarstic zone, is typically limited to the upper few tens of feet of the bedrock. Within the epikarst zone, water flow tends to converge towards drainage shafts, causing intensified dissolution and lowering of the rock in the vicinity of these shafts. This localized dissolution creates depressions in the carbonate rock, referred to as solution sinkholes. However, the visibility of these solution sinkholes depends on whether the bedrock is exposed at the ground surface, with minimal or no soil cover. Under certain circumstances, ongoing erosion of surface sediment can lead to the formation of a wide depression where the bedrock shaft becomes exposed at the base. This shaft can either be open, leading into a cave, or sealed with debris. In cases where the shaft is sealed, this condition is typically temporary and unstable. Eventually, the seal will be breached, and the erosion and subsidence process will resume. In some instances, sinkholes can be buried, meaning that solution or collapse sinkholes become filled with soil or sediment due to a change in the environmental conditions. As a result, there is no visible surface expression of these buried sinkholes.

The interplay between water circulation and rock dissolution in karst aquifers results in heterogeneity and anisotropy, where the extent of water circulation directly influences the degree of rock dissolution. As a consequence, the aquifers exhibit a combination of matrix voids, fractures, and caverns. Matrix voids refer to interconnected pores and vugs that store water and allow for laminar Darcian flow, where the viscosity and pressure of the fluid decrease as it moves through a porous medium over a given distance. Fractures in karst aquifers typically consist of joints, discontinuities, and bedding planes with a width of less than 1 cm. Water flow through these discrete fractures is often laminar, but it can transition to turbulent flow if there is a high hydraulic gradient, indicating a significant change in water pressure over a given distance. Caverns are formed through the dissolution of these fractures within the karst aquifer. They encompass enlarged fractures that exceed 1 cm in width, as well as conduits, caves, and underground rivers. The flow of water within these caverns resembles surface water flow and can become turbulent during recharge events when there is a substantial influx of water. It is important to recognize that groundwater flow within the karst aquifer can exhibit significant variability. While conduits and caves facilitate the movement of large volumes of water, there can also be areas of massive and impermeable rock with low hydraulic conductivity, impeding water transmission. These less permeable zones can be located in close proximity to areas

with high water storage capacity, resulting in a complex distribution of groundwater within the karst system.

7.2.1 Groundwater Flow

Figure 7.7 shows the layout of monitoring wells and general groundwater flow conditions. Based on the layout of monitoring wells and the observed groundwater flow conditions, it has been determined that the overburden formations have a hydraulic connection with the bedrock formations at the site. Both confined (where the aquifer is sandwiched between impermeable layers) and unconfined (where the aquifer is exposed to the surface) conditions exist in both the overburden and the bedrock aquifers. There was no hydrological barrier in the boreholes that would divide the groundwater flow in the overburden and the bedrock. The groundwater levels in the overburden and bedrock wells have a relatively uniform hydraulic gradient across the site. This uniform gradient suggests a good hydraulic connection between the overburden and the bedrock, allowing water to flow freely between the two. The average hydraulic gradient, measured at 0.015, indicates a southward flow towards the local river. This indicates that the groundwater is moving in a consistent direction, likely influenced by regional topography and hydraulic gradients. It is expected that the hydraulic connection can be enhanced a lot at the bedrock level due to the presence of a pinnacle-and-cutter bedrock surface. This type of bedrock surface typically exhibits irregularities and channels that can enhance the connectivity and flow of groundwater within the bedrock aquifer. These features promote the exchange of water between the overburden and the bedrock, further supporting the hydraulic connection observed at the site.

To determine the vertical gradients at the site, groundwater levels were measured in paired or clustered wells that are open to different depths. Several well pairs were utilized for this purpose, including FTMW-01 (shallow) and FTMW-01D (deep), FTMW-08 (shallow) and FTMW-08D (deep), and FTMW-13S (shallow) and FTMW-13D (deep). The measurements of hydraulic heads at FTMW-01 and FTMW-01D consistently showed higher groundwater elevations at FTMW-01. This indicates the presence of a vertical hydraulic gradient in this well pair, with groundwater flowing from the deep well (FTMW-01D) to the shallow well (FTMW-01). The consistent trend in hydraulic head measurements suggests a relatively stable flow pattern in this particular pair of wells. On the other hand, the measurements recorded at FTMW-08 and FTMW-08D, another pair of overburden monitoring wells, did not exhibit a similar consistency in hydraulic head measurements as observed in FTMW-01 and FTMW-01D. This suggests that the vertical hydraulic gradient in this well pair may be more variable or less pronounced compared to FTMW-01 and FTMW-01D. The hydraulic head measurements taken in October 2008 and December 2008 revealed that the groundwater table at FTMW-08 was lower than the groundwater table at FTMW-08D. This observation indicated an upward flow of groundwater in



Fig. 7.7 Monitoring well layout and groundwater flow in overburden aquifer

this specific timeframe. However, subsequent measurements taken after 2008 indicated a different hydraulic head pattern. The measurements showed that the groundwater table at FTMW-08 was higher than the groundwater table at FTMW-08D. This change in hydraulic head suggested a downward flow of groundwater.

Alternatively, data collected from the nested bedrock wells FTMW-13S and FTMW-13D showed a different hydraulic head pattern. In 2012 and 2013, the measurements indicated that the groundwater table at FTMW-13S was lower than the groundwater table at FTMW-13D. This observation suggests an upward flow of groundwater in this specific area. The data further suggests that in the northern part of the site, a dominant downward flow pattern is present. This downward flow may have played a role in transporting the constituents of potential concerns (COPCs) to deeper portions of the overburden and potentially laterally into the bedrock formation. At the center of the site, the flow pattern can vary, with both downward and upward flow possibilities. This variable flow pattern may have implications for the movement and distribution of COPCs within the groundwater system.

The groundwater elevation levels measured at FTMW-19 showed a distinct pattern in five zones. Zone 1 had the highest groundwater table, while the levels gradually decreased as it moved towards zone 5, which had the lowest groundwater levels. This observation of decreasing hydraulic head from zone 1 to zone 5 is indicative of a downward flow of groundwater in this specific area.

As the groundwater flows towards a local river, there is a transition in flow patterns at the southern part of the site. In this area, the upward flow becomes dominant, indicating that groundwater is being discharged into the river. This change in vertical gradient suggests that the river serves as the point of discharge for groundwater at the site. However, it is worth noting that during field reconnaissance along the northern bank of the river, no springs or seeps were observed.

7.2.2 Irregular Bedrock Surface

Figure 7.8 depicts a hydrogeological cross-section from north to south, showing two layers: overburden materials and bedrock. The overburden materials are composed of silt and clay, with some likely formed from the weathering of residual material from carbonate bedrock. One notable observation is the significant variation in depth to bedrock over a short distance along the cross-section. The depth to bedrock ranges from 13 to 129 feet below ground surface (bgs), which corresponds to approximately 280–160 feet above mean sea level (amsl). FTMW-15 and FTMW-1D are located at bedrock cutters where the overburden thickness exceeds 100 feet. These features may represent buried sinkholes that were formed in the past and subsequently eroded into the surrounding bedrocks. Furthermore, the bedrock elevation at FTMW-12, which is approximately 60 feet north of FTMW-15, is 116 feet higher than that at FTMW-15, resulting in a steep slope of 2 to 1. The presence of bedrock lows creates direct lateral contacts between the bedrock and overburden. At FTMW-16, a cavity was encountered at a depth of 59 to 61.5 feet below ground surface (bgs), and the cavity was filled with mud and silt. During drilling, approximately five drums of mud were generated as a result of encountering this cavity. Above the cavity, competent rock was observed at a depth of 43 feet. However, within the 43 feet of competent rock, low water productivity was exhibited. At FTMW-10, a layer of sand and silt measuring 9 feet in thickness observed between 26 and 35 feet bgs was encountered between the bedrock. The presence of the sand and silt layer indicates dissolution or erosion of the bedrock in that area. Similarly, the 5-port well FTMW-19 encountered voids between 78 and 79 feet bgs. These voids were filled with clay and sand. Figure 7.9 shows the irregular bedrock surface elevation configuration.

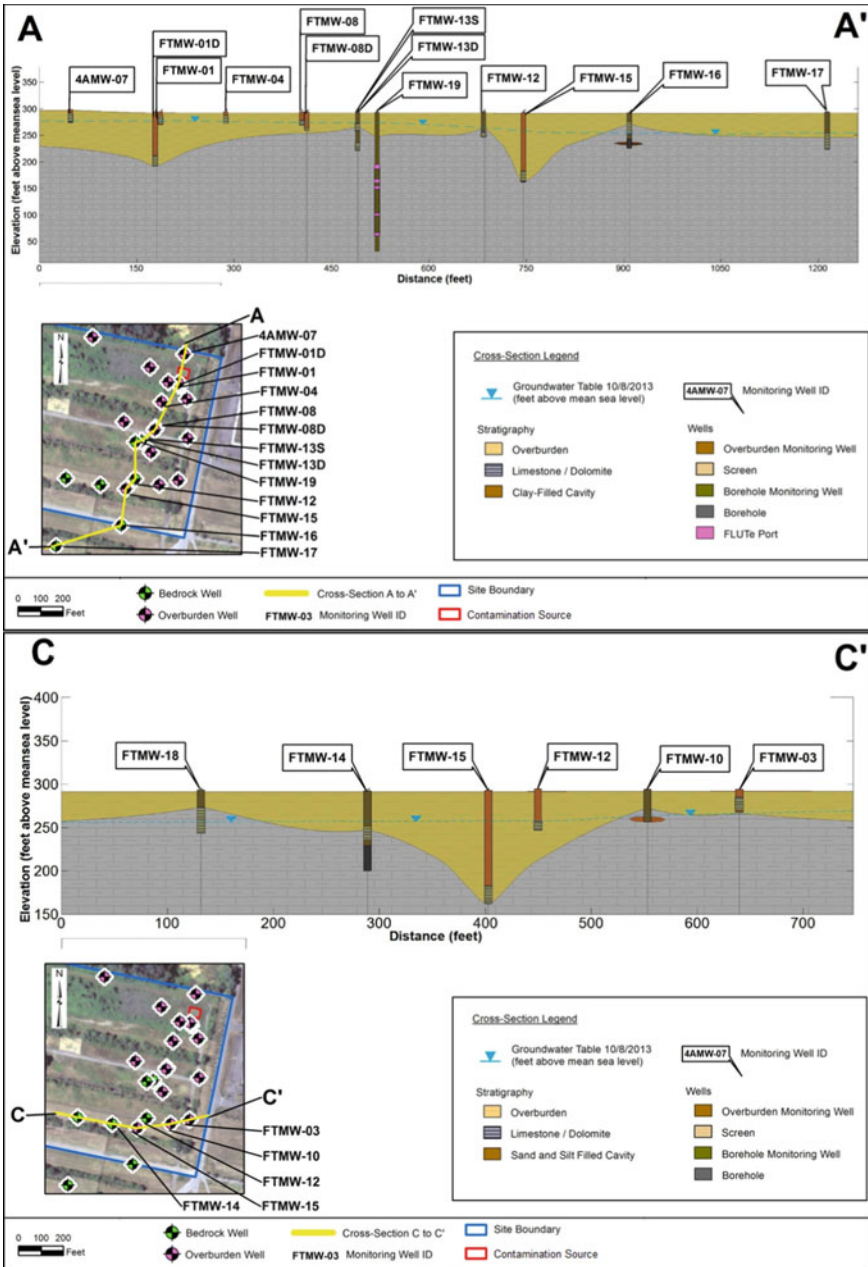


Fig. 7.8 Two-layer hydrogeological cross-sections (overburden and bedrock)

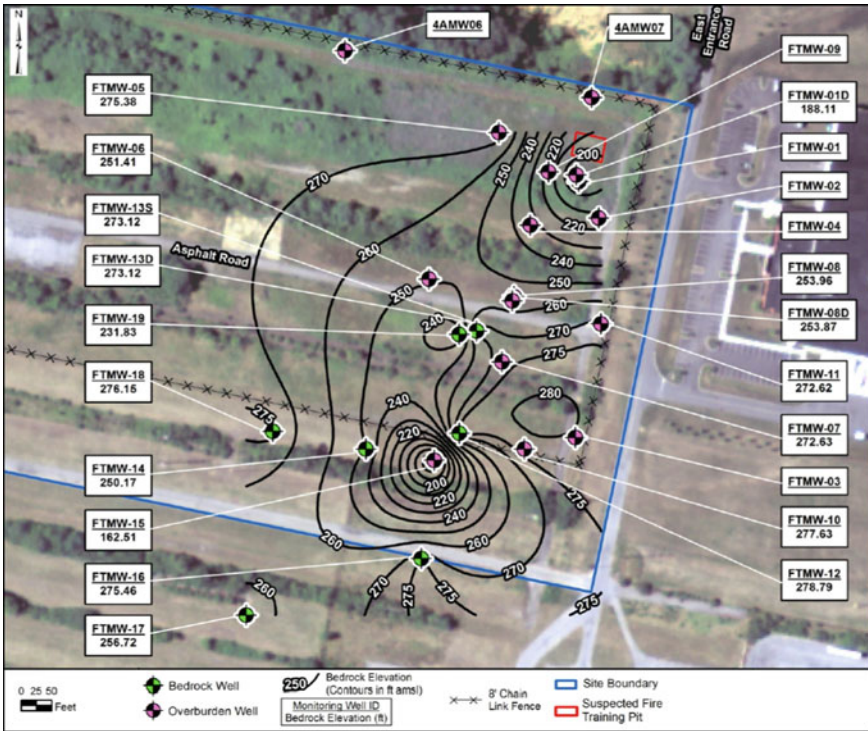


Fig. 7.9 Bedrock elevation contours

7.2.3 Unstable Boreholes

The encountered unstable boreholes and the presence of rounded gravel and cobbles at FTMW-14 indicate that this well is in a transmissive path for groundwater. The rounded nature of the quartz and dolomite cobbles indicates that they have been transported and shaped by water, further supporting the idea of a productive zone in this well. The unstable borehole at FTMW-19, where the casing was pushed in to prevent falling fragments of fractured dolomite, indicates the presence of fractured rock within the bedrock formation. At FTMW-13, discrete fracture zones were observed, indicating distinct areas of fractured rock within the bedrock. Borehole logging conducted at this well revealed jaggy borehole walls and the presence of water flow through three distinct fracture zones at different depths. These fracture zones were observed between 19 and 71 feet below ground surface (bgs). The packer tests showed that pumping at one zone produced simultaneous drawdowns at the other zones, indicating hydraulic interconnection between these fracture zones. Similarly, at FTMW-19, borehole logging showed jaggy borehole walls and groundwater flow occurring through five discrete fracture zones at different depths. These fracture zones were observed between 96.4 and 231.9 feet bgs. The observed fractures in

these different zones also appeared to be hydraulically connected. The presence of unstable boreholes, the occurrence of rounded gravel and cobbles, and the observation of discrete fracture zones with hydraulic interconnections suggest a complex and interconnected network of fractures within the bedrock formation. These fractures serve as preferential pathways for groundwater flow, allowing water to move through the bedrock aquifer. Understanding the distribution and connectivity of these fractures is crucial for assessing the movement and availability of groundwater in the karst system.

7.2.4 Large Variation in Aquifer Properties

The specific capacity, which is the yield of a well per unit of drawdown, varied across different wells and zones at the site. The range of specific capacity values observed was significant, ranging from 0.2 to 18.6 gallons per minute per foot. For example, FTMW-16 had the lowest specific capacity compared to the other wells, indicating a relatively lower yield per unit of drawdown. On the other hand, FTMW-14 exhibited the highest specific capacity, indicating a higher yield per unit of drawdown. At FTMW-13, the top zone demonstrated the highest specific capacity, suggesting a relatively higher yield per unit of drawdown in this zone. In contrast, the middle zone exhibited the lowest specific capacity, indicating a lower yield per unit of drawdown in that particular zone. This variation in specific capacity across different zones within the same well suggests heterogeneity in the hydraulic properties of the formation. Similarly, the specific capacity varied at the five zones of FTMW-19. The top zone had the highest specific capacity, indicating a higher yield per unit of drawdown, while the bottom zone showed a lower specific capacity, suggesting a relatively lower yield per unit of drawdown in that zone.

The calculated hydraulic conductivity, which represents the ability of the formation to transmit water, also varied significantly across the site. The range of hydraulic conductivity values spanned three orders of magnitude, with an average value of 17 feet per day. At FTMW-16, despite encountering a clay-filled cavity, the formation intercepted by the well exhibited very low hydraulic conductivity. The borehole could not produce enough water for a meaningful packer test, indicating limited water flow. The calculated hydraulic conductivity for this formation was 0.1 feet per day, although it is noted that this value may be an overestimate. In contrast, at FTMW-14, the presence of a paleochannel or a conduit in the formation resulted in a highly conductive formation, with a calculated hydraulic conductivity of 80 feet per day. This indicates that water can flow very easily through this formation. The hydraulic conductivity values obtained at FTMW-13 indicated vertical heterogeneity in the formation. The top zone had the highest conductivity, suggesting that water can flow most easily through this portion of the formation. Conversely, the middle zone had the lowest conductivity, indicating more restricted or limited water flow through that zone. Similarly, the purging data collected at the five zones of FTMW-19 exhibited a similar trend, with the top zone demonstrating the greatest hydraulic conductivity.

As the depth increased from the top zone to the bottom zone, the hydraulic conductivity progressively decreased. These variations in specific capacity and hydraulic conductivity indicate the heterogeneity and complexity of the subsurface hydrogeological conditions at the site. Understanding these variations is crucial for effective groundwater management and resource evaluation.

7.3 Extent of Contamination

The extent of pollution is represented by the concentrations of the COPCs based on data collected during a certain period. The extents of TCE, cis-DCE and VC were determined based on data collected in November 2013.

7.3.1 Extent of Contamination in the Overburden

Figures 7.10, 7.11 and 7.12 show plumes of TCE, cis-DCE, and VC, respectively. Two TCE plumes were observed in the overburden aquifer. The screening level for TCE is 5 micrograms/liter ($\mu\text{g/L}$), which defines the lateral extent of the plume. The larger plume, which has an elongated shape, exhibits the highest concentration of 98 $\mu\text{g/L}$ at FTMW-01, near the suspected source area of contamination. This plume spans approximately 100 feet between FTMW-06 and FTMW-10 in the northwest-southeast direction. On the contrary, the smaller plume is located around FTMW-15. Its presence may be attributed to the interaction between contaminant exchanges occurring between the bedrock aquifer and the overburden aquifer at the cutter.

The cis-DCE plume (Fig. 7.11) shows a general shape similar to the shape of the TCE plume. However, the highest cis-DCE concentration of 690 $\mu\text{g/L}$ was detected at further downgradient FTMW-08D, followed by FTMW-01 with a concentration of 100 $\mu\text{g/L}$. The project screening level for cis-DCE is 70 $\mu\text{g/L}$, which defines the lateral extent of the plume. At FTMW-09, the cis-DCE concentration was 26 $\mu\text{g/L}$ and at FTMW-15 the cis-DCE concentration was 29 $\mu\text{g/L}$.

The VC plume (Fig. 7.12) is much smaller than the TCE and cis-DCE groundwater plumes. It has a primarily circular shape. The highest concentration of VC, 430 $\mu\text{g/L}$, was detected at FTMW-08D, followed by 110 $\mu\text{g/L}$ at FTMW-08. The VC concentration was shown to decrease quickly because the samples at monitoring wells FTMW-06 to the west, FTMW-04 to the north, and FTMW-10/FTMW-15 to the south did not show any detection of VC. The project screening level for VC is 2 $\mu\text{g/L}$, which defines the lateral extent of the plume. VC was detected in a concentration of 5 $\mu\text{g/L}$ at FTMW-01.

The significant variation in overburden thickness at the site leads to a wide range of depths in the monitoring intervals, making it challenging to define the vertical extent of contamination with a single continuous contour line. However, by analyzing the data from different monitoring wells, some insights can be gained regarding the

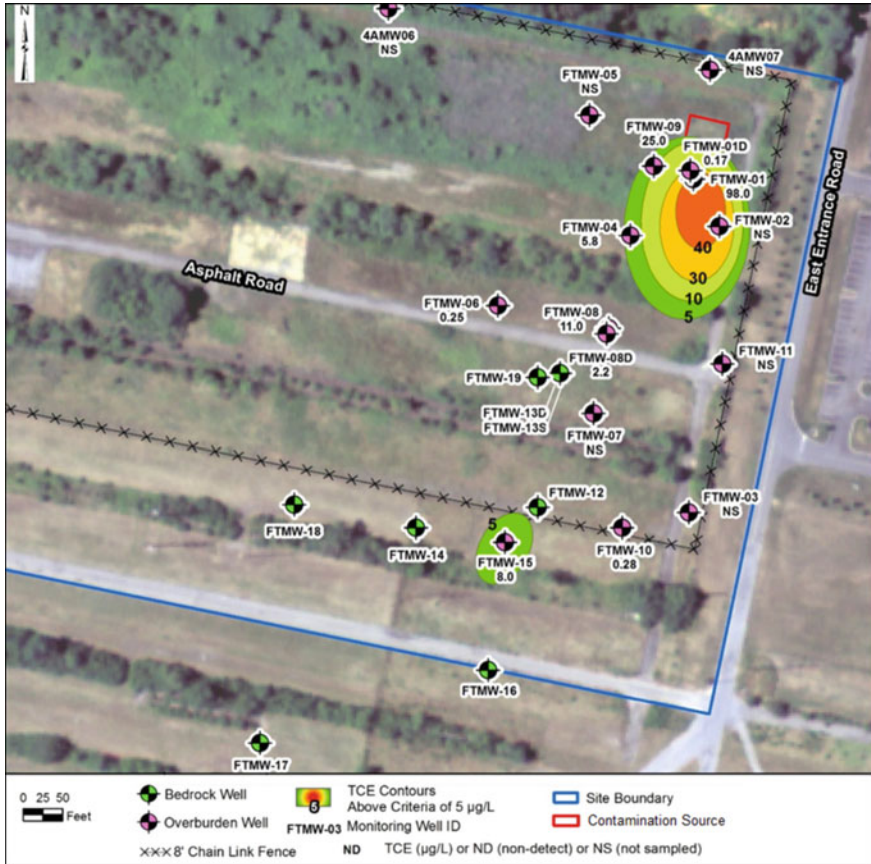


Fig. 7.10 Lateral extent of TCE plume in overburden

vertical extent of the contamination plume. In Fig. 7.13, the vertical profile of the distribution of TCE is illustrated. The deepest monitoring interval at FTMW-15, ranging from 108 to 118 feet bgs, detected TCE at a concentration of 8 µg/L. This suggests that the vertical extent of TCE contamination at FTMW-15 likely extends beyond 118 feet bgs, possibly reaching up to the top of the bedrock.

Overall, the vertical extent of the contamination plume cannot be precisely defined with a single contour line due to the variation in overburden thickness. However, by considering the data from different monitoring wells, it can be inferred that the contamination plume likely extends beyond the depths of the wells and reaches up to the top of the bedrock formation. Further investigation and monitoring are necessary to accurately determine the full vertical extent of the contamination plume.

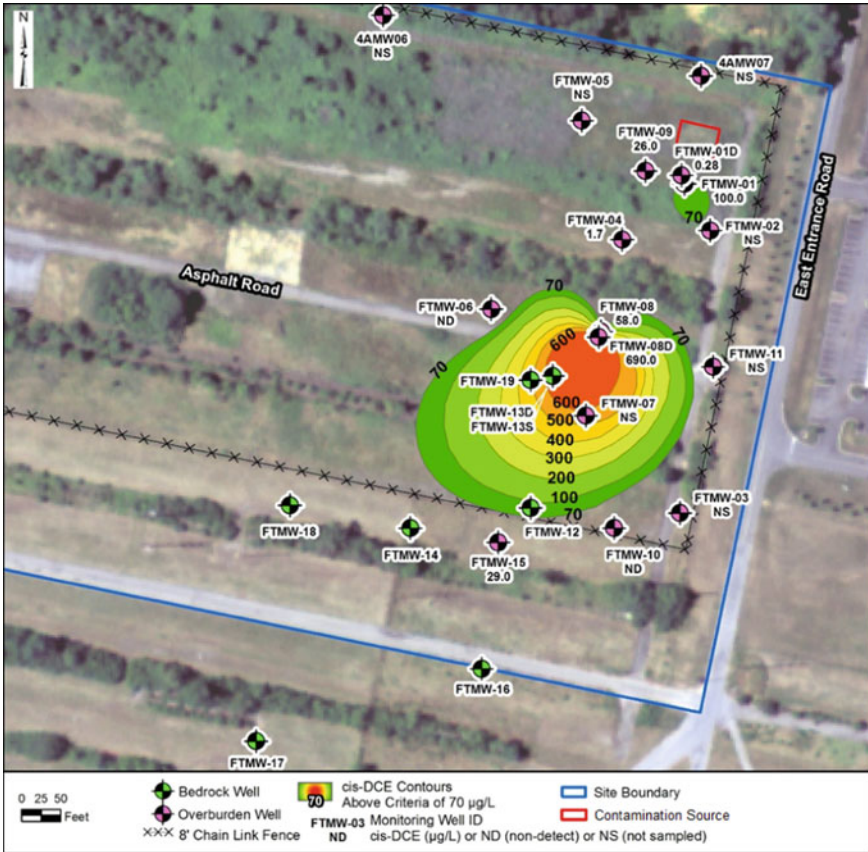


Fig. 7.11 Lateral extent of cis-DCE plume in overburden

7.3.2 Extent of Contamination in the Bedrock Formation

Figure 7.14 provides information on the TCE plume in the bedrock aquifer based on laboratory results collected in November 2013. The lateral extent of the TCE plume in the bedrock aquifer is determined to extend approximately 100 feet from the FTMW-13S/FTMW-13D area in an oval shape. It extends towards the southwest along the pattern of groundwater flow, reaching FTMW-14 and FTMW-18. The TCE concentration of 11 µg/L was detected at their respective depths of FTMW-13D and FTMW-13S. Zone 1 of FTMW-19 exhibits a TCE concentration of 6.6 µg/L.

The vertical extent of TCE contamination in the bedrock aquifer can be determined by examining the observed concentrations in different zones of FTMW-19. Zone 2 recorded an observed TCE concentration of 5.2 µg/L, while Zone 3 had an observed TCE concentration of 4.8 µg/L. Therefore, the vertical extent of contamination in the bedrock aquifer can be inferred to be between the terminus of Zone 2 in FTMW-19 at a depth of 131 feet bgs and the top of Zone 3 at a depth of 138 feet bgs. This

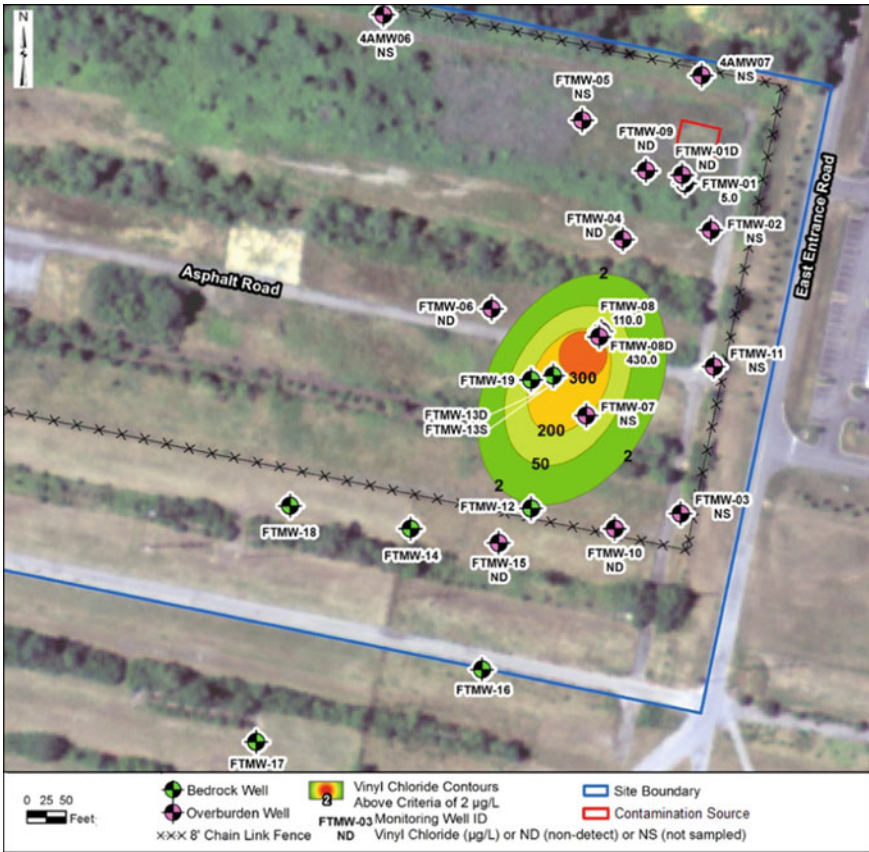


Fig. 7.12 Lateral extent of VC plume in overburden

represents the range of depths where TCE contamination is present in the bedrock aquifer. Figure 7.13 provides a graphical representation of the vertical extent of the TCE plume in the bedrock aquifer.

7.4 Fate and Transport Mechanisms of Chlorinated Hydrocarbon Contaminants

7.4.1 Dense Non-aqueous Phase Liquid Transport

DNAPLs (Dense Non-Aqueous Phase Liquids) are substances that are immiscible with water and have a higher specific gravity compared to water. They include primary halogenated solvents such as TCE, cis-DCE, and VC, as well as their associated

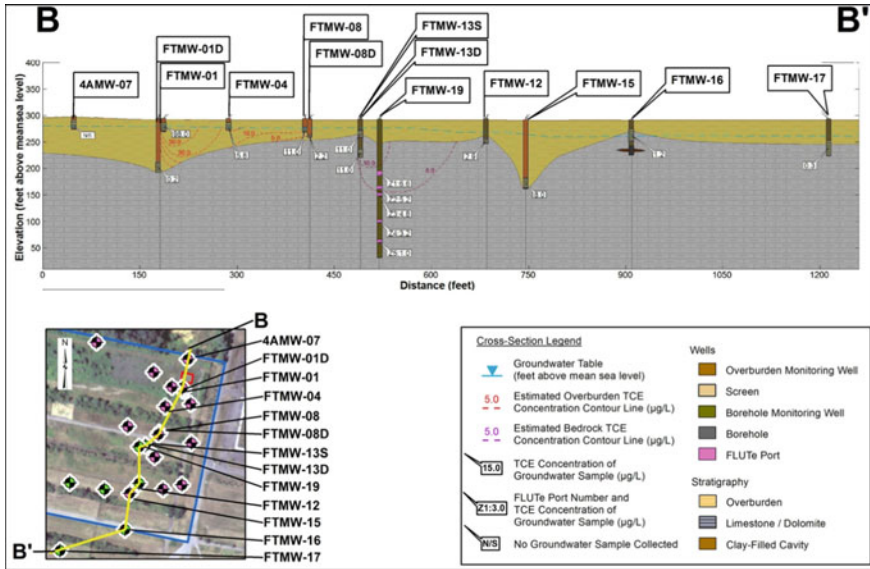


Fig. 7.13 Vertical cross-section of TCE plume in overburden and bedrock

daughter products. The transport of DNAPLs is heavily influenced by the geologic characteristics of the release site (Fig. 7.15). When DNAPLs are released into the subsurface soil in source areas, they typically move vertically downward through the unsaturated zone. However, the separate liquid phase can also move horizontally, depending on variations in soil water content, texture, and structure along the vertical profile. As the DNAPL release approaches the upper region of the capillary fringe (the saturated zone above the water table where water is retained under capillary forces), it begins to spread laterally. This lateral spreading occurs because displacing water from the water-filled voids in the saturated zone becomes more challenging. If enough DNAPL accumulates at the water table, it will enter the saturated zone. Within the saturated soil column, the DNAPL will continue to move downward, potentially being redirected horizontally in response to changes in soil texture. In cases where vertical erosion channels exist in the regolith (loose, fragmented material above bedrock), the DNAPL can migrate rapidly downward, following these channels. When the DNAPL encounters the top of the bedrock or a finer-textured soil layer like clay or silt beneath the upper soil or fill, it may spread out and create a zone of continuously DNAPL-saturated soil. In this zone, most of the water has been displaced by the DNAPL accumulation, forming a “pool” or DNAPL accumulation zone.

In the epikarst layer, the interface between the pinnacled soil and the underlying bedrock plays a significant role in the lateral migration of DNAPL. The DNAPL can accumulate in closed depressions on the bedrock surface or be directed along the relatively impermeable interface, further into the karstified aquifer. The DNAPL then moves through vertical and lateral solution channels, which can be open (filled

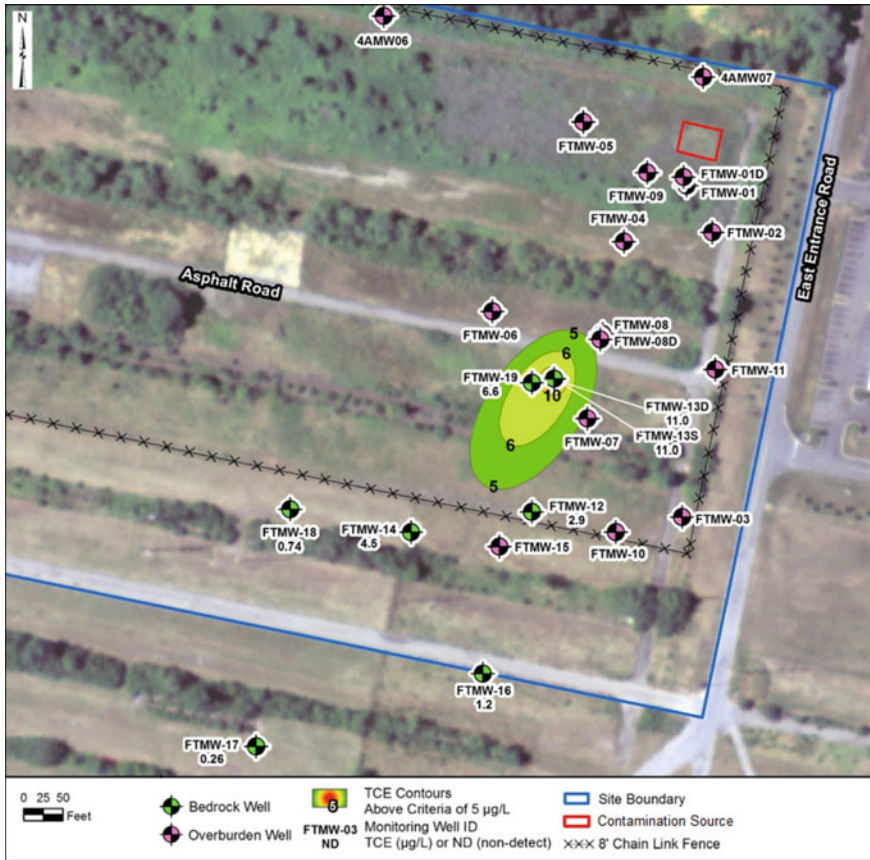


Fig. 7.14 Lateral extent of TCE plume in bedrock

with water) or filled with water-saturated residuum and sediment such as sand, silt, clay, gravels, and rock fragments. The movement of DNAPL in open voids is largely unimpeded by capillary forces due to the size of the openings. The primary driving forces for the downward transport are the DNAPL’s higher specific gravity compared to water and its immiscibility with water. In contrast, the movement of DNAPL into and through granular residuum is strongly influenced by the size and geometry of the pores and pore throats in that material. DNAPL accumulation zones in open voids can contain separate liquid phase “pools,” while the amount of DNAPL per unit volume in accumulation zones within residuum is limited by the porosity of the residuum itself. DNAPL can also migrate vertically and laterally into water-filled discontinuities such as joints, bedding-plane partings, and fractures in the bedrock, which are not enhanced by solution processes. The ease with which DNAPL penetrates such discontinuities is primarily determined by the aperture (size) of the parting in the rock, similar to how it is influenced by the geometry of pore throats in granular soils.

In karst aquifers, there is a unique mode of DNAPL transport known as bulk transport. This involves the movement of DNAPL in water flowing at high velocities through open voids. It can occur in sediment-free sections of solution cavities during periods of increased flow when water passes over a DNAPL accumulation zone and picks up droplets of the free DNAPL. Similarly, during open channel flow, sediment particles can be entrained along with DNAPL that may have penetrated into the porous residuum or sediment layer at the bottom of the channel.

7.4.2 Aqueous Phase Transport

Once a DNAPL release reaches equilibrium in the subsurface, where separate phase transport is no longer significant except for entrainment in high-velocity open-channel flow, the mass of DNAPL decreases gradually through two main mechanisms: dissolution in pore water in the vadose zone and groundwater in the saturated zone, and evaporation to the soil vapor in the vadose zone. The dissolution of DNAPL in pore water and groundwater leads to the formation of an aqueous (dissolved) phase of the chlorinated volatile organic compounds (CVOCs). This dissolved phase typically extends along the entire pathway of DNAPL migration. In the area directly affected by the DNAPL release (known as the source area), the concentrations of the dissolved CVOCs near the water-DNAPL interface will approach the solubility of the CVOCs. Figure 7.16 provides an overview of the fate and transport mechanisms for dissolved phase contaminants, illustrating the processes involved in the dissolution and subsequent transport of CVOCs in the subsurface.

Once DNAPL comes into contact with pore water and gravitational water in the vadose zone, as well as groundwater in the saturated zone, an aqueous phase of the CVOCs develops through direct dissolution from the DNAPL (Groundwater Sciences Corporation 2011). The dissolved CVOCs can be transported through the subsurface by two main mechanisms: lateral or vertical advection and diffusion. Aqueous phase advective transport is responsible for the movement of dissolved CVOCs over relatively large distances, from the source area into the plume. This occurs when the groundwater flow carries the dissolved CVOCs along with it. Lateral advection refers to the horizontal movement of the dissolved CVOCs, while vertical advection refers to their vertical movement. Aqueous diffusion, on the other hand, accounts for the movement of dissolved CVOCs over comparatively short distances. This process involves the movement of CVOCs from either the source area or the plume into the pores of the surrounding aquifer material through which advective transport is not occurring on a significant scale. Diffusion occurs due to concentration gradients, with CVOCs moving from areas of higher concentration to areas of lower concentration. These mechanisms of advection and diffusion play a crucial role in the transport of dissolved CVOCs in the subsurface, influencing the spread and migration of contaminants away from the source area and the overall shape and extent of the plume.

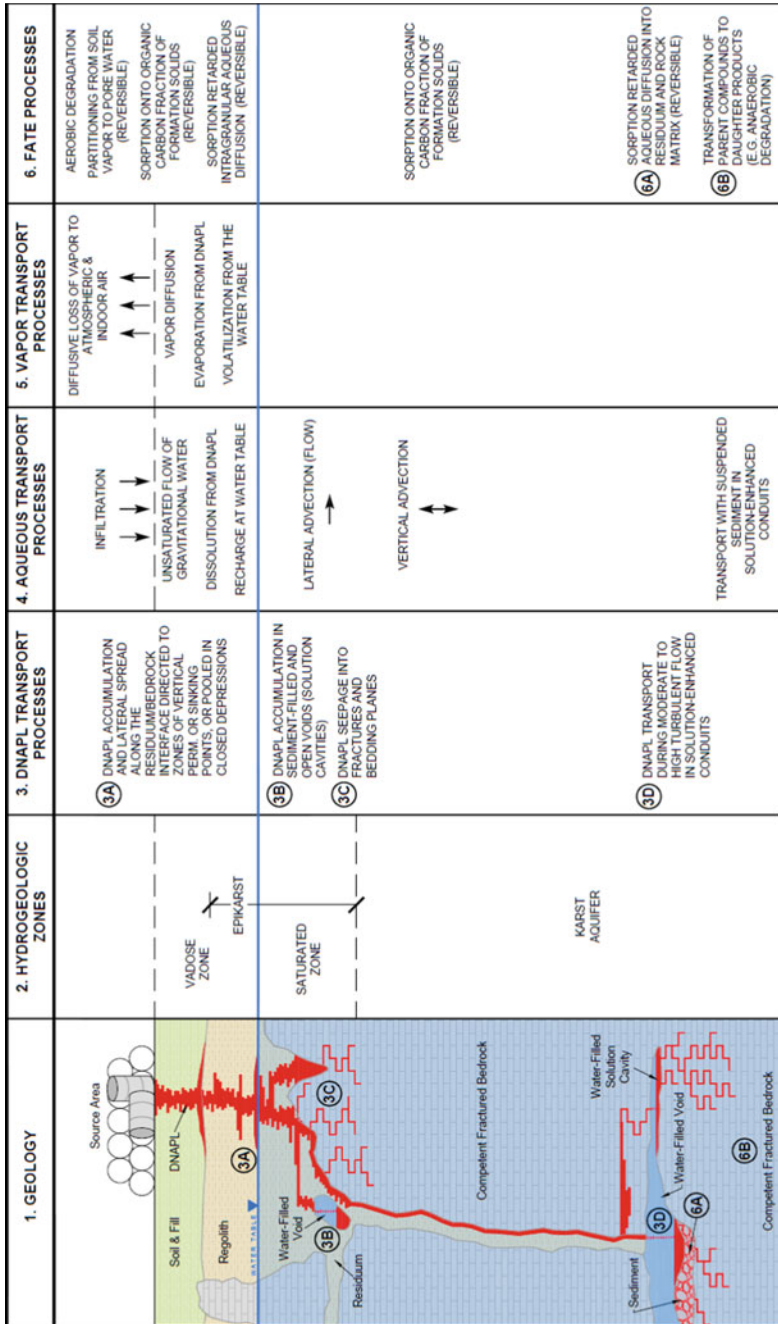


Fig. 7.16 Overview of fate and transport mechanisms for dissolved CVOCs

Aqueous phase advective transport: Aqueous phase advective transport is indeed a crucial process that leads to the formation of a plume consisting of dissolved CVOCs. This plume extends from the source area and can reach a point of discharge, such as surface water bodies or extraction wells. The movement of water from natural sources, including recharge from precipitation infiltration at the ground surface and upgradient groundwater flow, plays a significant role in this process. In the vadose zone (the unsaturated zone above the water table), water infiltrates and moves downward as gravitational pore water, draining freely towards the water table. Within a DNAPL source zone, this gravitational water can directly dissolve soluble compounds from the separate phase liquid associated with the DNAPL source in the vadose zone. The dissolved mass is then transported downward into the saturated zone (the region below the water table). Upgradient groundwater flow entering a specific area can be either uncontaminated if it has not been affected by a source or it can contain dissolved CVOCs. The presence of dissolved CVOCs in the upgradient groundwater can occur due to contact with an upgradient DNAPL source in the saturated zone or through mixing with contaminated recharge from an upgradient location. Recharge into the aquifer at the site serves multiple purposes. It provides the driving force for groundwater flow and the advective transport of CVOCs, allowing the dissolved contaminants to move through the subsurface. Additionally, recharge contributes to the dilution of CVOC concentrations over time, especially after the removal of the DNAPL source. As the diluted groundwater flows through the aquifer, it helps to attenuate and reduce the concentrations of CVOCs in the plume. Furthermore, there is the potential for vertical advection of groundwater downward into and through highly permeable fractured and solution-enhanced zones in the carbonate bedrock. This vertical advection can further influence the transport of CVOCs in the subsurface, allowing the dissolved contaminants to migrate vertically and potentially impact deeper aquifers or discharge points.

Aqueous phase dispersion: Hydrodynamic dispersion involves the mixing of a solute in both horizontal and vertical directions as it is transported through a medium. This process leads to the blending of neighboring aqueous solutions or the displacement of such solutions. In order to estimate the longitudinal dispersivity, researchers have collected data from various sources. A study conducted by Lallemand-Barres and Peaudecerf (1978) presented a graph that suggests the field-scale longitudinal dispersivity is approximately one-tenth of the characteristic length scale. Expanding on this research, Neuman (1990) further investigated the topic and proposed a universal scaling rule. Neuman established a correlation between longitudinal dispersivity and the investigation scales in different porous media, considering diverse conditions of groundwater flow and solute transport. The data utilized in Neuman's study were derived from both laboratory experiments and field-scale investigations. The most general equation derived by Neuman is Eq. 7.2:

$$\alpha_L = 0.0175L_s^{1.46} \quad (7.2)$$

where, α_L is the longitudinal dispersivity and L_s is the characteristic scale length.

The characteristic length is a unique parameter specific to each site, which relies on the distribution of hydraulic conductivity within a particular aquifer or groundwater flow system. It is defined as the minimum length of groundwater flowpaths where a migrating solute encounters all possible variations in hydraulic conductivity. The characteristic length is influenced by the heterogeneity and anisotropy of the aquifer.

In a study conducted by Gelhar et al. (1992), scatter diagrams similar to those presented by Neuman (1990) were published. These diagrams compared the longitudinal dispersivity to the observation scale. Within a given scale, the values of longitudinal dispersivity varied across 2–3 orders of magnitude. The authors emphasized that the lower end of this range was considered the most reliable. For instance, projecting a measurement scale of 250 feet to the approximate center of the scatter data corresponded to a longitudinal dispersivity of approximately 32 feet (10 m). Furthermore, Gelhar et al. (1992) highlighted that vertical dispersivities are typically one order of magnitude smaller than transverse dispersivities, and transverse dispersivities are typically one order of magnitude smaller than longitudinal dispersivities. This indicates significant differences in dispersivity values depending on the direction of dispersion (longitudinal, transverse, or vertical).

Aqueous phase diffusion: In addition to groundwater flow, dissolved chlorinated volatile organic compounds (CVOCs) can also be transported through aqueous diffusion. This diffusion process occurs in the groundwater present in the pores between individual soil particles in residuum or sediments, as well as in the primary porosity of bedrock, in response to a concentration gradient of the chemicals. Aqueous diffusion can occur both in the area where dense non-aqueous phase liquid (DNAPL) is present and in the plume that emanates from it. Research conducted at the University of Waterloo by Plett (2006) and Kennel (2008) has demonstrated that DNAPL held in bedrock fractures by capillary forces can gradually diffuse into the pore water contained within the rock, depending on the characteristics of the surrounding rock matrix. This phenomenon is known as “matrix diffusion.” As a result, the DNAPL in individual fractures can be completely eliminated, and the mass of CVOCs that was previously present as DNAPL becomes dissolved in the aqueous phase. This leads to high-concentration dissolved CVOCs in the pore water within the rock matrix adjacent to the fracture that previously contained the DNAPL.

Matrix diffusion can occur not only in the solid rock surrounding fractures and open voids but also in porous granular materials such as residuum and sediment that fill voids in carbonate bedrock. When DNAPL comes into contact with these materials, matrix diffusion can take place. The process of matrix diffusion in residuum and sediment is typically a two-stage process. Initially, the dissolved CVOCs diffuse into the intergranular pores, which are the water-filled spaces between individual soil grains. As the concentrations of CVOCs build up within these intergranular pores, diffusion then occurs into the intragranular pores. These intragranular pores are associated with the primary porosity of individual soil grains, which are eroded fragments of sedimentary rocks. This two-stage diffusion process continues as long as there is a concentration gradient between the groundwater in contact with the DNAPL and the aqueous concentrations within the intergranular and intragranular

pore water. DNAPL releases can persist for several decades without remediation, and during this time, substantial mass transfer can occur from the separate phase (DNAPL) to the aqueous phase through aqueous diffusion. As a result, a significant percentage of the originally released mass can be transferred to the aqueous phase, which becomes a repository for the dissolved CVOCs in the environment.

Estimating the amount of DNAPL released to the environment and determining the extent of matrix diffusion can be challenging. However, when separate phase DNAPL encounters a geological medium with interconnected pores containing clean pore water, a concentration gradient is established, leading to the diffusion of mass from the dissolving DNAPL into the neighboring pore water.

Matrix diffusion can also take place within the plume area. When advective transport takes place in fractures and solution conduits, a plume area is generated. Within this plume area, matrix diffusion is triggered by the significant chemical gradient between the open conduits in the carbonate aquifer, where preferential advective transport of dissolved CVOCs occurs, and the surrounding solid rock, residuum, or sediment. These geological materials typically have lower hydraulic conductivity and do not serve as the primary pathways for plume migration. As such, groundwater flowing through fractures and carrying dissolved CVOCs comes into direct contact with groundwater present in the pores of the adjacent rock matrix, residuum, and sediment. This contact creates a chemical diffusion gradient, causing the CVOCs to diffuse from the water within the fractures to the water in these pores of the surrounding geological materials.

7.4.3 Vapor Phase Transport Processes

The development of the vapor phase in the subsurface is influenced by two mechanisms: direct evaporation of chlorinated volatile organic compounds (CVOCs) from residual DNAPL in the vadose zone and volatilization of CVOCs from groundwater at the water table.

Evaporation from residual DNAPL in the vadose zone is predominantly controlled by the vapor pressure exhibited by each specific compound. In close proximity to the DNAPL source, this phenomenon typically gives rise to vapor phase concentrations that closely approach the saturation concentration of each substance in the surrounding air. The vapor pressure of a compound determines its tendency to evaporate, with higher vapor pressures leading to more significant evaporation. On the contrary, volatilization of CVOCs from the water table is influenced by the concentration of each compound in the groundwater and its Henry's Law constant. Henry's Law constant relates to the ability of a compound to partition between the water phase and the vapor phase. Generally, direct evaporation from residual DNAPL is expected to produce higher vapor phase concentrations compared to volatilization from groundwater. This is mainly because these substances have relatively low solubility in groundwater, meaning they are less likely to be present in high concentrations in the water phase.

Once in the vapor phase, the primary mechanism of transport for chlorinated volatile organic compounds (CVOCs) is vapor diffusion. Vapor diffusion takes place as a response to the concentration gradient between relatively high vapor concentrations in the soil air and negligible concentrations of these substances in the atmospheric air. Consequently, vapor diffusion primarily facilitates the upward movement of CVOCs (Chlorinated Volatile Organic Compounds) from DNAPL source zones in the vadose zone and from dissolved contaminants at the water table, directing them towards the ground surface. This process results in the loss of VOC mass through diffusion to the atmosphere.

In addition to vapor diffusion, vapor transport can also occur through advection. Advection refers to the movement of vapors due to the bulk flow of air. For example, in buildings constructed over a source or plume, vapor transport may happen across the concrete slab in response to a pressure difference across the slab. This can result in the movement of CVOC vapors along with the air flow. Another form of advective transport is known as “barometric pumping.” Barometric pumping occurs when changes in atmospheric pressure create a pressure gradient between the soil air and the atmospheric air. This pressure gradient can cause the movement of a volume of soil air containing CVOC vapors, in addition to the individual VOC molecules, as opposed to just the diffusion of VOCs.

7.4.4 CVOC Fate Processes

Fate processes lead to the depletion of chlorinated volatile organic compounds (CVOCs) through degradation, temporary storage via sorption, or transformation in both the saturated and unsaturated zones.

Partitioning from soil vapor to pore water in the vadose zone: Within the vadose zone, a fraction of the CVOCs found in the soil vapor undergoes partitioning, distributing into the pore water that envelops the individual soil grains. Similar to the volatilization process occurring at the water table, which contributes to the presence of CVOCs in the vapor phase, this partitioning mechanism from the vapor phase to the pore water is influenced by the unique Henry’s Law constant associated with each specific CVOC.

Sorption on formation solids: In both the saturated and unsaturated zones, sorption of VOCs onto the organic carbon fraction of formation solids can take place. In the zone of saturation, this sorption takes place through direct partitioning from the aqueous phase to the solid phase, irrespective of the presence of DNAPLs. In the vadose zone, the sorption process can occur directly from the aqueous phase to the solid phase if DNAPLs are in contact with the pore water. However, in the absence of DNAPLs, this sorption process follows a two-step pathway. Firstly, there is partitioning from the soil vapor to the pore water, as discussed earlier. Subsequently, the VOCs partition from the pore water to the solid phase.

Limited information is available regarding the organic carbon content of carbonate at the site. However, studies conducted at the University of Waterloo by Plett (2006) and Kennel (2008) have provided some insights into the fractional mass of organic carbon (foc) in the matrix of the Silurian dolostone, which was the focus of their research. Plett (2006) reported a range of foc values in dolostone of 0.003–0.125%, with an average of 0.017%. These results suggest a relatively low sorption potential for the dolostone. Similarly, Kennel (2008) provided data on various components of the dolostone bedrock. For the dolostone matrix, Kennel reported values ranging from 0.01 to 0.10%, with an average of 0.02%, which closely aligns with Plett's findings. However, Kennel's data revealed significant variations in sorption potential depending on the specific location within the dolostone. In a single sample from a stylolite layer, he reported a foc value of 3.5%, indicating a higher sorption potential in that particular layer. Notably, for 15 samples taken from fracture surfaces, Kennel reported a range of 0.08–6.36%, with an average of 2.31%. These results indicate a substantial sorption potential on fracture surfaces within the dolostone. In fact, the data suggest that the sorption potential on the surface of fractures is more than 100 times greater than that of the dolostone rock matrix. Sorption is quantified as a coefficient of retardation (R), which can be expressed as a function of the distribution of an organic compound between the aquifer matrix and the aqueous phase (Eq. 7.3):

$$R = 1 + \rho K_d / n \quad (7.3)$$

where R is the coefficient of retardation; ρ is the bulk density of the aquifer matrix. K_d is the distribution coefficient, as defined by sorbed concentration divided by dissolved concentration. The porosity is represented by n .

The distribution coefficient (K_d) can also be expressed as Eq. 7.4:

$$K_d = K_{oc} f_{oc} \quad (7.4)$$

where K_{oc} is the soil sorption coefficient to organic carbon and f_{oc} is the fractional mass of organic carbon in the matrix.

In addition to sorption onto organic carbon, Loop and White (2001) have reported that CVOCs can also adsorb to the surface of metal oxide coatings. These coatings are predominantly found in the quartzitic sandstones of the Antietam Formation but can also be present in the carbonate bedrock aquifer. Similar to sorption onto carbon, this adsorption process results in the removal of mass from the CVOCs present in groundwater, thus influencing their transport behavior. The adsorption onto metal oxide coatings provides an additional mechanism for the retention and attenuation of CVOCs in the subsurface. Assessing the significance of this mechanism for the study site requires site-specific determinations of fractional mass of organic carbon (f_{oc}) for granular materials such as residuum and sediment, as well as for the rock matrix and fracture surfaces, as performed in the studies conducted at the University of Waterloo (Plett 2006; Kennel 2008). Without such data, it is challenging to evaluate the importance of adsorption onto metal oxide coatings at the site. However,

if the site conditions are similar to those described in the previous studies, sorption onto fracture surfaces can remove a portion of the CVOC mass dissolved in groundwater as it flows through those fractures. This sorption process can contribute to secondary sourcing once CVOC concentrations start to decline and desorption occurs. Additionally, if the residuum and/or sediments at the site have a significant organic carbon fraction (foc), sorption and desorption processes associated with these materials can also be substantial, particularly if they result in sorption-retarded reverse diffusion. In such cases, CVOCs that have sorbed onto these materials may be gradually released back into the groundwater over time, potentially prolonging the persistence of contaminants in the subsurface environment. These sorption and desorption processes can have important implications for the fate and transport of CVOCs in the subsurface, as they can influence the overall mass balance and the long-term behavior of contaminants in the aquifer.

7.4.5 Bio-reductive Dechlorination of Organic Compounds

Under anaerobic conditions, the chlorinated solvents frequently detected in groundwater at contaminated sites have the potential to undergo biotic reductive degradation. This natural process involves the activity of specific microorganisms capable of utilizing the chlorinated solvents as electron acceptors during their metabolic activities. As a consequence, the chlorinated solvents undergo a series of sequential dechlorination reactions, leading to the formation of less chlorinated compounds. This process is facilitated by natural bacteria that possess the ability to carry out reductive dechlorination. Figure 7.17 summarizes the degradation pathways of CVOCs, starting from PCE. The pathways highlighted in red are the most commonly accepted degradation processes, although the actual degradation pathways are site-specific. Reductive dechlorination is often the dominant process for the more chlorinated CVOCs. PCE, with its four chlorine atoms, readily undergoes reductive dechlorination to TCE under anaerobic conditions. Furthermore, the tendency of chlorinated ethenes to undergo reductive dechlorination decreases as the number of chlorine substituents decreases.

In many water bearing formations, the rate of each step in the reductive dechlorination process tends to slow down as the transformation progresses. Consequently, the concentrations of later degradation products, such as cis-DCE or VC, may appear to increase relative to the concentrations of the parent solvents. This observation is commonly made when geochemical conditions continue to favor reductive dechlorination. In certain cases, the relative concentrations of degradation products may even increase with increasing distance from the source zone. This phenomenon occurs when the geochemical conditions required for reductive dechlorination remain favorable over a greater distance from the original source. Furthermore, the relative concentrations of transformation products can also exhibit an increase over time at a specific location. This is because the biogeochemical conditions may become more favorable for reductive dechlorination as time progresses.

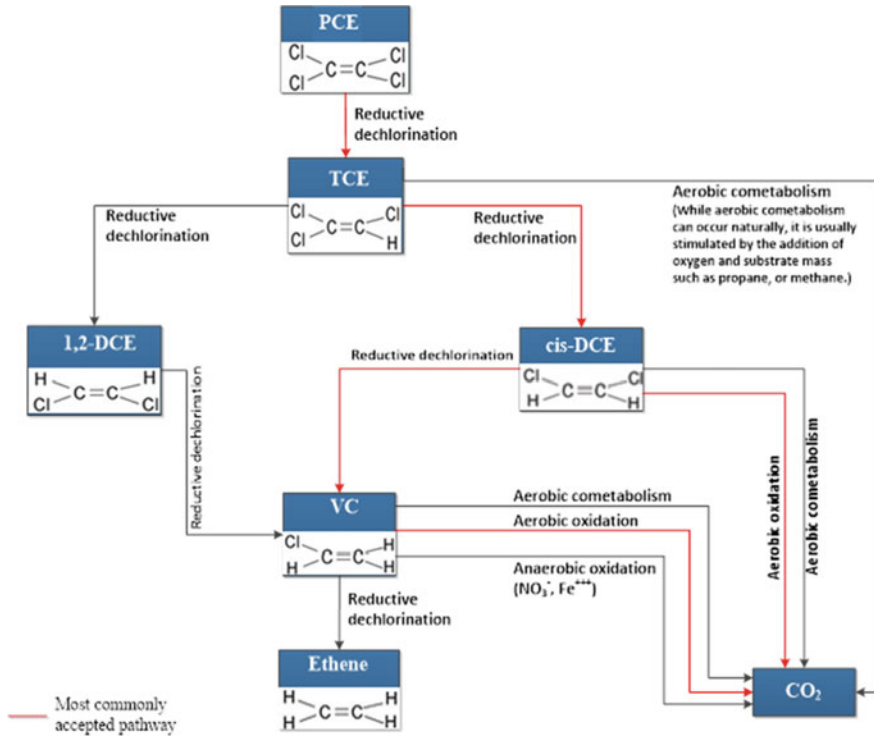


Fig. 7.17 Summary of microbial biodegradation pathways

These transformations typically take place in source areas where chlorinated volatile organic compounds (CVOCs) were co-disposed with other organic compounds, such as petroleum products. The biodegradation of these co-disposed substances often generates geochemical conditions, such as sulfate-reducing or methanogenic conditions, that are conducive to the reductive dechlorination of CVOCs. Rate of degradation is commonly expressed in degradation coefficient. The degradation coefficients for TCE, cis-DCE, and VC are shown in Table 7.8. The half-lives of the contaminants, in years, can be calculated by dividing 0.7 by the degradation coefficient.

Table 7.8 Select chemical properties of CVOCs

Compound	K_{oc} (l/kg)	Solubility (mg/l)	Degradation coefficient (1/year)	Half-life (years)
Trichloroethene	93	1100	0.02	35
cis-1,2-dichloroethene	49	3500	0.01	70
Vinyl chloride	10	2700	0.09	7.8

The degradation of organic compounds takes place through electron transfers between a donor and an acceptor, typically in an environment with reduced oxygen levels. These chemical reactions, known as biologically mediated redox reactions, are facilitated by naturally occurring microorganisms. Microbial degradation is most efficient when the concentrations of organic constituents are at low to moderate levels. Microorganism populations that are capable of effectively breaking down organic compounds thrive within a pH range of 5–9. As organic compounds undergo oxidation, carbon dioxide is produced, leading to the formation of carbonic acid in groundwater. This process effectively lowers the pH of the groundwater. The redox potential, which reflects the oxygenation potential of a groundwater environment, is typically above 50 millivolts (mV) in aerobic environments, accompanied by dissolved oxygen (DO) concentrations greater than 0.8 mg/L.

Microbial degradation of organic compounds can lead to the transition from an aerobic environment to an anaerobic one as electron acceptors are progressively depleted (Environmental Security Technology Certification Program 2011). Initially, when organic compounds are introduced, microbial populations consume the available oxygen in the environment. As oxygen becomes limited, microorganisms sequentially utilize alternative electron acceptors for respiration, such as nitrate, manganese oxide, ferrous oxide, and sulfate.

In the context of organic compound plumes, aerobic degradation typically occurs at the outer edges or limits of the plume where oxygen is still available. As the plume progresses inward, towards the center, the oxygen concentration decreases, creating an anaerobic environment. Within the anaerobic zone of the plume, microorganisms rely on alternative electron acceptors for their metabolic activities. Different zones of reduction, supported by specific electron acceptors, can be observed within contaminant plumes. For example, the presence of ferrous iron and manganese oxide can facilitate anaerobic degradation processes in certain zones. These compounds serve as electron acceptors for microorganisms, enabling their metabolic activities in the absence of oxygen.

7.4.6 *Abiotic Degradation*

Dechlorination without microbes was recognized in late 1980s. Research has demonstrated that chemically precipitated ferrous iron can serve as an active reductant for CVOCs. Additionally, the development of zero valent iron (ZVI) technology has contributed to the growing interest in abiotic degradation of contaminants. In 2002, a study by Ferrey and Wilson (2002) showed that a plume of cis-DCE, a CVOC, was abiotically degraded by magnetite, a mixed ferrous and ferric oxide. The degradation rates observed with magnetite were comparable to biological processes, indicating the effectiveness of abiotic degradation for CVOCs. In this context, ferrous iron plays a similar role to microbes in reductive dechlorination, acting as a reductant for CVOCs.

Figure 7.18 illustrates the common abiotic degradation pathways of CVOCs. The primary abiotic degradation mechanism for CVOCs is reductive elimination. This process involves a two-electron transfer to the target molecule, leading to the elimination of two chlorine atoms. The result is the formation of relatively benign degradation products. For instance, TCE can undergo dichloroelimination via reductive elimination, forming acetylene as an intermediate product. This reaction involves the removal of two chlorine atoms from TCE, resulting in the transient formation of chloroacetylene. Subsequently, acetylene may undergo further reactions, such as hydrogenation, under specific conditions (Arnold and Roberts 2000).

Hydrogenolysis is a commonly observed mechanism in abiotic degradation processes facilitated by reactive minerals, although its contribution is typically minor compared to reductive elimination. Hydrogenolysis involves the reductive breaking of a carbon-chlorine bond, with hydrogen replacing chlorine and the addition of two electrons to the molecule (Tobiszewski and Namiesnik 2012). Butler and Hayes

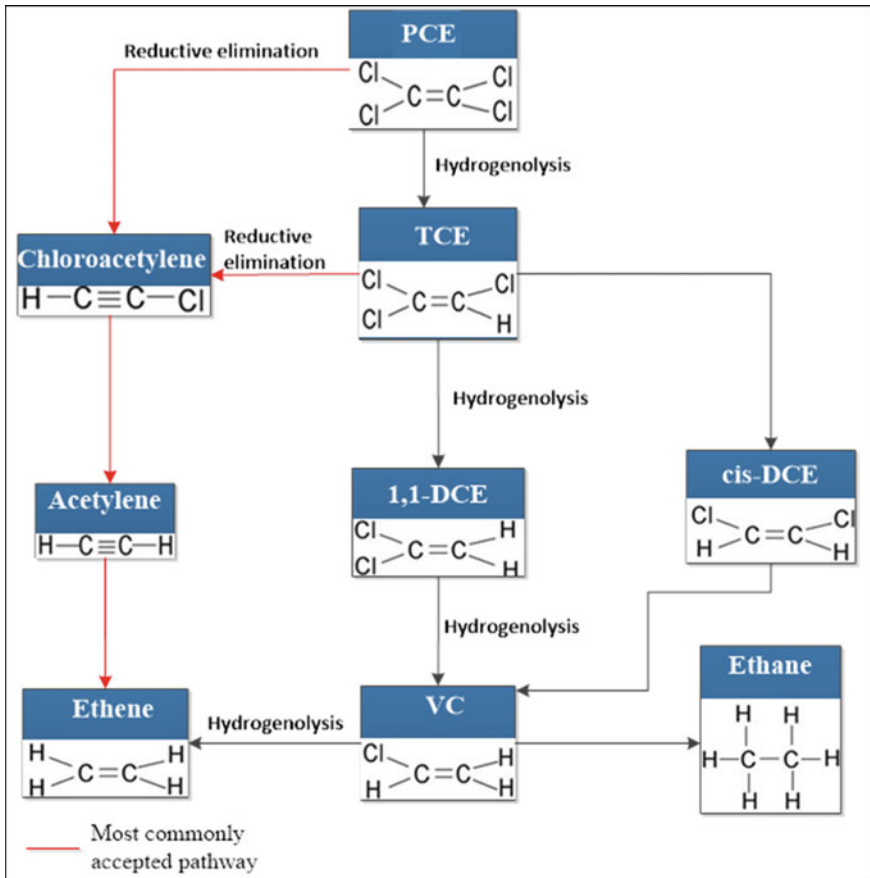


Fig. 7.18 Summary of abiotic biodegradation pathways

(1999) demonstrated that in iron sulfide (FeS) systems at pH 8.3, trichloroethylene (TCE) was transformed to acetylene 11.8 ± 1.1 times faster than to cis-DCE, while tetrachloroethylene (PCE) was transformed to acetylene 8.2 ± 1.8 times faster than to TCE.

Acetylene is the most common degradation product resulting from reductive elimination and is often considered a characteristic product of the abiotic degradation of chlorinated solvents (He et al. 2015). The specific degradation product resulting from the hydrogenolysis pathway depends on the parent compound, with each step sequentially removing one chlorine atom.

Butler and Hayes (1999) proposed that FeS can transform PCE through parallel reaction pathways, leading to the formation of acetylene, TCE, and cis-DCE. Jeong and Hayes (2007) reported that PCE can be transformed to TCE via hydrogenolysis, forming acetylene and 1,1-DCE. Similar mechanisms and degradation products have been observed for the degradation of PCE by pyrite and green rust (Lee and Batchelor 2002).

Likewise, the transformation of TCE by FeS occurs through parallel reaction pathways. TCE can be converted to acetylene through reductive elimination, with chloroacetylene as an intermediate, or via hydrogenolysis to cis-DCE (Butler and Hayes 1999; Jeong and Hayes 2007). Acetylene was identified as the major product in the reductive transformation of TCE by FeS, followed by cis-DCE. Similar degradation mechanisms and product distributions have been observed for TCE degradation by troilite, pyrite, and green rust (Lee and Batchelor 2002).

Regarding the reductive dechlorination of cis-DCE by pyrite, Lee and Batchelor (2002) suggested that the main pathway is reductive elimination. However, cis-DCE does not appear to react with FeS (Jeong and Hayes 2007). The dechlorination of vinyl chloride by pyrite follows a hydrogenolysis pathway, resulting in the production of ethene and ethane, with ethene further reduced to ethane. The major abiotic degradation pathways and products for the degradation of PCE and TCE are similar for minerals such as FeS, magnetite, green rust, and Fe^{2+} -sorbed minerals. Reductive elimination is the primary degradation pathway, with acetylene being the major degradation product.

7.4.7 *Aerobic/Anaerobic Oxidation*

The primary solvents, PCE and TCE, do not undergo significant biodegradation under oxidizing conditions in groundwater. However, under appropriate conditions, their daughter products, cis-1,2-dichloroethylene (cis-DCE) and vinyl chloride (VC), can undergo degradation through aerobic or anaerobic oxidation processes. These degradation pathways occur without the formation of easily identifiable degradation products. Depending on the depth to the water table, cis-DCE and VC may degrade aerobically in the vadose zone, which reduces their potential impact as concerns for vapor intrusion into occupied structures. Table 7.9 summarizes the various degradation mechanisms of CVOCs. Degradation through either microbial or abiotic process

is a destructive mechanism that leads to reduction in loads of CVOCs in groundwater. The degradation together with the nondestructive natural attenuation mechanisms including sorption, dispersion, and dilution controls fate and transport of CVOCs in many groundwater systems. Complete degradation of CVOCs can result in the transformation of these compounds into environmentally benign substances such as carbon dioxide (CO₂), ethene, and chloride ions. However, it is important to note that some transformation products, like vinyl chloride (VC), can actually increase the toxicity of chlorinated solvents. To comprehensively understand the fate of CVOCs and their degradation, it is crucial to establish a conceptual site model that can be used for contaminant transport modeling, characterizing exposure pathways, and conducting analyses to select appropriate remedial alternatives. The effectiveness of CVOC degradation is highly dependent on the site-specific hydrologic, biologic, and geochemical characteristics of the groundwater system. These factors play a significant role in determining the availability of electron acceptors or donors, the presence of suitable microbial communities, and the overall conditions necessary for degradation processes to occur.

7.4.8 Secondary Sourcing

Figure 7.16 highlights several processes that have been identified as reversible in the context of the topic discussed. These reversible processes include.

Aqueous diffusion refers to the movement of water molecules into the pore spaces of different geological formations, including carbonate rock matrices, residua, and sediments that fill voids within the carbonate rock. This diffusion process occurs in both dense non-aqueous phase liquid (DNAPL) source areas and chlorinated volatile organic compound (CVOC) plume areas. This means that the movement of water into these porous media can occur in both directions, allowing for the exchange of dissolved contaminants.

Partitioning from soil vapor or DNAPL to pore water in the vadose zone. This indicates that contaminants can move between the vapor phase and the water phase in the unsaturated zone. They can either partition from the vapor phase into the pore water or vice versa, depending on the prevailing conditions.

Sorption onto the organic carbon fraction of formation solids and metal oxide coatings in both the saturated and unsaturated zones. This refers to the reversible process of contaminants attaching to the organic carbon present in the solid formations and the coatings of metal oxides. Contaminants can desorb from these surfaces back into the water phase under certain conditions. These processes effectively retain mass within the solid phase of soil and bedrock, with the extent of mass storage and its persistence influenced by various factors. The presence of dense non-aqueous phase liquid (DNAPL) as a primary source of contamination in water and vapor, as well as the existence of groundwater containing constituents at higher concentrations than the original levels, play a crucial role in determining the amount of sorbed and diffused mass.

Table 7.9 Summary of degradation mechanisms of CVOCs

Environment	Mechanism	Processes
Microbial degradation	Anaerobic conditions	Reductive dechlorination
		<ul style="list-style-type: none"> • Microbial reductive dechlorination is a widespread process observed in anaerobic aquifers contaminated with CVOCs) However, the degree of dechlorination can vary significantly from one site to another • The reductive dechlorination process tends to decrease in efficiency as the number of chlorine atoms in the molecule decreases. For example, PCE, which contains four chlorine atoms, readily undergoes reductive dechlorination to form TCE. However, this transformation is less likely to occur in aerobic aquifers where oxygen is present • The reductive dechlorination of TCE to cis-dichloroethene (cis-DCE) occurs under conditions where Fe(III) is being reduced and in more strongly reducing environments • The reductive dechlorination of cis-DCE to vinyl chloride (VC) typically requires the presence of sulfate (SO₄)-reducing conditions, although it can also occur in methanogenic environments • The reductive dechlorination of VC to non-chlorinated ethene is known to be slow and significant only under highly reducing, methanogenic conditions • In groundwater systems, the reductive dechlorination of chloroethene contaminants is often incomplete, leading to the accumulation of cis-DCE and VC as intermediate products • Complete reductive dechlorination to ethene may be possible when dehalococoides (DHC) microbes are present in substantial numbers in groundwater systems

(continued)

Table 7.9 (continued)

Environment	Mechanism	Processes
	Anaerobic oxidation	<ul style="list-style-type: none"> • Under anaerobic conditions, the oxidation of cis-DCE and VC can occur if there is a strong oxidant present to drive microbial degradation • Fe(III) oxides are strong oxidants when it is present in groundwater systems. Low but significant VC mineralization has been detected in anaerobic microcosms under ambient Fe(III) conditions • The combination of reductive dechlorination of PCE and TCE in anaerobic conditions, followed by the subsequent anaerobic microbial oxidation of cis-DCE and VC, presents a potential microbial pathway for achieving the complete degradation of CVOCs within groundwater system
Aerobic conditions	Aerobic oxidation	<ul style="list-style-type: none"> • The tendency to undergo oxidation increases as the number of chlorine substituents decreases. VC, being the least chlorinated among the CVOCs, exhibits the highest propensity for oxidation • Microbial oxidation of DCE and VC to CO₂ has been observed under aerobic conditions, however, this mechanism is of limited relevance in most groundwater systems • The aerobic biodegradation of CVOCs in groundwater systems is likely restricted to the periphery of the contaminant plume, where the dissolved oxygen (DO) has not been depleted due to microbial respiration

(continued)

Table 7.9 (continued)

Environment	Mechanism	Processes
	Aerobic cometabolism	<ul style="list-style-type: none"> • Cometabolic oxidation is generally not regarded as a significant mechanism for the biodegradation of CVOCs in groundwater • Aerobic cometabolism requires the presence of oxygen and a primary substrate to initiate the production of a suitable oxygenase • Aerobic microorganisms, including methane, propane, ethene, aromatic compound, ammonium, isoprene, and VC oxidizers, are capable of oxidizing TCE, cis-DCE, and VC to CO₂ without accumulation of toxic intermediates • In aerobic aquifers contaminated with TCE, biodegradation can occur through the activity of methanotrophic microorganisms when an adequate supply of methane is introduced into the subsurface to stimulate and support their activity
Abiotic degradation	Anaerobic conditions	<ul style="list-style-type: none"> • Reductive elimination primarily takes place under methanogenic conditions, where the presence of methanogenic microorganisms facilitates the process. However, it can also occur under partially aerobic conditions, although to a lesser extent • Reductive elimination is a chemical process that involves a two-electron transfer to the target molecule, resulting in the elimination of two chlorine atoms • PCE and TCE undergo dichloroelimination, leading to the formation of acetylene through the transient intermediate chloroacetylene. Acetylene can then undergo further reactions, such as hydrogenation, resulting in the formation of ethene and/or ethane • Iron-bearing minerals, such as iron sulfides (pyrite and mackinawite), green rust, iron oxides (magnetite), and iron-bearing clays, play a crucial role in these processes • Reactive iron minerals are commonly found in subsurface environments under conditions characterized by iron reduction and sulfate reduction
Anaerobic conditions	Hydrogenolysis	<ul style="list-style-type: none"> • Hydrogenolysis is a reductive reaction that involves the cleavage of a carbon-chlorine bond, resulting in the replacement of chlorine with hydrogen • Sequential hydrogenolysis involves the sequential replacement of chloro-substituents with H from protons, releasing chloride • TCE can undergo sequential hydrogenolysis, forming cis-DCE, followed by VC, and ethene in the presence of iron sulfide and/or zero valent iron (ZVI)

As groundwater concentrations experience significant decreases, a reversal of these processes occurs, commonly referred to as reverse diffusion and desorption. This reversal leads to the release of previously stored mass back into the flowing groundwater within the saturated zone and the gravitational water within the vadose zone. Through desorption and reverse diffusion, the mass, previously held within the solid phase, is reintroduced into the aqueous phase. Since this stored mass can re-enter the aqueous phase, it acts as a secondary source of groundwater contamination, potentially impeding the decline of groundwater concentrations over time. These processes often contribute to the observed tailing effect in groundwater monitoring data at sites undergoing remediation for chlorinated volatile organic compounds (CVOCs).

7.4.9 Evidence of Natural Attenuation

The confirmation of natural attenuation typically involves assessing a series of evidence that supports the overall degradation process. One primary piece of evidence is the evaluation of historical analytical data.

Concentration reduction indicators: The geochemical groundwater data collected from the monitoring wells are the best indicators of biodegradation occurrence. Based on chemographs of CVOCs, results of monitored natural attenuation parameters (e.g., sulfate, nitrate, chloride, iron, etc.) and the presence and distribution of cis-DCE and VC (byproducts of biodegradation of TCE), conditions for natural attenuation can be determined. The presence of VC, in addition to cis-cis-DCE, is a strong indicator of chemical and natural attenuation of the CVOC plumes. Given the correct environmental conditions, over time VC may mineralize into CO₂, H₂O, and a chloride ion in addition to ethene and ethane which readily volatilize into the vadose zone and ultimately the atmosphere. Figure 7.19 shows a pie diagram for TCE, cis-DCE, and VC to demonstrate their relative distributions. The size of the pie indicates the relative magnitude of the total concentration of three chemicals. Because of the heterogeneous nature of the site, a definitive pattern is not obvious. In general, the data show some diminishing levels of TCE downgradient, but also increases in the concentrations of breakdown products (cis-DCE and VC).

The concentration changes tend to be great where the groundwater was firstly contaminated the most. The maximum concentration of cis-DCE was detected in FTMW-08D at 2900 µg/L in October 2008. In a groundwater sample collected in November 2013, the cis-DCE concentration had decreased to 690 µg/L. In FTMW-04, the cis-DCE concentration decreased by a factor of 70 from 2008 to 2013. The greatest decrease was observed in FTMW-08, where the cis-DCE concentration decreased from 2600 µg/L in October 2008 to 58 µg/L in November 2013. The most obvious TCE concentration change occurred in FTMW-04, decreasing from 180 µg/L in June 2008 to 5.8 µg/L in November 2013. The maximum TCE concentration decrease took place in FTMW-01 from 850 µg/L in June 2008 to

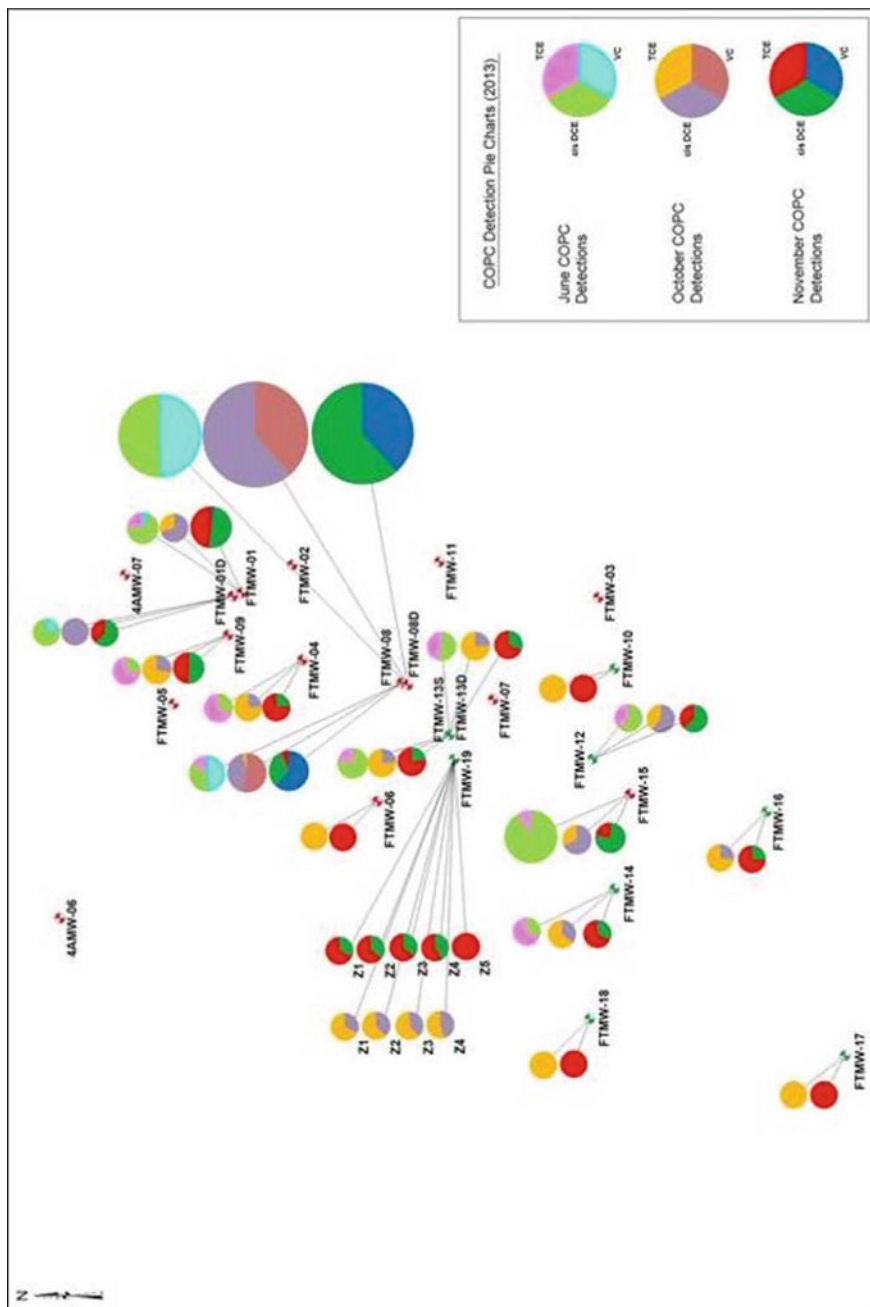


Fig. 7.19 TCE, cis-DCE, and VC pie charts

120 $\mu\text{g/L}$ in November 2013, while the sample in October 2013 had a TCE concentration of 3.8 $\mu\text{g/L}$. The TCE concentration decrease is also obvious in FTMW-08D and FTMW-06. However, the TCE concentration in FTMW-01 shows fluctuation without a significant decrease. The VC concentration decreases are the most obvious in FTMW-08, FTMW-08D, and FTMW-01, where the VC concentrations in other wells are either in concentrations less than 1 $\mu\text{g/L}$ or non-detects.

Geochemical environmental indicators: Geochemical data can serve as a secondary form of evidence to support natural attenuation. Table 7.10a provides a summary of relevant geochemical data for MNA evaluation. This data encompasses groundwater quality parameters such as redox potential, pH, and dissolved oxygen levels. The data collected at the site indicates that groundwater and soil pH ranges from 6 to 8, indicating a neutral pH level. A pH range between 5 and 9 is generally considered favorable for supporting aerobic degradation of organic compounds. Within the shallow groundwater unit (the overburden aquifer), redox potential varies greatly at the site between -96 and 189 mV. Also, if ferrous iron is abundant, a redox potential reading could be inaccurate and should not be used to assess degradation potential (Interstate Technology and Regulatory Cooperation Work Group [ITRC] 1999). Dissolved oxygen ranged between 0.38 and 8.73 mg/L. Anaerobic bacteria cannot typically survive if the dissolved oxygen is above 0.5 mg/L.

Biological indicators: The presence and activity of the dehalogenating microbes is responsible for each step of the sequential dechlorination of TCE to ethene. Table 7.10b summarizes biological indicator data pertinent to MNA evaluation. While a number of bacterial cultures capable of utilizing PCE or TCE as growth supporting electron acceptors, Dehalococcoides (Dhc) may be the most important ones. They are the only identified bacterial group that is capable of complete reductive dechlorination to ethane. Lu and others (2006) suggest a concentration of 10^4 Dhc cells per milliliter as a screening criterion to identify areas where reductive dechlorination will yield a generally useful biodegradation. Complete reductive dechlorination will be unlikely to occur if Dhc concentrations are less than 10 cells/mL. Like Dhc, the Desulfotomaculum (Dsm) genus is capable of reductively dechlorinating PCE and TCE to cis-DCE (cis-dichloroethylene). What sets Dsm apart from other dechlorinating bacteria is not the range of electron acceptors it can utilize (PCE and TCE), but rather the electron donors that support reductive dechlorination. Dsm species are known to utilize more complex electron donors such as acetate, lactate, pyruvate, and succinate. On the other hand, methanogens utilize hydrogen to produce methane and can therefore compete with dechlorinating bacteria, including Dhc, for available hydrogen resources.

Table 7.10a Field measurement results for MNA parameters

Well ID	Field parameters by multi-parameter instrument										Field analysis by test kits (mg/L)		
	pH (pH units)	Conductivity (mS/cm)	Turbidity (NTU)	DO (mg/L)	Temperature (°C)	ORP (mv)	CO ₂	Fe ²⁺	H ₂ S				
4AMW-07	6.66	0.676	72	4.46	11.23	152	25	ND	ND				
FTMW-03	6.85	0.801	10.8	1.18	12.04	129	55	ND	ND				
FTMW-06	6.84	0.732	0.0	8.61	10.15	166	20	ND	ND				
FTMW-08D	6.95	0.934	5.9	1.10	10.86	-96	50	3	ND				
FTMW-08	6.69	0.820	0.0	7.82	9.21	147	40	ND	ND				
FTMW-09	6.73	0.698	0.0	4.63	10.75	163	45	ND	ND				
FTMW-14	6.90	0.781	0.0	7.26	11.96	144	45	ND	ND				
4AMW-07	7.14	0.601	9.6	5.28	14.04	144	25	ND	ND				
FTMW-03	6.89	0.688	9.8	3.01	13.95	164	40	ND	ND				
FTMW-06	7.02	0.636	0.0	3.27	13.77	189	40	ND	ND				
FTMW-08D	7.13	0.780	9.4	0.38	14.98	-95	60	3.4	ND				
FTMW-08	6.99	0.753	12.6	0.96	14.16	110	25	ND	ND				
FTMW-09	7.22	0.601	2.2	8.73	13.82	148	30	ND	ND				
FTMW-14	6.95	0.639	4.2	2.54	14.46	139	35	ND	ND				
Optimal natural attenuation conditions	5-9	2 × background		<0.5	> 20	< 50	2 × background	> 1					

Values in bold indicate active biodegradation conditions (USEPA 1998)
 4AMW-07 is the background well

Table 7.10b Laboratory analysis results for MNA parameters

Well ID	Bacteria analysis results (cells/mL)				Gas analysis results ($\mu\text{g/L}$)				Geochemical analysis results (mg/L)			
	DHC	DSM	IRB/ SRB	MGN	Ethane	Ethene	Methane	Nitrate Nitrite as N	Sulfate	Total iron	TOC	
4AMW-07	< 2	< 4	< 3	390	0.0027	0.033	0.16	9.2	24	1.5	0.91	
FTMW-03	1.0	< 1	231	6930	0.0012	0.028	0.039	4.4	32	0.38	1.1	
FTMW-06	1.3	< 1	< 0.8	36,000	0.0027	0.029	0.026	11	26	0.04	0.67	
FTMW-08D	6.7	< 1	1090	80,000	0.01	4.6	6.4	0.099	120	5.2	1.6	
FTMW-08	22.3	< 1	< 0.8	465,000	0.003	0.077	0.22	3.2	78	0.044	1.1	
FTMW-09	1.8	< 1	< 0.8	5460	0.0035	0.035	0.54	8.7	26	0.04	0.75	
FTMW-14	1.2	< 1	< 0.8	66,900	0.0024	0.028	0.05	7.2	42	0.04	0.76	
4AMW-07	1.3	< 1	< 0.8	51,200	0.0021	0.02	0.17	10	26	0.43	0.84	
FTMW-03	2.3	< 1	< 0.8	199,000	0.032	0.026	0.36	5.7	30	0.052	1	
FTMW-06	1.5	< 1	< 0.8	104,000	0.0034	0.016	0.2	12	20	0.04	0.77	
FTMW-08D	1.0	< 1	< 0.8	41,500	0.025	0.025	0.1	ND	120	4.3	1.5	
FTMW-08	42.6	2.8	< 0.8	1,100,000	0.0047	0.088	1.3	1.2	100	0.43	1.4	
FTMW-09	6.0	< 1	< 0.8	617,000	0.004	0.025	0.14	9.5	26	0.15	0.86	
FTMW-14	0.7	< 1	< 0.8	190,000	0.0069	0.015	0.36	7.7	38	0.097	0.77	
Optimal Natural attenuation conditions	> 10				> 0.01	> 0.01	> 0.5	< 1	< 20	2 \times background	> 20	

Values in bold indicate active biodegradation conditions (USEPA 1998) conditions

4AMW-07 is the background well

DHC dehalococoides

DSM desulfuromonas

IRB/SRB iron-reducing bacteria/sulfur reducing bacteria

MGN methanogen

7.5 Pathway-Focused Risk Assessment

A human health risk assessment (HHRA) was performed to establish the initial risks linked to groundwater exposure. The HHRA examined the reasonable maximum exposure (RME) that could potentially occur at the site. The findings of the HHRA are indicative and should serve as a reference when making decisions regarding risk management. In accordance with USEPA (1989) guidance, the HHRA methodology followed the following five elements:

- **Data evaluation and hazard assessment:** The review of available data was conducted to compile datasets for utilization in the risk assessment process. This involved identifying contaminants of potential concern (COPCs) that are closely associated with the site and are detected at a frequency exceeding 5% and concentrations surpassing background levels and/or conservative screening levels. Additionally, exposure point concentrations were calculated to represent the upper-bound conditions of exposure in each affected medium.
- **Exposure assessment:** The human population, i.e., groups potentially exposed to COPCs (referred to as potential human receptors), is characterized. Potential pathways of exposure are identified, specifically those applicable to potential receptors at the site, such as ingestion and inhalation. Estimated COPC exposure concentrations are derived from site-specific monitoring data. The concentrations of COPCs in relevant media, such as groundwater, are converted into systemic doses, considering factors like contact rates (e.g., ingestion rates, exposure frequency, and exposure duration) and absorption rates of each COPC. The magnitude, frequency, and duration of these exposures are then integrated to estimate daily intakes over a specified period, such as a lifetime or activity-specific duration.
- **Toxicity assessment:** The toxicity assessment has two primary objectives: (1) to identify the nature and extent of toxicity associated with each COPC, and (2) to characterize the dose-response relationship, which describes the relationship between the level of exposure and the magnitude of adverse health effects for each COPC. The assessment presents the connection between the extent of exposure and the degree of toxic injury or disease for each COPC. It includes chemical-specific toxicity values, such as cancer slope factors (SFs) and inhalation unit risks (IURs) for carcinogens, as well as reference doses (RfDs) or reference concentrations (RfCs) for non-carcinogens. The scientific basis and derivation of these toxicity values are discussed in detail.
- **Risk characterization:** Risk characterization combines the findings from the toxicity assessment and the exposure assessment to obtain quantitative estimates of human health risk, encompassing both the risk of cancer and non-carcinogenic effects. The US Environmental Protection Agency (USEPA) has established an acceptable target range for cancer risk, which ranges from one in ten thousand

(0.0001 or 10^{-4}) to one in one million (0.000001 or 10^{-6}). Additionally, a non-cancer target hazard level of 1 (USEPA 1991) is defined. During risk characterization, the significant uncertainties and limitations associated with the risk estimates are identified and documented.

- **Uncertainty analysis:** Risk assessment, like any modeling process, involves assumptions and estimates that introduce uncertainty into the results. Uncertainty analysis is an important component of risk assessment as it considers both the variability in measured and estimated parameters and the lack of knowledge surrounding them. By accounting for uncertainty, decision makers can better understand the reliability and limitations of the risk estimates based on the assumptions and data used in the assessment. There are several major sources of uncertainty in risk assessment: (1) Natural variability. This refers to inherent differences among individuals or populations, such as variances in body weight or genetic susceptibility, which can affect the response to a given exposure. (2) Lack of knowledge. Uncertainty arises from gaps in our understanding of basic physical, chemical, and biological properties and processes. For example, limited knowledge about the affinity of a chemical for soil or its solubility in water can introduce uncertainty into exposure estimates. (3) Model accuracy. The models used to estimate key inputs, such as dose-response relationships, may have inherent limitations or uncertainties. These models rely on data from experiments or studies and may not perfectly represent real-world scenarios. (4) Measurement error. Errors in the measurement of exposure levels or biomarkers can introduce uncertainty into the assessment. Among these sources of uncertainty, dose-response relationships and the classification of carcinogenicity based on weight-of-evidence are often associated with greater uncertainties compared to other elements. Extrapolating data from high-dose exposures in animal studies or occupational settings to lower levels of exposure involves numerous assumptions, including effects thresholds, interspecific extrapolation, high- to low-dose extrapolation, and route-to-route extrapolation. The scientific validity of these assumptions is uncertain, and while each individual extrapolation is designed to prevent underestimation of risk, collectively they can result in unquantifiable but potentially significant overestimation of risk. It is important to acknowledge and communicate these uncertainties to ensure that the risk assessment results are appropriately interpreted and used for decision-making purposes.

7.5.1 Exposure Pathway Model

In a Human Health Risk Assessment (HHRA), scenarios are developed to define the conditions under which individuals may be exposed to Contaminants of Potential Concern (COPCs). These scenarios are typically summarized in an Exposure Pathway Model (EPM), which serves as a framework for estimating the risks and hazards associated with each COPC, exposure pathway, and receptor. The preliminary EPM presented in Fig. 7.20 represents understanding of:

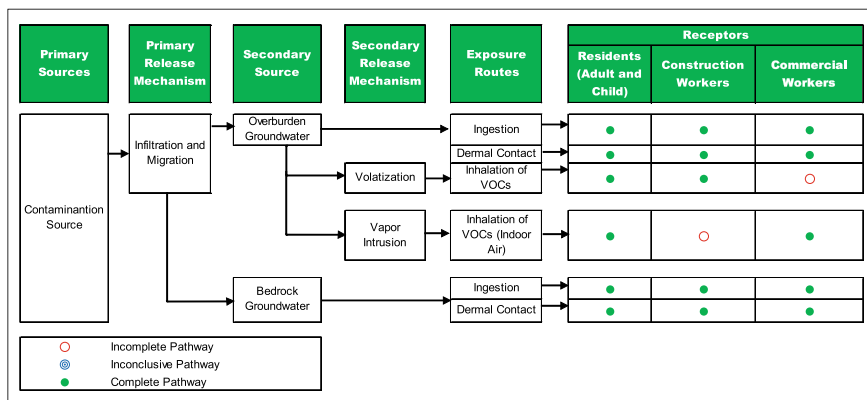


Fig. 7.20 Exposure pathway model for HHRA

- Known or potential sources of COPC in groundwater;
- Primary and secondary release mechanisms that may result in transfer among media;
- Potentially complete exposure pathways for defined receptor populations, based on collected data or expected pathways; and
- Current and potential future on- and off-Site human receptor populations.

7.5.2 Exposure Point Concentrations

Intake serves as a quantitative estimation of the exposure levels. It is determined for each identified complete exposure pathway within the Exposure Pathway Model (EPM) (refer to Fig. 7.20). Intake is expressed as the mass of the substance that comes into contact with the body per unit body weight per unit time. This measurement is typically denoted as milligrams of chemical per kilogram of body weight per day (mg/kg bw-day). The calculation of intakes involves the consideration of several variables. These variables include chemical concentrations, contact rates, exposure frequency, exposure duration, body weight, and exposure averaging time. In the context of the Human Health Risk Assessment (HHRA), exposure point concentrations (EPC) indicate the concentrations of Contaminants of Potential Concern (COPCs) in the relevant environmental media that a selected receptor is expected to come into contact with over a designated exposure period. The reported concentrations of COPCs are used to calculate the 95% upper confidence limit of the mean, following the guidelines provided by the US Environmental Protection Agency (USEPA 1989, 1992). The use of the 95% upper confidence limit (95% UCL) is preferred because assuming long-term contact with the maximum concentration is not considered reasonable according to USEPA guidelines (USEPA 1989). The determination of the 95%UCL is performed using the USEPA ProUCL program (USEPA 2013). The EPC is based on

Table 7.11 Exposure point concentrations of select COPCs

COPC	Mean detected concentration (ug/L)	95% UCL (ug/L)	Maximum detected concentration (ug/L)	EPC value (ug/L)
CIS-DCE	1.91E+02	3.86E+02	2.90E+03	3.86E+02
TCE	3.16E+01	7.72E+01	8.50E+02	7.72E+01
VC	2.09E+02	6.14E+01	8.80E+02	6.14E+01

the lower value between the maximum detected concentration for a specific medium and the 95%UCL. The ProUCL results for cis-DCE, TCE, and VC in groundwater are summarized in Table 7.11.

7.5.3 Exposure Parameters and Exposure Intake Equations

Rates of contact (e.g., ingestion rates, skin surface areas, etc.), exposure frequency and duration, body weight, and averaging time constitute the exposure parameters. The amount of contaminated media contacted per unit time or event is defined as the rate of contact. Exposure frequency and duration are used to determine the duration of exposure to COPCs in the media of concern. The body weight represents the average body weight over an exposure period (USEPA 1989). Tables 7.12, 7.13, 7.14 and 7.15 detail the exposure parameters for the resident adult, resident child, construction worker, and commercial worker, respectively.

7.5.4 Toxicity Assessment for Non-carcinogens

The USEPA provides comprehensive guidance on the methodology used to establish non-cancer reference values or non-carcinogens, as well as considerations for site-specific modifications or applications of these concentrations (USEPA 2014). Non-carcinogens refer to substances that are generally believed to have a threshold daily dose below which harmful effects are unlikely to occur. The concentration associated with this threshold is known as the no-observed-adverse-effect-level (NOAEL). The NOAEL can be derived from various sources, including animal laboratory experiments or human epidemiology investigations, often based on studies conducted in occupational settings. When developing a toxicity value or human NOAEL for non-carcinogens, such as a reference dose (RfD), the regulatory approach involves several steps. First, the critical toxic effect associated with exposure to the chemical is identified, focusing on the most sensitive adverse effect observed. Next, the threshold

Table 7.12 Parameter values for daily groundwater intake of adults

Exposure route	Parameter code	Parameter definition	Units	RME value	Intake equation/ model name
Ingestion	CW	Contaminant concentration in the assessed water	mg/L	EPC table	$\text{CDI (mg/kg/day)} = \text{CW} \times \text{CR} \times \text{EF} \times \text{ED}/(\text{BW} \times \text{AT})$ Mutagenic chronic daily intake (MCDI) (mg/kg/day) = $\text{CW} \times \text{EF} \times [(\text{ED}_{6-16} \times \text{CR} \times 3) + (\text{ED}_{16-30} \times \text{CR} \times 1)]/\text{BW}/(\text{AT})$
	CR	Daily intake rate	L/day	2	
	EF	Annual frequency of exposure	day/year	350	
	ED-NC	Duration of exposure—noncancer	year	30	
	ED-C	Duration of exposure—cancer	year	24	
	BW	Body weight	kg	70	
	AT-NC	Average time—noncancer	days	10,950	
	AT-C	Average time—cancer	days	25,550	
Dermal	CW	Contaminant concentration in the assessed water	mg/L	EPC table	$\text{CDI (mg/kg/day)} = \text{DA}_{\text{event}} \times \text{SA} \times \text{EF} \times \text{ED} \times \text{CF}/(\text{BW} \times \text{AT})$ Mutagenic chronic daily intake (MCDI) (mg/kg/day) = $\text{CW} \times \text{EF} \times \text{PC} \times \text{ET} \times [(\text{ED}_{6-16} \times \text{SA} \times 3) + (\text{ED}_{16-30} \times \text{SA} \times 1)]/\text{BW} \times \text{CF}/(\text{AT})$
	SA	Surface area for dermal contact	cm ²	18,000	
	PC	Permeability coefficient of the skin	cm/h	Chemical-specific	
	ET	Event time	h/day	0.58	
	EF	Annual frequency of exposure	day/year	350	
	ED-NC	Duration of exposure—noncancer	year	30	
	ED-C	Duration of exposure—cancer	year	24	
	BW	Body weight	kg	70	
	AT-NC	Average time—noncancer	days	10,950	
	AT-C	Average time—cancer	days	25,550	
	CF	Conversion factor	L/cm ³	0.001	

(continued)

Table 7.12 (continued)

Exposure route	Parameter code	Parameter definition	Units	RME value	Intake equation/ model name
Inhalation	CA	Contaminant concentration in the air	$\mu\text{g}/\text{m}^3$	Chemical-specific	Exposure concentration ($\mu\text{g}/\text{m}^3$) = $CA \times ET \times EF \times ED / AT \times CF$ where, $CA = VF \times CW$ Mutagenic chronic daily intake (MCDI) ($\mu\text{g}/\text{m}^3$) = $CA \times ET \times EF \times [(ED_{6-16} \times 3) + (ED_{16-30} \times 1)] / (AT)$
	ET	Event time	h/day	24	
	EF	Annual frequency of exposure	day/year	350	
	VF	Volatilization factor	L/m^3	0.5	
	CF	Conversion factor	h/day	24	
	ED-NC	Duration of exposure—noncancer	year	30	
	ED-C	Duration of exposure—cancer	year	24	
	AT-NC	Averaging time—noncancer	days	10,950	
	AT-C	Average time—cancer	days	25,550	

RME reasonable Maximum Exposure
 kg kilogram
 CDI chronic daily intake
 DA Dermal absorbed dose
 mg/L milligrams per liter
 h hour
 cm^2 square centimeter
 $\mu\text{g}/\text{m}^3$ micrograms per cubic meters
 L/m^3 liters per cubic meter

dose is identified from either animal or human studies. Finally, this dose is modified to account for factors such as interspecies variability (when applicable), differences in individual sensitivity (within-species variability), and other uncertainties and modifying factors.

For the derivation of the Reference Concentration (RfC), experimental exposures are extrapolated to a Human Equivalent Concentration (HEC). This process involves two steps: the determination of a point of departure (POD) and the adjustment of the POD by a Dosimetric Adjustment Factor (DAF). The POD can be based on various measurements, such as a No-Observed-Adverse-Effect-Level (NOAEL), Lowest-Observed-Adverse-Effect-Level (LOAEL), benchmark concentration, lower confidence limit, or the lower limit on an effective concentration using a 10% response level (LEC10). The DAF is specific to the site in the body where the toxic effects of the chemical occur, such as the respiratory tract.

Uncertainty factors (UFs) are employed to address the inherent uncertainties involved in extrapolating data. Typically, UFs are default factors of tenfold used in deriving the Reference Concentration (RfC) and Reference Dose (RfD) from experimental data. However, UFs lower than 10 can also be utilized depending on the

Table 7.13 Parameter values for daily groundwater intake of children

Exposure route	Parameter code	Parameter definition	Units	RME value	Intake equation/ model name
Ingestion	CW	Contaminant concentration in the assessed water	mg/L	EPC table	$\text{CDI (mg/kg/day)} = \text{CW} \times \text{CR} \times \text{EF} \times \text{ED}/(\text{BW} \times \text{AT})$ Mutagenic chronic daily intake (MCDI) (mg/kg/day) = $\text{CW} \times \text{EF} \times [(\text{ED}_{0-2} \times \text{CR} \times 10) + (\text{ED}_{2-6} \times \text{CR} \times 3)]/\text{BW}/(\text{AT})$
	CR	Daily intake rate	L/day	1	
	EF	Annual frequency of exposure	day/year	350	
	ED	Duration of exposure	year	6	
	BW	Body weight	kg	15	
	AT-NC	Average time—noncancer	days	2190	
	AT-C	Average time—cancer	days	25,550	
Dermal	CW	Contaminant concentration in the assessed water	mg/L	EPC table	$\text{CDI (mg/kg/day)} = \text{DA}_{\text{event}} \times \text{SA} \times \text{EF} \times \text{ED}/(\text{BW} \times \text{AT})$ Mutagenic chronic daily intake (MCDI) (mg/kg/day) = $\text{CW} \times \text{EF} \times \text{PC} \times \text{ET} \times \text{CF} \times [(\text{ED}_{0-2} \times \text{SA} \times 10) + (\text{ED}_{2-6} \times \text{SA} \times 3)]/\text{BW}/(\text{AT})$
	SA	Surface area for dermal contact	cm ²	6600	
	PC	Permeability coefficient of the skin	cm/h	Chemical-specific	
	ET	Event time	h/day	1	
	EF	Exposure frequency	day/year	350	
	ED	Duration of exposure	year	6	
	BW	Body weight	kg	15	
	AT-NC	Average time—noncancer	days	2190	
	AT-C	Average time—cancer	days	25,550	
	CF	conversion factor	L/cm ³	0.001	

circumstances. In certain cases, a UF of 3 can be employed instead of the standard one-half power ($10^{0.5}$) when deemed appropriate. UFs are utilized to account for the following sources of uncertainty: (1) Variability in susceptibility among individuals in the human population, known as inter-individual or intra-species variability, (2) Uncertainty when extrapolating animal data to humans, referred to as interspecies uncertainty, (3) Uncertainty when extrapolating from subchronic to chronic exposure scenarios, (4) Uncertainty when extrapolating from a Lowest Observed Adverse Effect Level (LOAEL) rather than a No-Observed-Adverse-Effect Level (NOAEL),

Table 7.14 Parameter values for daily groundwater intake of construction workers

Exposure route	Parameter code	Parameter definition	Units	RME value	Intake equation/ model name
Ingestion	CW	Contaminant concentration in the assessed water	mg/L	EPC table	$CDI \text{ (mg/kg/day)} = CW \times CR \times EF \times ED / (BW \times AT)$
	CR	Daily intake rate	L/day	0.05	
	EF	Annual frequency of exposure	day/year	50	
	ED	Duration of exposure	year	1	
	BW	Body weight	kg	70	
	AT-NC	Average time—noncancer	days	365	
	AT-C	Average time—cancer	days	25,550	
Dermal	CW	Contaminant concentration in the assessed water	mg/L	EPC table	$CDI \text{ (mg/kg/day)} = DA_{\text{event}} \times SA \times EF \times ED \times CF / (BW \times AT)$
	SA	Surface area for dermal contact	cm ²	3300	
	PC	Permeability coefficient of the skin	cm/h	Chemical-specific	
	ET	Event time	h/day	4	
	EF	Annual frequency of exposure	day/year	50	
	ED	Duration of exposure	year	1	
	BW	Body weight	kg	70	
	AT-NC	Averaging time—noncancer	days	365	
	AT-C	Averaging time—cancer	days	25,550	
	CF	Conversion factor	L/cm ³	0.001	
Inhalation	CA	Contaminant concentration in the air	mg/m ³	Chemical-specific	$\text{Exposure concentration } (\mu\text{g}/\text{m}^3) = CA \times ET \times EF \times ED / AT \times CF$
	ET	Event time	h/day	4	
	EF	Annual frequency of exposure	day/year	50	
	CF	Conversion factor	h/day	24	

(continued)

Table 7.14 (continued)

Exposure route	Parameter code	Parameter definition	Units	RME value	Intake equation/ model name
	ED	Duration of exposure	year	1	
	AT-NC	Averaging time—noncancer	days	365	
	AT-C	Averaging time—cancer	days	25,550	

- (1) Construction workers ingestion of groundwater is incidental and assumed at 5% of the industrial worker ingestion rate
- (2) It is assumed that construction workers come into contact with groundwater only once a week
- (3) Construction events are assumed to have a maximum duration of one year
- (4) Contact with groundwater is limited to specific body parts, namely the head, hands, and forearms, as construction workers are expected to wear short-sleeved shirts, long pants, and shoes
- (5) During construction events, it is assumed that contact with groundwater occurs for half of the time spent on the construction site each day

and (5) Uncertainty associated with incomplete data. The maximum UF for deriving RfCs in this context is 3000, while the maximum UF for deriving RfDs is 1000. Modifying factors (MFs) are also considered, taking into account the confidence in the scientific studies used to derive toxicity values. The combination of UFs and MFs ensures a conservative and protective approach in the derivation of RfCs and RfDs from available data for human health risk assessments (HHRA).

MF is incorporated in the risk assessment process to account for additional uncertainties in the critical study and the overall database that are not addressed by the uncertainty factors. It is a qualitative professional assessment that ranges from 1 to 10. The default value for the MF is 1, indicating no additional adjustment. However, it is important to note that the USEPA discontinued the use of the modifying factor in 2004. However, toxicity values derived before 2004 may still contain a modifying factor if they were developed using the previous methodology. In addition, the oral RfD for manganese contains an MF of 3 based upon guidance set forth by USEPA (USEPA 2014).

The RfD is determined by dividing the relevant NOAEL by the product of all applicable UFs and the MF. This is expressed in units of mg/kg-day and is calculated as Eq. 7.5:

$$\text{RfD} = \text{NOAEL}/(\text{UF}_1 \times \text{UF}_2 \cdots \times \text{MF}) \quad (7.5)$$

The resulting RfD is expressed in units of milligrams of chemical per kilogram of body weight per day (mg/kg-bw/day).

For the inhalation pathway, an RfC is calculated. To calculate the RfC, the human equivalent concentration (HEC) is divided by UFs and is expressed in units of mg/m³ (Eq. 7.6).

Table 7.15 Parameter values used for daily groundwater intake of commercial workers

Exposure route	Parameter code	Parameter definition	Units	RME value	Intake equation/ model name
Ingestion	CW	Contaminant concentration in the assessed water	mg/L	EPC table	$CDI (mg/kg/day) = CW \times CR \times EF \times ED / (BW \times AT)$
	CR	Daily intake rate	L/day	1	
	EF	Annual frequency of exposure	day/year	250	
	ED	Duration of exposure	yr	25	
	BW	Body weight	kg	70	
	AT-NC	Average time—noncancer	days	9125	
	AT-C	Average time—cancer	days	25,550	
Dermal	CW	Contaminant concentration in the assessed water	mg/L	Chemical-specific	$CDI (mg/kg/day) = DA_{event} \times SA \times EF \times ED \times CF / (BW \times AT)$
	SA	Surface area for dermal contact	cm ²	1980	
	PC	Permeability coefficient of the skin	cm/h	Chemical-specific	
	ET	Event time	h/day	0.5	
	EF	Annual frequency of exposure	day/year	250	
	ED	Duration of exposure	year	25	
	BW	Body weight	kg	70	
	AT-NC	Average time—noncancer	days	9125	
	AT-C	Average time—cancer	days	25,550	
	CF	conversion factor	L/cm ³	0.001	

- (1) Assumes the commercial worker dermal contact is limited to hand and lower forearm
- (2) Total washing time based on an 8-h workday

$$RfC = HEC / (UF_1 \times UF_2 \dots) \tag{7.6}$$

7.5.5 Toxicity Assessment for Carcinogenicity

Carcinogens are different from non-carcinogens in that they are generally believed to have no threshold. It is presumed that there is no level of exposure below which carcinogenic effects will not occur. This concept of a “non-threshold” is based on the understanding that even small levels of exposure to a potential carcinogen carry a finite probability of inducing a carcinogenic response.

The USEPA utilizes a two-part evaluation approach to assess carcinogenic effects. This approach involves assigning a weight-of-evidence classification and quantifying the cancer toxic potency concentration (EA Engineering, Science, and Technology, Inc. 2021). The quantification is expressed through a slope factor (SF) for oral and dermal exposures and an inhalation unit risk (IUR) for inhalation exposures. These factors reflect the dose-response relationship observed in the available data for the specific carcinogenic endpoint(s) (USEPA 1989).

To communicate the hazard associated with carcinogens, the USEPA has established five recommended standard hazard descriptors: “Carcinogenic to Humans,” “Likely to Be Carcinogenic to Humans,” “Suggestive Evidence of Carcinogenic Potential,” “Inadequate Information to Assess Carcinogenic Potential,” and “Not Likely to Be Carcinogenic to Humans” (USEPA 2005). The weight-of-evidence classification is determined through a comprehensive scientific evaluation of the available data. Only compounds that receive a weight-of-evidence classification of C or above are considered to have carcinogenic potential in the risk assessment process.

The weight-of-evidence classifications established by the USEPA (USEPA 1989) and currently displayed in the toxicity profiles on the IRIS system were utilized for interpreting the carcinogenic toxicity of Concerned Organic Pollutants and Contaminants (COPCs) due to the incomplete integration of the revised cancer guidelines (USEPA 2005) into the IRIS chemical profiles. The weight-of-evidence classification system assigns a letter or alphanumeric code (A through E) to each potential carcinogen, indicating its assessed potential to cause cancer in humans.

Assessing the potential carcinogenic effects involves the utilization of slope factors (SF) for oral and dermal exposures, as well as inhalation unit risks (IUR) for inhalation exposures. These factors are derived from observed dose-response relationships for specific carcinogenic endpoints (USEPA 1989). SF and IUR represent the upper 95th percentile confidence limit of the probability of an individual experiencing a response per unit daily intake of a chemical throughout their lifetime. The SF is measured as the proportion of the population affected per milligram/kilogram per day, while the IUR is expressed in micrograms per cubic meter ($\mu\text{g}/\text{m}^3$). Their primary purpose is to estimate the upper-bound lifetime probability of an individual developing cancer due to exposure to a specific concentration of a carcinogen. Typically, SFs and IURs are derived from experimental animal data, unless suitable epidemiological studies are available. However, detecting and measuring carcinogenic effects at low exposure concentrations pose challenges. Therefore, SFs and IURs are developed by fitting a model to the available high-dose experimental animal data and extrapolating it to the low-dose range, which is more representative of human

exposure. The linear multistage model is recommended by the USEPA as a conservative approach that provides an upper bound estimate of excess lifetime cancer risk. For more comprehensive information on these methods and approaches, please refer to the USEPA Cancer Guidelines (USEPA 2005).

Apart from evaluating the carcinogenic effects of compounds, it is also important to assess their mutagenic modes of action. Some specific compounds of potential concern (COPCs), such as TCE and VC, have been identified as having mutagenic properties. When considering exposures during early life and the mutagenic mode of action, adjustments are made to cancer potency estimates. In situations where there is a lack of chemical-specific data, the USEPA recommends a default approach that utilizes estimates from chronic studies, known as cancer slope factors, with appropriate modifications to account for the potential differential risk associated with early-life exposure (USEPA 2005). This adjustment is necessary because studies have indicated that a given exposure occurring early in life poses a higher cancer risk compared to the same exposure during adulthood (USEPA 2005). Therefore, for this human health risk assessment (HHRA), the intakes of methylene chloride, TCE, and VC are adjusted in accordance with the guidelines provided by the USEPA (2005).

In this HHRA, only the resident population falls within the age range that necessitates adjustment for a mutagenic mode of action. The residential scenario considers two age groups: adults and children. The child age group is assumed to be from 0 to 6 years old, while the adult age group spans from 7 to 30 years old (USEPA 1991). Although adults are typically considered to be older than 16 years of age, the resident adult in this assessment is evaluated for long-term exposure, which is characteristic of residents (USEPA 1991). Since residents are assumed to have a duration of exposure of 30 years, the resident adult age range extends from 7 to 30 years beyond childhood (USEPA 1991). Therefore, both the resident child and the resident adult require adjustment for potential mutagenic modes of action in this HHRA.

7.5.6 Toxicity Assessment for TCE

The USEPA released a Toxicity Assessment for TCE in 2011. Carcinogenic SFs and IURs are presented for based on three separate target tissue sites—kidney, lymphoid tissue, and liver. Within IRIS, one SF and IUR is presented for TCE that represents the sum of the SF and IUR estimates for the three individual cancer types (USEPA 2014). Additionally, TCE is identified with a mutagenic mode of action for the kidney only. Therefore, application of the mutagenic adjusted DAF to the summed SF and IUR presented in IRIS results in an over-estimate of cancer risk estimates for TCE. According to the Integrated Risk Information System (IRIS) guidelines, the risk assessment for kidney cancer should be conducted using the mutagenic equations. On the other hand, the risk assessments for liver cancer and non-Hodgkin lymphoma (NHL) should be addressed using the standard cancer intake equations (USEPA 2014). To determine cancer risk estimates for the resident adult and child exposure to TCE, the following steps were performed:

- Calculate the TCE intake with the mutagenic mode of action to incorporate the adjusted DAF based on kidney mutagenic endpoint [IUR of $1 \times 10^{-6} (\mu\text{g}/\text{m}^3)^{-1}$ and oral SF of $9.3 \times 10^{-3} (\text{mg}/\text{kg}/\text{day})^{-1}$].
- Calculate a TCE intake based on non-kidney (NHL/liver) cancer endpoint [IUR of $3.1 \times 10^{-6} (\mu\text{g}/\text{m}^3)^{-1}$ and oral SF of $3.7 \times 10^{-2} (\text{mg}/\text{kg}/\text{day})^{-1}$]. These toxicity values represent the sum of the NHL and liver IUR and SF.

Therefore, two separate intakes for carcinogenic effects are presented for TCE. One intake is based upon the kidney endpoint and takes into account an adjusted DAF for a mutagenic mode of action. The second intake is based upon the NHL/liver endpoint and does not have an adjustment for a mutagenic mode of action. Intakes for non-carcinogenic effects are based upon a single endpoint and are not modified as discussed above.

7.5.7 Risk Characterization

In the risk characterization process, the aim is to assess the potential risks associated with human exposure to contaminants of potential concern (COPCs) in groundwater. This involves summarizing and integrating the chemical intake levels and toxicity values to provide quantitative expressions of risk. By doing so, a numerical representation of the risk level for human contact with COPCs in groundwater can be obtained. To evaluate potential non-carcinogenic effects, the chemical intake levels are compared to the corresponding toxicity values. This comparison allows for an assessment of the potential for non-carcinogenic health effects resulting from exposure to COPCs. For potential carcinogenic effects, the risk characterization involves estimating the incremental probabilities of an individual developing cancer over a lifetime of exposure. This estimation is based on the chemical intake levels and specific dose-response information for each chemical. The dose-response information includes parameters such as slope factors (SFs) and inhalation unit risks (IURs), which reflect the relationship between the dose of a carcinogen and the likelihood of developing cancer. Separate discussions are conducted for carcinogenic and non-carcinogenic effects due to the differing methodologies used to assess these two modes of chemical toxicity.

Hazard index for non-carcinogenic effects: To assess the potential human health risks associated with exposures to non-carcinogenic COPCs, a comparison is made between the average daily intake (ADI) and the chemical-specific RfD or RfC. A hazard quotient (HQ) is derived for each COPC, as shown in Eq. 7.7:

$$\text{HQ} = \frac{\text{ADI}}{\text{RfD}} \quad \text{or} \quad \text{HQ} = \frac{EC}{\text{RfC} \times 1000 \mu\text{g}/\text{m}^3} \quad (7.7)$$

where, HQ indicates the Hazard Quotient, which is a dimensionless ratio defined as the average daily intake level divided by the acceptable daily intake level. ADI

represents the calculated non-carcinogenic average daily intake in mg/kg/day. The RfD denotes the reference level for oral and dermal exposure, which is also expressed in mg/kg/day. The EC is the concentration of a contaminant ($\mu\text{g}/\text{m}^3$), and RfC is the reference level for inhalation exposure, expressed in mg/m^3 .

When the ADI of a chemical exceeds the RfD or RfC, the HQ value will be greater than 1.0. This suggests a potential concern for adverse systemic health effects in the populations exposed to the chemical. Conversely, if the ADI is below the RfD or RfC, the HQ value will be below 1.0, indicating no immediate concern for adverse systemic health effects in the exposed populations. However, if the sum of multiple HQ values exceeds 1.0, and these compounds affect the same target organ, there may be a concern for potential adverse systemic health effects in the exposed populations. This implies that the combined exposure to multiple chemicals may have a cumulative effect on the target organ, increasing the likelihood of adverse health effects. It is important to note that the HQ value represents the level of concern but does not provide a statistical probability of adverse health effects occurring.

When multiple chemicals are present and can cause systemic toxicity through different pathways, the individual Hazard Quotients (HQs) can be combined to calculate an overall Hazard Index (HI). The HI provides an assessment of the potential health effects associated with exposures at the site. If the calculated HI is below 1.0, it suggests that the exposures are unlikely to cause adverse health effects. However, if the total HI exceeds 1.0, it indicates that further analysis is required. In such cases, separate HIs can be calculated for specific toxic endpoints or target organs of concern. For instance, the HQs for neurotoxic compounds can be summed separately from the HQs for renal toxins. By calculating endpoint-specific HIs, a more detailed evaluation can be conducted to determine if there is a reason for concern regarding potential health effects associated with a specific endpoint. This approach allows for a focused assessment of the potential risks related to specific health endpoints, providing a more comprehensive understanding of the overall health risk.

Carcinogenic risks: Carcinogenic risk is determined as the increased probability of an individual developing cancer throughout their lifetime due to exposure to a potential carcinogen. The numerical estimation of the additional lifetime cancer risk is obtained by multiplying the Lifetime Average Daily Intake (LADI) by the risk per unit dose, which is represented by either the Slope Factor (SF) or the Inhalation Unit Risk (IUR). This is shown in Eq. 7.8:

$$\begin{cases} \text{Risk} = \text{LADI} \times \text{SF} \\ \text{Risk} = EC \times \text{IUR} \end{cases} \quad (7.8)$$

where, Risk is the unitless probability of an exposed individual developing cancer; LADI is the lifetime cancer average daily intake ($\text{mg}/\text{kg}\text{-day}$ or $\mu\text{g}/\text{m}^3$); SF is the cancer slope factor ($\text{mg}/\text{kg}\text{-day}$)⁻¹; EC is the exposure concentration ($\mu\text{g}/\text{m}^3$); and IUR is the inhalation unit risk ($\mu\text{g}/\text{m}^3$)⁻¹.

Because the SF and the IUR are the statistical 95th percent upper-bound confidence limit on the dose-response slope, this method provides a conservative, upper-bound estimate of risk. The carcinogenic risk thresholds are defined as cumulative carcinogenic risks that exceed the risk range of 1 in 1 million (1×10^{-6}) to 1 in 10,000 (1×10^{-4}).

According to Table 7.16, the HHRA evaluated the potential cumulative risks associated with groundwater exposure for different populations, including residents (adult and child), construction workers, and commercial workers. The assessment considered ingestion, dermal contact, and inhalation of VOCs present in groundwater. For the resident (adult and child) and commercial worker, the non-carcinogenic hazards exceeded a HQ of 1.0, indicating potential risks. Specifically, cis-DCE, TCE, and VC had chemical-specific HQs greater than 1.0. Additionally, the liver, kidney, and immunological system had Hazard Indices (HIs) greater than 1.0, suggesting potential adverse effects on these systems. The incremental lifetime carcinogenic risks for the resident (adult and child combined) and the commercial worker were found to be above the upper end of the risk threshold range (10^{-6} – 10^{-4}) set by the USEPA. TCE and VC were identified as having carcinogenic risks above 10^{-4} , indicating significant concerns regarding their potential to cause cancer. Concerns were raised about the use of groundwater as a tap water source due to these findings. Furthermore, the resident adult was evaluated for potential concerns related to VOC vapor intrusion from groundwater into indoor air. The USEPA Johnson and Ettinger model suggested that volatilization of Contaminants of Potential Concern (COPCs) in groundwater into site buildings could be a potential concern (USEPA 2004). Specifically, TCE had a non-cancer HQ greater than 1.0, indicating a potential risk.

The construction worker's exposure to groundwater, including incidental ingestion, dermal contact, and inhalation while in a trench, was found to be below the risk thresholds established by the USEPA. Therefore, the risks associated with groundwater exposure for the construction worker were deemed to be acceptable.

7.5.8 Risk Assessment Uncertainty

Analyzing uncertainties is crucial in exposure assessment, providing risk assessors and reviewers with information on individual uncertainties linked to exposure factor assumptions and their potential impact on the final assessment. Conservative assumptions are employed regarding exposure to groundwater, potentially leading to an overestimation of potential health risks. For this HHRA, the most conservative land use scenario (residential) is included in the evaluation. Groundwater within the site is assumed as a tap water source although public water is available. In addition, the HHRA does not take into account any restrictions on groundwater use or exposure. Exposure parameters (e.g., body weight, ingestion rates, time spent in one place, etc.) used in estimating COPC intakes are a combination of an average and upper bound levels taken from USEPA sources. The use of upper-bound estimates tends to overestimate exposure; therefore, the potential risks presented in the HHRA are

Table 7.16 Summary of HHRA carcinogenic risks and noncarcinogenic hazards

Receptor	Exposure pathway	Carcinogenic risks	Non-carcinogenic hazards	COPC contributing significantly to results
Child resident	Ingestion	1.3×10^{-3}	25	VC, TCE, cis-DCE
	Dermal contact	1.8×10^{-4}	5.4	VC, TCE, cis-DCE
	Inhalation	–	–	Not applicable
	Cumulative results	1.5×10^{-3}	30	VC, TCE, cis-DCE
Adult resident	Ingestion	8.0×10^{-4}	11	VC, TCE, cis-DCE
	Dermal contact	1.2×10^{-4}	2.3	VC, TCE, cis-DCE
	Inhalation	2.3×10^{-4}	23	TCE
	Cumulative results	1.2×10^{-3}	36	
Adult and child resident (combined)	Ingestion	2.1×10^{-3}	–	VC, TCE, cis-DCE
	Dermal contact	3.0×10^{-4}	–	VC, TCE, cis-DCE
	Inhalation	2.3×10^{-4}	–	VC, TCE, cis-DCE
	Total risk across groundwater (adult and child)	2.6×10^{-3}	–	VC, TCE, cis-DCE
	Total risk across all media and all exposure routes (adult and child)	3×10^{-3}	–	VC, TCE, cis-DCE
	Total hazard index across all media and all exposure routes (child)	–	30	VC, TCE, cis-DCE
	Total hazard index across all media and all exposure routes (adult)	–	36	VC, TCE, cis-DCE
Construction worker	Ingestion	7×10^{-8}	0.04	Not applicable
	Dermal contact	3×10^{-7}	0.2	Not applicable
	Inhalation	1×10^{-13}	0.000006	Not applicable
	Cumulative results	1×10^{-6}	0.2	
Commercial worker	Ingestion	2×10^{-4}	3.8	VC, TCE, cis-DCE

(continued)

Table 7.16 (continued)

Receptor	Exposure pathway	Carcinogenic risks	Non-carcinogenic hazards	COPC contributing significantly to results
	Dermal contact	6×10^{-6}	0.2	VC
	Inhalation	–	–	Not applicable
	Cumulative results	2×10^{-4}	4	

likely to be greater than actual risks. However, the residential exposure to groundwater presents a baseline exposure assessment that should be taken into account for any risk management decisions made for the site.

7.6 Cost-Effective Approach for Groundwater Contamination Induced Risk Mitigation

Aquifer remediation is necessary when the risks associated with groundwater contamination exceed acceptable levels. The primary objectives of aquifer remediation can be summarized as follows:

Health protection: The remediation aims to prevent exposure to groundwater contamination at concentrations that pose risks above acceptable levels. This objective focuses on safeguarding human health by ensuring that the groundwater is free from contaminants or that exposure pathways are effectively eliminated.

Plume containment: Another objective is to prevent or minimize the further migration of the contaminant plume. This involves implementing measures to contain the spread of contamination within the aquifer and prevent its migration to unaffected areas. By containing the plume, the remediation efforts limit the potential for additional contamination and reduce the overall extent of the affected area.

Source control: The remediation seeks to prevent or minimize the migration of contaminants from source materials (such as contaminated soil or waste sites) into the groundwater. Source control measures focus on addressing and mitigating the primary sources of contamination to prevent ongoing or future contamination of the aquifer.

Aquifer restoration: Wherever practicable, the objective of aquifer remediation is to restore the groundwater to its expected beneficial uses. This involves reducing contaminant concentrations to acceptable levels and ensuring that the aquifer can support its intended uses, such as drinking water supply, irrigation, or industrial purposes.

Figure 7.21 presents a decision framework for selecting remediation methods in karst aquifers. The framework emphasizes the importance of addressing source materials, which typically contain the highest concentrations of contaminants. Remediation measures focused on removing or addressing these source materials are considered to provide the greatest value in terms of contaminant reduction per unit of expenditure. Source control measures, such as removal or containment of the source materials, are often considered cost-effective steps in groundwater restoration programs. Pathway elimination is another valuable approach in karst aquifers. While it doesn't directly address the contaminated groundwater, eliminating the exposure pathway by using an alternative water supply source can prevent receptors from being exposed to the contaminated groundwater. Treating impacted groundwater is a well-researched topic, and various technologies are available for addressing contamination in karst aquifers. However, the selection of the most appropriate method should consider the site-specific conditions, as each karst aquifer has unique hydrogeological characteristics and contaminant distribution. Technical impracticability is regarded as a last resort in the decision framework. It suggests that a regulatory waiver for remediation requirements may only be granted when other options have been thoroughly evaluated and proven to be impractical or unfeasible. Based on the information provided, managing impacted groundwater appears to be the most applicable remediation option for the study site within the context of the decision framework presented in Fig. 7.21.

In Fig. 7.22, specific techniques are depicted for each remediation option, along with an outline of the associated challenges. The management of impacted groundwater encompasses various technologies, including pump and treat, permeable reactive barriers, enhanced chemical oxidation and/or bioremediation, as well as monitoring of natural attenuation. Historically, pump and treat has been widely employed for groundwater remediation and management. However, there has been a recent shift towards the adoption of in-situ technologies. Considering the hydrogeological conditions and the delineated extents of COPCs in both the overburden and bedrock formations, alternative approaches for groundwater remediation included in-situ chemical oxidation and enhanced bioremediation. It is important to note that monitored natural attenuation plays a significant role in these remediation techniques.

7.7 Summary

Groundwater contamination was identified in the unconsolidated overburden and the underlying karst formations at the study site. The overburden aquifer is comprised of silt and clay, with varying thicknesses ranging from 13 to 129 feet. On the contrary, the karst aquifer consists of carbonate rock, characterized by an irregular surface, water-filled or clay-filled voids, and discrete fracture zones. Within the bedrock aquifer, significant variations in specific capacity and hydraulic conductivity have been observed, along with the coexistence of confined and unconfined conditions. The presence of preferential flow pathways and interconnected fractures further adds

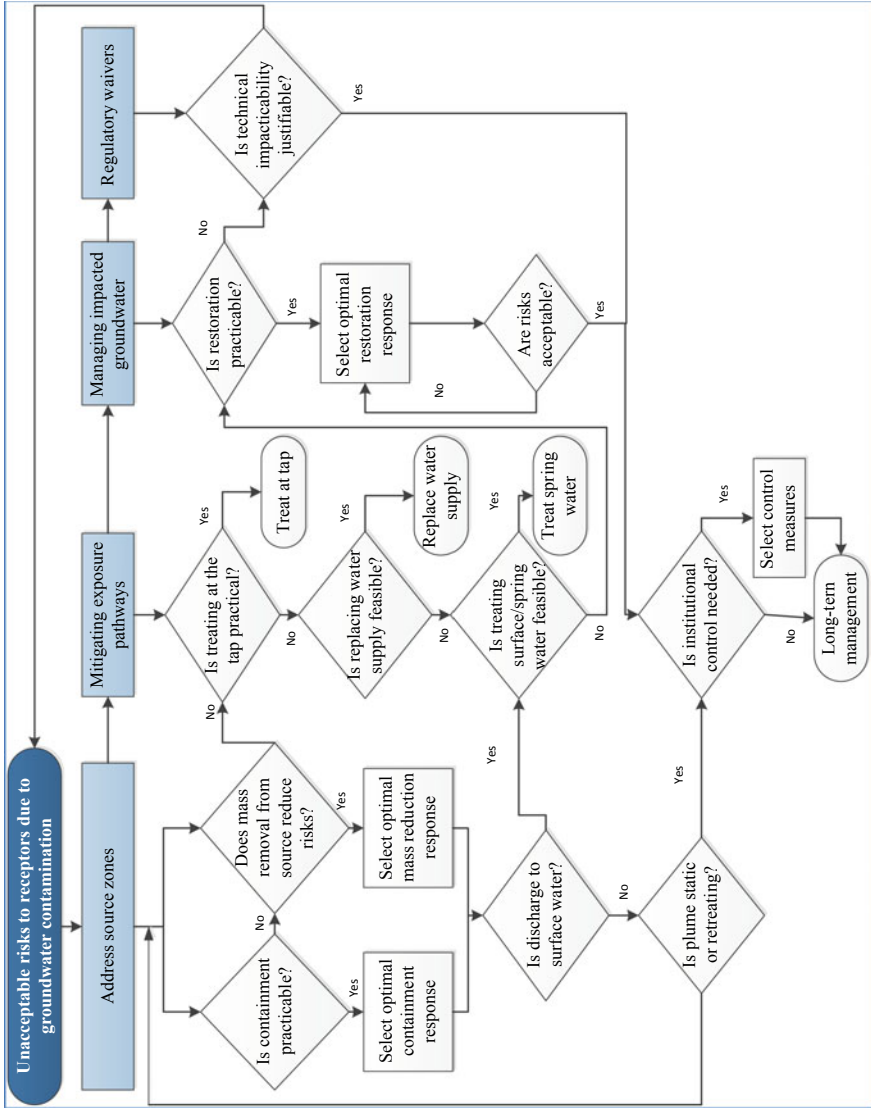


Fig. 7.21 Decision framework of addressing contaminated groundwater in karst aquifers (Randrianarivelo et al. 2019)

Karst Aquifer Remediation Strategy	Remediation Techniques	Challenges
Address source zones: reduce mass flux into the aquifer to the extent practicable	<ul style="list-style-type: none"> <input type="checkbox"/> Soil excavation (most common) <input type="checkbox"/> Mass reduction via NAPL removal (Commonly employed with pooled NAPL) <input type="checkbox"/> Mass reduction via vapor removal <input type="checkbox"/> Physical, chemical, or hydraulic containment <input type="checkbox"/> In-situ remediation technologies 	<ul style="list-style-type: none"> <input type="checkbox"/> Much of the mass may reside in the epikarst or underlying bedrock and be inaccessible to excavation <input type="checkbox"/> Volumes of pooled NAPL may be large due to the high porosity of the epikarst. <input type="checkbox"/> Accumulation may be more episodic than continual <input type="checkbox"/> Air-filled, interconnected nature of many epikarsts lend themselves to epikarst vapor extraction technology <input type="checkbox"/> Pumping wells cannot be relied upon to effect capture; capture zones cannot be reliably modeled using numerical codes such as MODFLOW <input type="checkbox"/> Often costly and challenging to construct any hydrogeologic barriers in karst
Mitigating exposure pathways: perhaps the most useful active remedial component in karst	<ul style="list-style-type: none"> <input type="checkbox"/> Treating at the tap <input type="checkbox"/> Replacing potable water supplies <input type="checkbox"/> Treating spring water by capturing and treating spring flow or "passive"TM treatment by constructing a treatment wetland or filtration system <input type="checkbox"/> Land use control including fences, signage, deed restrictions, local ordinances 	<ul style="list-style-type: none"> <input type="checkbox"/> Long-term operation and maintenance costs <input type="checkbox"/> Costs can be offset somewhat if treatment of groundwater between the source and the potential receptors is not attempted <input type="checkbox"/> Water from more than one spring needs to be treated <input type="checkbox"/> Spring biota will likely be affected and requires an evaluation <input type="checkbox"/> Educate people of land use control as a component of remedies
Managing impacted groundwater	<ul style="list-style-type: none"> <input type="checkbox"/> Pump and treat <input type="checkbox"/> Permeable reactive barriers <input type="checkbox"/> Spot treatment using enhanced chemical oxidation, enhanced bioremediation, thermal destruction <input type="checkbox"/> Monitored Natural Attenuation <input type="checkbox"/> Performance Monitoring 	<ul style="list-style-type: none"> <input type="checkbox"/> Primary challenge is to identify the zone requiring treatment <input type="checkbox"/> Effective technologies tailored to site conditions and specific contaminants <input type="checkbox"/> An appropriate monitoring approach and high-quality monitoring data are critical to evaluate effectiveness. <input type="checkbox"/> Monitoring locations consist of springs, streams, extraction systems (if any), and monitoring wells previously shown by testing to be relevant <input type="checkbox"/> Water-quality sampling may need to be based on precipitation events
Regulatory waivers	<ul style="list-style-type: none"> <input type="checkbox"/> Not applicable 	<ul style="list-style-type: none"> <input type="checkbox"/> Justification requirements: complex hydrogeology, dense non-aqueous phase liquids, or diffusion-limited or sorption limited contaminant behavior <input type="checkbox"/> Given the uncertainty of karst, a robust, karst-specific monitoring program would still be required

Fig. 7.22 Remediation strategies for karst aquifers and their challenges (Randrianarivelo et al. 2019)

to the complexity. The presence of karst features has made it challenging to determine both the vertical and lateral extents of contamination plumes. However, a phased approach involving multiple disciplines and techniques made it possible to successfully delineate the groundwater contamination in both formations. To assess potential risks associated with exposure to contaminated groundwater, a human health risk assessment (HHRA) was conducted. The assessment evaluated the cumulative risks for residents (including adults and children), construction workers, and commercial workers. The results of the HHRA indicate concerns regarding the use of groundwater as a source of tap water. There is also a potential concern for the volatilization of Contaminants of Potential Concern (COPCs) from groundwater into site buildings. However, the results for construction worker exposure to groundwater are below the established risk thresholds. Despite the lower risks for construction workers, the unacceptable health risks identified for residents and other individuals have necessitated the remediation of groundwater. Two viable alternatives for groundwater remediation including in-situ chemical oxidation and in-situ enhanced bioremediation have been identified to mitigate the unacceptable risks. It is worth noting that monitored natural attenuation is considered a common component of the selected remedy, playing a crucial role in the overall remediation process.

References

- Arnold WA, Roberts AL (2000) Pathways and kinetics of chlorinated ethylene and chlorinated acetylene reaction with Fe(0) particles. *Environ Sci Technol* 34:1794–1805
- Butler EC, Hayes KF (1999) Kinetics of the transformation of trichloroethylene and tetrachloroethylene by iron sulfide. *Environ Sci Technol* 33:2021–2027
- EA Engineering, Science, and Technology, Inc. (2021) Human health risk assessment: remedial investigation American Creosote Deridder Superfund Site Deridder, Beauregard Parish, Louisiana EPA Identification No. LAN000604293. <https://semspub.epa.gov/work/06/100023204.pdf?cv=1>. Accessed 20 Sept 2023
- Environmental Security Technology Certification Program (2011) Guidance protocol: environmental restoration project ER-0518, application of nucleic acid-based tools for monitoring monitored natural attenuation (MNA), biostimulation, and bioaugmentation at chlorinated solvent sites
- Ferrey M, Wilson JT (2002) Complete natural attenuation of PCE and TCE without the accumulation of vinyl chloride. In: Third international conference on remediation of chlorinated and recalcitrant compounds, Monterey, CA
- Gelhar LW, Welty C, Rehfeldt KR (1992) A critical review of data on field-scale dispersion in aquifers. *Water Resour Res* 28(7):1955–1974
- Groundwater Sciences Corporation (2011) Supplemental remedial investigation groundwater report (Part 1). <https://www.yorksiteremedy.com/Documents/Final%20Supl%20R1%20GW%20Rprt-Sept2011.pdf?cv=1>. Accessed 20 Nov 2023
- He YT, Wilson JT, Su C, Wilkin RT (2015) Review of abiotic degradation of chlorinated solvents by reactive iron minerals in aquifers. *Groundwater Monitor Remed* 35(3):57–75. <https://doi.org/10.1111/gwmr.12111>
- Interstate Technology and Regulatory Cooperation Work Group (1999) natural attenuation of chlorinated solvents in groundwater: principles and practices

- Jeong H, Hayes KF (2007) Reductive dichlorination of tetrachloroethylene and trichloroethylene by mackinawite (FeS) in the presence of metals: reaction rates. *Environ Sci Technol* 41:6390–6396
- Kennel JR (2008) Advances in rock core VOC analyses for high resolution characterization of chlorinated solvent contamination in a dolostone aquifer (thesis), Waterloo, Ontario, Canada
- Lallemand-Barres A, Peaudecerf P (1978) Recherche de relations entre la valeur de la dispersivité macroscopique d'un milieu aquifère, ses autres caractéristiques et les conditions de mesure. *Bulletin Bureau de Recherches Géologique et Minières, France, Section III* 2:277–284
- Lee W, Batchelor B (2002) Abiotic reductive dichlorination of chlorinated ethylenes by iron-bearing soil minerals. I. Pyrite and magnetite. *Environ Sci Technol* 36:5147–5154
- Loop CM, White WB (2001) A Conceptual model for DNALP transport in karst ground water basins. *Groundwater* 39(1):119–127
- Lu X, Wilson JT, Kampbell DH (2006) Relationship between Dehalococoides DNA in ground water and rates of reductive dechlorination at field scale. *Water Res* 40:3131–3140
- National Research Council (1994) Alternatives for ground water cleanup. National Academies Press, Washington, DC
- Neuman SP (1990) Universe scaling of hydraulic conductivities in geologic media. *Water Resour Res* 26(8):1749–1758
- Plett JH (2006) Metolachlor and TCE plume characteristics in a dolostone aquifer using a transect (thesis), Waterloo, Ontario, Canada
- Randrianarivelo M, Zhou W, Barsa M (2019) Remedial investigations of karst aquifers: a case study at former Marietta Air Force Station, Lancaster County, Pennsylvania. *Carbonates Evaporites* 34:233–247. <https://doi.org/10.1007/s13146-017-0369-y>
- Terzaghi K, Peck RB, Mesri G (1996) Soil mechanics in engineering practice, 3rd edn. Wiley, New York
- Teutsch G, Sauter M (1991) Groundwater modeling in karst terranes—scale effects, data acquisition, and field verification. In: Proceedings of the third conference on hydrogeology, ecology, monitoring, and management of ground water in Karst Terranes, Nashville, Tennessee, December 4–6, 1991. National Ground Water Association, pp 17–54
- Tobiszewski M, Namiesnik J (2012) Abiotic degradation of chlorinated ethanes and ethenes in water. *Environ Sci Poll Res* 19:1994–2006
- USEPA (1989) Risk assessment guidance for superfund, volume I: human health evaluation manual (part a) (interim final). Report No. EPA/540/1 89/002. Office of Emergency and Remedial Response, Washington, D.C.
- USEPA (1991) Memorandum: human health evaluation manual, supplemental guidance: “standard default exposure factors.” Office of Solid Waste and Emergency Response. OSWER Directive: 9285.6-03
- USEPA (1992) Guidelines for data usability in risk assessment (part A). Office of Solid Waste and Emergency Response (OSWER), Publication OSWER9285.7-09A
- USEPA (2004) Risk assessment guidance for superfund. Volume I: human health evaluation manual (part E: supplemental guidance for dermal risk assessment) final. OSWER. EPA-540-R-99-005
- USEPA (2005) Guidelines for carcinogen risk assessment. EPA/630/P-03/001F. Risk assessment forum
- USEPA (2013) Regional screening levels summary table and regional screening levels summary table user guide. http://www.epa.gov/reg3hwmd/risk/human/rb-concentration_table/usersguide.htm
- USEPA (2014) IRIS (integrated risk information system) database. <http://www.epa.gov/iris>. Environmental Criteria and Assessment Office, Cincinnati
- USEPA (1998) Technical protocol for evaluating natural attenuation of chlorinated solvents in ground water, EPA/600/R-98/128

Index

A

Absorption, 92, 93, 235
Acquisition, 63
Adhesion, 4
Aeolian, 20
Affinity, 236
Algorithm, 67, 188
Alkaline, 115, 125, 127
Anisotropy, 200, 217
Aqueous, 214, 216–218, 220, 226, 230
Assembly, 190
Attenuation, 221, 226, 230, 232, 234, 252, 255

B

Backfill, 139, 146
Bacterial, 232
Baseline, 249
Bedrock water, 8, 105, 113, 164, 165
Benchmark, 48, 150, 240
Bioassay, 15
Biodiversity, 12, 25
Bioremediation, 252, 255
Blockage, 19, 21, 30, 31, 147
Borehole, 12, 129, 139, 147, 174, 190–196, 198, 205, 206
Boundary, 55, 90, 132, 144, 154, 155, 158, 159, 161, 162, 166–168, 171, 175
Breakthrough, 30, 32, 114
Byproduct, 230

C

Calcium, 139

Capacity, 3, 12, 46, 59, 66, 134, 143, 145, 146, 150, 166, 201, 206, 207, 252
Capillary, 34, 38, 67, 211, 212, 217
Catchment, 152
Chloroacetylene, 224, 229
Circulation, 145, 190, 200
Circumstances, 30, 99, 149, 200, 240
Coal-bearing, 148, 163
Coal mine, 11, 45, 97, 143, 145, 148, 149, 162, 163
Coefficient, 33, 34, 36, 53, 55–57, 60–62, 68, 168, 170, 220, 222, 241, 242, 244
Comparison, 9, 65, 173, 247
Conjunction, 159, 186
Contradiction, 65, 76
Conversion, 239–242, 244
Corrosion, 119, 145
Cost-effective, 175, 251
Coverage, 19, 125

D

Debris, 23, 25, 200
Decision-making, 14, 128, 236
Dehalococoides, 227, 232
Dehydration, 92, 95
Demolition, 99–101
Densification, 51, 160
Department, 143, 150
Depression, 8, 9, 45, 79, 97, 110, 113, 115, 125, 126, 166, 200, 212
Depressurization, 112, 154
Descriptions, 77, 133, 180
Descriptors, 133, 245
Desert, 2

Desorption, 221, 230
 Dichloroelimination, 224, 229
 Disaster, 19, 20, 23, 25, 33, 39, 47, 48, 75,
 76, 83–89, 92, 99, 101, 127, 143,
 145, 148
 Discharge, 13, 26, 34, 36, 41, 50, 111, 114,
 124–126, 134, 137, 144, 155, 166,
 169, 203, 216
 Discrepancy, 48, 175
 Disintegration, 37
 Disposal, 2, 3, 13
 Dissipation, 50, 51, 53, 80, 96
 Dolomite, 8, 9, 185, 186, 198, 205
 Downgradient, 181, 207, 230
 Drawdown, 58, 137, 157, 171, 205, 206
 Drought, 77–80, 125, 126

E

Earth fissure, 2, 3, 75–77, 80–102
 Ecosystem, 24, 25
 Electrode, 185, 187
 Electron, 184, 221, 223, 224, 226, 232
 Embankment, 4, 66, 67, 86, 89
 Engineering, 1, 8, 19, 21, 22, 25, 39–42, 48,
 66, 76, 86, 98, 99, 106, 110, 125,
 127, 128, 132, 134, 139, 244
 Evaporation, 30, 92, 166, 168, 169, 214,
 219
 Explosion, 11, 145
 Exposure, 1, 2, 12–15, 171, 235–251, 255
 Extrusion, 78

F

Fabric, 198
 Facies, 163, 196
 Facilities, 21, 26, 38, 47, 48, 83, 99, 131,
 132
 Farmland, 19, 21, 24, 25
 Fertility, 24
 Fillers, 34
 Fluid, 4, 45, 47, 64, 121, 187, 192, 194,
 196, 200
 Fly ash, 86
 Fragments, 188, 205, 212, 218
 Framework, 37, 168, 251–253
 Frequency, 3, 15, 75, 108, 134, 235, 238,
 239, 241, 242, 244
 Freshwater, 64

G

Geologic hazard, 1, 2, 21–26, 75, 86, 105,
 128, 141
 Geology, 98, 128, 132, 136, 163, 187, 188
 Geometry, 157, 214
 Geomorphology, 23, 97, 129
 Geoprobe, 181, 183, 184
 Geothermal, 46
 Granular, 96, 214, 217, 221
 Gravitational, 68, 97, 119, 214, 216, 230
 Groundwater contamination, 2, 13, 14, 179,
 182, 187, 230, 251, 252
 Guidance, 127, 129, 235, 238
 Guideline, 237, 245, 246
 Gypsum, 8, 9, 122

H

Halite, 8, 9
 Heterogeneous, 124, 159, 166, 230
 High-intensity, 37, 173
 High-latitude, 20
 High-velocity, 113, 114, 214
 Highway, 4, 48
 Hillslope, 4
 Homogeneous, 30, 53, 62, 123, 124, 156,
 157
 Hourglass, 107, 118, 120, 132, 133
 Hydration, 33, 35
 Hydraulic gradient, 27, 29, 37, 95, 111,
 112, 137, 200, 201
 Hydrocarbon, 186, 211
 Hydrodynamic, 2, 8, 9, 36, 37, 159, 216
 Hydrogen, 145, 224, 229, 232
 Hydrogenolysis, 224, 225, 229
 Hydrogeology, 4, 98, 151, 164, 198
 Hydrologic, 4, 226
 Hydrolysis, 33, 35

I

Impoundment, 111, 125, 138
 Increment, 49, 58
 Incubation, 27, 89
 Inflection, 194–196
 Inflow, 37, 114, 134, 137, 138, 143–146,
 150, 155–158, 161, 162, 165,
 171–175
 Infrastructure, 2, 3, 131
 Instability, 36, 39
 Interference, 108, 137, 186
 Intergranular, 80, 218
 Interpolation, 67, 160
 Intrusion, 3, 64, 140, 144, 226, 249

Inverse, 161, 196
 Irrigation, 20, 22, 24, 26–29, 75, 251
 Iterations, 170, 186

K

Karst collapse, 8, 91, 92, 105–109, 111, 115–118, 121–123, 125–128, 131–138, 141, 149
 Karstification, 108, 110, 198
 Karstified, 108, 121, 212

L

Landforms, 21, 23, 77, 79, 105, 110, 122, 126
 Landscape, 25, 66
 Landslide, 2, 4, 8, 19–34, 36–42, 77, 79, 90, 91, 99
 Layout, 99, 172, 201, 202
 Leakage, 48, 107, 108, 111, 112, 114, 120, 121, 124, 138, 140
 Lifespan, 41, 106, 145
 Limestone, 8, 110, 123, 149, 180, 186, 188, 198
 Liquefaction, 29, 33, 37, 111, 114, 125, 126
 Lithology, 29, 97, 105, 126, 129, 134, 159, 163, 191–193, 198
 Livelihood, 25, 26
 Livestock, 19, 21, 24
 Logarithm, 55

M

Macroscopic, 35, 75, 80, 107, 117, 119, 128, 159
 Makers, 15, 236
 Manganese, 223, 243
 Marks, 50
 Massive, 200
 Matrix, 187, 200, 217, 218, 220, 221
 Matter, 158, 198
 Membrane, 187
 Microbes, 223, 224, 227, 232
 Microorganism, 145, 221, 223, 229
 Microscopic, 35, 117, 119, 128
 Modification, 140, 238, 246
 Modulus, 63
 Moisture, 4, 20, 23, 27, 30, 32, 38, 67, 68, 80, 92, 95, 123
 Mudflow, 107, 118, 121, 129, 131–133
 Mudization, 34, 35
 Mudstone, 23, 174

N

Nitrate, 223, 230, 234
 Noise, 117, 138
 Non-aqueous, 179, 180, 211, 217, 226, 230
 Non-carcinogens, 235, 238, 243
 Non-Darcy, 154

O

Occupational, 15, 236, 238
 Offset, 183, 188
 Ore, 143, 144, 150
 Outlet, 29, 31
 Output, 144, 194
 Overburden, 95, 106, 107, 121, 179, 180, 190–192, 201–204, 207–210, 232, 252
 Overexploitation, 46, 76
 Over-extraction, 94, 96
 Overflow, 33, 146, 159, 165
 Oxygen, 223, 227–229, 232

P

Particle, 2, 20, 23, 33–35, 37, 41, 46, 47, 49, 53, 62, 79, 80, 95, 96, 105–108, 112, 114, 116, 118, 120, 121, 124, 129, 132, 187, 214, 217
 Passageways, 145
 Percolates, 9
 Perennial, 146
 Periphery, 95, 168, 228
 Persist, 93, 218
 Personnel, 145
 Pertinent, 232
 Petroleum, 45, 47, 80, 222
 Physiographic, 180
 Pipeline, 48, 99, 145
 Pit, 4, 10, 29, 65, 90, 91, 95, 114, 137, 138, 143, 147, 155, 162, 165, 173, 174
 Placement, 139, 190
 Pollution, 64, 207
 Pore water, 2, 3, 26, 30, 33, 35, 37, 38, 46, 47, 49–53, 60–62, 65, 80, 111, 112, 147, 198, 214, 216–220, 226
 Porosity, 32, 35, 46, 60–62, 121, 180, 196, 217, 220
 Porous, 19, 20, 49, 51, 62, 116, 124, 148, 165, 200, 214, 217, 226
 Potency, 244, 245
 Precursor, 90
 Precursory, 138
 Procedure, 136, 158
 Proportion, 38, 245

Prospect, 149, 175
 Pyrite, 150, 224, 225

Q

Qualitative, 128, 151, 187, 241
 Quantification, 161, 245
 Quantify, 13
 Quartz, 20, 205
 Quotient, 247, 248

R

Radiative, 155
 Rainstorms, 29, 150
 Rainwater, 20, 25, 31, 32, 64, 79, 92, 93
 Random, 120
 Reaction, 9, 25, 33, 35, 221, 223, 224, 229
 Reactive, 224, 229, 252
 Realigned, 102
 Reality, 20, 22
 Recognize, 200
 Recovery, 51, 65, 110, 145
 Redox, 223, 232
 Relief, 145
 Representation, 159, 196, 210, 247
 Resembling, 81, 82, 91
 Reservoir, 4, 22, 25, 29, 36, 37, 64, 65, 109,
 111, 112, 114, 115, 122, 125, 126,
 134, 138, 140, 146, 147
 Resolution, 100, 186, 188
 Respiration, 223, 228
 Ridges, 21, 23
 Rodent, 15

S

Sandstone, 8, 165, 166, 174, 188, 220
 Scatter, 217
 Seawater, 3, 64, 144
 Sediment, 19, 20, 31, 34, 105, 113,
 116–118, 123, 138, 145, 159, 169,
 200, 212, 214, 217, 218, 221, 226
 Sedimentary, 45, 98, 108, 113, 218
 Seismic, 3, 23, 45, 77, 89, 106
 Sequence, 149, 160
 Share, 107
 Shrinkage, 64, 78, 92, 93, 95
 Shutdowns, 145
 Signal, 190, 195
 Software, 60, 161, 162, 168
 Solid, 2, 34, 45, 47, 49, 53, 62, 95, 114, 128,
 139, 196, 217, 218, 220, 226, 230
 Solidification, 38

Solution-enhanced, 216
 Solution-widened, 198
 Species, 2, 25, 232, 238, 240
 Spherical, 119, 124
 Stationary, 90
 Steady-flow, 173, 175
 Steady-state, 4, 152–154, 161, 162, 175
 Steel, 139, 194
 Stem, 115, 190
 Storage, 3, 22, 46, 61, 62, 64, 65, 107, 112,
 120, 121, 123, 125, 126, 129, 134,
 138, 153, 154, 167, 168, 171, 173,
 175, 219, 230
 Strategy, 29, 66, 100, 159, 179, 254
 Stratigraphic, 163, 186
 Stratigraphy, 21, 23, 97, 129
 Stratum, 163, 168
 Stream, 138, 163, 180, 183
 Subdivision, 108, 110, 129
 Substituents, 221, 228, 229
 Suction, 33, 107, 113, 116–119, 125
 Suffosion, 109, 113, 114
 Sulfate, 9, 222, 223, 227, 229, 230, 234
 Superposition, 106, 129
 Symbols, 2, 4, 61–63
 Syncline, 163

T

Technician, 22, 183
 Tectonic, 21, 45, 75–78, 86, 89, 97,
 99–101, 123, 134
 Tendency, 219, 221, 228
 Terrain, 21, 67, 79, 91, 125, 163, 164
 Texture, 20, 211
 Tissue, 246
 Topography, 66, 97, 129, 134, 163, 164,
 198, 201
 Trajectory, 91, 158, 198
 Transducer, 190, 194
 Transient, 4, 152, 224, 229
 Transverse, 84, 217
 Traverse, 48, 185, 188
 Treatment, 40, 100–102, 139
 Triangle, 160
 Turbulent, 180, 200

U

Unsteady-state, 153, 154
 Upgradient, 216

V

Vacuum, [101](#), [107](#), [116–119](#), [126](#)
Valley, [25](#), [33](#), [66](#), [69](#), [70](#), [80](#), [112](#), [122](#),
[125](#), [126](#), [164](#), [166](#), [168](#)
Vegetation, [24](#), [138](#), [198](#)
Velocity, [9](#), [31](#), [91](#), [113](#), [116](#), [124](#), [125](#)
Vibration-induced, [109](#), [114](#), [126](#)
Vicinity, [4](#), [41](#), [81](#), [84](#), [200](#)
Viscosity, [57](#), [200](#)
Viscous, [95](#)
Volcanic, [45](#), [77](#), [78](#)

W

Wastewater, [3](#), [13](#), [115](#)
Water-bearing, [10](#), [12](#), [33](#), [41](#), [146](#), [148](#),
[157](#), [166](#), [179](#), [221](#)
Watershed, [25](#), [28](#)
Wellbore, [174](#)
Wetland, [2](#), [27](#)
Withdrawal, [9](#)